

Sites U1428 and U1429¹

R. Tada, R.W. Murray, C.A. Alvarez Zarikian, W.T. Anderson Jr., M.-A. Bassetti, B.J. Brace, S.C. Clemens, M.H. da Costa Gurgel, G.R. Dickens, A.G. Dunlea, S.J. Gallagher, L. Giosan, A.C.G. Henderson, A.E. Holbourn, K. Ikehara, T. Irino, T. Itaki, A. Karasuda, C.W. Kinsley, Y. Kubota, G.S. Lee, K.E. Lee, J. Lofi, C.I.C.D. Lopes, L.C. Peterson, M. Saavedra-Pellitero, T. Sagawa, R.K. Singh, S. Sugisaki, S. Toucanne, S. Wan, C. Xuan, H. Zheng, and M. Ziegler²

Chapter contents

Background and objectives	1
Operations	2
Lithostratigraphy	4
Biostratigraphy	7
Geochemistry	10
Paleomagnetism	15
Physical properties	17
Downhole measurements	19
Stratigraphic correlation and sedimentation rates	20
References	21
Figures	24
Tables	114

Background and objectives

Integrated Ocean Drilling Program (IODP) Site U1428 is in the northernmost part of the East China Sea at 31°40.64'N, 129°02.00'E and 724 meters below sea level (mbsl), whereas IODP Site U1429 is only 7.4 km away at 31°37.04'N, 128°59.85'E and 732 mbsl (Fig. F1). The sites are in the southern part of the Danjo Basin, which is in the northern tip of the Okinawa Trough. The Danjo Basin is a depression ~80 km wide and ~800 m deep with a sill depth at ~700 m and is surrounded by continental shelves to its west, north, and east. Only its south side is open to the Okinawa Trough (Fig. F2).

Currently, the >500 km wide continental shelf of the East China Sea spreads to the west of the Danjo Basin and also extends further to the northwest to the Yellow Sea. Because the two large rivers, the Yangtze and Yellow Rivers, drain into the Yellow Sea, a significant contribution of fine detrital material from the west is expected. During glacial lowstands, about one-half of the shelf was subaerially exposed and the mouth of the Yellow River advanced southeastward toward the Danjo Basin. Thus, the mouth of the Yellow River was perhaps located only ~150 km northwest of Sites U1428 and U1429 during glacial maxima. During glacial periods, the mouth of the Yangtze River instead advanced to the southeast and was located ~400 km to the southwest.

Sites U1428 and U1429 lie beneath the Tsushima Warm Current, which branches from the Kuroshio Current ~250 km to the south. The sites are also under the influence of East China Sea Coastal Water, which expands eastward from the continental shelf of the northern East China Sea because of the larger discharge of the Yangtze River during summer. Studies on piston cores retrieved from nearby locations suggest fast sedimentation rates of ~300–800 m/m.y. (Kubota et al., 2010; Kubota, 2013), which should allow for high-resolution paleoceanographic reconstruction of the northern East China Sea.

One of the major objectives of IODP Expedition 346 is to reconstruct high-resolution changes in East Asian summer monsoon (EASM) intensity since the Pliocene. The locations of Sites U1428 and U1429 were selected to explore high-resolution changes in Yangtze River discharge through reconstruction of sea-surface salinity (Kubota et al., 2010). Because the Yangtze River drainage basin occupies the portion of southern China where EASM precipitation is most intense, it is reasonable to consider that Yangtze

¹Tada, R., Murray, R.W., Alvarez Zarikian, C.A., Anderson, W.T., Jr., Bassetti, M.-A., Brace, B.J., Clemens, S.C., da Costa Gurgel, M.H., Dickens, G.R., Dunlea, A.G., Gallagher, S.J., Giosan, L., Henderson, A.C.G., Holbourn, A.E., Ikehara, K., Irino, T., Itaki, T., Karasuda, A., Kinsley, C.W., Kubota, Y., Lee, G.S., Lee, K.E., Lofi, J., Lopes, C.I.C.D., Peterson, L.C., Saavedra-Pellitero, M., Sagawa, T., Singh, R.K., Sugisaki, S., Toucanne, S., Wan, S., Xuan, C., Zheng, H., and Ziegler, M., 2015. Sites U1428 and U1429. *In* Tada, R., Murray, R.W., Alvarez Zarikian, C.A., and the Expedition 346 Scientists, *Proc. IODP*, 346: College Station, TX (Integrated Ocean Drilling Program). doi:10.2204/iodp.proc.346.109.2015

²Expedition 346 Scientists' addresses.



River discharge reflects the intensity of EASM precipitation.

The influx of water through the Tsushima Strait is the major source of nutrients as well as freshwater to the marginal sea between the Eurasian continent and the Japanese Islands. Therefore, data from Sites U1428 and U1429 will constrain the history of surface water salinity and nutrient concentration of water that flows into the marginal sea.

The difference in salinity of surface water relative to that of deep water is one of the major controls of deepwater ventilation in the marginal sea west of Japan. The nutrient influx together with the deepwater ventilation rate is the major control of biological productivity in the surface as well as of bottom water oxygenation. Therefore, it is important to document the freshwater and nutrient budgets to best understand the origin of the dark and light layers in the sedimentary record as well as the overall paleoceanographic evolution of this marginal sea.

Operations

Two holes were cored at Site U1428 (proposed Site ECS-1B) and three holes were cored at Site U1429 (alternate Site ECS-1C) using the full and half advanced piston corer (APC) and the extended core barrel (XCB). At both sites, nonmagnetic core barrels were used with the APC system. Only full APC core barrels were oriented. In Hole U1428A, 26 cores extended from the seafloor to 211.5 m core depth below seafloor (CSF-A) (see the “[Methods](#)” chapter [Tada et al., 2015b]), including seven drilled intervals (totaling 37.6 m) through thick sand beds. The cored interval in Hole U1428A was 173.9 m with a recovery of 178.86 m of core (103%) (Table [T1](#); see also Fig. [F2](#) in the “Expedition 346 summary” chapter [Tada et al., 2015a]). After completing Hole U1428A, we moved to Site U1429, which was anticipated to have higher linear sedimentation rates and, therefore, an expanded Late Pleistocene section.

APC coring at Site U1429 was uneventful. Hole U1429A penetrated to 188.3 m CSF-A, including two drilled intervals totaling 4.1 m. Core recovery for Hole U1429A was 190.3 m (103%). Hole U1429B penetrated to 186.2 m CSF-A with a core recovery of 200.9 m (108%). Hole U1429C penetrated to 179.2 m CSF-A, including two drilled intervals totaling 4.9 m. Core recovery for Hole U1429C was 180.7 m (104%) (Table [T2](#); see also Fig. [F2](#) in the “Expedition 346 summary” chapter [Tada et al., 2015a]).

After completing the three holes at Site U1429, we returned to Site U1428 to drill a second, additional hole that provided material to build a complete

spliced section at this site spanning at least the last ~0.3 m.y. and to provide additional material for high-resolution paleoceanographic studies. Hole U1428B was subsequently APC cored to 143.3 m CSF-A (16 cores), with a recovery of 145.85 m (102%).

Transit to Site U1428

The transit to Site U1428 from IODP Site U1427 included a short stop offshore at Kitakyushu, Japan, to evacuate a scientist suffering from kidney stones. The 248 nmi transit between Site U1427 and the evacuation rendezvous coordinates (34°30.0'N, 130°23.0'E) was covered at an average speed of 10.8 kt. The designated rendezvous time was 0800 h on the morning of 11 September 2013. Coordination of the medical evacuation was provided by the Sea Trade and Agency Yokohama and locally by Green Shipping in Moji, Japan. The R/V *JOIDES Resolution* was on location for the evacuation at 0736 h. The sea-going tug *MusashiMaru 2* was alongside by 0752 h. The transfer was completed safely and efficiently by 0754 h. The tug was clear by 0755 h and headed back to shore. The *JOIDES Resolution* then resumed course for Site U1428. The remaining 228 nmi distance was covered in 21 h at an average speed of 10.9 kt. Sea passage ended at 0500 h on 12 September. The vessel was maneuvered over the location coordinates, thrusters were lowered into position, and the vessel was turned over to dynamic positioning control. By 0530 h on 12 September, the vessel was stabilized and rig floor operations began. A Falmouth Scientific positioning beacon (model BAP-547; SN1028W, 16 KHz, 206 dB) was deployed at 0614 h.

Hole U1428A

A three-stand APC/XCB bottom-hole assembly (BHA) was assembled, and the drill string was run to bottom. During the pipe trip, the vibration-isolated television (VIT) subsea camera was deployed. The top drive was picked up, and the drill string was spaced out to just above the seafloor. Because of the presence of submarine cables in the vicinity of this site, a camera survey of the seafloor was conducted to ensure that no holes were spudded into a submarine cable. This was considered precautionary only because the closest cables to the drill site should have been nearly 2 nmi away. A box survey was conducted radiating out from the drill site coordinates in 5 m increments. The total outside diameter of the box was 25 m. This ensured that any of the holes spudded within 15 m of Hole U1428A would be well within the preinspected area. The survey was completed at 1200 h on 12 September 2013, and after re-

turning to zero-zero coordinates, a tag of the seafloor with the drill bit was observed on camera. This established a drill string tag depth of 735.3 meters below rig floor (mbrf), or 1.6 m shallower than the depth predicted with the precision depth recorder (PDR). The pipe was then picked up 3 m, placing the bit at 732.3 mbrf, and Hole U1428A was spudded at 1230 h. The first core barrel recovered 6.37 m of core, establishing an “official” seafloor depth of 735.4 mbrf. Oriented APC coring continued using full-length nonmagnetic core barrels through Core 346-U1428A-18H to a depth of 150.1 m CSF-A. Half APC coring continued from that point through Core 346-U1428A-32H to a total depth of 211.5 m CSF-A. Because of the large accumulation of sand in the formation, further coring at this site was abandoned. The hole was displaced with 80 bbl of 10.5 ppg weighted mud, and the drill string was pulled clear of the seafloor at 0735 h on 13 September. The bit was clear of the rotary table by 0930 h. The positioning beacon was recovered at 0811 h, and the ship was secured for transit by 0940 h. Thrusters and hydrophones were pulled, and the sea voyage to Site U1429 was initiated at 1024 h on 13 September. Total recovery for Hole U1428A was 178.86 m (103%). There were no half APC cores taken in this hole; however, there were seven drilled intervals totaling 37.6 m. Four formation temperature measurements were taken using the advanced piston corer temperature tool (APCT-3) temperature shoe at 34.9, 63.4, 91.9, and 120.4 m CSF-A.

Transit to Site U1429

The transit to Site U1429 from Site U1428 included a brief stop while en route to discharge another scientist, this one suffering from a severe case of shingles. The scientist was evacuated from the *JOIDES Resolution* by a Japanese Coast Guard helicopter. The transfer was completed safely and efficiently by 1100 h on 13 September 2013. The *JOIDES Resolution* then resumed full speed for Site U1429. The 228 nmi to Site U1429 was covered in 1.6 h at an average speed of 7.4 kt. Sea passage ended at 1200 h on 13 September. The vessel was maneuvered over the location coordinates, thrusters were lowered into position, and the vessel was turned over to dynamic positioning control. By 1215 h, the *JOIDES Resolution* was stabilized, and rig floor operations began.

Hole U1429A

A three-stand APC/XCB BHA was assembled, and the drill string was run to the bottom. During the pipe trip, the VIT subsea camera was deployed. The top drive was picked up, and the drill string was spaced

out to just above the seafloor. As at the previous site, a camera survey of the seafloor was conducted to ensure that no holes were spudded into a submarine cable. As before, a box survey was conducted radiating out from the drill site coordinates in 5 m increments. The total outside diameter of the box was again 25 m. This ensured that any of the holes spudded within 15 m of Hole U1429A would be well within the preinspected area. The survey began at 1735 h on 13 September 2013 and was completed by 1945 h. After returning to zero-zero coordinates, a tag of the seafloor with the drill bit was observed on camera. This established a drill string tag depth of 743.6 mbrf, or 2.8 m shallower than the depth predicted with the PDR. The pipe was then picked up 3 m, placing the bit at 740.6 mbrf, and Hole U1429A was spudded at 2045 h. The first core barrel recovered 6.4 m of core, establishing an “official” seafloor depth of 743.7 mbrf. Oriented APC coring continued using full-length nonmagnetic core barrels through Core 346-U1429A-23H to 188.3 m CSF-A. As at Site U1428, large accumulations of volcanic sand in the formation prevented coring to the original deeper objectives. This led to the decision to complete three APC holes through the upper section (~200 m CSF-A) and then abandon the site. The hole was displaced with 75 bbl of 10.5 ppg weighted mud, and the drill string was pulled clear of the seafloor at 0900 h on 14 September, ending Hole U1429A and beginning Hole U1429B. Total recovery for this hole was 190.29 m (103%). No half APC cores were taken in this hole; however, there were two drilled intervals totaling 4.1 m to adjust the core breaks. Four formation temperature measurements were taken using the APCT-3 temperature shoe at 34.9, 61.1, 89.6, and 116.4 m CSF-A.

Hole U1429B

Because a massive sand horizon was also present at this site, the operations plan was revised to eliminate any deep penetration attempt. Instead, the focus was on obtaining two additional ~200 m holes to thoroughly recover the upper section. Hole U1429B began as the drill string cleared the seafloor. The ship was offset 15 m north of Hole U1429A. The bit was positioned at 736.6 mbrf. An APC core barrel was deployed, and Hole U1429B was spudded at 0935 h on 14 September 2013. The 2.93 m of core recovered established a seafloor depth of 743.2 mbrf. APC coring with full-length core barrels continued through Core 346-U1429B-22H to 186.2 m CSF-A. Partial strokes were experienced on Cores 6H, 18H, and 22H; however, all others were full stroke. Hole U1429B was once again terminated just into the volcanic sand.

The hole was displaced with 75 bbl of 10.5 ppg mud, and the drill string was pulled clear of the seafloor at 2210 h on 14 September, ending Hole U1429B. Total recovery for this hole was 200.92 m (108%). Of the 22 cores recovered, all were full-barrel cores. There were no attempted half APC cores.

Hole U1429C

Hole U1429C began as the drill string cleared the seafloor. The ship was offset 15 m south of Hole U1429A. The bit was positioned at 738.6 mbrf. An APC core barrel was deployed, and Hole U1429C was spudded at 2235 h on 14 September 2013. The 4.16 m of core recovered established a seafloor depth of 744.0 mbrf. APC coring with full-length core barrels continued through Core 346-U1429C-24H to 179.2 m CSF-A. Partial strokes were experienced on Cores 6H, 16H, 20H, and 24H; however, all others were full stroke. The hole was once again terminated just into the volcanic sand. Total recovery for Hole U1429C was 180.70 m (103.7%). Of the 22 cores recovered, all were full-barrel cores. There were no attempted half APC cores.

Hole U1429C was displaced with 75 bbl of 10.5 ppg mud, the top drive was set back, and the drill string was pulled clear of the seafloor at 1055 h on 15 September. The pipe was tripped back to the surface, and the BHA racked back in the derrick. Because the move back to Site U1428 was only 4 nmi, the last stand with the bit and outer core barrel components was left hanging on the hook through the rotary table. This saved time and allowed the ship to get under way faster. The positioning beacon was recovered back aboard during the pipe trip at 1142 h. The ship was secured for transit by 1225 h. Thrusters and hydrophones were pulled, and the brief sea voyage to Site U1428 was initiated at 1242 h on 15 September.

Return to Site U1428

The transit back to Site U1428 was quickly accomplished. The 4.0 nmi distance was covered in only 0.75 h at an average speed of 5.3 kt. Sea passage ended at 1330 h on 15 September 2013. The vessel was maneuvered over the location coordinates, thrusters were lowered into position, and the vessel was turned over to dynamic positioning control. By 1345 h, the *JOIDES Resolution* was stabilized, and rig floor operations began.

Hole U1428B

Because of the shallow nature of the single hole and short duration on site, a positioning beacon was not deployed to the seabed. The APC/XCB BHA was quickly assembled, and the drill string was run to

bottom. The ship was offset 15 m north of Hole U1428A. The top drive was picked up, and the pipe was spaced out, positioning the bit at 728.8 mbrf. Hole U1428B was spudded at 1635 h on 15 September 2013. The first core barrel recovered 2.49 m of core, establishing a seafloor depth of 735.8 mbrf. APC coring continued using full-length nonmagnetic core barrels through Core 346-U1428B-16H to 143.3 m CSF-A. Hole U1428B was displaced with 55 bbl of 10.5 ppg weighted mud, the top drive was set back, and the drill string was pulled clear of the seafloor at 0130 h on 16 September. The bit was clear of the rotary table by 0330 h. The bit and bit sub were removed, and the ship was secured for transit by 0345 h. Thrusters and hydrophones were pulled, and the sea voyage to Site U1430 was initiated at 0418 h on 16 September. Total recovery for this hole was 145.85 m (102%). Of the 16 cores recovered, all were full-barrel cores. There were no attempted half APC cores.

Lithostratigraphy

Drilling at Site U1428 penetrated to a maximum subbottom depth of 211.56 m in Hole U1428A, recovering a total of 178.86 m of sediment for a recovery rate of 84.5%. The low recovery rate in Hole U1428A was due to high sand content in the lower part, which required drilling six intervals totaling 37.6 m (see “[Operations](#)”). Otherwise, the recovery rate in the upper part (Cores 346-U1428-1H to 15H; 0–137.13 m CSF-A) was 104%. Drilling at Site U1429 penetrated to a maximum subbottom depth of 188.3 m in Hole U1429A, recovering a total of 190.3 m of sediment for a recovery rate of 103%.

The shipboard lithostratigraphic program involved detailed visual assessment of sediment composition, color, sedimentary structures, and bioturbation intensity, supplemented by petrographic analysis of smear slides (29 from Hole U1428A, 15 from Hole U1428B, 33 from Hole U1429A, and 6 from Hole U1429B) and bulk mineralogic analysis by X-ray diffraction (XRD) (14 from Hole U1428A, 20 from Hole U1429A, and 3 from the sand unit in Hole U1428A). These were used to describe and define major and minor lithologies, define facies and facies associations, and divide the stratigraphic section into major lithostratigraphic units (Figs. [F3](#), [F4](#), [F5](#), [F6](#), [F7](#)).

The sedimentary succession recovered at Sites U1428 and U1429 is divided into two major lithologic units (A and B) distinguished on the basis of sediment composition, referring particularly to the abundance of biogenic components and terrigenous fractions such as clay and sand. Unit A is dominated by calcareous nannofossil ooze and calcareous nannofossil-

rich clay with diatoms and foraminifers throughout. Meter-scale downhole color changes, ranging from olive-gray to greenish gray and light greenish gray are visible but rather subtle. The color changes are better captured by the physical property “color reflectance.” When correlated with downhole variations of carbonate content, all these changes exhibit glacial–interglacial style variability. Moderate to heavy bioturbation is observed throughout the unit. Discrete tephra (i.e., volcanic ash) layers, with thicknesses ranging from decimeters to >0.5 m, occur throughout Unit A at a relatively regular frequency, and dispersed volcanoclastic material represents a minor component throughout the succession. Unit B is dominated by fine- to medium-grained, rounded to subrounded, massive sand. Quartz is the predominant mineral in this mostly unconsolidated unit. Mica is abundant, whereas feldspar, plagioclase, calcite, and hornblende are also commonly present. Physical property measurements, including natural gamma radiation (NGR), magnetic susceptibility, color reflectance, and dry bulk density profiles, reflect the various lithologies and unit boundaries (see “[Physical properties](#)”). The major characteristics of the sedimentary sequences at Sites U1428 and U1429, together with some of the physical properties, are summarized in Figures [F3](#), [F4](#), [F5](#), [F6](#), and [F7](#). Hole-to-hole correlation of the lithostratigraphic units between the two sites is shown in Figure [F8](#).

Unit A

Intervals: 346-U1428A-1H-1, 0 cm, to 15H-CC, 12 cm; 346-U1428B-1H-1, 0 cm, to 16H-1, 84 cm; 346-U1429A-1H-1, 0 cm, to 22H-3, 127 cm; 346-U1429B-1H-1, 0 cm, to 22H-1, 34 cm; 346-U1429C-1H-1, 0 cm, to 24H-1, 54 cm

Depths: Hole U1428A = 0–137.30 m CSF-A; Hole U1428B = 0–136.34 m CSF-A; Hole U1429A = 0–179.36 m CSF-A; Hole U1429B = 0–179.34 m CSF-A; Hole U1429C = 0–178.34 m CSF-A

Age: Holocene to Middle Pleistocene (~0.4 Ma)

Lithologies and structures

Unit A consists of olive-gray, greenish gray, and light greenish gray nannofossil ooze and nannofossil-rich clay with diatoms and foraminifers. The sediment is generally moderately to heavily bioturbated with a fairly homogeneous, structureless appearance. Some intervals have subhorizontal burrows, many of which group together (Fig. [F9](#)). Well-preserved gastropods, scaphopods, and bivalves are observed throughout the unit (Fig. [F10](#)). The major lithology is interbedded with 11 tephra layers with thicknesses ranging from decimeter to 0.5 m, which can be reliably correlated between holes and sites. A thick tephra layer

in the uppermost part of the sequence (interval 346-U1428A-1H-2, 73–118 cm) corresponds to the Kikai-Akahoya (K-Ah) tephra with a ^{14}C age of ~6.82 k.y. before present (BP) (Fukusawa, 1995), whereas a second tephra covering the interval 2H-6, 100–108 cm, corresponds to the Aira-Tanzawa tephra with a ^{14}C age of ~25.9 k.y. BP (Kitagawa and van der Plicht, 1998), suggesting the same tephrostratigraphy as that of Ijiri et al. (2005). Two different types of vitric tephra are observed: one is dark colored and coarse grained, containing glass as well as minor quartz and other minerals, and the other is whitish colored and very fine grained, containing pure volcanic glass (Fig. [F11](#)).

Downhole color changes are rather subtle. Meter-scale variations of colors ranging from olive-gray to greenish gray and light greenish gray are observed and reflect changes in carbonate content based on smear slide observations (Fig. [F12](#)). This is further confirmed by XRD results (Figs. [F13](#), [F14](#)). In general, light greenish gray colors reflect a higher nannofossil content. Although the color contrast is low and the transitions are gradual, these alternations of lithologies are better reflected in records of NGR, magnetic susceptibility, and color reflectance (see “[Physical properties](#)”).

Composition

The principal components of lithologies in Unit A are mainly biogenic with minor amounts of terrigenous and volcanic material (see Site U1428/U1429 smear slides in “[Core descriptions](#)”). Calcareous nannofossils dominate the biogenic fraction, foraminifers are commonly present, and diatoms represent a relatively low component (Fig. [F15](#)). Among the biosiliceous components, radiolarians and silicoflagellates (usually rare because they are too fragile) are also easily found.

The terrigenous fraction in this unit is dominated by clay and fine silty clay and occasionally by fine-grained sand fractions. Volcanic glass and pumice account for nearly 100% of the discrete tephra layers. Variable abundances of calcareous nannofossils within Unit A are observed, but a quantitative estimate of the amplitude of their variations cannot be performed based solely on smear slide analyses. However, the most abundant nannofossil contents clearly match the lighter sediment colors (light greenish gray) and vice versa.

In Unit A, the terrigenous component is low and mostly consists of quartz grains and rare clay minerals. Authigenic pyrite and dolomite represent occasionally important lithologic accessories. The fine-grained sand that is found in thinly bedded layers

appears well sorted and made of quartz and abundant mica and occurs only intermittently.

Bulk mineralogy

The XRD analysis results are listed in Tables T3 and T4. In general, the Middle Pleistocene–Holocene sediment at these two sites is composed mainly of quartz, plagioclase, clay minerals (including smectite, illite, and kaolinite and/or chlorite), and calcite, as well as minor amounts of halite and pyrite. Dolomite is sparsely present between 50 and 100 m CSF-A in Hole U1428A and between 60 and 150 m CSF-A in Hole U1429A. There may be other minor minerals that were not identified by the XRD analysis of bulk samples. Calcite is mostly derived from nanfossils and foraminifers, both of which are abundant in the calcareous nanfossil ooze throughout the unit at the two sites.

Figures F13 and F14 show the downhole variations in peak intensity of the identified minerals at Sites U1428 and U1429. In general, the peak intensities of quartz, plagioclase, K-feldspar, and clay minerals (smectite, illite, kaolinite and/or chlorite) in Unit A show four cycles. For example, quartz shows relatively higher peak intensity at 7.3, 52.8, 93.0, and 113.6 m CSF-A at Site U1428 and at 7.6, 90.8, 128.3, and 157.2 m CSF-A at Site U1429. In contrast, the calcite peak intensities display opposing variations from the detrital minerals. Cyclic variations in mineral composition are also reflected by color and physical properties, as discussed above. Pyrite shows higher intensity peaks between 70 and 110 m CSF-A at Site U1428 and between 130 and 170 m CSF-A at Site U1429. In addition, halite shows a generally increased downhole trend at both sites.

Unit B

Intervals: 346-U1428A-15H-CC, 12 cm, to 32H-4, 1.16 cm; 346-U1428B-16H-1, 84 cm, to 16H-7, 80 cm; 346-U1429A-22H-4, 0 cm, to 23H-4, 98 cm; 346-U1429B-22H-1, 34 cm, to 22H-4, 136 cm; 346-U1429C-24H-1, 54–141 cm

Depths: Hole U1428A = 137.30–211.53 m CSF-A; Hole U1428B = 136.34–143.3 m CSF-A; Hole U1429A = 179.36–188.23 m CSF-A; Hole U1429B = 179.34–186.22 m CSF-A; Hole U1429C = 178.34–179.21 m CSF-A

Age: Middle Pleistocene (~0.4 Ma)

Lithologies and structures

The principal lithology of Unit B consists of unconsolidated fine- to medium-grained, well-sorted, rounded to subrounded, massive sand (Fig. F16). No sedimentary structures can be observed because of

heavy drilling disturbance and very poor recovery. Between 159.50 and 167.25 CSF-A in Hole U1428A (Sections 346-U1428A-23H-1A to 23H-6A), a nanfossil-rich clay unit with a thickness of 7.7 m is observed.

Composition

Unit B is composed predominantly of fine- to medium-grained sand. The mineralogical composition consists of abundant quartz and mica. Other minerals include feldspar, plagioclase, calcite, hornblende, zircon with minor clay minerals, and volcanic glass. Shell fragments and foraminifers are also present (Fig. F16).

Bulk mineralogy

The results of XRD analyses conducted on sand from Hole U1428B are listed in Table T5. The sand consists mainly of quartz, K-feldspar, plagioclase, detrital calcite, muscovite with minor hornblende, pyroxene, dolomite, smectite, and chlorite (Fig. F17). Zircon was also observed in smear slides but not detected by XRD, possibly because of very low zircon content in the bulk sand. In addition, some opaque black mineral/rock fragments are observed by microscope but their identity remains unknown. These black minerals are likely to be weathered volcanic rock (with smectite coating). However, exact identification requires further onshore observation. Most of the minerals/rock fragments have very similar grain size (60–120 μm) and are characterized by very rounded to subrounded shape, suggesting a fairly long transport distance, during which the grains were sorted.

Summary and discussion

The sedimentary successions at Sites U1428 and U1429 record the paleoceanographic history of the northwestern end of the Okinawa Trough from the Middle Pleistocene to Holocene. The lithostratigraphic characteristics appear to act as a sensitive recorder of regional oceanographic changes, with far-reaching linkages to global climatic variations. Furthermore, owing to their targeted locations, the sedimentary successions at these two sites bear great potential for studying sediment source and sediment transport dynamics, with paleoenvironmental implications closely associated with the Asian continent.

The lithology of Sites U1428 and U1429 consists of two units (A and B) based on biocalcareous and terrigenous content including clay and sand. Unit A is composed mainly of calcareous nanfossil ooze and calcareous nanfossil-rich clay and is the predominant unit at both sites. Subtle color changes are

observed downhole, presumably as a result of variations in nannofossil content. This inference is further supported by variations of calcite content measured through XRD analysis. The meter-scale color changes through the unit imply, in general, that the paleoceanographic conditions responded to glacial–interglacial variations of global climate during the last 400 k.y. Of more region-specific relevance to eventual interpretation of the sequence will be sea level changes and the associated repeated emergence and exposure of wide continental shelves, and the evolution of the Kuroshio Current. Terrigenous sediment flux to the sites is expected to closely respond to the emergence and exposure of the continental shelves on glacial–interglacial timescales. However, shipboard observations did not provide strong lithologic and sedimentological evidence. Further onshore investigation is highly needed in this regard.

Unit B is a sand unit, consisting of fine- to medium-grained, rounded to subrounded, massive sand with a thickness reaching 74 m in Hole U1428A. The upper age limit of the sand unit is ~0.4 Ma, which is equivalent to the bottom age of the overlying Unit A (see “[Biostratigraphy](#)”). Drilling at neither site penetrated through this unit and therefore did not allow determination of the bottom age of the sand unit. Little in the way of sedimentary structure is preserved because of drilling disturbance and low recovery of the mostly unconsolidated sand and facies or facies associations could not be classified. However, given that the sand is well sorted, rounded to subrounded in grain shape, and contains a high concentration of mica, it strongly suggests that the unit formed by upward accumulation of sand, which had been transported a long distance by currents (e.g., bottom currents), as opposed to gravity (debris) flow, such as in the case of the formation of turbidites. Further mineralogical and geochemical investigations should lead to a better understanding of the provenance of the sand, together with the transportation dynamics and paleoceanographic implications.

Biostratigraphy

At Sites U1428 and U1429, two Late Pleistocene sedimentary successions (~212 and ~178 m thick, respectively) were recovered. With the exception of the sand intervals in Hole U1428A, nannofossils are generally abundant and exhibit good preservation. One calcareous nannofossil datum, the first occurrence (FO) of *Emiliania huxleyi*, is documented. Diatoms are generally common and exhibit good preservation. No biostratigraphically useful marker species are recorded. Variable abundances of *Chaetoceros*

spores and *Paralia sulcata* indicate the occasional presence of a productive coastal environment. Freshwater diatoms show significant peaks throughout the succession. Planktonic foraminifers are abundant and well preserved, except in the sand horizons, which are barren. Planktonic foraminiferal assemblages are diverse and typical of subtropical environments. The last occurrence (LO) of *Globigerinoides ruber* (pink) recorded at Sites U1428 and U1429 is consistent with the calcareous nannofossil datum. Benthic foraminifers vary markedly in abundance but are generally well preserved. The overall composition of assemblages indicates upper bathyal paleodepths. Downcore changes in assemblage composition at Sites U1428 and U1429 reflect variations in organic export fluxes to the seafloor and bottom water ventilation that are probably linked to glacial–interglacial oscillations in surface productivity and ocean circulation. The integrated calcareous microfossil biozonation is shown in Figure F18 with microfossil datums presented in Table T6. A biostratigraphic age-depth plot is shown in Figure F19. See “[Stratigraphic correlation and sedimentation rates](#)” for a discussion of sedimentation rates at Sites U1428 and U1429.

Calcareous nannofossils

Calcareous nannofossil biostratigraphy is based on the analysis of 62 core catcher and split-core section samples from Holes U1428A (25 samples), U1428B (15 samples), and U1429A (22 samples). Nannofossils are present throughout the Pleistocene succession, but the sand intervals tend to contain few or no nannofossils. A barren sand interval is present in Hole U1428A near 91.8 m CSF-A (Sample 346-U1428A-10H-CC), and few to no nannofossils are recorded deeper than 137.3 m CSF-A (Sample 15H-CC), also corresponding to sand layers (Table T7; Fig. F20). Outside of the sand intervals, nannofossils are generally abundant and preservation is mostly good (Table T7).

Nannofossil diversity at Sites U1428 and U1429 is high. The nannofossil assemblage consists of 29 taxa, including *Braarudosphaera bigelowii*, *Calcidiscus leptopus*, *Calciosolenia murrayi*, *Ceratolithus cristatus*, *Coccolithus pelagicus*, *E. huxleyi*, *Florisphaera profunda*, *Gephyrocapsa caribbeanica*, *Gephyrocapsa muelleriae*, *Gephyrocapsa oceanica*, *Gephyrocapsa* spp. (>4 µm), *Gephyrocapsa* spp. large (>5.5 µm), small *Gephyrocapsa* spp. (<4 µm), *Helicosphaera carteri*, *Helicosphaera inversa*, *Helicosphaera pavementum*, *Helicosphaera* spp., *Helicosphaera wallichii*, *Oolithothus fragilis*, *Pontosphaera japonica*, *Pontosphaera multipora*, *Pontosphaera* spp., *Reticulofenestra minuta*, *Rhabdosphaera clavigera*, *Syracosphaera* spp., *Umbellosphaera irregularis*, *Umbel-*

losphaera tenuis, *Umbilicosphaera foliosa*, and *Umbilicosphaera sibogae* (Fig. F21). Reworked species include *Discoaster barbadiensis* (LO at 34.76 Ma) in Sample 346-U1428A-1H-CC (6.32 m CSF-A); *Pseudoemiliana lacunosa* (LO at 0.44 Ma) in Samples 346-U1428A-12H-5W, 75 cm, 346-U1428B-13H-CC, and 346-U1429A-12H-CC (108.1, 107.2, and 109.1 m CSF-A, respectively); and *Sphenolithus* spp. (LO at 3.54 Ma) in Sample 346-U1428B-12H-CC (107.2 m CSF-A) (Table T7).

The base of nannofossil Zones CN15/NN21 is recognized (Fig. F18) based on the FO of *E. huxleyi* in all three holes drilled at Sites U1428 and U1429. Although *E. huxleyi* is generally common to dominant when present, its distribution is discontinuous, particularly near the beginning of its range (Table T7). As such, *E. huxleyi* may occur deeper than Section 346-U1429A-13H-4W (114.6 m CSF-A), although it was not observed in the studied core catcher samples. The underlying strata are included in nannofossil Zones CN14b/NN20 based on the absence of *P. lacunosa*, but the base of these zones (i.e., the LO of *P. lacunosa*) is not identified.

Radiolarians

A total of 26 core catcher samples from Holes U1428A and U1429A were prepared for radiolarian analyses. Radiolarians are generally abundant throughout the section (Table T8; Fig. F20).

Buccinosphaera invaginata and *Collosphaera tuberosa*, which are key species of the tropical radiolarian zonal scheme, are scarce in Holes U1428A and U1429A (Table T8); therefore, datum levels are not specified. Because *Stylatractus universus*, which became extinct at 0.44 Ma in the Pacific, is absent in the whole section, the section may be placed in Zones RN16 (Middle Pleistocene) and RN17 (Late Pleistocene) in the low-latitude radiolarian zonation (Fig. F18).

Radiolarian assemblages in Holes U1428A and U1429A are mainly composed of subtropical species (e.g., *Dictyocoryne profunda*, *Dictyocoryne truncatum*, *Didymocorytis tetrathalamus*, *Euchitonia furcata*, *Hymeniastrum euclidis*, and the *Octopyle/Tetrapyle* group). In addition to those radiolarians, *Actinomma boreale*, *Actinomma leptodermum*, *Cycladophora davisiana*, and *Lithomelissa setosa* are common.

Based on counts of >200 specimens in 19 core catcher and mudline samples from Hole U1429A, significant changes in the relative abundance of seven radiolarian groups are documented in Figure F22. The *Octopyle/Tetrapyle* group fluctuates significantly through the section, with a similar trend to the sediment color index L* (e.g., high abundances

of this taxon coincide with high L* values). Such increasing abundance of this radiolarian group suggests higher nutrient supply from the shelf area of the East China Sea (Chang et al., 2003). In contrast, *A. boreale* and *A. leptodermum* show low abundances coinciding with high L* values. Common occurrences of both species might be associated with the presence of cold water at any depth in the water column as demonstrated in the shallow water of the Norwegian fjords (Bjørklund, 1974), the Arctic Seas (Itaki et al., 2003), and the deep water of the marginal sea between the Korean Peninsula and the Japanese Islands (Itaki, 2003).

Diatoms

Diatom biostratigraphy was based on smear slides from core catcher and toothpick samples. A total of 37 core catcher samples were examined (18 from Hole U1428A and 19 from Hole U1429A). In addition, two toothpick samples from Hole U1429A were also observed. Because no biostratigraphically useful marker species were found, age assignments were not possible. Preservation is good in the upper 63 m CSF-A in Hole U1428A, becoming moderate toward the base of the succession. In Holes U1428A and U1429A, preservation is good throughout the succession. Significant amounts of reworked diatom specimens are found in both sites, and no diatoms were observed in the sand samples (Table T9; Fig. F23).

Diatom abundances decrease from abundant to rare toward the base of the succession at Sites U1428 and U1429. *Chaetoceros* spores and *P. sulcata* abundances vary from barren to abundant throughout the succession (Table T9; Fig. F23), indicating the occasional presence of a productive coastal environment. Diatom freshwater species show significant peaks in abundance at both sites.

Planktonic foraminifers

Planktonic foraminifers were examined in core catcher samples from Holes U1428A and U1429A (41 samples). Relative abundance of taxa and visual estimates of assemblage preservation are presented in Table T10. Planktonic foraminifers are abundant and well preserved, accounting for >99% of the total foraminiferal assemblage, except in samples from sand horizons, which are barren (Samples 346-U1428A-15H-CC, 18H-CC, 21H-CC, 24H-CC, and 26H-CC) (Fig. F20).

Planktonic foraminiferal assemblages are diverse and typical of subtropical environments. Common species include *Globigerina bulloides*, *Globigerinoides glutinata*, *G. ruber*, *Globigerinoides sacculifer*, *Globorotalia menardii*, *Globorotalia truncatulinoides*, *Neogloboquad-*

rina dutertrei, *Neogloboquadrina incompta*, *Neogloboquadrina pachyderma* (dextral), *Orbulina universa*, and *Pulleniatina obliquiloculata* (Fig. F24). The LO of *G. ruber* (pink), which is recorded at 0.12 Ma in the Pacific and Indian Oceans, occurs between Samples 346-U1428A-5H-CC (44.83 m CSF-A) and 6H-CC (54.7 m CSF-A), between Samples 346-U1428B-5H-CC (40.62 m CSF-A) and 6H-CC (50.1 m CSF-A), and between Samples 346-U1429A-7H-CC (61.38 m CSF-A) and 8H-CC (71.0 m CSF-A). The species *Globigerinella calida* is recorded in Samples 346-U1428A-1H-CC through 14H-CC (6.3–129.9 m CSF-A), except for Sample 10H-CC. In Hole U1429A, this species is observed intermittently in Samples 346-U1429A-1H-CC through 16H-CC (6.4–137.6 m CSF-A) (Table T10). The FO of this species, recorded at 0.22 Ma in the South Pacific (Chapronière et al., 1994), may occur earlier in the East China Sea, as this species was found in Pliocene sediment from the Okinawa-jima Island, southern Japan (Hanagata, 2004). The species *Globorotalia flexuosa* is observed in Samples 346-U1428A-14H-CC (129.88 m CSF-A), 346-U1429A-7H-CC (61.4 m CSF-A), and 346-U1429A-21H-CC (175.8 m CSF-A). However, the LO of this species is difficult to constrain, as it is extremely rare at Sites U1428 and U1429. The co-occurrence of *G. ruber* (pink) and *G. flexuosa* in Samples 346-U1428A-14H-CC, 346-U1428B-14H-CC, and 346-U1429A-21H-CC indicates an age younger than 0.4 Ma for these samples. Based on these occurrences, the planktonic foraminiferal Zone PT1b (Pleistocene) is recognized, which is in agreement with the calcareous nannofossil biostratigraphy (Fig. F18; Table T6).

G. ruber and *G. bulloides* show relatively constant abundances except for a few horizons, where foraminifera are rare (Fig. F24; Table T10). In modern conditions, *P. obliquiloculata* is more abundant along the edge of the continental shelf within the main path of the Kuroshio Current (Xu and Oda, 1999). The absence of *P. obliquiloculata* in Samples 346-U1428A-7H-CC (63.8 m CSF-A) and 346-U1429A-8H-CC (71.0 m CSF-A) suggests that these intervals correspond to glacial episodes, when the warm water inflow from the Pacific through the Okinawa Trough is restricted due to topographic changes during lowstands. In the East China Sea, *Globigerina quinqueloba* shows higher abundance near river mouths, where surface seawater is characterized by low temperature (<13°C in winter and <27.5°C in summer) and low salinity (<34‰ in winter and <32‰ in summer) (Xu and Oda, 1999). This species occurred more abundantly (~30% of assemblages) at ~19–10 ka during the last deglaciation. In Sites U1428 and U1429, this species exhibits relatively high abundance in several horizons (Fig. F24), which may correspond to sea

level lowstands. Detailed quantitative assemblage study is required to clarify the timing and amplitude of these assemblage changes.

Benthic foraminifers

Benthic foraminifers were examined in core catcher samples from Holes U1428A (23 samples) and U1429A (19 samples). Samples with an average volume of ~20 cm³ were processed from all core catchers to obtain quantitative estimates of benthic foraminiferal distribution patterns downhole. The mudline sample recovered in Hole U1428A was also investigated. To assess assemblage composition and variability, all specimens from the >150 µm fraction were picked and transferred to slides for identification and counting. The presence and distribution of benthic foraminifers was additionally checked in the 63–150 µm fraction to ensure that assemblages in the >150 µm fraction were representative and that small species such as phytodetritus feeders or small infaunal taxa were not overlooked. Core catcher samples were also examined for the presence of ostracods during shipboard preparation of benthic foraminifer samples.

Benthic foraminifers vary markedly in abundance but are generally well preserved throughout the ~212 and ~178 m thick Pleistocene successions recovered in Holes U1428A and U1429A (Figs. F20, F25; Table T11). However, Samples 346-U1428A-15H-CC through 18H-CC (137.3–153.83 m CSF-A), 346-U1428A-24H-CC through 26H-CC (172.91–182.9 m CSF-A), and 346-U1429A-13H-CC (116.42 m CSF-A), which correspond to sand horizons, are barren. Sample 346-U1428A-10H-CC, which is from a reworked ash layer, contains only rare benthic specimens. A total of 89 benthic foraminiferal taxa were identified. Table T11 summarizes the downcore distribution of benthic foraminifers in core catcher samples from Holes U1428A and U1429A. Figures F26 and F27 illustrate characteristic taxa.

The overall composition of assemblages indicates upper bathyal paleodepths throughout the Late Pleistocene. Species frequently recorded through the succession include the calcareous species *Ammonia takanabensis*, *Amphicoryna scalaris*, *Bolivina robusta*, *Bulimina aculeata*, *Bulimina marginata*, *Chilostomella oolina*, *Cibicidoides lobatulus*, *Cibicidoides pachyderma*, *Globobulimina pacifica*, *Globobulimina pupoides*, *Hoeglundina elegans*, *Melonis barleeanus*, *Planulina wuellerstorfi*, *Pullenia bulloides*, *Quinqueloculina* spp., and *Uvigerina peregrina* as well as the agglutinated species *Martinotiella communis* and *Sigmoilopsis schlumbergeri*. Downcore changes in assemblage composition at Sites U1428 and U1429 reflect variations

in organic export fluxes to the seafloor and bottom water ventilation that are probably linked to glacial–interglacial oscillations in surface productivity and ocean circulation. In particular, the buliminids, globobuliminids, uvigerinids, and miliolids, which can be used to track changes in productivity and dysoxia (Jorissen et al., 2007), show marked fluctuations in abundance throughout the succession (Fig. F25). Higher abundance of these taxa during intervals of lower carbonate content and lower L^* values reflect enhanced productivity, possibly associated with increased monsoonal winds during glacials. Higher frequency variability associated with millennial-scale climate events may be identified in higher resolution studies but is not detected in core catcher samples because of the coarse shipboard sampling resolution.

Ostracods

Ostracods were examined in core catchers and the mudline sample from Hole U1428A during shipboard examination for benthic foraminifers. All specimens present in the $>150\ \mu\text{m}$ fraction were picked and transferred to slides for identification and counting. Ostracod taxa were identified to genus level and in some cases to species level. Their preservation varies from moderate to very good, and their abundance varies from absent (deeper than 137 m CSF-A) to ~ 30 specimens per sample in the upper part of the record (Fig. F20). About 20 genera were recognized, including reworked shallow taxa (e.g., *Aurila*, *Callistocythere*, and *Puriana*) (Table T12). The general assemblage composition indicates upper bathyal paleodepths. The main genera recorded through the succession include (in order of decreasing abundance) *Krithe*, *Legitimocythere*, *Bradleya*, *Argilloecia*, *Cytheropteron*, and *Amphileberis*. Figure F28 shows characteristic ostracods found in Hole U1428A. Downhole changes in assemblage composition in Hole U1428A suggest variability in organic flux to the seafloor and bottom water ventilation. Detailed postexpedition examination will be carried out to complete the characterization of the ostracod assemblage at this site.

Mudline samples

The mudline sample from Hole U1428A was gently washed in order to preserve fragile, agglutinated foraminifer specimens with extremely low fossilization potential. The mudline sample contains rare specimens of the agglutinated species *Reophax scorpiurus* and *Reophax spiculifer* and abundant calcareous taxa including *Bolivina pacifica*, *Bolivina subspinescens*, *B. aculeata*, *C. oolina*, *Fursenkoina bradyi*, *G. pacifica*, *Hyalinea balthica*, *P. wuellerstorfi*, *P. bulloides*, and *U. peregrina* (Figs. F29, F30). The dominance of *Globobulim-*

ina, *Chilostomella*, and *Fursenkoina* spp. in the mudline assemblage points to a high organic export flux and dysoxic conditions at the seafloor and upper centimeters of the sediment. The mudline sample contains few planktonic foraminifers, *G. bulloides*, *G. calida*, *Globigerina aequilateralis*, *G. ruber*, *G. inflata*, *N. dutertrei*, *N. incompta*, *O. universa*, and *P. obliquiloculata*.

The calcareous nannofossil assemblage recovered in the mudline sample from Hole U1428A shows high diversity and good preservation as indicated by the presence of coccospheres, as well as fragile species (e.g., *E. huxleyi*). Specimens found in the mudline sample include *C. leptoporus*, *C. murrayi*, *E. huxleyi*, *F. profunda*, *G. oceanica*, *H. carteri*, *H. wallichii*, *R. clavigera*, *Syracosphaera* cf. *pulchra*, *U. sibogae*, and small *Gephyrocapsa* spp. ($<4\ \mu\text{m}$) (Fig. F31).

Geochemistry

Sites U1428 and U1429 are located in the East China Sea, just west of the southern Japanese island of Kyushu (“**Background and objectives**”). These sites are located ~ 7.4 km from each other and have high sedimentation rates with relatively high carbonate contents compared to other sites drilled during Expedition 346. As this location sediments offer a prime opportunity to reconstruct paleoceanographic records from a variety of proxies based on foraminiferal carbonate and organic geochemistry, it is important to establish the baseline geochemical properties of the interstitial water and solid samples to support these efforts.

The terrestrial source of material is an important component at Sites U1428 and U1429, as these sites are possibly under the influence of the Yangtze (Changjiang) and Yellow (Huanghe) Rivers. A piston core (MD98-2195), collected from the IMAGES IV cruise near this site, served as one of the presite survey data sources. According to a broad array of geochemical analyses performed on this core (Kawahata et al., 2006; Ijiri et al., 2005; Kawahata and Oshima, 2004), the site has a high sedimentation rate along with high organic carbon contents (1.5 wt% for the last ~ 42 k.y.). During Expedition 346, core recovery of the sites was limited to 150 and 186 m CSF-A, respectively, because of the presence of sand layers at deeper depths.

The very rapid sedimentation rates determined for piston Core MD98-2195 are intriguing to interstitial water studies. At such rates, downward advection of water can generally outpace upward diffusion for most dissolved species. Consequently, unusual interstitial water profiles can develop. However, the geochemistry program at Sites U1428 and U1429 began

as an effort to construct carbonate and organic matter profiles in line with the paleoceanographic objectives of the expedition.

Sampling

The initial geochemistry plan was a straight path. As there would be three deep holes and multiple logging exercises at a single location (Site U1428), we would take routine sets of samples for solid-phase, interstitial water, and gas analyses in Hole U1428A. The solid-phase samples would be a mix of squeeze cake and discrete samples because the squeeze cake samples represent an amalgamation of sediment over 5 cm or more. The water samples would include one squeezed interstitial water (IW-Sq) sample for Cores 346-U1428A-1H through 3H, one IW-Sq every other core for Cores 4H through 9H, and one IW-Sq every 30 m over the next several hundred meters. The water program would be limited partly because we knew that the high sedimentation rate might lead to complicated profiles of dissolved species, difficult to interpret without numerous measurements. We would, however, supplement the routine water sampling with 15 Rhizon samples at the top of Hole U1428A, primarily to connect shallow and deep interstitial water profiles of certain dissolved constituents (Mn, Fe, and NH_4^+). The gas samples would be one headspace sample per core, as mandated for safety reasons.

Interstitial water alkalinity is the first measurement completed in the Geochemistry Laboratory. The limited sampling in Hole U1428A provided an intriguing result within hours after drilling commenced: the alkalinity profile (presented below) had an unusual convex upward profile that peaked somewhere between 36 and 55 m CSF-A. We noted this oddity but placed minimal effort toward understanding its cause, given objectives and scheduling for Site U1428 and our preconceived ideas regarding profiles of dissolved constituents in rapidly accumulating sediment. The termination of Hole U1428A in sand horizons deeper than 140 m CSF-A, the detour to Site U1429, and the return to Hole U1428B (“**Operations**”) modified geochemistry plans at this location considerably, and we put effort into generating potential glacial–interglacial oscillations in sediment composition and constraining the cause of the alkalinity peak.

Upon completing both sites, the geochemistry group collected and analyzed a range of samples. These included the following (Tables **T13**, **T14**, **T15**, **T16**, **T17**, **T18**):

- 102 sediment samples taken from interstitial water squeeze cakes and also additional core sampling (CARB and SRA).
- 2 mudline (ML) samples, representing water from inside the liner of the uppermost cores in Holes U1428A and U1429A.
- 18 interstitial water samples from whole-round squeezing (IW-Sq) of discrete intervals in Holes U1428A and U1429A (9 samples from each hole).
- 59 interstitial water samples from Rhizons (IW-Rh) of discrete points: 15 over the upper 8.5 m in Hole U1428A as planned, 20 in Hole U1429A, and 24 in Hole U1428B to “chase” the origin of the alkalinity peak (below).
- 41 headspace (HS) gas samples.

Interstitial water sampling modifications

Several aspects of interstitial water sampling at Sites U1428 and U1429 warrant further mention. For all IW-Sq samples, a 0.20 μm Whatman Puradisc filter was added “in series” to the standard 0.45 μm filter between the squeezer and the sample syringe. This approach was chosen to address the consistent offset in concentrations of certain dissolved constituents between IW-Sq and IW-Rh samples, as the discrepancy might reflect filter size (discussed in previous Expedition 346 site chapters).

Rhizon sampling in Holes U1429A and U1428B was carried out in an unconventional manner in an effort to locate the precise depth of the alkalinity peak in these holes, and therefore, the sequence and timing of Rhizon sampling proceeded on the basis of initial “low-resolution” alkalinity measurements. For example, once it was established that the alkalinity peak in Hole U1428B lay between Sections 346-U1428B-6H-1 and 7H-4, we pulled the remaining sections from Core 6H-1 while they equilibrated for NGR logging and took second and third batches of Rhizons. The procedure is not ideal for absolutely accurate and precise alkalinity measurements because it adds time between sample recovery and extraction. However, such “real-time” geochemical tracking may be ideal for addressing certain questions and cannot be accomplished practically with IW-Sq samples.

We had difficulty inserting Rhizons into cores deeper than 40 m CSF-A at previous sites (see “**Geochemistry**” in the “Site U1422” chapter and “**Geochemistry**” in the “Site U1424” chapter [Tada et al., 2015c, 2015d]). To conduct the above sampling, we used the end of a “swizzle stick” to make a small hole in

the sediment before inserting the Rhizon. This is a piece of wood with a diameter slightly smaller than the Rhizon.

Interstitial water observations

While chasing the alkalinity peak at these sites with Rhizons, we made two observations that seem pertinent to understanding the geochemistry. First, the odor of H₂S was detectable in core sections between 42 and 54 m CSF-A. Second, the water flow was extremely fast for several Rhizons. In particular, 10 mL of water was collected within 12 min for Samples 346-U1428A-6H-1, 50 cm, 12H-2, 80 cm, and 15H-1, 55 cm, and Samples 346-U1428B-5H-7, 20 cm, and 6H-2, 30 cm. These are very porous (and permeable) horizons, as also seen in the gamma ray attenuation (GRA) density records (“[Physical properties](#)”). Additionally, it is important to note that newer syringes have better suction than preused syringes and reduce extraction time.

Carbonate and organic carbon

A relatively high resolution solid-phase analysis plan was conducted at Sites U1428 and U1429. In addition to squeeze cake samples, two additional discrete sediment samples were collected per core for the measurement of carbonate and organic carbon contents (CARB and SRA samples).

Calcium carbonate contents in Hole U1428A display a cyclic pattern, alternating between low values of ~15 wt% and high values of ~35 wt% (Fig. [F32](#)). It appears that the profile illustrates glacial–interglacial changes since marine isotope Stage (MIS) 11. CaCO₃ contents increase during the interglacial period and decrease during glacial times. Deeper than 124 m CSF-A, CaCO₃ contents fluctuate significantly, which is associated with the alternating mud and sand layers near the bottom of the hole. CaCO₃ contents at Site U1429 (Fig. [F33](#)) have a similar CaCO₃ profile to Site U1428, but the stratigraphy is different because Site U1429 has a higher sedimentation rate. CaCO₃ analyses were normally performed only in samples from the first hole of each drilled site, but for Site U1428, CaCO₃ determinations were also performed in Hole U1428B. This approach was used in order to better constrain the observed long-term variability as first measured in Hole U1428A.

The organic carbon contents vary from a relative high in the uppermost samples at Site U1428 (total organic carbon [TOC] = ~1.5 wt%) to almost zero in the basal sand layers. This change is a gradual decrease with depth but exhibits a sawtooth pattern with up to 0.20 wt% variance. However, at Site U1429 there is no apparent decrease and TOC con-

tents remain fairly stable, close to 1 wt%, all along the record with variation from 0.7 to 1.6 wt%. An exception to this is seen in samples taken at tephra horizons (80–90 m CSF-A for Hole U1428A and 64–65 m CSF-A for Hole U1429A) and sand layers (starting at 133 m CSF-A for Hole U1428A and 156 m CSF-A for Hole U1429A). The higher sedimentation rate found at Site U1429 appears to enhance the preservation of the sedimentary organic matter, as can be perceived by the relatively high and constant TOC contents at that site.

Total nitrogen (TN) contents are low, as observed at previous sites (Figs. [F32](#), [F33](#)). However, they closely follow the TOC pattern of each site, decreasing over depth. Site U1428 shows slightly higher TN concentrations for the uppermost 50 m CSF-A and slightly lower TN concentrations deeper than 115 m CSF-A. The C:N ratio is low and follows the TOC trend but is meaningful because of very low N content, as discussed by Kawahata et al. (2006). Ship conditions (sea state, which interferes with the weighing of sample) and low TOC and N contents at this site caused measured values to be near the error for this method, thus the C:N values are not necessarily reflecting a definitive origin for the organic matter.

Alkalinity and sulfate

The most immediate and perhaps most unusual shipboard geochemical finding at Sites U1428 and U1429 is the alkalinity profile (Fig. [F34](#)). Alkalinity is 2.37 mM in both mudline samples. This value is very close to the sum of dissolved inorganic carbon and dissolved B for deep water with a salinity of 35 (Table [T10](#) in the “Methods” chapter [Tada et al., 2015b]). Below the seafloor, alkalinity rises to a maximum between 45 and 48 m CSF-A. The rise is complicated and convex downward at both sites. In Hole U1428B, where a series of Rhizons were placed to find the depth, the maximum is at 47.5 ± 0.8 m CSF-A. Although nearly coincident in terms of depth, maximum alkalinity is greater at Site U1429 (29.6 mM at 46 m CSF-A) than at Site U1428 (23.5 mM). From 48 m CSF-A to the base of the holes at both sites, alkalinity generally decreases, reaching 7.4 at ~162 m CSF-A in Hole U1428A and 12.8 mM at ~177 m CSF-A in Hole U1429A.

The shapes of the alkalinity profiles at Sites U1428 and U1429, at least over the uppermost 45–48 m, are different from most marine sediment sequences, including the sites drilled previously during Expedition 346. They strongly suggest very rapid sedimentation and a “point source” of alkalinity. An extreme sedimentation rate would lead to a convex downward alkalinity profile because dissolved HCO₃⁻ cannot diffuse through porous media very fast. Such a

rate is also consistent with age determinations of piston Core MD98-2195 (Kawahata and Ohshima, 2004). Although multiple sources for the excess alkalinity at 45–48 m CSF-A might be suggested, the dissolved SO_4^{2-} profiles (Fig. F34) indicate the proximal cause.

The two mudline samples have dissolved SO_4^{2-} concentrations of 29.1 and 29.4 mM. These values are slightly higher than that for seawater with a salinity of 35 (29.0 mM). Dissolved SO_4^{2-} concentrations decrease below the seafloor. The decrease is somewhat complicated, with the rate of concentration change varying with depth. In general, however, the rate accelerates toward 0 mM at ~47 m CSF-A. For example, at Site U1428, SO_4^{2-} decreases by 9 mM over the uppermost 36 m of sediment but 20 mM over the next 11 m of sediment. Deeper than 47 m CSF-A, SO_4^{2-} concentration is 0 mM. In summary, shallower than 47 m CSF-A, the dissolved SO_4^{2-} profiles at Sites U1428 and U1429 are near mirror images of the alkalinity profiles.

Anaerobic oxidation of methane (AOM), a recurring theme in geochemistry discussions of Expedition 346 drill sites, provides the basic explanation for the alkalinity and SO_4^{2-} profiles at Sites U1428 and U1429. Methane produced at depth reacts with SO_4^{2-} in the interstitial water. This microbial reaction generates HCO_3^- and HS^- , which collectively manifest as an inflection in interstitial water alkalinity profiles. Indeed, core sections around 47 m CSF-A had a very strong H_2S odor.

Volatile hydrocarbons

The headspace gas profiles at Sites U1428 and U1429 (Fig. F35) enhance the above interpretation involving AOM. CH_4 concentrations at Site U1428 are <10 ppmv from the seafloor to ~45 m CSF-A. Deeper than ~45 m CSF-A, CH_4 values increase relatively slowly, at least compared to several previous sites, reaching 7900 ppmv at ~55 m CSF-A. The beginning of this increase corresponds to the horizon where interstitial water SO_4^{2-} concentrations approach the detection limit. Deeper than ~55 m CSF-A, CH_4 values fluctuate between 8800 and 2200 ppmv until 180 m CSF-A. No ethane or higher hydrocarbons were found in samples from this site.

The downhole CH_4 profile at Site U1429 has a similar trend. CH_4 concentrations are <10 ppmv for the upper ~50 m CSF-A. At this depth, CH_4 values increase slowly, with a maximum value of 13,500 ppmv at ~62 m CSF-A. Deeper than ~62 m CSF-A, CH_4 concentrations fluctuate between 11,200 and 2,500 ppmv until 180 m CSF-A.

In summary, headspace CH_4 concentrations support our inferences from the alkalinity and sulfate profiles. There is a relatively sharp sulfate–methane transition (SMT) somewhere between ~47 and 50 m CSF-A at both Sites U1428 and U1429.

Barium

At locations with a prominent SMT, dissolved Ba concentrations typically rise when sulfate disappears and barite begins dissolving. At Site U1428, dissolved Ba concentrations are very low (<15 μM) until 45.3 m CSF-A and then begin to increase rapidly, reaching a maximum of 540 μM at 74.35 m CSF-A (Table T14; Fig. F36). This coincides with the depth interval over which sulfur disappears, which likely causes barite to dissolve. Site U1429 shows a similar trend at similar depths, but with a lower resolution of samples (Table T17; Fig. F36).

Calcium, magnesium, and strontium

The Ca profile exhibits a concave upward profile beginning at 10.1 mM at the mudline and decreasing to 2.6 mM at 48.97 m CSF-A at Site U1428 (Table T14; Fig. F37). The Site U1429 mudline has a Ca concentration of 10.1 mM and a similar shape to Site U1428 (Table T17; Fig. F37). Concentrations appear to decline slightly quicker than at Site U1428, reaching 2.3 mM by 45.85 m CSF-A, but this may be an artefact of sampling resolution. Ca remains low for the rest of the site (<6 mM).

The Mg profile for Site U1428 is similar to Ca, expressing a concave upward trend in the upper ~50 m CSF-A. Bottom water has a Ca concentration of 52.1 mM and concentrations rapidly decline from 51.7 to 36.9 mM between 32.8 and 64.31 m CSF-A. Deeper than this, concentrations decline more gradually, reaching a minimum of 30.6 mM at 131.35 m CSF-A. Site U1429 shows a similar trend, but with lower sampling resolution, starting at 52.5 mM in the mudline and decreasing to 27.9 mM at 176.54 m CSF-A.

The Sr profile at Site U1428 is also concave upward for the upper ~50 m CSF-A, starting at 91.5 μM at the mudline and decreasing to 77.95 μM at 46.8 m CSF-A. Deeper than 46.8 m CSF-A, concentrations increase to 120.36 μM at 102.85 m CSF-A. Site U1429 has a similar shaped profile with a Sr concentration of 91.7 μM at the mudline and reaching a minimum of 69.54 μM at 44.2 m CSF-A before increasing to ~115 μM at the deepest samples from 124 to 176 m CSF-A.

Bromide

The dissolved Br^- concentration profiles are very similar at Sites U1428 and U1429 (Fig. F38). Br^- concen-

tration in the mudline is 0.87 mM for both sites, followed by a downhole increase in concentration that occurs in a step-wise fashion. Br⁻ concentrations remain relatively constant from the seafloor to 45 m CSF-A at 0.85–0.88 mM, whereas deeper than 45 m CSF-A there is a step-wise increase in concentrations, which continue to increase downhole to a maximum of 1.04 and 0.97 mM at Sites U1428 and U1429, respectively.

Ammonium and phosphate

The NH₄⁺ and PO₄³⁻ profiles at Sites U1428 and U1429 display the same general trends, but with overall higher concentrations observed at Site U1429 (Tables T14, T17; Fig. F39). Concentrations of both nutrients are relatively low in the mudline sample with dissolved NH₄⁺ and PO₄³⁻ concentrations being 26 and 3 μM for Site U1428, and 25 and 1.7 μM for Site U1429 (Fig. F40), respectively. Below the seafloor, NH₄⁺ concentrations increase gradually downhole, reaching higher absolute concentrations at Site U1429, which probably reflects increased organic carbon degradation at that site. PO₄³⁻ also reaches higher absolute concentrations at Site U1429, further suggesting that this site experiences increased organic carbon degradation. The general trend of the PO₄³⁻ profiles shows an increase downhole to a maximum at ~50 m CSF-A at both sites, with concentrations of ~58 and ~89.5 μM at Sites U1428 and U1429, respectively. PO₄³⁻ concentrations then decrease downhole to a minimum of <5 μM by ~160 m CSF-A at Site U1428 and ~177 m CSF-A at Site U1429.

Manganese and iron

Mn concentration at the mudline is 20.8 μM at Site U1428 (Table T14; Fig. F41). Mn concentrations reach a maximum of 68.2 μM in the uppermost Rhizon sample at 0.05 m CSF-A. Mn concentrations decline to 40.8 μM at 0.5 m CSF-A, where there is an inflection point and the rate of decline decreases, reaching 27.2 μM at 2.1 m CSF-A. The decline continues, reaching 6.8 μM at 17.35 m CSF-A and remaining <5 μM for the remainder of the hole, with many samples dropping below the detection limit (0.2 μM). At Site U1429, the overall trend is similar (Table T17; Fig. F41). The Site U1429 mudline sample has a lower concentration of 4.71 μM than Site U1428, and the maximum measured Mn concentration at Site U1429 (22.0 μM) occurs at 7.85 m CSF-A.

At Site U1428, Fe concentration in the mudline is below the detection limit (0.9 μM) and reaches a maximum of 4.1 μM at 0.05 m CSF-A. Concentrations rapidly decline to below the detection limit again at

0.15 m CSF-A and remain at, or near, detection for the remainder of the hole. Fe concentration in one anomalous Rhizon sample is 2.4 μM at 64.31 m CSF-A. Sampling resolution is low at Site U1429 and does not capture any Fe concentrations >3 μM, except for one anomalous value of 7.13 μM at 64.36 m CSF-A.

Chlorinity and sodium

Both Cl⁻ and Na show little variation with depth (Figs. F42, F43). At Site U1428, chlorinity is 549.3 mM in the bottom water sample and varies between 545 and 562 mM for all the samples (Table T14). The range of chloride concentrations at Site U1429 is between 547 and 567 mM, with 552.3 mM at the mudline and no trend with depth (Table T17).

The mudline has a Na concentration of 468.0 mM at Site U1428 and 471.0 mM at Site U1429. Concentrations vary between 454 and 475 mM for all the samples at both sites, with no downhole trends.

Potassium

K concentration in the mudline is 10.4 mM at Site U1428 and 10.3 mM at Site U1429 (Tables T14, T17). Just below the seafloor, K concentrations at Site U1428 increase to 11.24 mM at 0.05 m CSF-A and continue to increase to 12.0 mM at 7.85 m CSF-A (Fig. F44). K then decreases to a minimum of 9.2 mM in the deepest sample (131.35 m CSF-A). Site U1429 expresses a similar trend at lower resolution sampling.

The rise in K immediately below the seafloor is similar to other sites drilled during Expedition 346 and may reflect exchange during authigenic mineral formation. The decrease in K with depth perhaps results from further reactions with ash and basalt (Murray et al., 1992), although formation of glauconite would also remove K⁺ from interstitial water (Föllmi et al., 1992).

Lithium and boron

At the mudline, Li concentration is 25.35 μM at Site U1428 and 25.62 μM at Site U1429 (Tables T14, T17). Li concentrations remain fairly constant, ranging from 25.35 to 32.28 μM at Site U1428 until 55.35 m CSF-A; deeper than this depth Li concentrations begin to increase (Fig. F45). Site U1429 follows a similar trend. The maximum Li concentration in Site U1428 (55.4 μM) is reached at the deepest sample analyzed (at 102.85 m CSF-A). At Site U1429, the maxima in concentrations of Li (59.77 and 70.11 μM) occur at 100.55 and 124.05 m CSF-A, respectively. The deepest sample at Site U1429, 176.54 m CSF-A, has a lower concentration of 41.74 μM.

At the mudline, B concentration is 414.0 μM at Site U1428 and 413.1 μM at Site U1429 (Fig. F45). Just below the seafloor at Site U1428, B concentrations are enriched to 474.1 μM at 0.05 m CSF-A and reach a maximum of 495.5 μM at 7.85 m CSF-A. B then declines gradually to concentrations similar to bottom water at 409.7 μM at 102.85 m CSF-A. Site U1429 shows that this trend continues and has a minimum concentration of 346.46 μM at the deepest sample, 176.54 m CSF-A.

Silica

H_4SiO_4 concentrations measured by spectrophotometry and Si concentrations measured by inductively coupled plasma-atomic emission spectroscopy (ICP-AES) agree within 2% of the measured value for all of the squeezed samples (Tables T14, T17). Bottom water has Si concentrations of 165.4 μM at Site U1428 and 103.7 μM at Site U1429. The squeezed samples at Site U1429 show a slight overall increase with depth, reaching 905.89 μM at 131.35 m CSF-A before declining to 200.28 μM at 161.67 m CSF-A (Fig. F46).

Rhizon samples from Site U1428, measured only by ICP-AES, add detail to the Si profile and show enrichment of Si in interstitial water up to 676.1 μM just below the seafloor at 0.05 m CSF-A. Si concentrations decline to 580.2 μM at 2.1 m CSF-A, but squeezer samples show increases deeper than 2.1 m CSF-A to 783.8 μM at 36.35 m CSF-A. High-resolution Rhizon samples detail a rapid decline in Si concentrations to 589.14 μM at 40.8 m CSF-A and then an increase to the maximum concentration of 981.17 μM at 55.35 m CSF-A. There is a rapid decrease to 878.2 μM at 64.31 m CSF-A and concentrations vary between ~860 and 900 μM for the remainder of Site U1428. Site U1429 shows a similar trend but at lower resolution.

Rhizon commentary

Our experimentation with Rhizon sampling continued at Sites U1428 and U1429. As at previous sites, the chemistry of water from IW-Sq and IW-Rh samples is similar. Two findings are worth highlighting.

First, water can be extracted from deeper sediment than we have previously managed by using a wooden swizzle stick, which is thinner in diameter than the Rhizon, to make a pathway for the Rhizon to be inserted into the sediment.

Second, the ultimate geochemistry program suggests a powerful future for such sampling. In Holes U1428B and U1430B, Rhizon sample locations were selected based on the multisensor loggers (Whole-Round Multisensor Logger [WRMSL] and/or Special

Task Multisensor Logger [STMSL]) for GRA density and magnetic susceptibility records. This meant that the location of Rhizon samples could be selected in real time to target interesting centimeter scale intervals from the physical property record.

Preliminary conclusions

The carbonate content and interstitial water geochemistry stand out as unique features of Sites U1428 and U1429. Carbonate contents display cyclic features, which upon initial assessment are most likely related to glacial cycles and eustatic sea level changes. Upon further shore-based analyses, carbonate contents will likely help to support correlation between the two sites. Interstitial water chemistry indicates that the SMT at both sites is located at very similar depths near 47 m CSF-A, which is an unusual finding, as the stratigraphy does not correlate exactly at this depth between the sites because of differing sedimentation rates. Our preliminary conclusion based on both the geochemistry and sedimentology is that a volcanic tephra at this horizon affects the geochemical profiles at these sites. This tephra appears to have a much higher porosity and permeability than the upper and lower sedimentary mud that bound it. Therefore, the more typical diffusion gradients observed in interstitial water geochemistry at the other sites of Expedition 346 were not observed at Sites U1428 and U1429. Future and further geochemical study, including modeling, of these systems will be required to better constrain how the local (to regional) physical and chemical oceanographic processes affect the unusual aqueous geochemistry at these locations.

Paleomagnetism

Paleomagnetic samples and measurements

Paleomagnetic investigations at Sites U1428 and U1429 included measurement of magnetic susceptibility of whole-core and archive-half split-core sections and natural remanent magnetization (NRM) of archive-half sections. NRM was measured before and after alternating field (AF) demagnetization with a 20 mT peak field for most archive-half sections from Holes U1428A and U1429A at 5 cm intervals. Because of increased core flow and limited measurement time available at the paleomagnetism station, NRM of archive-half core sections from the rest of the holes at Sites U1428 and U1429 were measured only after 20 mT peak field AF demagnetization at every 5 cm interval resolution. NRM of a list of archive-half core sections dominated by disturbance, sand, or soupy ash were not measured (see Table T19). The FlexIT core orientation tool (“Paleomag-

netism” in the “Methods” chapter [Tada et al., 2015b]) was used to orient Cores 346-U1428A-2H through 16H and 18H, as well as Cores 346-U1429A-2H through 13H, 15H through 18H, and 20H through 23H. The APC-collected core orientation data for Holes U1428A and U1429A are reported in Table T20.

A total of 15 paleomagnetic discrete cube samples were collected from Hole U1428A, and a total of 20 discrete cubes were taken from Hole U1429A. Discrete samples (see “**Paleomagnetism**” in the “Methods” chapter [Tada et al., 2015b]) were typically collected from the first section of each core in Holes U1428A and U1429A and occasionally from deep sections when the first section is not suitable for collecting a discrete cube sample (triangles in Fig. F47A, F47C). Stepwise AF demagnetization on all collected discrete samples was performed at successive peak fields of 0, 5, 10, 15, 20, 25, 30, 40, 50, and 60 mT to verify the reliability of the split-core measurements and to determine the demagnetization behavior of the recovered sediment. Following each demagnetization step, NRM of the discrete samples was measured with the samples placed in the “top-toward” or “+z-axis toward magnetometer” (see “**Paleomagnetism**” in the “Methods” chapter [Tada et al., 2015b]) on the discrete sample tray.

We processed data extracted from the shipboard Laboratory Information Management System (LIMS) database by removing all measurements collected from disturbed and void intervals and all measurements that were made within 10 cm of the section ends, which are slightly biased by measurement edge effects. For declination data from cores in Holes U1428A and U1429A where FlexIT tool data are available, we corrected the declination values for each core using the estimated orientation angles. A modified version of the UPmag software (Xuan and Channell, 2009) was used to analyze the NRM data of both the split-core section and the discrete cube samples. The disturbed and void intervals used in this process are reported in Table T19. The processed NRM inclination, declination, and intensity data after 20 mT peak field AF demagnetization are reported in Table T21 and shown in Figure F47.

Natural remanent magnetization and magnetic susceptibility

NRM intensity after 20 mT peak field AF demagnetization in the two measured holes at Site U1428 and three holes at Site U1429 is similar in magnitude for overlapping intervals, mostly ranging between $\sim 10^{-4}$ and 10^{-3} A/m. For the uppermost ~ 80 m of the recov-

ered sediment at Site U1428 and uppermost ~ 110 m of sediment at Site U1429, NRM intensity of the measured core sections after 20 mT peak field AF demagnetization is mostly on the order of 10^{-3} A/m. Deeper than ~ 80 m CSF-A until the bottom of the two holes at Site U1428, NRM intensity drops to the order of 10^{-4} A/m except for Core 346-U1428A-23H, which has NRM intensity on the order of 10^{-3} A/m. For Site U1429, NRM intensity after 20 mT peak field AF demagnetization appears to be largely varying between $\sim 10^{-4}$ and 10^{-3} A/m deeper than ~ 110 m CSF-A. Many of the drilled cores appear to have steep inclinations and unusually high intensity near the core tops that gradually decrease to around the expected normal polarity inclination and average intensity within a few tens of centimeters. This may be related to stronger deformation and overprint in part of the core top sediment during coring.

The AF demagnetization behavior of all measured discrete samples is illustrated in Figures F48 and F49. Declination and inclination values acquired from the discrete sample measurement generally agree well with the split-core measurement after 20 mT AF demagnetization. All samples exhibit a steep, normal overprint that was generally removed after AF demagnetization at peak fields of ~ 15 – 20 mT, demonstrating that the 20 mT peak field AF demagnetization is, in general, sufficient to eliminate the drilling overprint. All measured discrete samples of Sites U1428 and U1429 show a well-defined characteristic NRM component with positive inclinations. Most samples appear to acquire an anhysteretic remanent magnetization at high demagnetization steps (>50 mT), possibly due to bias caused by ambient magnetic field during demagnetization.

The steep inclinations observed in pass-through measurement near the core tops are not seen in measurement of discrete samples collected near the core tops. As discrete samples are taken from the less disturbed center part of the core sections, the absence of steep inclination (after 15–20 mT peak field AF demagnetization) in discrete sample measurements indicates that the steep inclinations observed in pass-through measurements near the core tops are mainly due to stronger overprint in the outer part of the cores. During the coring process, the upper part of each core must slide further along the inside wall of the core liner than the lower portion of the core, which could cause more deformation for the upper part of the cores (e.g., Acton et al., 2002). Further study is needed to understand why the usual steep inclination and high intensity near the core tops are more apparent in some cores such as those cored at Sites U1428 and U1429.

Magnetic susceptibility measurements were made on whole cores from all holes as part of the WRMSL analysis and on archive-half split-core sections using the Section Half Multisensor Logger (SHMSL) (see “[Physical properties](#)”). The WRMSL acquired susceptibility was stored in the database in raw meter units. These were multiplied by a factor of 0.68×10^{-5} to convert to the dimensionless volume SI unit (Blum, 1997). A factor of $(67/80) \times 10^{-5}$ was multiplied by the SHMSL acquired susceptibility stored in the database. The magnetic susceptibility measurement is consistent between the two instruments and across the different holes for overlapping intervals, and varies mostly between 5×10^{-5} and 20×10^{-5} SI (Fig. [F47](#), fourth panel). Magnetic susceptibility of sediment from both sites, in general, mimics NRM intensity, suggesting that the magnetic minerals that carry NRM are the same or at least coexist with those that dominate magnetic susceptibility. For sediment recovered deeper than ~95 m CSF-A at Site U1428, NRM intensity of the core sections after 20 mT AF demagnetization shows changes that agree less well with variations in magnetic susceptibility.

Magnetostratigraphy

Both magnetic declination and inclination after 20 mT peak field AF demagnetization were used when possible for the magnetostratigraphic interpretation at Sites U1428 and U1429. The geomagnetic field at the latitudes of Sites U1428 (31.68°N) and U1429 (31.62°N) have expected inclinations of 50.99° and 50.92°, respectively, assuming a geocentric axial dipole field model, which is sufficiently steep to determine magnetic polarity in APC cores that lack horizontal orientation. Paleomagnetic inclination of all holes at Sites U1428 and U1429 is dominated by positive values around the expected normal polarity dipole inclinations, suggesting that all recovered sediment from the two sites was deposited during the Brunhes Chron (C1n, 0–0.781 Ma). Except Core 346-U1429A-21H where the FlexIT tool appears to fail in orienting the core, the FlexIT-corrected declinations for all other oriented cores in Holes U1428A and U1429A (green dots in Fig. [F47A](#), [F47C](#)) vary mostly around 0° or 360°, agreeing with our interpretation of Brunhes age for the recovered sediment. This interpretation is also consistent with the discrete sample measurement results and agrees with many identified biostratigraphic events (see “[Biostratigraphy](#)”).

Physical properties

Physical properties measurements at Sites U1428 and U1429 were conducted to provide high-resolution

data on the bulk physical properties and their down-hole variations in Holes U1428A, U1428B, U1429A, U1429B, and U1429C. After the sections reached thermal equilibrium with the ambient room temperature of ~20°C, thermal conductivity (one per core) and NGR measurements (eight per full section) completed the suite of whole-core measurements. One-half of each split core was reserved for archiving and the other half was reserved for analysis and sampling (working half). Shear stress measurements were performed (most commonly one per core) on the working halves of Holes U1428A and U1429A. Moisture and density (MAD) measurements were performed on discrete core samples (most commonly one or two per core) collected from the working halves of Holes U1428A and U1429A. Diffuse spectral reflectance (most commonly at 5 cm intervals) and point magnetic susceptibility (most commonly at 5 cm intervals) were measured using the SHMSL on the archive halves. Physical properties measurements are presented synthetically in Figures [F50](#), [F51](#), [F52](#), [F53](#), [F54](#), [F55](#), and [F56](#).

Thermal conductivity

Thermal conductivity was measured once per core using the full-space probe, usually near the middle of Section 4. Overall, thermal conductivity values range from 0.7 to 1.9 W/(m·K). Thermal conductivity follows porosity and GRA bulk density, and thus, in part, lithology. A slight increasing trend with depth shallower than ~180 m CSF-A is found in lithologic Unit A. Significant increasing of thermal conductivity values deeper than ~180 m CSF-A corresponds to the lithologic Unit A/B boundary.

Moisture and density

Although measurement errors exist in GRA bulk density data because of the presence of air between a core and a core liner, in general the GRA bulk density at Sites U1428 and U1429 reflects the core’s lithologic characteristic (Figs. [F50](#), [F51](#); see “[Lithostratigraphy](#)”). GRA bulk density at Site U1428 ranges from 0.80 g/cm³ to values >2.10 g/cm³ and generally increases with depth (Fig. [F50](#)). A minimum value was measured at ~87 m CSF-A, and a maximum value was measured at ~170 m CSF-A. The values of GRA bulk density linearly increase from 0 to ~135 m CSF-A, generally coinciding with lithologic Unit A (see “[Lithostratigraphy](#)”). High peaks of GRA bulk density (up to 1.6 g/cm³) occur at 3, 16, 41, 55, and 114 m CSF-A. High values at 3, 16, and 41 m CSF-A are due to coarse-grained sediment in the bottom of tephra/ash layers, whereas fine-grained sand layers are responsible for other high GRA bulk density values at 55 and 114 m CSF-A. GRA bulk density largely

decreases between 83 and 92 m CSF-A, where a ~9 m thick spongy or soupy tephra/ash layer exists. From ~135 m CSF-A, GRA bulk density increases abruptly, and the highest values of GRA bulk density occur to the bottom of the hole with high scatter. This interval (between 135 and 210 m CSF-A) of high GRA bulk density consists of almost sandy sediment and largely reflects lithologic Unit B. High scatter of GRA bulk density values in this interval is closely related to disturbed sandy sediment with limited recovery.

Although the detailed pattern is different, the primary trends of GRA bulk density at Site U1429 agree well with Site U1428 (Fig. F51). GRA bulk density at Site U1429 generally increases with depth, ranging from 1.02 to 2.09 g/cm³, high GRA bulk density values related to identical lithologic characteristics with Site U1428 occur at 3, 17, 48, 70, and 157 m CSF-A (see “[Lithostratigraphy](#)”). Site U1429 also shows low GRA bulk density values (<1.3 g/cm³) with high scatter between 115 and 122 m CSF-A because of spongy and soupy state of a thick tephra/ash layer. GRA bulk density largely increases from ~175 to the bottom of the hole, which generally reflects lithologic Unit B.

Discrete wet bulk density and derived parameters (i.e., porosity and water content) at Sites U1428 and U1429 agree well with the primary trends in GRA bulk density (Figs. F52, F53), varying with the lithology. At Site U1428, discrete wet bulk density increases with depth, ranging from 1.39 to 2.02 g/cm³, whereas porosity and water content show generally reversed trends when compared to density, ranging from 42.8% to 77.7% and from 21.8% to 57.4%, respectively. Grain density, however, is relatively constant for the entire core interval, ranging from 2.48 to 2.80 g/cm³. Discrete bulk density, porosity, and water content show large shifts close to the lithologic Unit A/B boundary, whereas grain density is not influenced. At the thick tephra/ash layer between 83 and 92 m CSF-A, discrete bulk density slightly increases, whereas grain density largely decreases with porosity and water content. This is related to the tephra/ash materials that have relatively low solid mass compared with solid volume. Because of this, although the tephra/ash layer consists of relatively coarse grains in this interval, grain density (calculated by mass and volume of solid) decreases with the increase of wet bulk density (primarily controlled by wet mass of sediment).

MAD data at Site U1429 also show a similar trend pattern with Site U1428 (Fig. F53). At ~180 m CSF-A close to the lithologic Unit A/B boundary, discrete bulk density, porosity, and water content show large changes. Although grain density is relatively constant downhole, low grain density values occur in te-

phra/ash layers at ~100 and ~115 m CSF-A, with decreases in porosity and water content.

Magnetic susceptibility

Whole-core magnetic susceptibility at Sites U1428 and U1429 shows consistently low values in lithologic Unit A, typically <15 × 10⁻⁵ SI with the exception of several high magnetic susceptibility values (Figs. F50, F51). Point magnetic susceptibility from the SHMSL closely tracks whole-core magnetic susceptibility. Although the mean values stay between 5 × 10⁻⁵ and 10 × 10⁻⁵ SI for Unit A at Site U1428, high magnetic susceptibility maxima (up to 30 × 10⁻⁵ SI) occur at 3, 43, 52, and 110 m CSF-A. These high magnetic susceptibility intervals are due to highly magnetic authigenic minerals within tephra/ash layers (see “[Lithostratigraphy](#)”). Magnetic susceptibility largely increases in the lithologic Unit A/B boundary, and a maximum occurs at ~165 m CSF-A where values up to 170 × 10⁻⁵ SI were measured. Magnetic susceptibility at Site U1429 is also relatively constant between 5 × 10⁻⁵ and 10 × 10⁻⁵ SI for Unit A and largely increases from 178 m CSF-A to the bottom of the hole, coinciding with Unit B. High magnetic susceptibility values (up to 30 × 10⁻⁵ SI) related to tephra/ash layers occur at 3, 52, 65, and 118 m CSF-A.

Natural gamma radiation

Total NGR counts at Sites U1428 and U1429 range from 13 to 59 cps and from 18 to 53 cps, respectively, and generally increase downhole with a closely similar trend pattern (Figs. F50, F51). Minimum values were determined in the top of the hole, and maximum values were measured in lithologic Unit B. NGR shows strong cyclicity, which is similar to the GRA bulk density cyclicity. Relatively high NGR counts occur at identical depths with high GRA bulk density. The upper ~130 m CSF-A show lower values compared to the rest of the hole, likely reflecting the abundance of nonradioactive elements within lithologic Unit A (calcareous nannofossils and other siliceous components, see “[Lithostratigraphy](#)”). The increased NGR counts deeper than ~130 m CSF-A may reflect the abundance of mica (and the common presence of other minerals such as K-feldspar) in the sands forming lithologic Unit B, although quartz (nonradioactive mineral) is the predominant mineral in this unit (see “[Lithostratigraphy](#)”).

Compressional wave velocity

Compressional *P*-wave velocity at Sites U1428 and U1429 was measured with the WRMSL in Sections 1,

2, and 3 of each core for Holes U1428A, U1428B, U1429A, U1429B, and U1429C and then combined as one data set of values for each site. Although compressional P -wave velocity was only measured in the upper ~50 m CSF-A at these two sites because of the poor sediment-to-liner coupling or the influence of small cracks in the relatively stiff and brittle sediment, meter-scale cyclicity is evident, following the cycles in GRA bulk density and NGR (Figs. F50, F51). The mean values of P -wave velocity at Sites U1428 and U1429 are 1527 and 1525 m/s, respectively. P -wave velocity largely increases up to 1600 m/s at ~3, ~16, and ~40 m CSF-A at Site U1428 and ~3, ~17, and ~50 m CSF-A at Site U1429. These depths of high P -wave velocity agree well with high GRA bulk density and NGR.

Vane shear stress

Shear stress measurements were performed (one per core) on the working halves of Holes U1428A and U1429A using an analog vane shear device. The shear strength at Site U1428 ranges from 5.8 to 65.7 kPa and linearly increases to ~103 m CSF-A (Fig. F52). Deeper than ~103 m CSF-A, shear strength shows little scatter and then largely decreases to ~6 kPa in lithologic Unit B because of disturbed sandy sediment. Site U1429 also shows a similar shear strength trend, with data ranging from 10 to 66 kPa (Fig. F53). After the linear increase to ~105 m CSF-A, shear strength shows relatively high scatter to the lithologic Unit A/B boundary.

Diffuse reflectance spectroscopy

Spectral reflectance data measured on the split archive-half sections at Sites U1428 and U1429 are distinctly different from the previously drilled sites. At previous sites, L^* , a^* , and b^* show variability caused by the alternating dark organic-rich and greenish organic-poor lithologic packages or between clay-rich and biogenic component-rich sediment, whereas these two sites show a trend pattern mainly controlled by carbonate content, color of tephra/ash layers, and a sand layer (see “**Lithostratigraphy**”). Although the variability in the upper part of the sequence is lower than at previous sites, the trends of color reflectance at Sites U1428 and U1429 agree well with changes in the content of carbonate and other physical properties related to tephra/ash and sand layers (Figs. F54, F55). In particular, L^* better reflects the lithologic characteristic of these two sites. This can be observed in the parameters L^* and a^* combined that is primarily variable in dark-light compounds (Fig. F56). L^* of Sites U1428 and U1429 extends more widely between values of 23 and 58, compared to L^* of Site U1427 extended between val-

ues of 24 and 43. This wide range of L^* values is due to the high carbonate content, light or dark tephra/ash layers, and dark sand in Unit B. This high content of carbonate may also be responsible for the higher mean value of L^* than found at IODP Sites U1425 and U1427. Comparison of L^* - a^* color spaces, which are plotted without the sand layer, indicates that the color of sand in Unit B dominates in compounds of high a^* and low L^* .

Summary

Physical properties measured at Sites U1428 and U1429 show similar trends and follow sediment lithology. Bulk density and NGR gradually increase downhole in lithologic Unit A, and the highest values occur in the sandy sediment of lithologic Unit B. Porosity and water content show the trend opposite to bulk density and NGR. Magnetic susceptibility shows high values in tephra/ash layers and also largely increases in lithologic Unit B. At these two sites, the downhole profiles of color reflectance agree well with changes in the carbonate content and other physical properties related to tephra/ash and sand layers. Comparison of L^* - a^* color spaces indicates that color changes at these two sites are mainly controlled by carbonate content, color of tephra/ash layers, and a sand layer.

Downhole measurements

In situ temperature and heat flow

Five formation temperature measurements, including one at the mudline, were performed in Holes U1428A and U1429A using the APCT-3.

In Hole U1428A, in situ temperatures range from 10.30°C at 34.9 m CSF-A to 20.56°C at 120.4 m CSF-A (Table T22), with a linear downhole increase indicating that the gradient is uniform with depth (Fig. F57) despite a small offset of the measurement taken at 91.9 m CSF-A. A linear fit of temperature versus depth yields a geothermal gradient of 116°C/km. The trend line of the in situ temperature measurements intersects the seafloor at 6.26°C, giving a lower value than the average mudline temperature in the four APCT-3 measurements (7.61°C) (Fig. F57A).

Thermal conductivity under in situ conditions was estimated from laboratory-determined thermal conductivity using the method of Hyndmann et al. (1974) (see “**Physical properties**” in the “Methods” chapter [Tada et al., 2015b]). Thermal resistance was calculated by cumulatively adding the inverse of the in situ thermal conductivity values over depth intervals downhole (Fig. F57). A heat flow of 126 mW/m² was obtained from the slope of the linear fit between

in situ temperature and calculated in situ thermal resistance (Pribnow et al., 2000).

In Hole U1429A, in situ temperatures range from 8.93°C at 34.9 m CSF-A to 14.78°C at 118.1 m CSF-A (Table T22). There was an important uncertainty in fitting to the APCT-3 temperature equilibration curve to obtain the formation temperature at 118.1 m CSF-A, probably because of poor contact of the temperature probe with the formation during in situ temperature measurement. The temperature measured from Core 346-U1429-13H depth thus deviates from the linear downhole increasing gradient (Fig. F58) and was not taken into account in the successive calculations. A linear fit of temperature versus depth gives a geothermal gradient of 94°C/km. This is lower than the geothermal gradient measured at Site U1428 (116°C/km), located only 15 km away. The trend line of the in situ temperature measurements intersects the seafloor at 6.94°C (Fig. F58). This is lower than the average mudline temperature in the four APCT-3 measurements (7.77°C) and slightly warmer than the seafloor temperature calculated at Site U1428 (6.26°C, Fig. F57A). A heat flow of 88 mW/m² was obtained from the slope of the linear fit between in situ temperature and calculated in situ thermal resistance (Fig. F58) (Pribnow et al., 2000).

Stratigraphic correlation and sedimentation rates

Real-time tracking of the relative positions of core gaps among holes at Sites U1428 and U1429 was accomplished using magnetic susceptibility and GRA density data from the WRMSL and STMSL. Data were collected at a resolution of 5 cm, which was sufficient to keep up with core recovery rates. Compositing and splicing (see “[Stratigraphic correlation and sedimentation rates](#)” in the “Methods” chapter [Tada et al., 2015b]) are based on the high-resolution RGB color data (blue) recovered from the Section Half Imaging Logger at 0.5 cm resolution as well as the magnetic susceptibility and GRA density data. For detailed discussion of these data sets, see “[Physical properties](#)” in the “Methods” chapter (Tada et al., 2015b).

At Sites U1428 and U1429, sea state was relatively calm and gas expansion was limited compared to some of the previous sites. Voids within the liners and extrusion of sediment out the top of the core barrel were minimal to nonexistent. Although only 7.5 km apart and at similar water depths, there are differences in sedimentation rates and interbedded sands. For these reasons, separate splices were produced for each site.

Two holes were drilled at Site U1428. These two holes were composited (Table T23) and spliced (Table T24) from the mudline to ~145 m CCSF-D (as defined in the “[Methods](#)” chapter [Tada et al., 2015b]) near the top of the massive unconsolidated sand layers encountered near the bottom of the hole (Fig. F59). A gap in the splice occurs from 88.71 to 93.82 m CCSF-D, where Section 346-U1428B-10H-4, 130 cm, is appended to 346-U1428B-11H-1, 0 cm. This gap reflects strongly disturbed intervals identified in both Holes U1428A and U1428B. Sedimentation rate analysis (discussed below) suggests that the gap spans ~12 k.y. Preliminary correlation of the spliced magnetic susceptibility data from the two sites (Fig. F60) indicates that some or all of this gap may have been successfully recovered at Site U1429; the resolution of this question awaits detailed correlation using additional data. Comparison of the CCSF-D and CSF-A depths at the bottom of the spliced interval indicates expansion of ~7% at this site.

Three holes were drilled at Site U1429. These holes were composited (Table T25) and spliced (Table T26) from the mudline to ~191 m CCSF-D near the top of the sand layers encountered near the bottom of the hole (Fig. F61). Two gaps occur in this splice. The first gap occurs from 49.99 to 53.11 m CCSF-D, where Section 346-U1429B-6H-4, 149 cm, is appended to 346-U1429C-8H-1, 0 cm. This gap reflects strongly disturbed intervals identified in both holes and the 0% recovery in Core 346-U1429C-7H. Sedimentation rate assessment suggests that this gap spans ~10 k.y. However, correlation of the spliced magnetic susceptibility data from Sites U1428 and U1429 (Fig. F60) indicates that all of this gap was successfully recovered at Site U1428; a more precise definition of the correlative interval awaits detailed analysis. The second gap in the Site U1429 splice occurs from 123 to 125.76 m CCSF-D, where Section 346-U1429A-13H-5, 71 cm, is appended to 346-U1429A-15H-1, 0 cm. This gap reflects strong coring disturbance and the 0% recovery for Core 346-U1429A-13H. Sedimentation rate assessment suggests that this gap spans ~8.5 k.y. Preliminary correlation of the spliced magnetic susceptibility data from Sites U1428 and U1429 indicates that some or all of this gap may have been successfully recovered in Site U1428; the resolution of this question also awaits detailed correlation using additional data. Comparison of the CCSF-D and CSF-A depths at the bottom of the spliced interval indicates expansion of ~7% at this site.

Neither Site U1428 nor Site U1429 was logged. Thus, the length of the gaps was estimated using drillers depth (CSF-A) offsets for the appended cores. Experience during this expedition at sites drilled during calm conditions has been that the CSF-A scale is re-

markably accurate. Our requests for mudline cores of specific lengths were consistently met with accuracies of ± 1 m or better once the drillers had established the relationship between recovery length of the first mudline core and bit depth at which the core was taken.

Age model and sedimentation rates

Preliminary age models (Fig. F62) were established for both sites on the basis of a very limited number of biostratigraphic age control points. For details, see “**Biostratigraphy.**” No datums were excluded from the assessment. At Site U1428, a linear fit to the two datums (and constrained to pass through the origin) indicates an average sedimentation rate of ~ 42 cm/k.y. and an age of ~ 350 ka at the bottom of the spliced interval (~ 145 m CCSF-D). A linear fit to the three datums at Site U1429 indicates an overall average sedimentation rate of ~ 32 cm/k.y. but does not pass through the origin, suggesting a somewhat higher sedimentation rate over the upper ~ 50 m of the section (~ 76 cm/k.y.). Extrapolation to the bottom of the splice yields an age of ~ 500 ka at 190 m CCSF-D. This is inconsistent with the spliced magnetic susceptibility correlation between the two sites (Fig. F60). Alternatively, placing highest confidence in the LO of *G. ruber* (pink) datum and forcing a fit through the origin yields a sedimentation rate of 56 cm/k.y. and an age of ~ 340 ka at the bottom of the spliced interval. This scenario is consistent with the magnetic susceptibility-based correlation between the two sites.

References

- Acton, G.D., Okada, M., Clement, B.M., Lund, S.P., and Williams, T., 2002. Paleomagnetic overprints in ocean sediment cores and their relationship to shear deformation caused by piston coring. *J. Geophys. Res.: Solid Earth*, 107(B4):2067–2081. doi:10.1029/2001JB000518
- Alvarez Zariqian, Carlos A., in press. Pleistocene deep sea ostracods from the Bering Sea (IODP Expedition 323). *Deep-Sea Res., Part II*. doi:10.1016/j.dsr2.2014.05.010
- Bjørklund, K., 1974. The seasonal occurrence and depth zonation of radiolarians in Korsfjorden, western Norway. *Sarsia*, 56:13–42.
- Blum, P., 1997. Physical properties handbook: a guide to the shipboard measurement of physical properties of deep-sea cores. *ODP Tech. Note*, 26. doi:10.2973/odp.tn.26.1997
- Brouwers, E.M., 1990. Systematic paleontology of Quaternary ostracode assemblages from the Gulf of Alaska, Part 1. Families Cytherellidae, Bairdiidae, Cytheridae, Leptocytheridae, Limnocytheridae, Eucytheridae, Krithidae, Cushmaniidae. *U.S. Geol. Surv. Prof. Pap.*, 1510. <http://pubs.er.usgs.gov/publication/pp1510>
- Chang, F., Zhuang, L., Li, T., Yan, J., Cao, Q., and Cang, S., 2003. Radiolarian fauna in surface sediments of the northeastern East China Sea. *Mar. Micropaleontol.*, 48(3–4):169–204. doi:10.1016/S0377-8398(03)00016-1
- Chapronière, G.C.H., Styzen, M.J., Sager, W.W., Nishi, H., Quinterno, P.J., and Abrahamsen, N., 1994. Late Neogene biostratigraphic and magnetostratigraphic synthesis, Leg 135. In Hawkins, J., Parson, L., Allan, J., et al., *Proc. ODP, Sci. Results*, 135: College Station, TX (Ocean Drilling Program), 857–877. doi:10.2973/odp.proc.sr.135.116.1994
- Föllmi, K.B., Cramp, A., Föllmi, K.E., Alexandrovich, J.M., Brunner, C., Burckle, L.H., Casey, M., deMenocal, P., Dunbar, R.B., Grimm, K.A., Holler, P., Ingle, J.C., Jr., Kheradyyar, T., McEvoy, J., Nobes, D.C., Stein, R., Tada, R., von Breyman, M.T., and White, L.D., 1992. Dark-light rhythms in the sediments of the Japan Sea: preliminary results from Site 798, with some additional results from Sites 797 and 799. In Pisciotto, K.A., Ingle, J.C., Jr., von Breyman, M.T., Barron, J., et al., *Proc. ODP, Sci. Results*, 127/128 (Pt. 1): College Station, TX (Ocean Drilling Program), 559–576. doi:10.2973/odp.proc.sr.127128-1.159.1992
- Fukusawa, H., 1995. Nonglacial varved lake sediment as a natural timekeeper and detector on environmental changes. *Quat. Res. (Daiyonki-Kenkyu)*, 34(3):135–149. (in Japanese) doi:10.4116/jaqua.34.135
- Hanagata, S., 2004. Pliocene–Pleistocene planktonic foraminiferal biostratigraphy in the Miyagijima and adjacent islands, off Katsuren Peninsula, east of Okinawajima, Japan. *Bull. Mizunami Fossil Mus.*, 31:37–62. (in Japanese with English abstract)
- Hyndman, R.D., Erickson, A.J., and Von Herzen, R.P., 1974. Geothermal measurements on DSDP Leg 26. In Davies, T.A., Luyendyk, B.P., et al., *Init. Repts. DSDP*, 26: Washington, DC (U.S. Govt. Printing Office), 451–463. doi:10.2973/dsdp.proc.26.113.1974
- Ijiri, A., Wang, L., Oba, T., Kawahata, H., Huang, C.-Y., and Huang, C.-Y., 2005. Paleoenvironmental changes in the northern area of the East China Sea during the past 42,000 years. *Palaeogeogr., Palaeoclimatol., Palaeoecol.*, 219(3–4):239–261. doi:10.1016/j.palaeo.2004.12.028
- Itaki, T., 2003. Depth-related radiolarian assemblage in the water-column and surface sediments of the Japan Sea. *Mar. Micropaleontol.*, 47(3–4):253–270. doi:10.1016/S0377-8398(02)00119-6
- Itaki, T., Ito, M., Narita, H., Ahagon, N., and Sakai, H., 2003. Depth distribution of radiolarians from the Chukchi and Beaufort Seas, western Arctic. *Deep-Sea Res., Part I*, 50(12):1507–1522. doi:10.1016/j.dsr.2003.09.003
- Jorissen, F.J., Fontanier, C., and Thomas, E., 2007. Paleooceanographical proxies based on deep-sea benthic foraminiferal assemblage characteristics. In Hillaire-Marcel, C. and De Vernal, A. (Eds.), *Proxies in Late Cenozoic Paleooceanography*. *Dev. Mar. Geol.*, 263–325. doi:10.1016/S1572-5480(07)01012-3
- Kawahata, H., Nohara, M., Aoki, K., Minoshima, K., and Gupta, L.P., 2006. Biogenic and abiogenic sedimentation in the northern East China Sea in response to sea-level change during the late Pleistocene. *Global Planet. Change*, 53(1–2):108–121. doi:10.1016/j.glopla-cha.2006.01.013

- Kawahata, H., and Ohshima, H., 2004. Vegetation and environmental record in the northern East China Sea during the late Pleistocene. *Global Planet. Change*, 41(3–4):251–273. doi:10.1016/j.gloplacha.2004.01.011
- Kitagawa, H., and van der Plicht, J., 1998. A 40,000-year varve chronology from Lake Suigetsu, Japan: extension of the ^{14}C calibration curve. *Radiocarbon*, 40(1):505–515.
- Kubota, Y., 2013. Millennial scale changes in East Asian summer monsoon in the East China Sea during the last glacial period and the Holocene [Ph.D. thesis]. Univ. Tokyo.
- Kubota, Y., Kimoto, K., Tada, R., Oda, H., Yokoyama, Y., and Matsuzaki, H., 2010. Variations of East Asian summer monsoon since the last deglaciation based on Mg/Ca and oxygen isotope of planktic foraminifera in the northern East China Sea. *Paleoceanography*, 25(4):PA4205. doi:10.1029/2009PA001891
- Murray, R.W., Brumsack, H.J., von Breymann, M.T., Sturz, A.A., Dunbar, R.B., and Gieskes, J.M., 1992. Diagenetic reactions in deeply buried sediments of the Japan Sea: a synthesis of interstitial-water chemistry results from Legs 127 and 128. In Tamaki, K., Suyehiro, K., Allan, J., McWilliams, M., et al., *Proc. ODP, Sci. Results*, 127/128 (Pt. 2): College Station, TX (Ocean Drilling Program), 1261–1274. doi:10.2973/odp.proc.sr.127128-2.177.1992
- Pribnow, D., Kinoshita, M., and Stein, C., 2000. *Thermal Data Collection and Heat Flow Recalculations for Ocean Drilling Program Legs 101–180*: Hanover, Germany (Inst. Joint Geosci. Res., Inst. Geowiss. Gemeinschaftsauf. [GGA]). <http://www-odp.tamu.edu/publications/heatflow/ODPreprt.pdf>
- Tada, R., Murray, R.W., Alvarez Zarikian, C.A., Anderson, W.T., Jr., Bassetti, M.-A., Brace, B.J., Clemens, S.C., da Costa Gurgel, M.H., Dickens, G.R., Dunlea, A.G., Gallagher, S.J., Giosan, L., Henderson, A.C.G., Holbourn, A.E., Ikehara, K., Irino, T., Itaki, T., Karasuda, A., Kinsley, C.W., Kubota, Y., Lee, G.S., Lee, K.E., Lofi, J., Lopes, C.I.C.D., Peterson, L.C., Saavedra-Pellitero, M., Sagawa, T., Singh, R.K., Sugisaki, S., Toucanne, S., Wan, S., Xuan, C., Zheng, H., and Ziegler, M., 2015a. Expedition 346 summary. In Tada, R., Murray, R.W., Alvarez Zarikian, C.A., and the Expedition 346 Scientists, *Proc. IODP*, 346: College Station, TX (Integrated Ocean Drilling Program). doi:10.2204/iodp.proc.346.101.2015
- Tada, R., Murray, R.W., Alvarez Zarikian, C.A., Anderson, W.T., Jr., Bassetti, M.-A., Brace, B.J., Clemens, S.C., da Costa Gurgel, M.H., Dickens, G.R., Dunlea, A.G., Gallagher, S.J., Giosan, L., Henderson, A.C.G., Holbourn, A.E., Ikehara, K., Irino, T., Itaki, T., Karasuda, A., Kinsley, C.W., Kubota, Y., Lee, G.S., Lee, K.E., Lofi, J., Lopes, C.I.C.D., Peterson, L.C., Saavedra-Pellitero, M., Sagawa, T., Singh, R.K., Sugisaki, S., Toucanne, S., Wan, S., Xuan, C., Zheng, H., and Ziegler, M., 2015b. Methods. In Tada, R., Murray, R.W., Alvarez Zarikian, C.A., and the Expedition 346 Scientists, *Proc. IODP*, 346: College Station, TX (Integrated Ocean Drilling Program). doi:10.2204/iodp.proc.346.102.2015
- Tada, R., Murray, R.W., Alvarez Zarikian, C.A., Anderson, W.T., Jr., Bassetti, M.-A., Brace, B.J., Clemens, S.C., da Costa Gurgel, M.H., Dickens, G.R., Dunlea, A.G., Gallagher, S.J., Giosan, L., Henderson, A.C.G., Holbourn, A.E., Ikehara, K., Irino, T., Itaki, T., Karasuda, A., Kinsley, C.W., Kubota, Y., Lee, G.S., Lee, K.E., Lofi, J., Lopes, C.I.C.D., Peterson, L.C., Saavedra-Pellitero, M., Sagawa, T., Singh, R.K., Sugisaki, S., Toucanne, S., Wan, S., Xuan, C., Zheng, H., and Ziegler, M., 2015c. Site U1422. In Tada, R., Murray, R.W., Alvarez Zarikian, C.A., and the Expedition 346 Scientists, *Proc. IODP*, 346: College Station, TX (Integrated Ocean Drilling Program). doi:10.2204/iodp.proc.346.103.2015
- Tada, R., Murray, R.W., Alvarez Zarikian, C.A., Anderson, W.T., Jr., Bassetti, M.-A., Brace, B.J., Clemens, S.C., da Costa Gurgel, M.H., Dickens, G.R., Dunlea, A.G., Gallagher, S.J., Giosan, L., Henderson, A.C.G., Holbourn, A.E., Ikehara, K., Irino, T., Itaki, T., Karasuda, A., Kinsley, C.W., Kubota, Y., Lee, G.S., Lee, K.E., Lofi, J., Lopes, C.I.C.D., Peterson, L.C., Saavedra-Pellitero, M., Sagawa, T., Singh, R.K., Sugisaki, S., Toucanne, S., Wan, S., Xuan, C., Zheng, H., and Ziegler, M., 2015d. Site U1424. In Tada, R., Murray, R.W., Alvarez Zarikian, C.A., and the Expedition 346 Scientists, *Proc. IODP*, 346: College Station, TX (Integrated Ocean Drilling Program). doi:10.2204/iodp.proc.346.105.2015
- Xu, X., and Oda, M., 1999. Surface-water evolution of the eastern East China Sea during the last 36,000 years. *Mar. Geol.*, 156(1–4):285–304. doi:10.1016/S0025-3227(98)00183-2
- Xuan, C., and Channell, J.E.T., 2009. UPmag: MATLAB software for viewing and processing U channel or other pass-through paleomagnetic data. *Geochem., Geophys., Geosyst.*, 10(10):Q10Y07. doi:10.1029/2009GC002584
- Zhao, Q., Whatley, R., and Zhou, B., 2000. The taxonomy and distribution of recent species of the ostracod genus *Cytheropteron* in the South China Sea. *Rev. Esp. Micro-paleontol.*, 32(2):259–281.

Publication: 28 March 2015
MS 346-109

Figure F1. Bathymetric map of Expedition 346 sites (red circles). Sites previously drilled by the Deep Sea Drilling Project (DSDP) and Ocean Drilling Program (ODP) (white circles) are also shown. Also illustrated are the regional surface current systems.

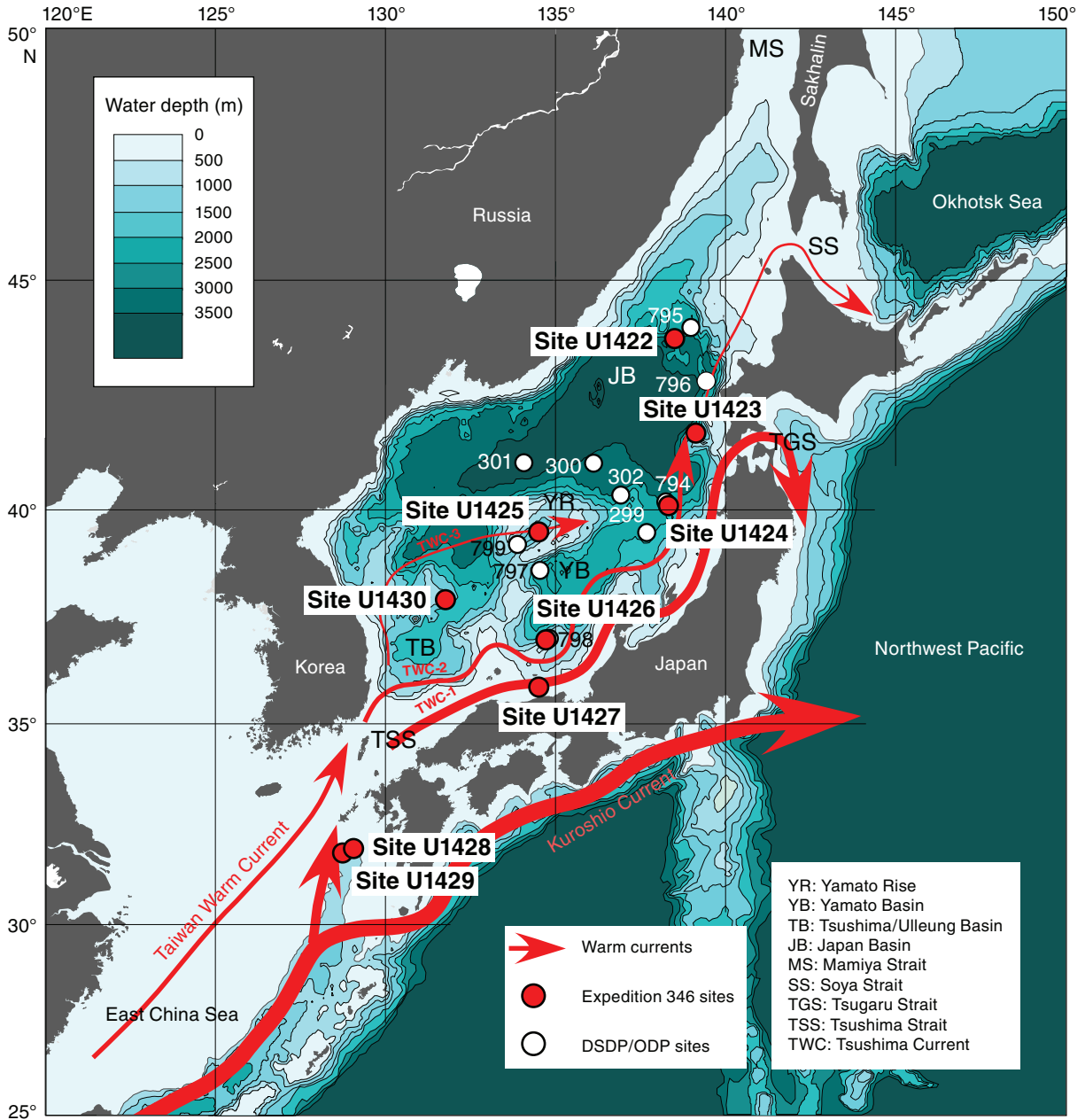


Figure F3. Lithologic summary, Hole U1428A. GRA = gamma ray attenuation.

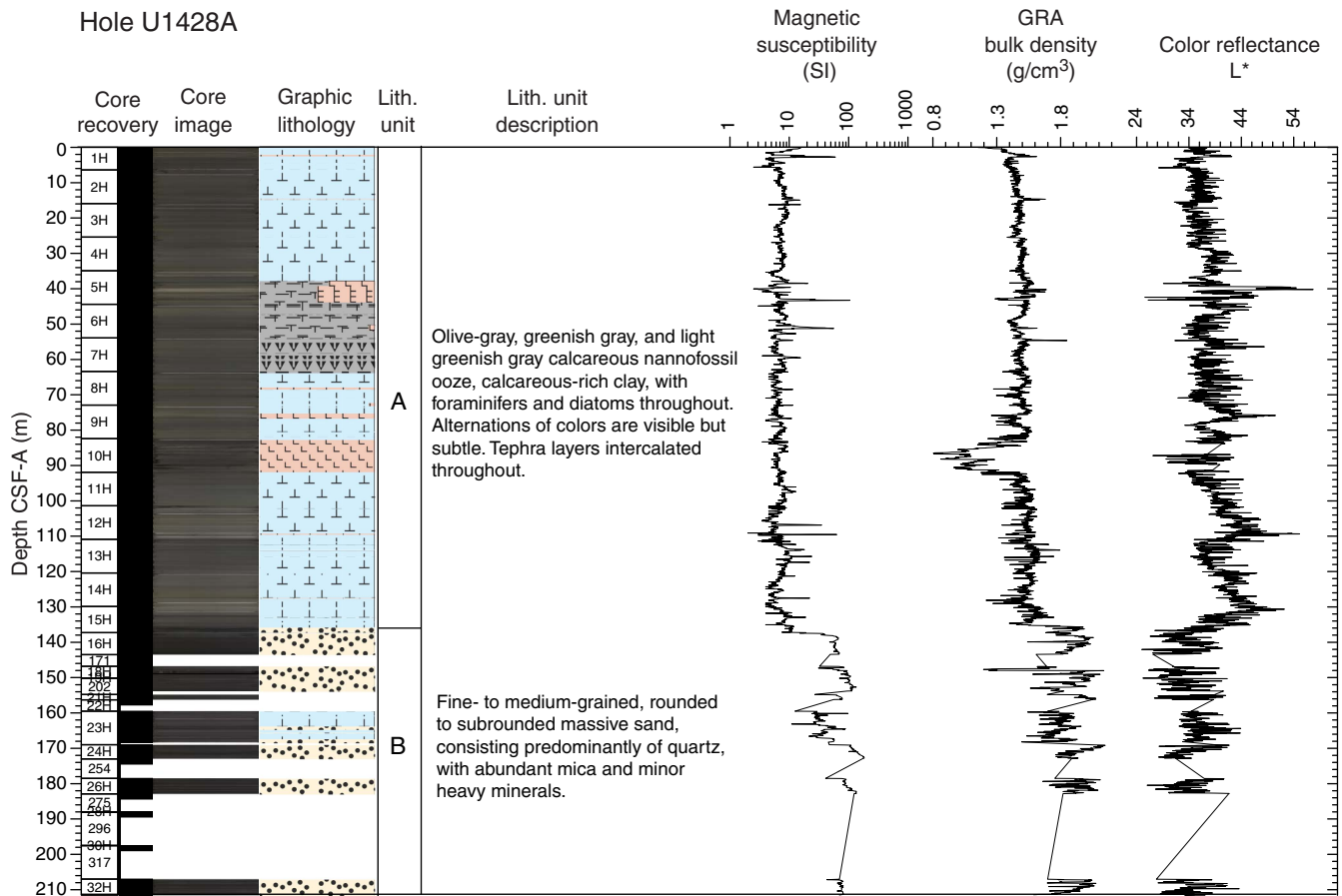


Figure F4. Lithologic summary, Hole U1428B. GRA = gamma ray attenuation.

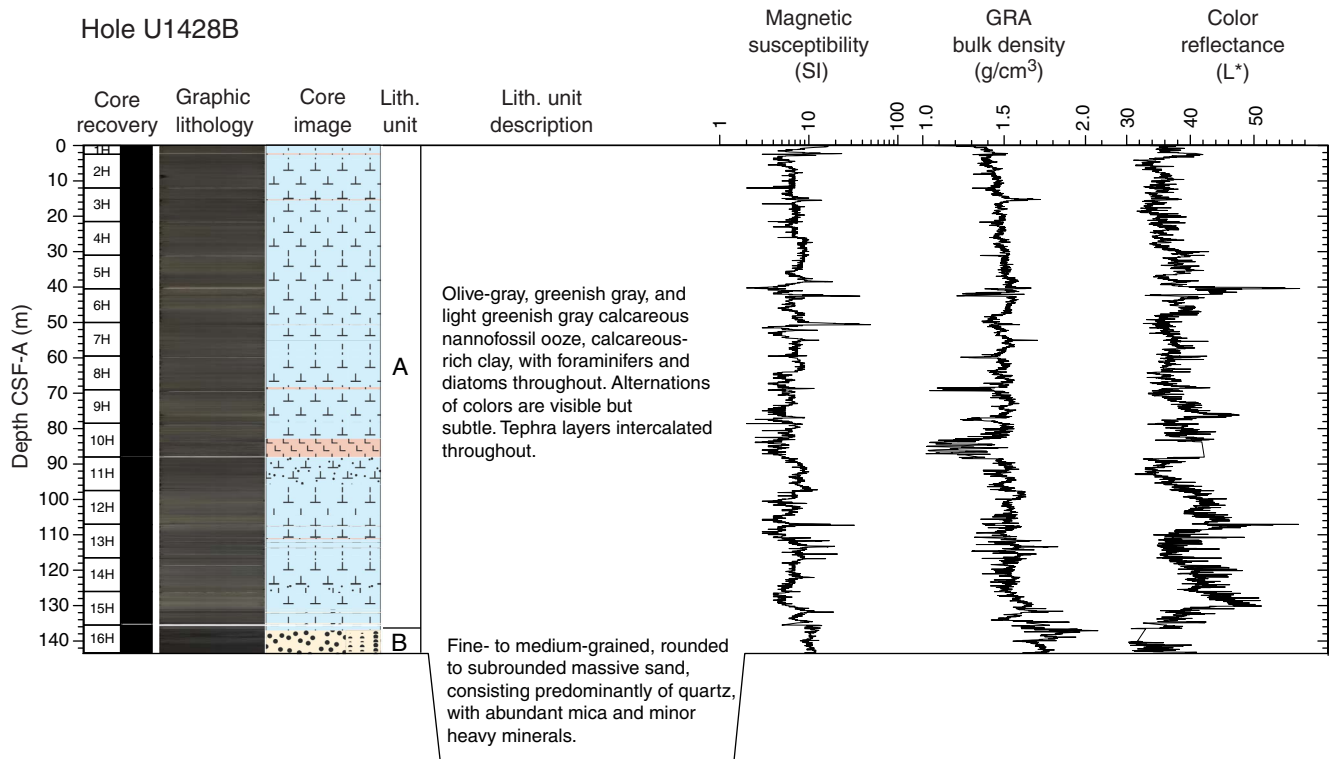


Figure F5. Lithologic summary, Hole U1429A. GRA = gamma ray attenuation.

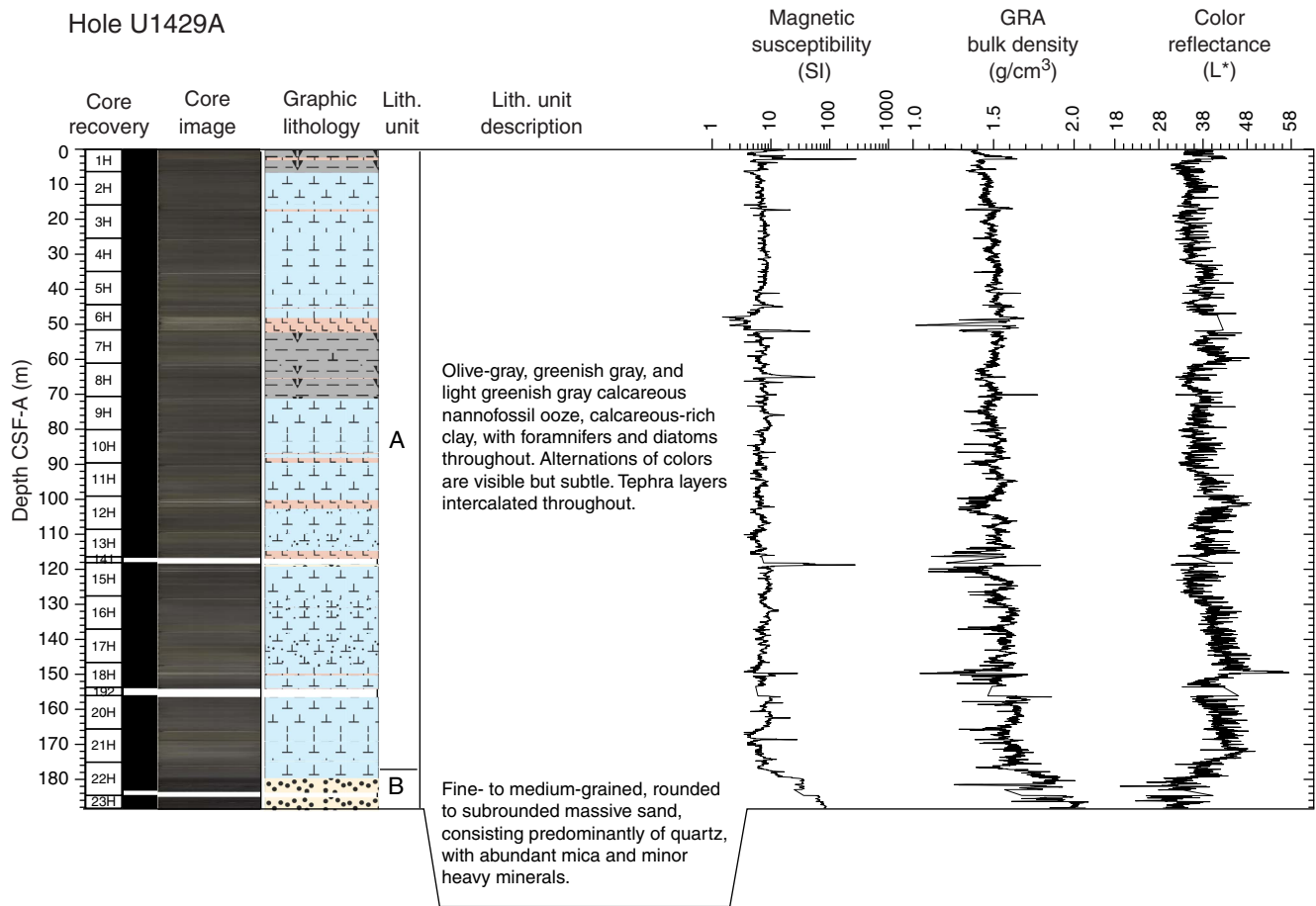


Figure F6. Lithologic summary, Hole U1429B. GRA = gamma ray attenuation.

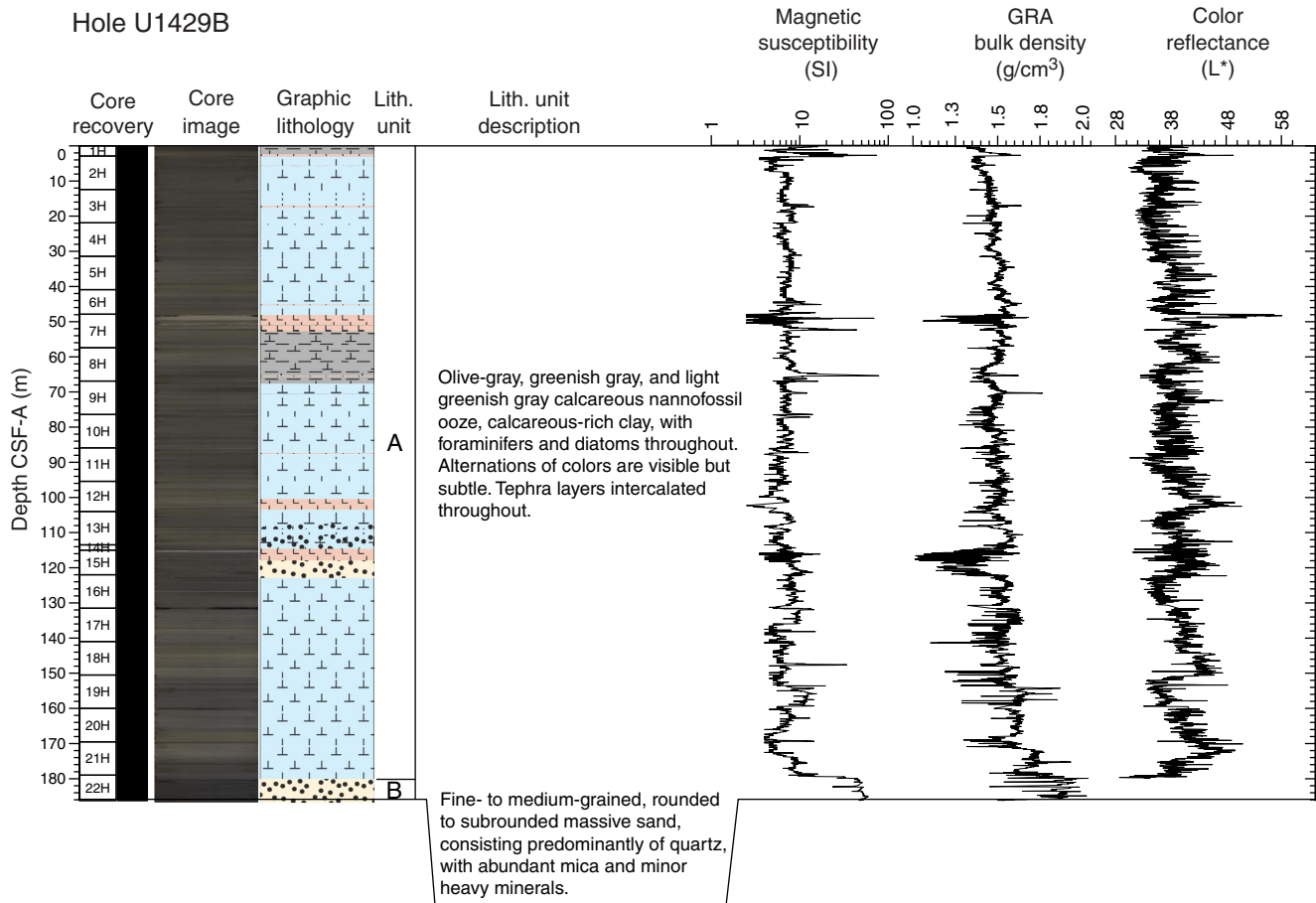


Figure F7. Lithologic summary, Hole U1429C. GRA = gamma ray attenuation.

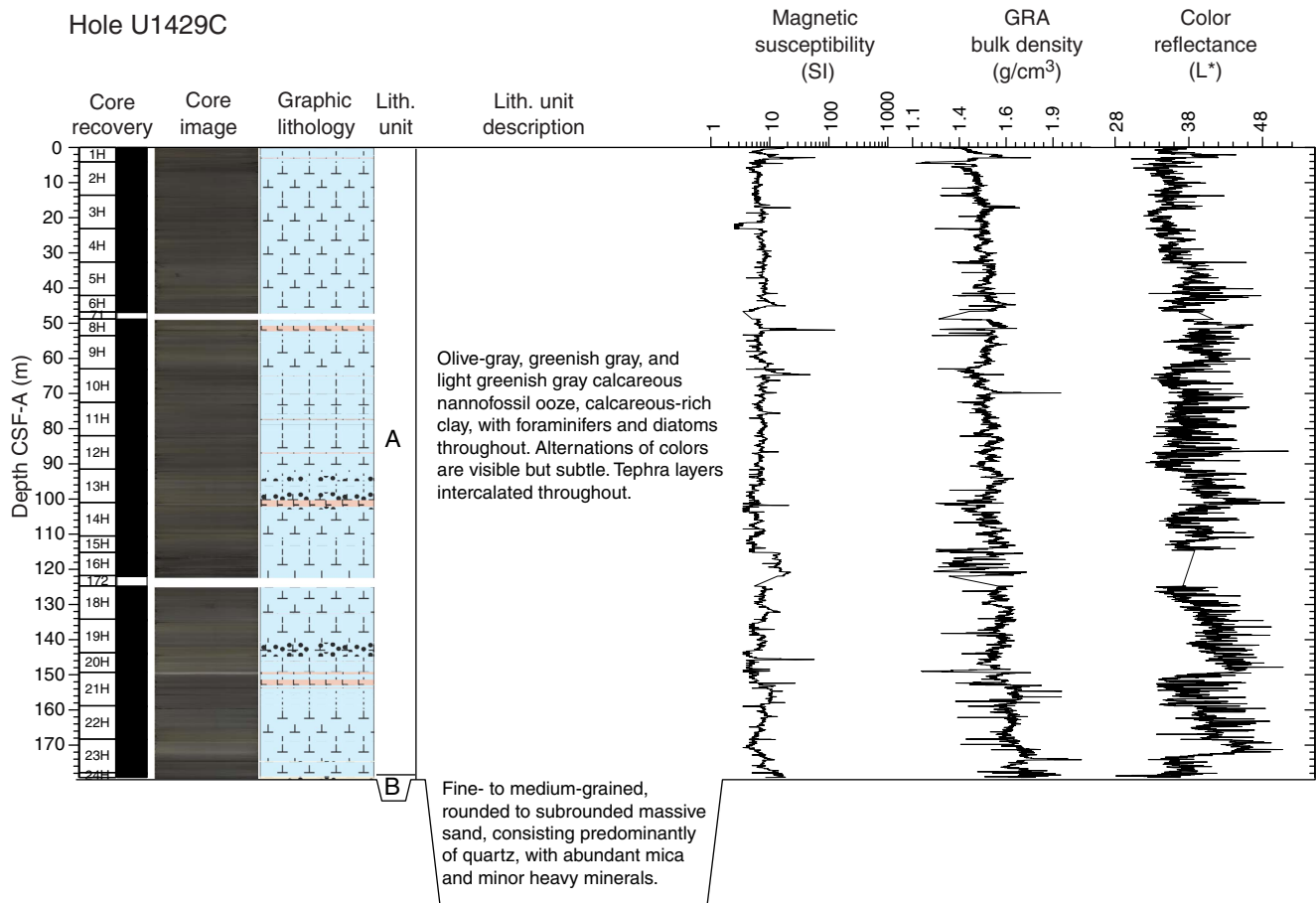




Figure F8. Hole-to-hole lithostratigraphic correlation, Sites U1428 and U1429.

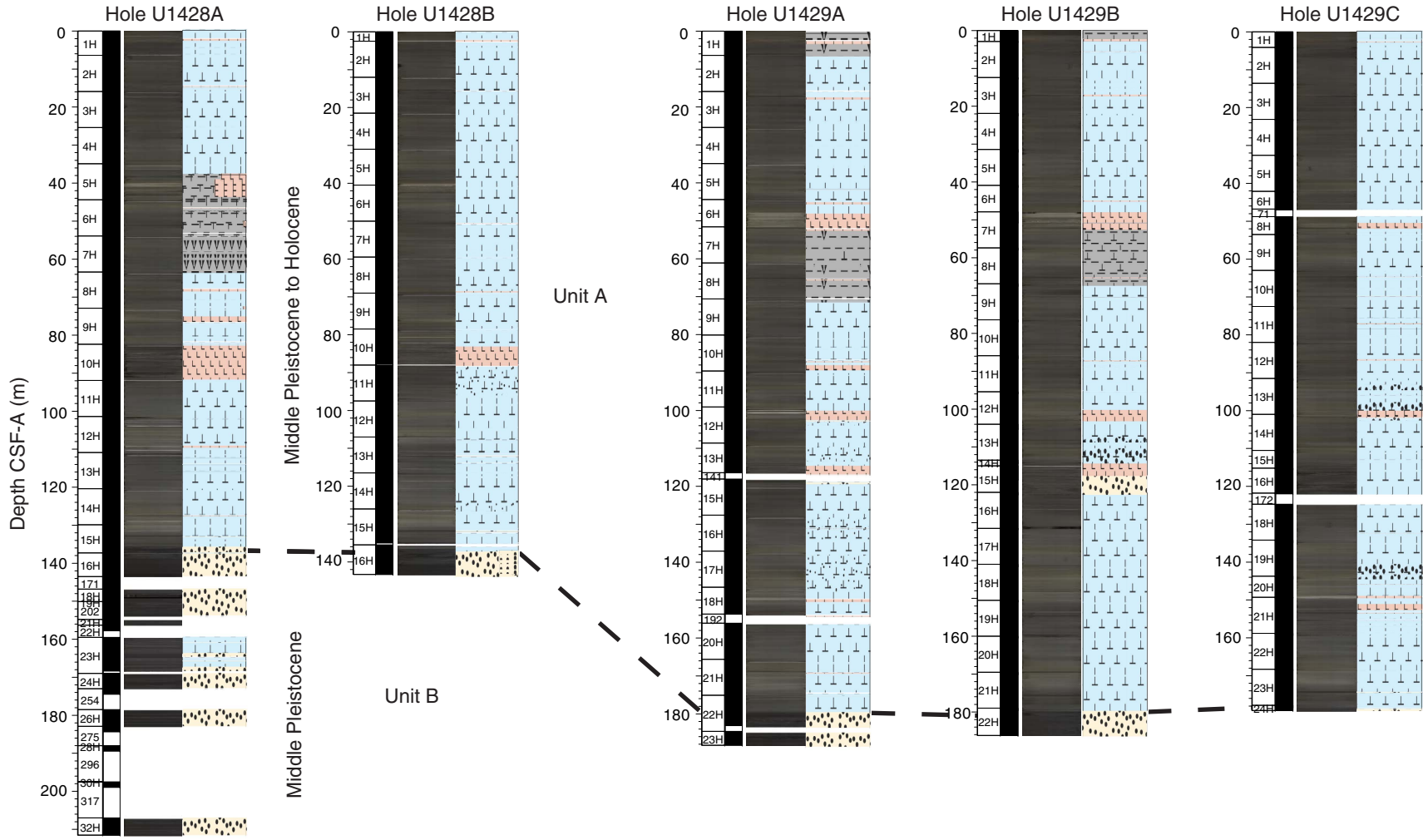


Figure F9. Photographs showing typical examples of sediment bioturbation. Note enhanced color contrast to highlight sedimentary structures.

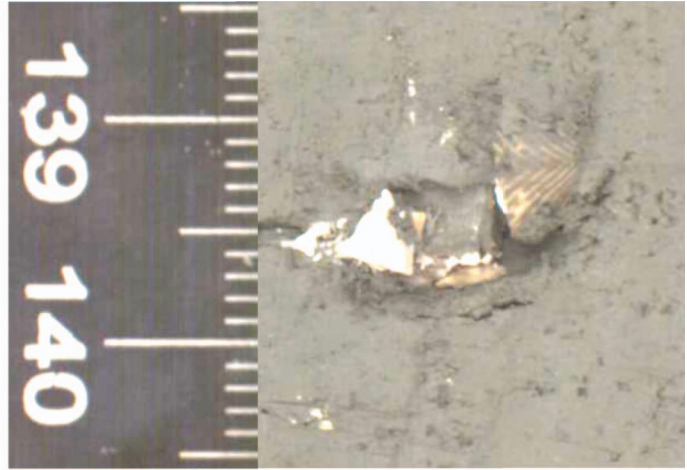


Figure F10. Photographs showing examples of well-preserved gastropod, scaphopod, and bivalve fossils recovered from holes at Site U1428/1429. Note enhanced color contrast to highlight sedimentary structures.

U1428B-2H-7, 49-51 cm
11.99-12.01 m CSF-A



U1429A-8H-5, 139-140 cm
68.45-68.46 m CSF-A



U1429A-9H-5, 50-51 cm
77.10-77.11 m CSF-A



U1429A-10H-2, 55-56 cm
82.15-82.16 m CSF-A

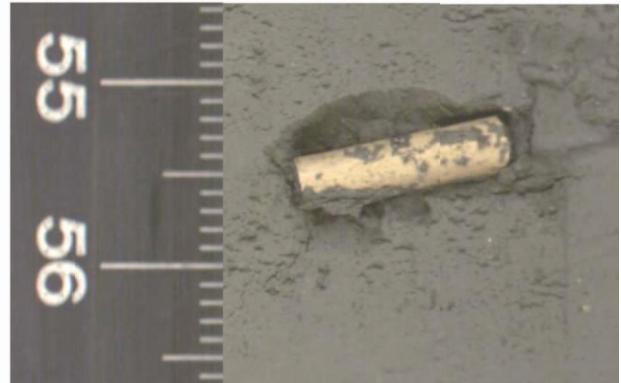


Figure F11. Photographs and photomicrographs showing different representative tephra layers. Note enhanced color contrast to highlight sedimentary structures.

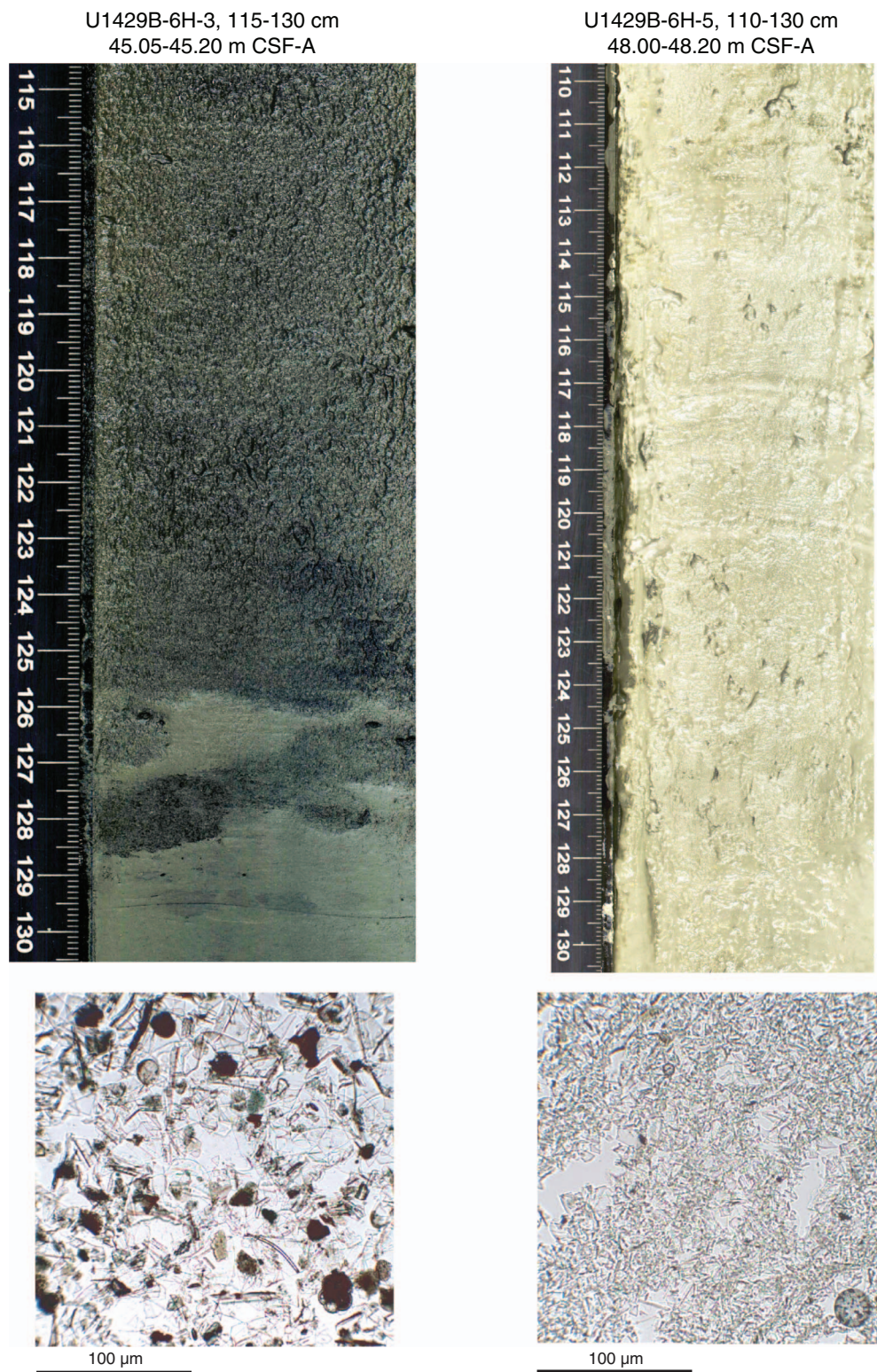


Figure F12. Section photographs from Core 346-U1428B-12H showing subtle meter-scale color changes that primarily reflect variations in nannofossil carbonate content. Note enhanced color contrast to highlight sedimentary structures.

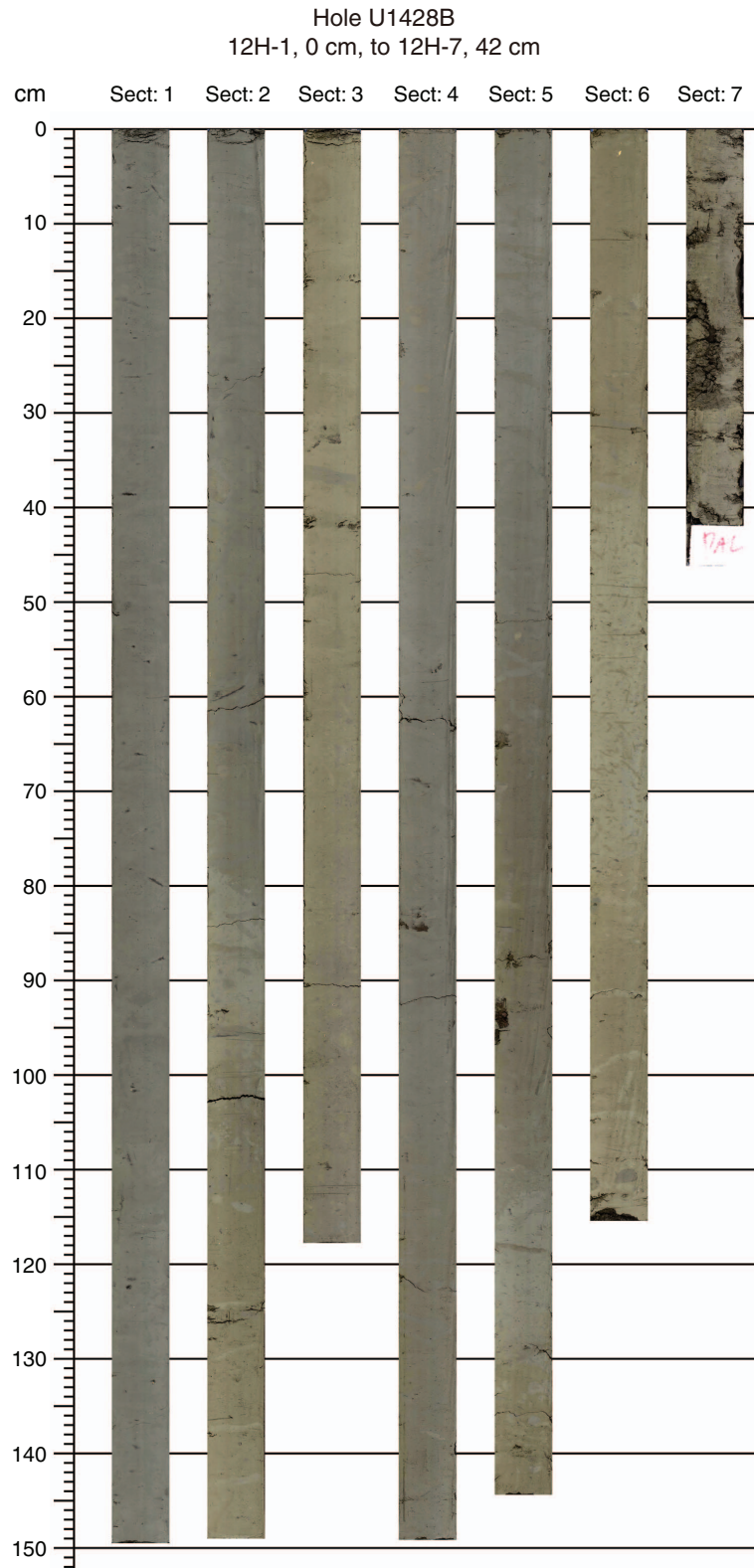




Figure F13. Variation of bulk sediment sample XRD peak intensity of identified minerals with depth, Hole U1428A. XRD data are entirely from lithologic Unit A.

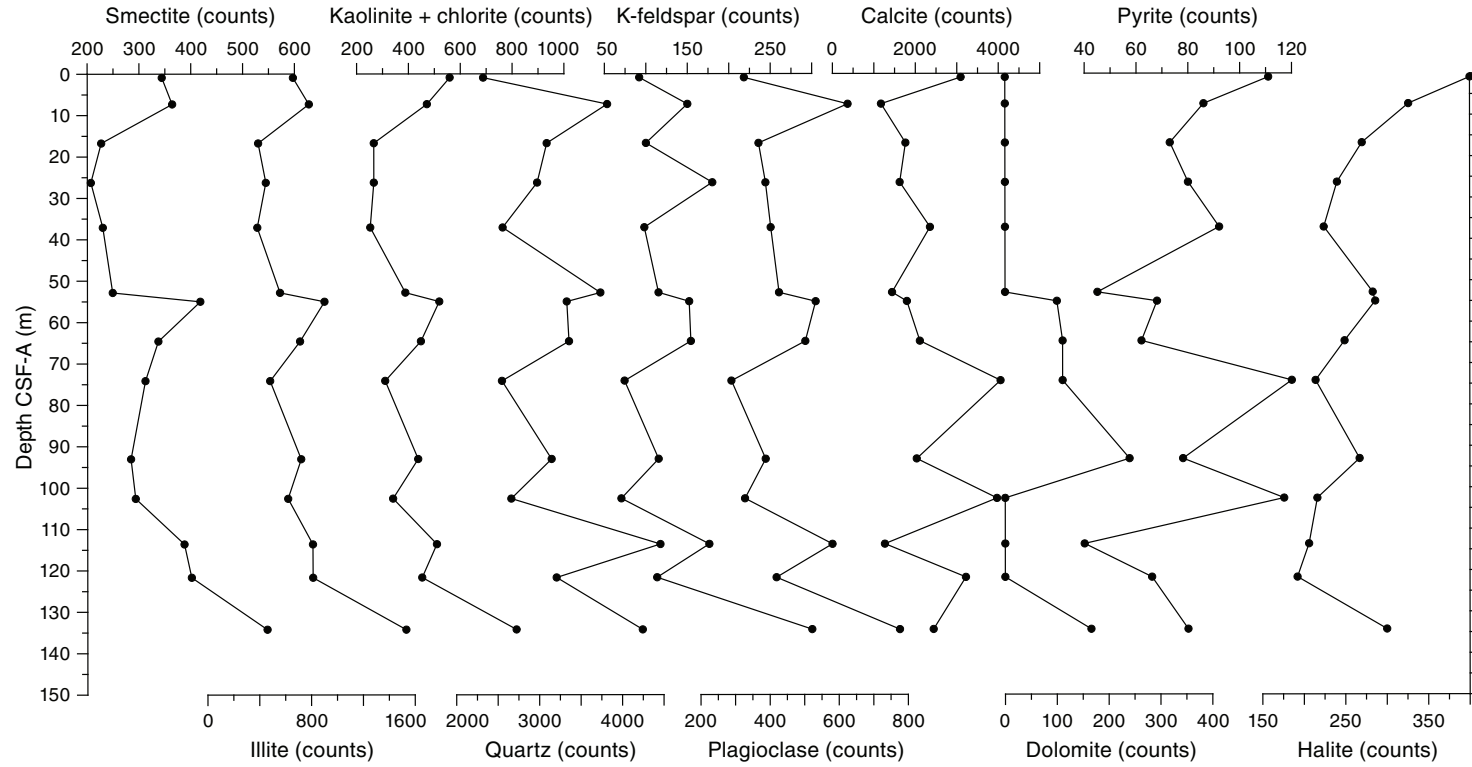




Figure F14. Variation of bulk sediment sample XRD peak intensity of identified minerals with depth, Hole U1429A. XRD data are entirely from lithologic Unit A.

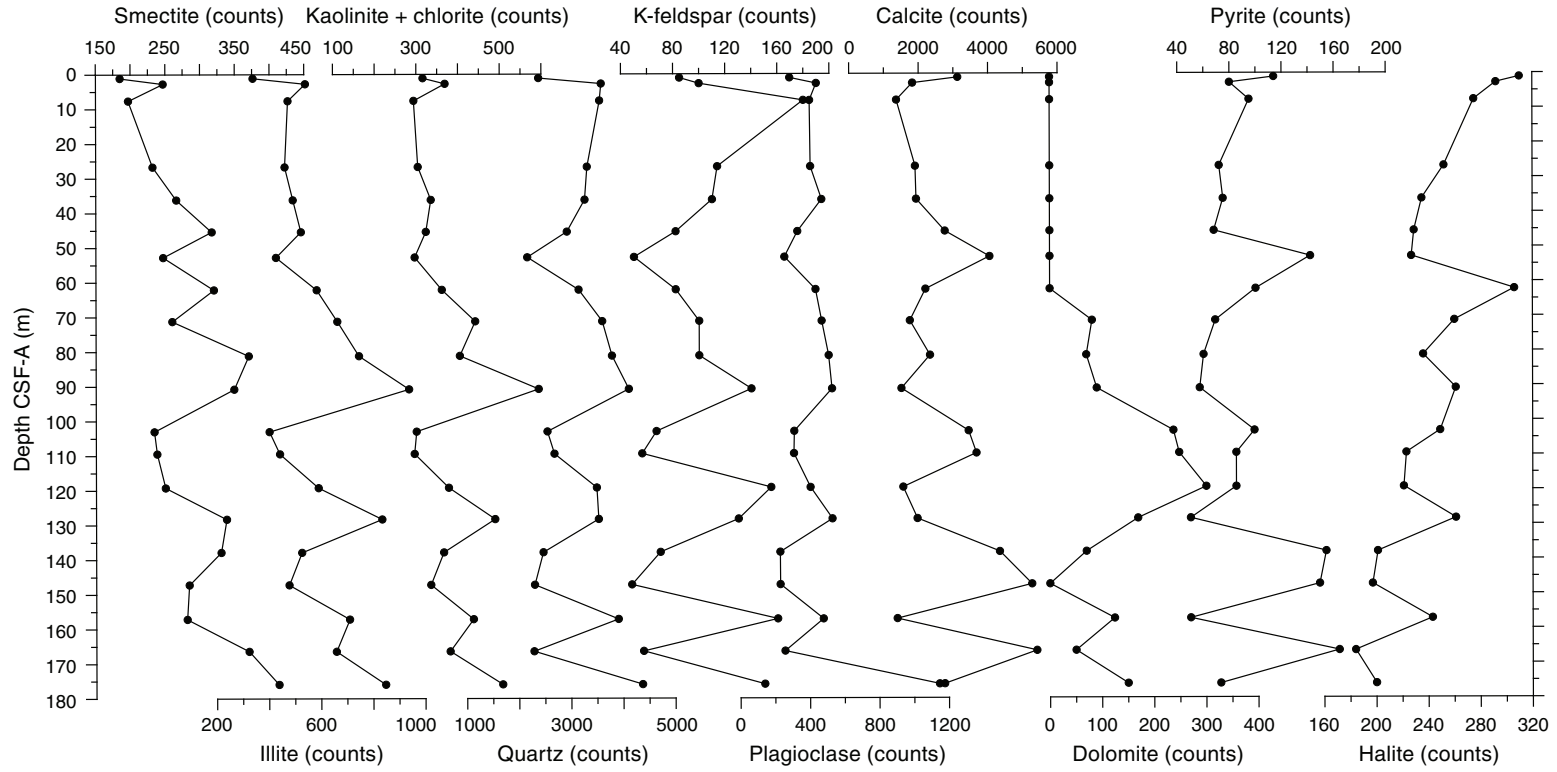
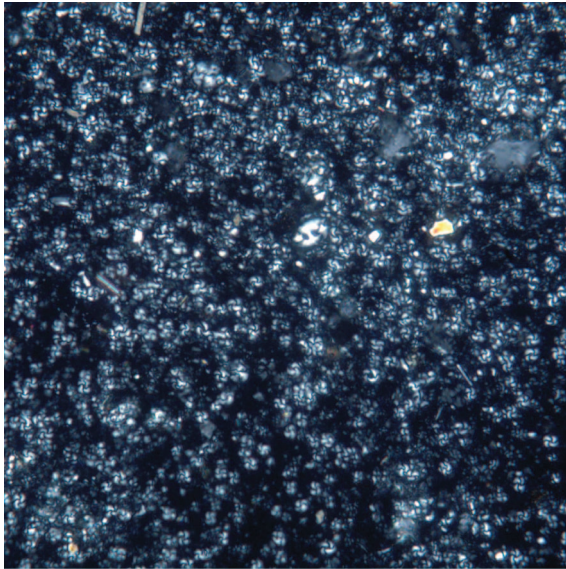


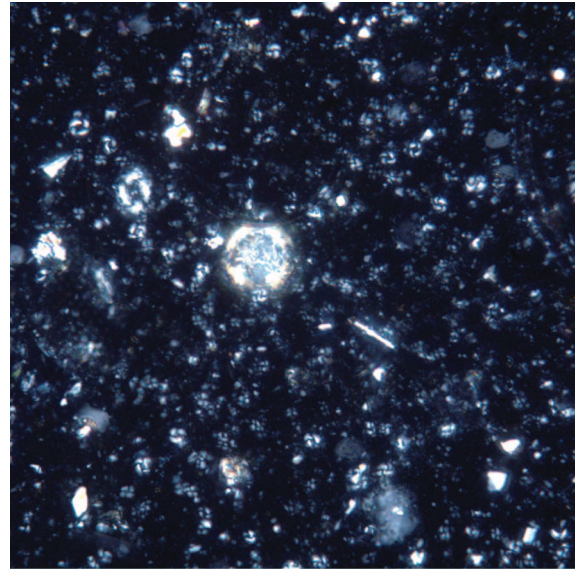
Figure F15. Photomicrographs and SEM images showing typical examples of calcareous nannofossil ooze at Sites U1428 and U1429.

U1248B-14H-CC, 9-15 cm
126.13-126.19 m CSF-A



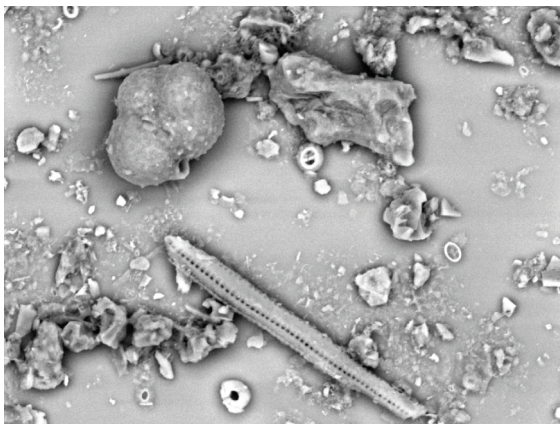
100 μm

U1429B-2H-CC, 10 cm
12.59 m CSF-A



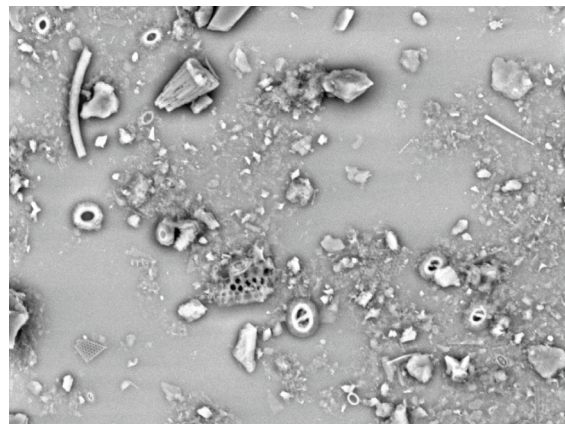
100 μm

U1428B-2H-CC, 10-16 cm
12.24-12.30 m CSF-A



50 μm

U1428B-2H-CC, 10-16 cm
12.24-12.30 m CSF-A



30 μm

Figure F16. Photograph and photomicrographs of smear slides showing the composition of Unit B sand.

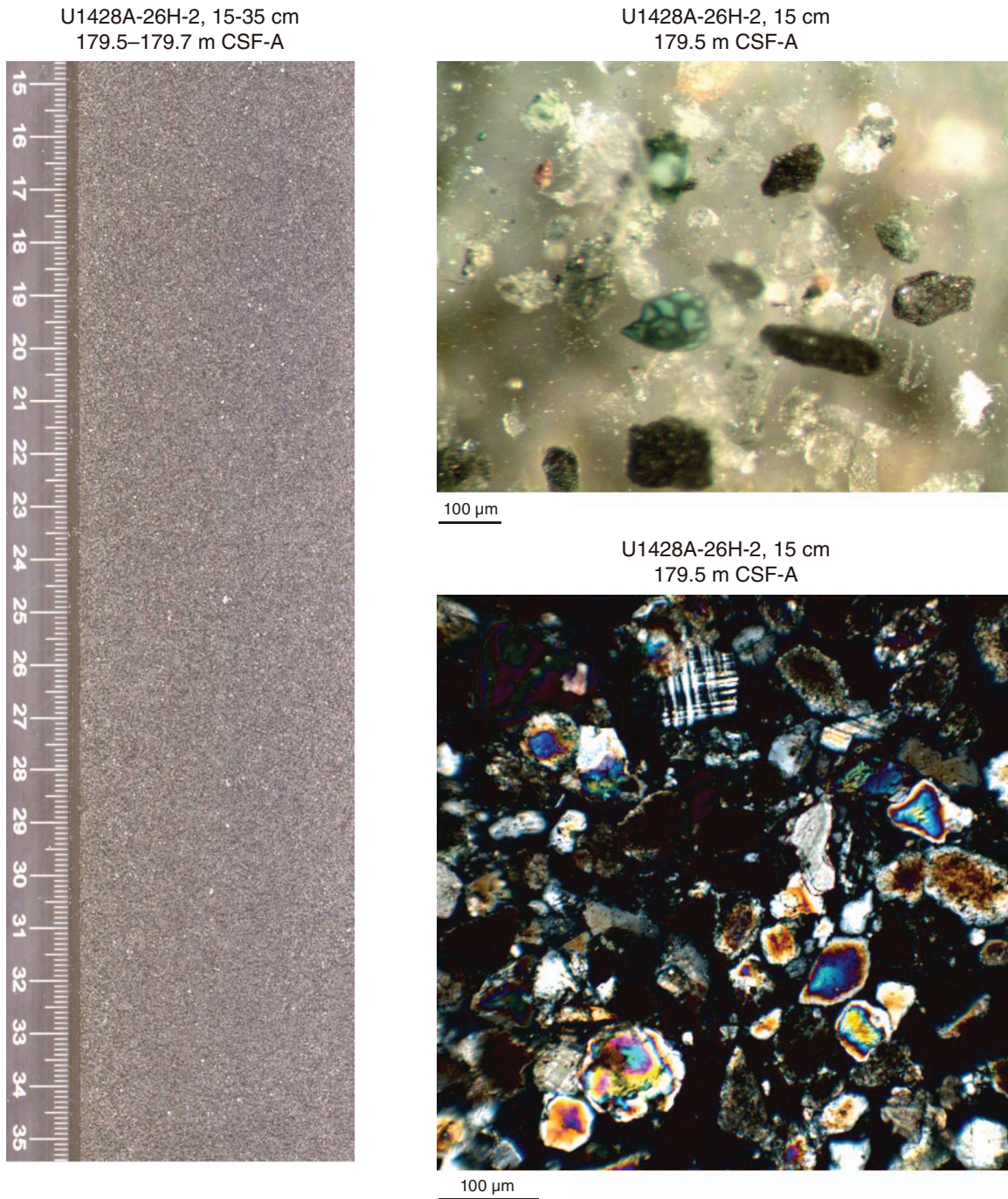


Figure F17. X-ray diffractogram of a representative sand from Unit B (Sample 346-U1428A-32H-2, 10 cm; 208.24 m CSF-A).

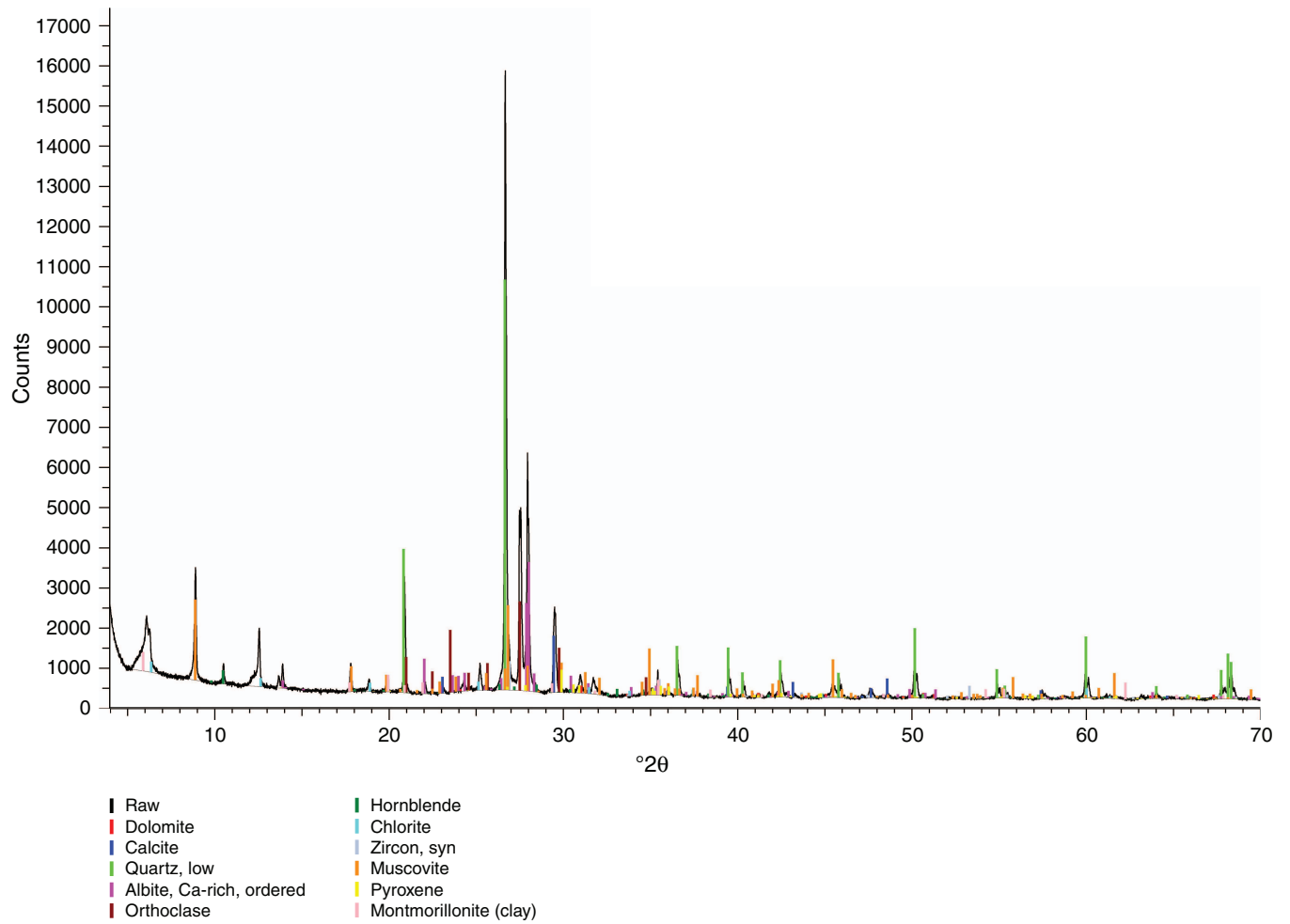


Figure F18. Integrated calcareous and siliceous microfossil biozonation, Sites U1428 and U1429.

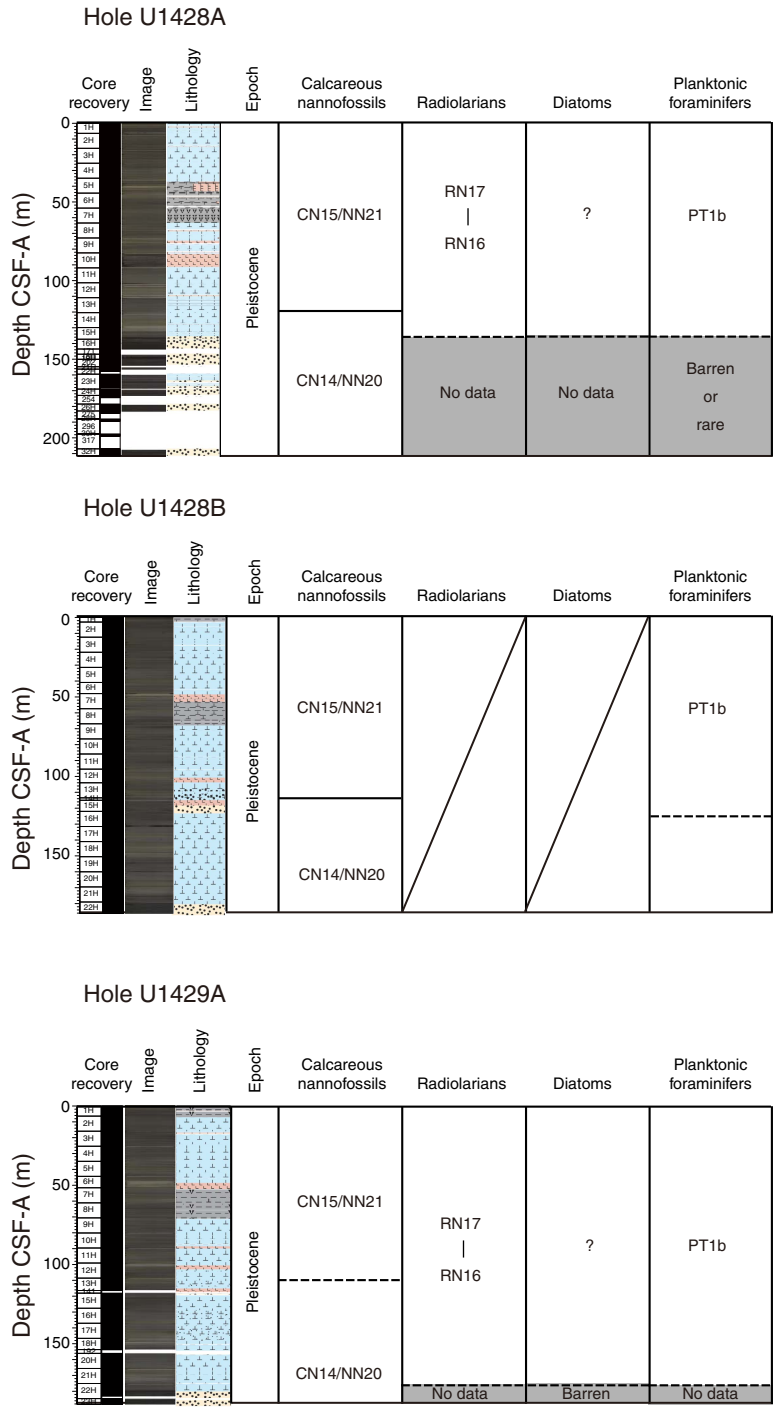


Figure F19. Age-depth profiles for (A) Site U1428 and (B) Hole U1429A. LO = last occurrence, FO = first occurrence.

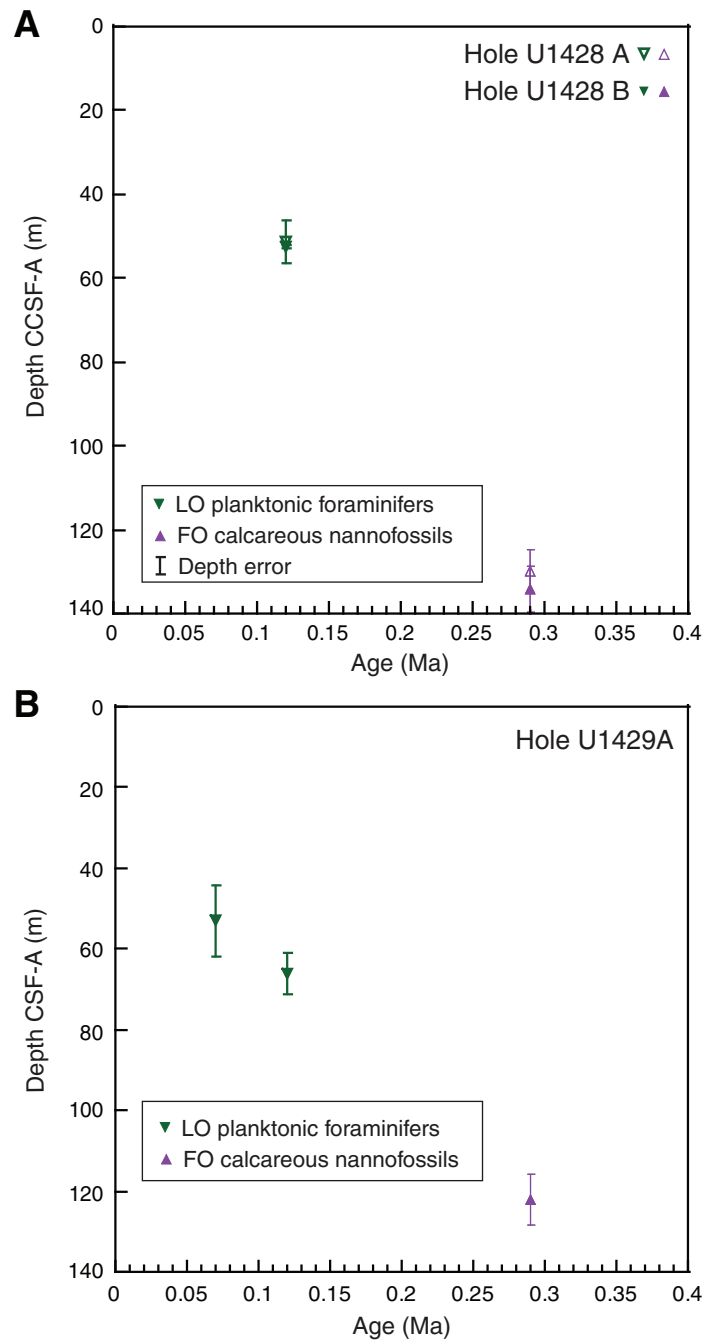




Figure F20. Distribution of siliceous and calcareous microfossils at Sites U1428 and U1429. B = barren, R = rare, F = few, C = common, A = abundant, D = dominant.

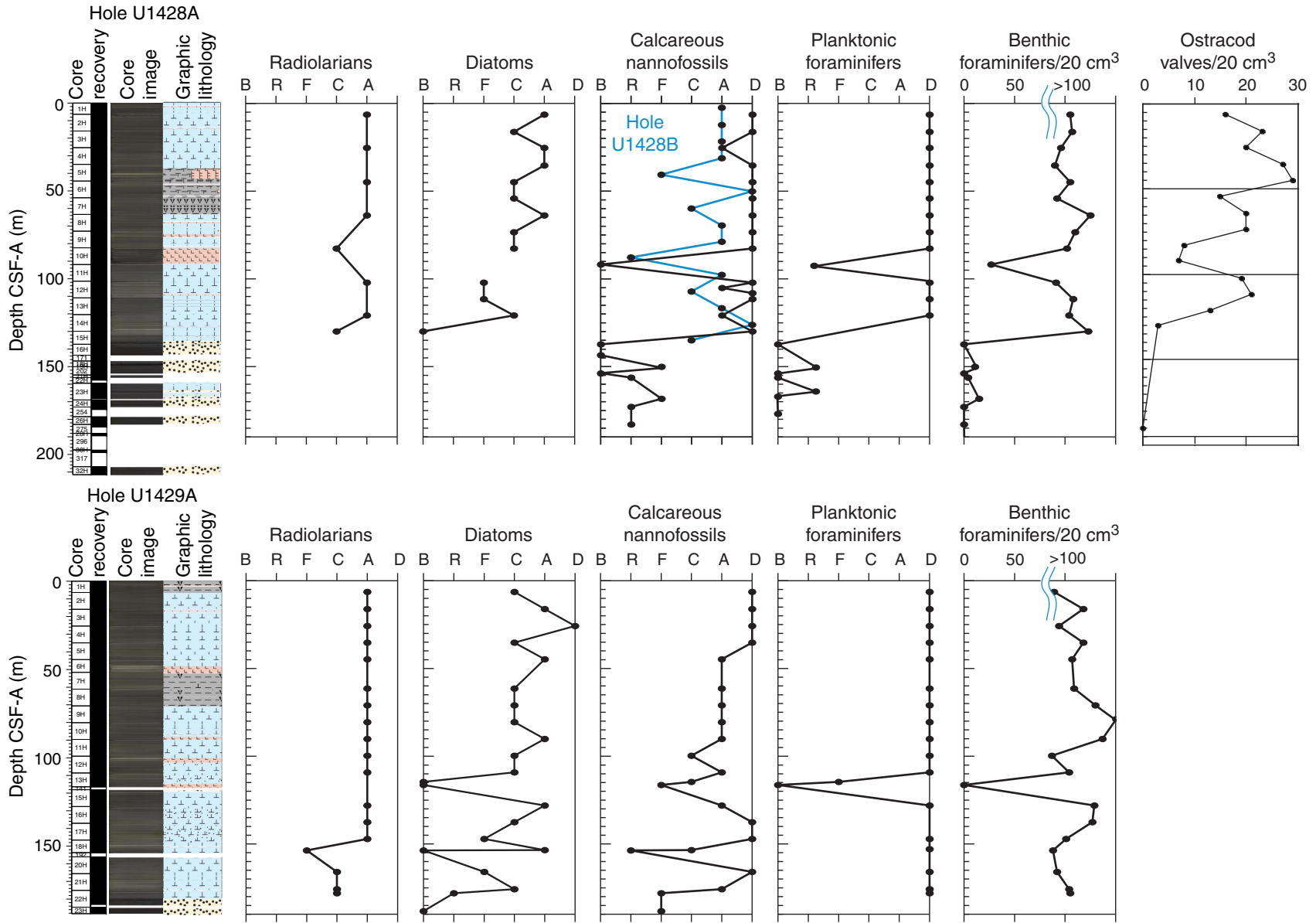


Figure F21. Calcareous nannofossils. Scale bars = 2 μm . 1. *Helicosphaera carteri* (Sample 346-U1429A-5H-CC). 2. *Helicosphaera wallichii* (Sample 346-U1428A-1H-CC). 3. *Helicosphaera inversa* (Sample 346-U1428A-14H-CC). 4. *Rhabdosphaera clavigera* (Sample 346-U1429A-1H-CC). 5. *Ceratolithus cristatus* (Sample 346-U1428A-5H-CC). 6. *Coccolithus pelagicus* (Sample 346-U1429A-1H-CC). 7. *Emiliania huxleyi* (Sample 346-U1429A-1H-CC). 8. *Calciolenia murrayi* (Sample 346-U1429A-5H-CC). 9. *Oolithotus fragilis* (Sample 346-U1429A-7H-CC). 10. *Umbilicosphaera sibogae* (Sample 346-U1429A-7H-CC). 11. *Syracosphaera* spp. (Sample 346-U1429A-5H-CC). 12, 13. Small *Gephyrocapsa* (<4 μm) (Sample 346-U1429A-5H-CC). 14. *Gephyrocapsa caribbeanica* (Sample 346-U1428A-14H-CC). 15, 16. *Gephyrocapsa oceanica* (Sample 346-U1429A-1H-CC). Photos were taken using the light microscope (cross-polarized light) at 1000 \times magnification.

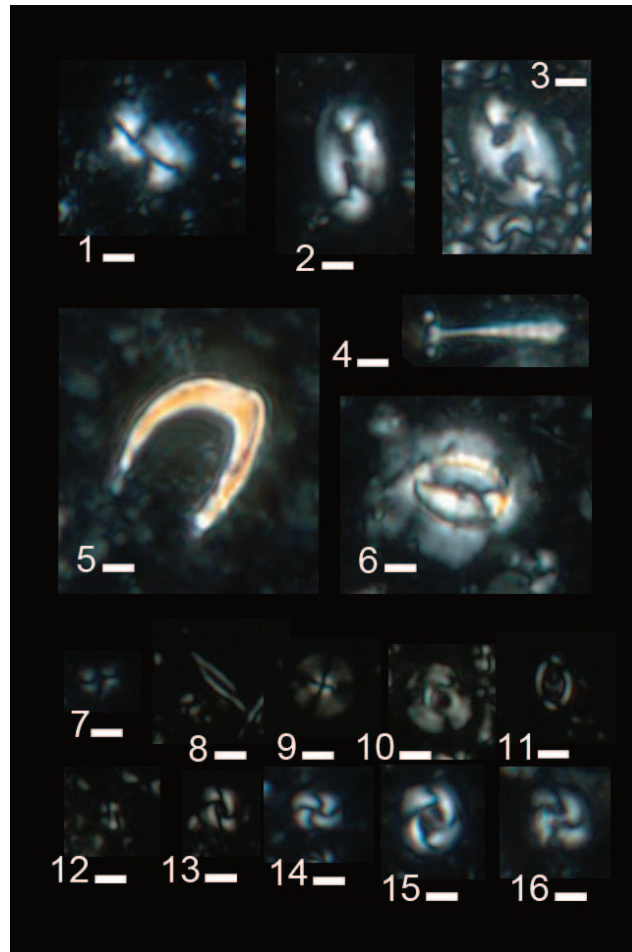




Figure F22. Relative abundance changes of seven most abundant radiolarian groups (% of total assemblage) in Hole U1429A. Variations in color reflectance L* value are shown in the lowest panel (gray line).

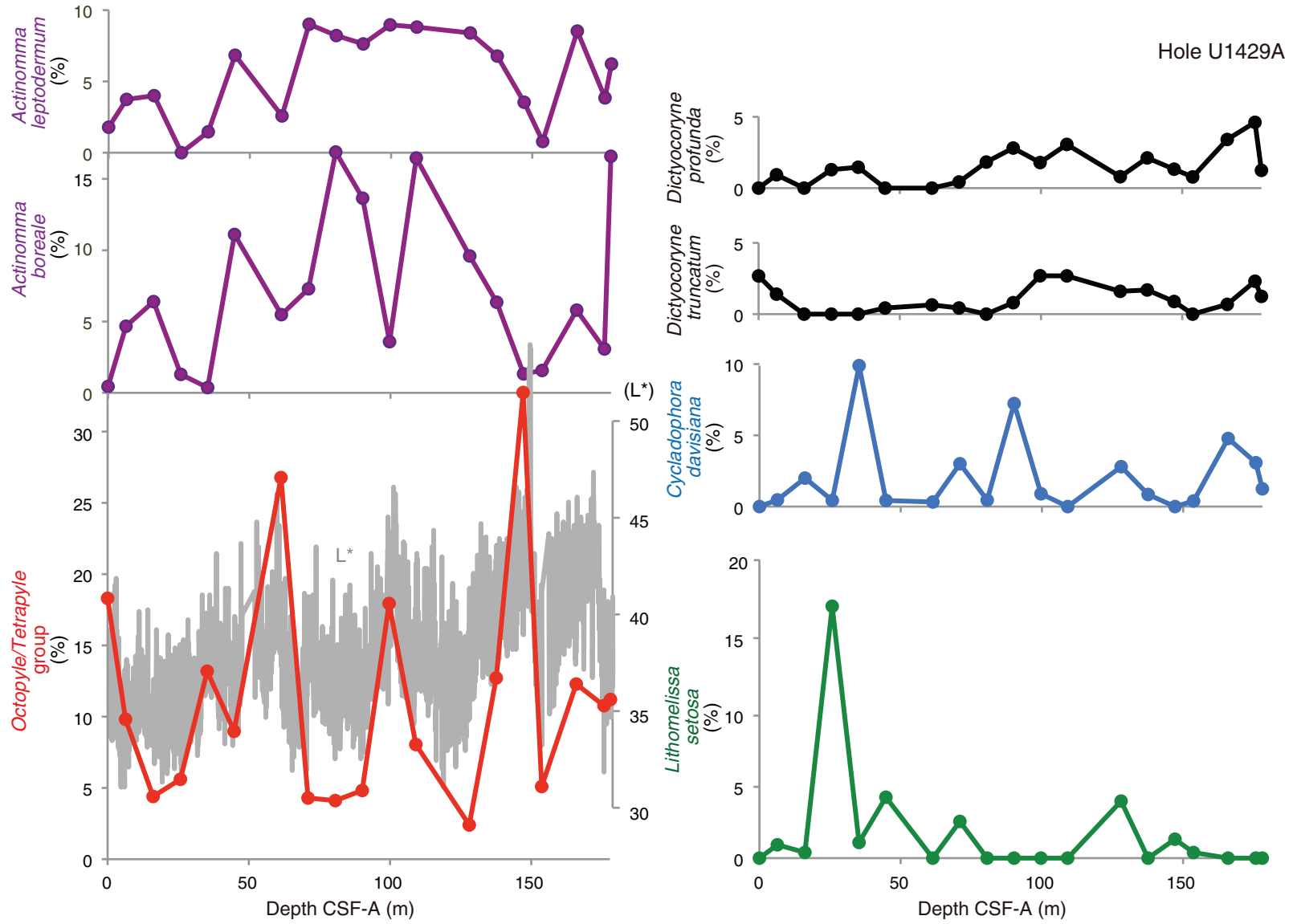




Figure F23. Relative abundances of diatoms, *Chaetoceros* spores, *Paralia sulcata*, and freshwater species in Holes U1428A and U1429A. B = barren, R = rare, F = few, C = common, A = abundant, D = dominant.

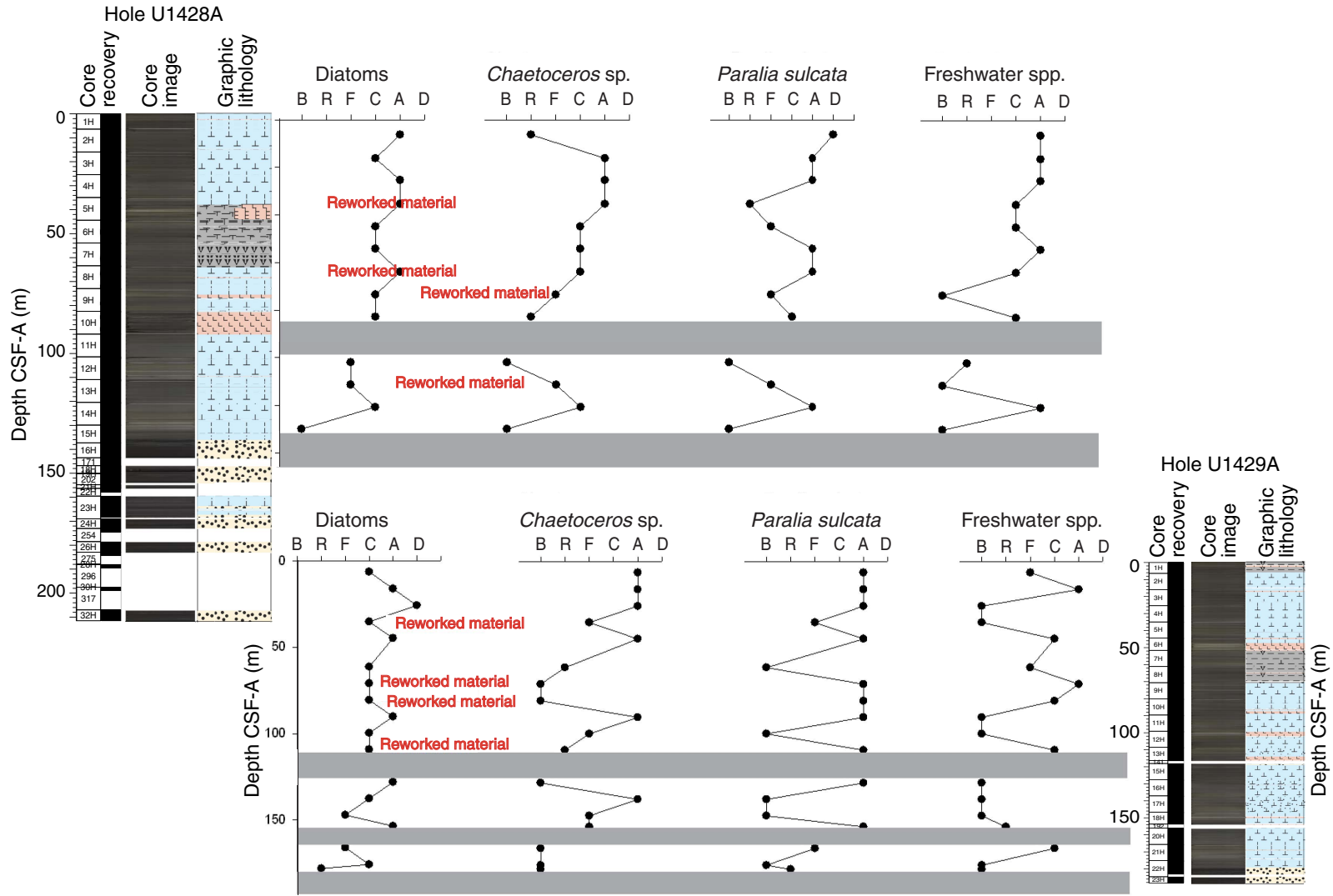




Figure F24. Planktonic foraminiferal distribution data in Holes U1428A and U1429A. B = barren, R = rare, F = few, A = abundant, D = dominant. Yellow shading indicates sand intervals.

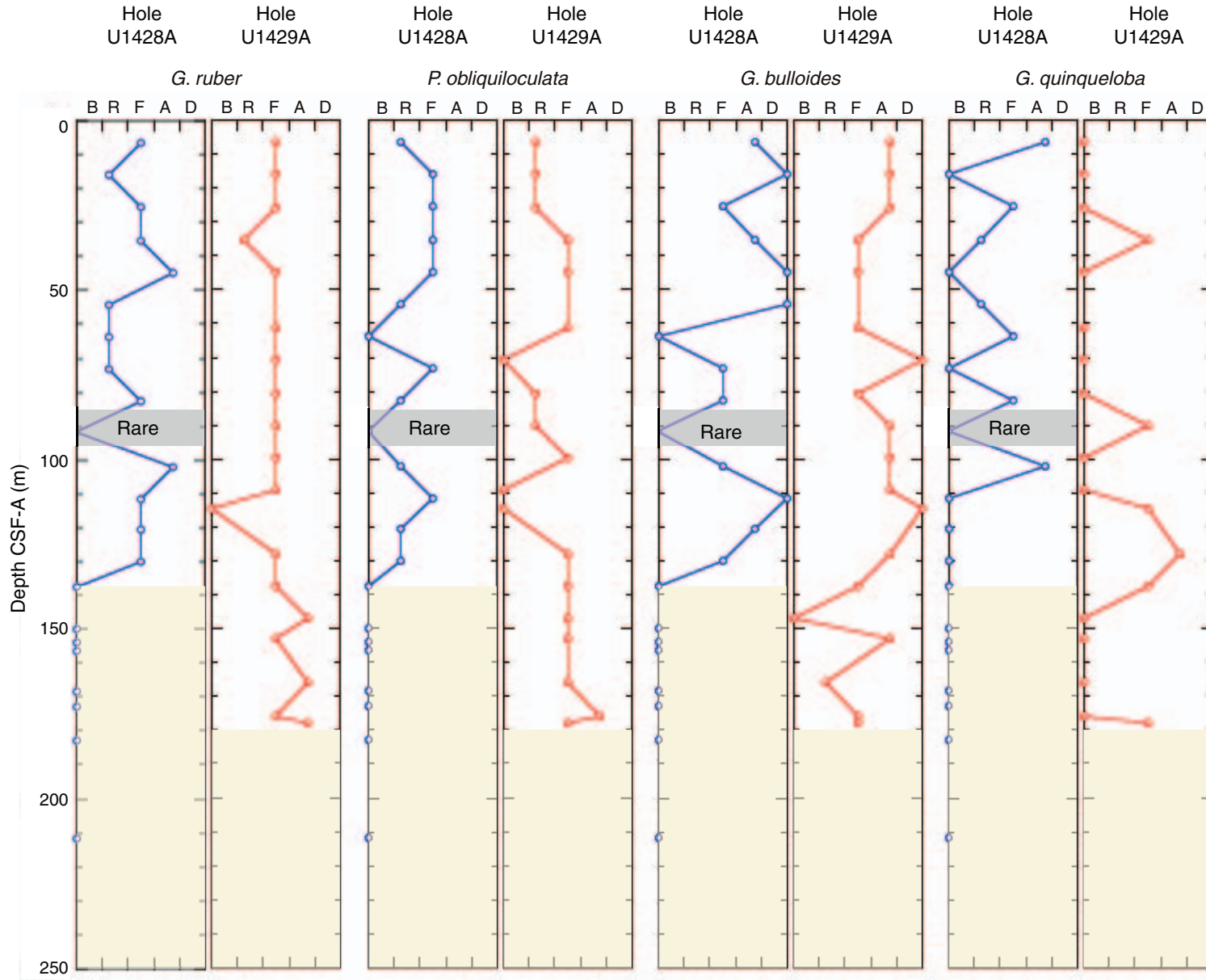




Figure F25. Comparison of color reflectance L* and benthic foraminiferal distribution data in Holes U1428A and U1429A. The percentage of benthic foraminifers refers to the total foraminiferal assemblage. The percentage of various species is expressed as a percentage of the total benthic assemblage. Blue shading indicates reworked ash layer containing benthic foraminifers, yellow shading indicates barren sand intervals.

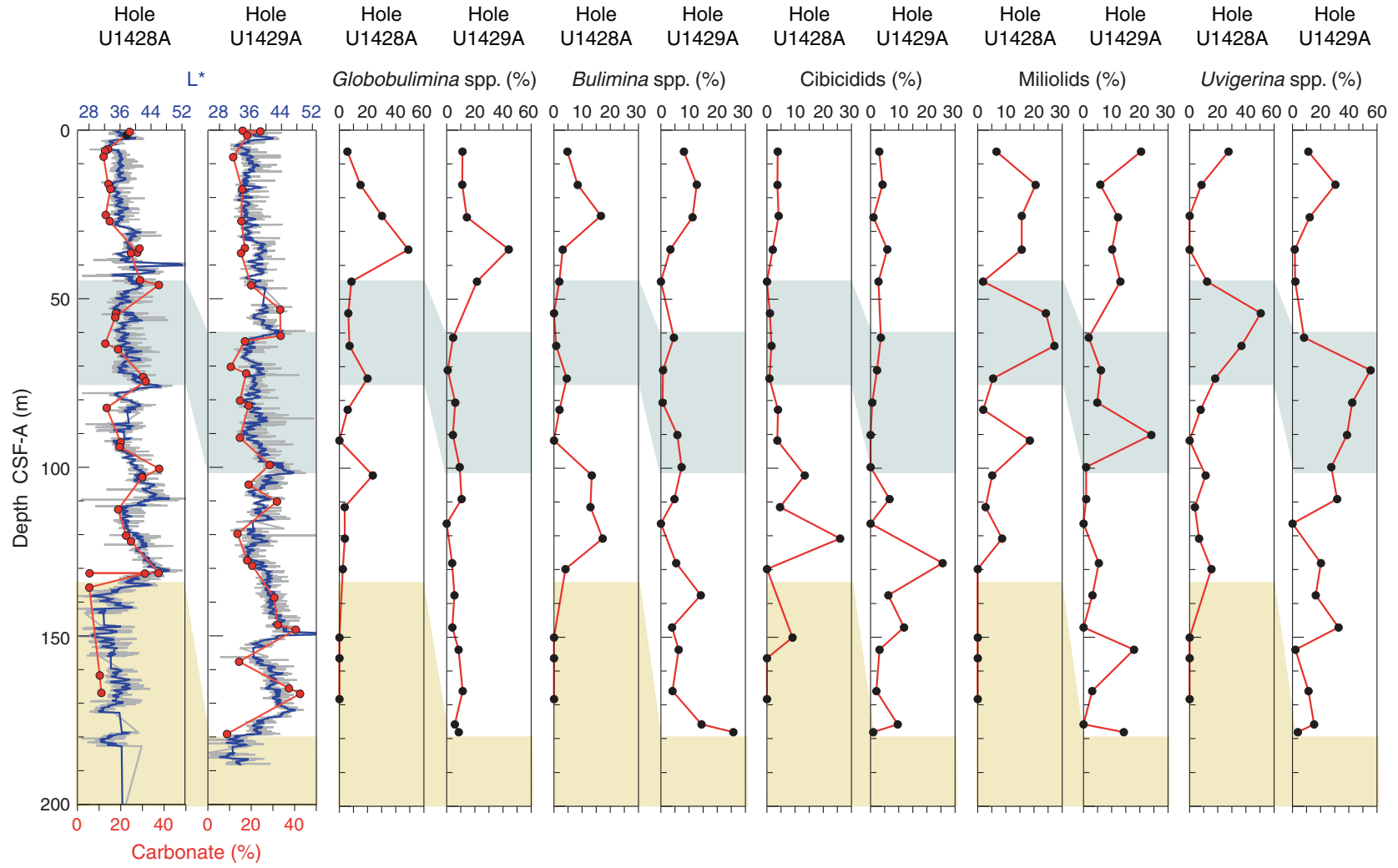


Figure F26. Benthic foraminifera (Part 1). Scale bars = 50 μm . 1, 2. *Planulina wuellerstorfi*; (1) Sample 346-U1428A-13H-CC; (2) Sample 346-U1428A-11H-CC. 3, 4. *Cibicidoides pachyderma* (Sample 346-U1428A-13H-CC). 5. *Pullenia bulloides* (Sample 346-U1428A-7H-CC). 6. *Hyalinea balthica* (Sample 346-U1428A-11H-CC). 7, 8. *Melonis barleeanus* (Sample 346-U1428A-13H-CC). 9. *Hoeglundina elegans* (Sample 346-U1428A-11H-CC). 10, 11. *Oridorsalis umbonatus*; (10) Sample 346-U1428A-11H-CC; (11) Sample 346-U1428A-13H-CC. 12. *Fissurina* sp. (Sample 346-U1429A-4H-CC). 13. *Neolenticulina peregrina* (Sample 346-U1428A-11H-CC). 13. *Bulimina marginata* (Sample 346-U1428A-11H-CC). 14. *Gavelinopsis lobatulus* (Sample 346-U1429A-4H-CC). 15, 16. *Ammonia takanabensis* (Sample 346-U1429A-8H-CC).

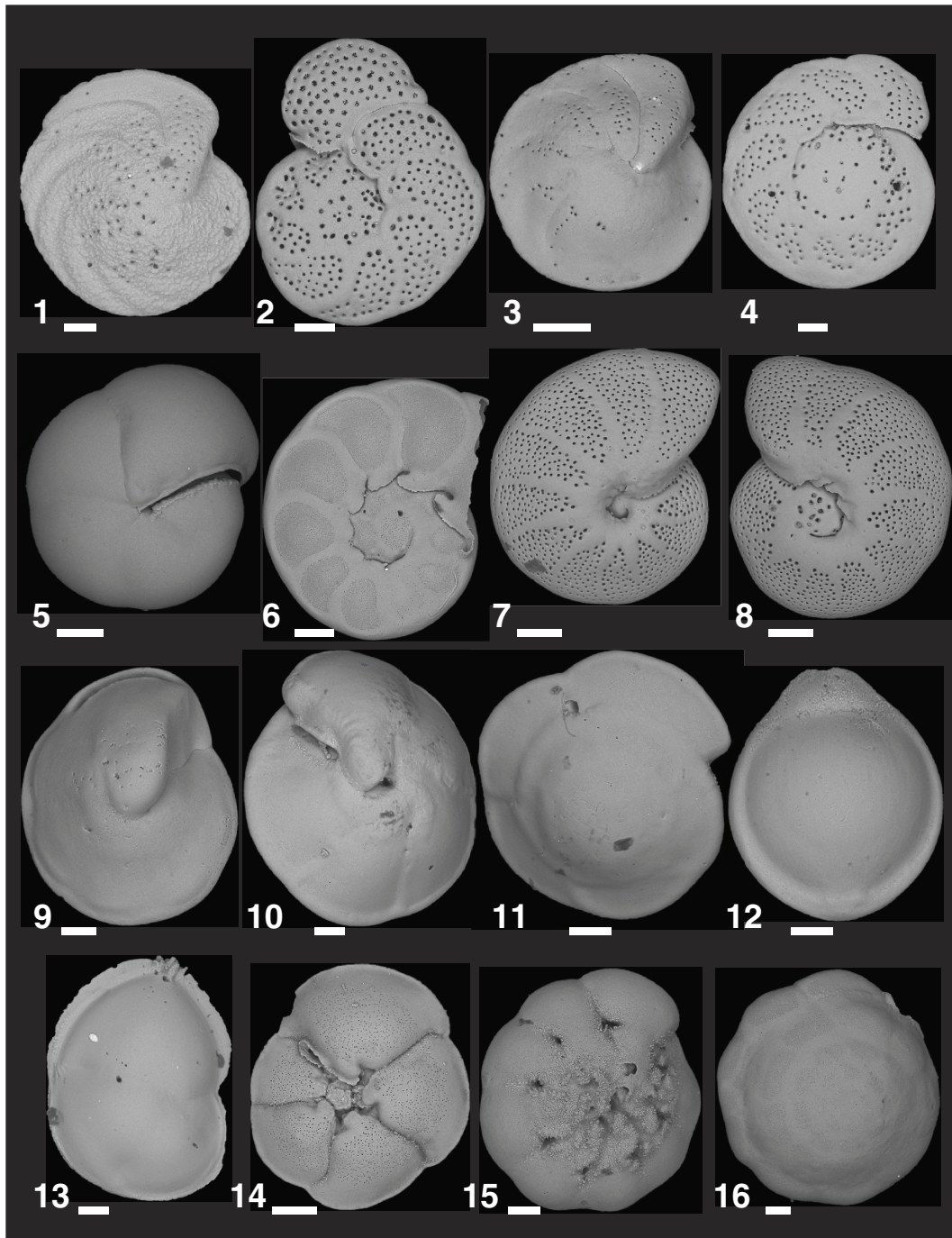


Figure F27. Benthic foraminifera (Part 2). Scale bars = 50 μm . 1, 2. *Chilostomella oolina* (Sample 346-U1428A-1H-CC). 3. *Fursenkoina bradyi* (Sample 346-U1428A-8H-CC). 4. *Fursenkoina bradyi* (Sample 346-U1428A-1H-CC). 5. *Globobulimina pacifica* (Sample 346-U1428A-7H-CC). 6. *Textularia* sp. (Sample 346-U1428A-1H-CC). 7. *Bolivinita quadrilatera* (Sample 346-U1428A-13H-CC). 8. *Bolivina robusta* (Sample 346-U1429A-4H-CC). 9. *Bolivina robusta* (Sample 346-U1428A-7H-CC). 10. *Uvigerina peregrina* (Sample 346-U1429A-8H-CC). 11, 12. *Uvigerina peregrina* (Sample 346-U1428A-7H-CC). 13. *Bulimina marginata* (Sample 346-U1428A-11H-CC). 14. *Bulimina marginata* (Sample 346-U1429A-4H-CC). 15. *Bulimina aculeata* (Sample 346-U1429A-4H-CC). 16. *Bulimina aculeata* (Sample 346-U1429A-13H-CC). 17. *Laevidentalina* sp. (Sample 346-U1428A-5H-CC). 18. *Pyrgo* sp. (Sample 346-U1428A-1H-CC). 19. *Sigmoilopsis schlumbergeri* (Sample 346-U1428A-7H-CC). 20. *Sigmoilopsis* sp. (Sample 346-U1428A-7H-CC). 21. *Quinqueloculina* sp. (Sample 346-U1429A-4H-CC). 22. *Amphycorina scalaris* (Sample 346-U1429A-4H-CC).

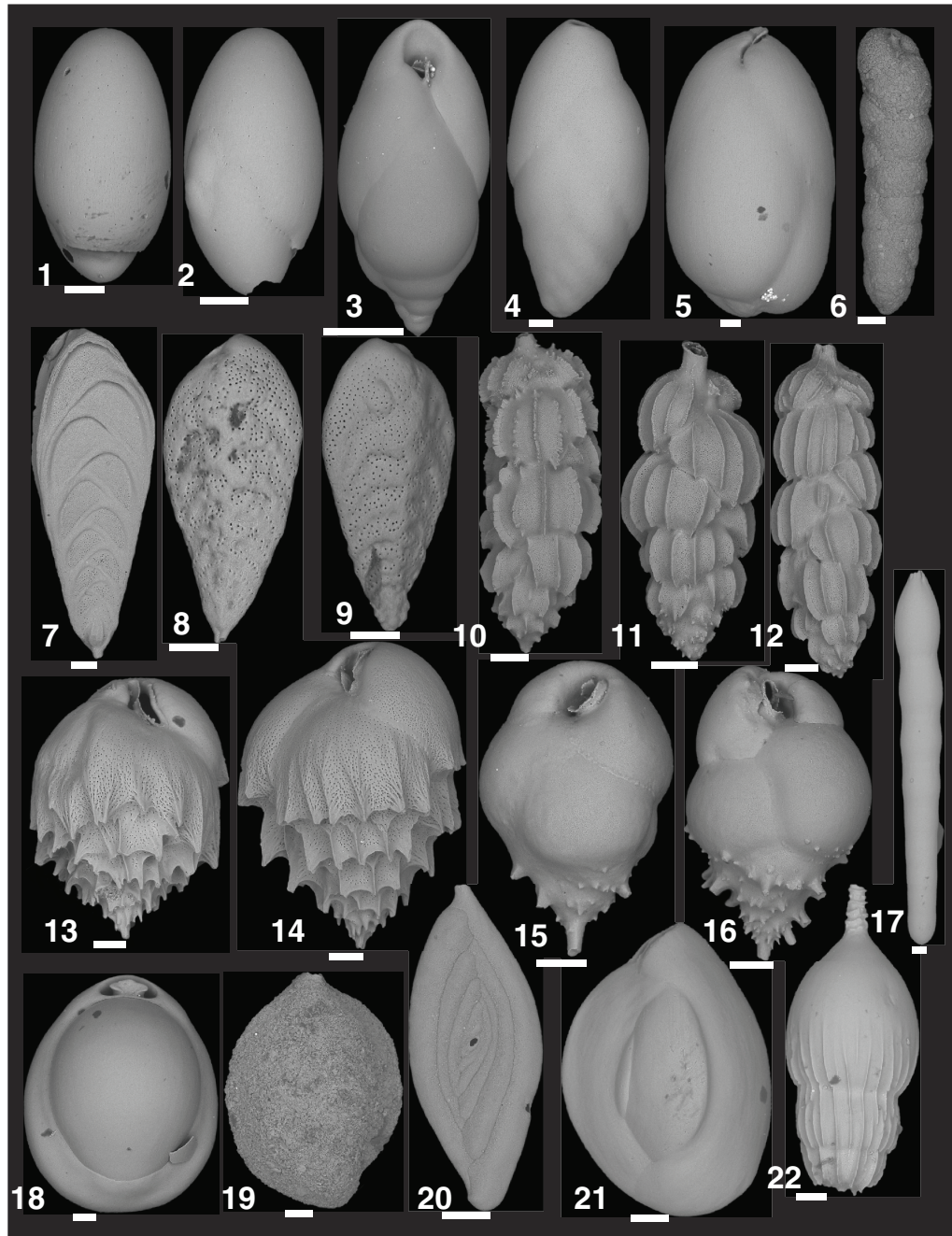


Figure F28. Scanning electron microscope illustrations of representative ostracods, Hole U1428A. 1–4. *Krithe* spp. 5, 6. *Argilloecia elliptica* Ruan, 1988. 7. *Argilloecia* cf. *A. acuminata* Mueller, 1894. 8. *Pseudocythere caudata* Sars, 1866. 9–10. *Macrocypris* sp. 11–12. *Amphileberis nipponica* (Yajima, 1978) Paik and Lee, 1988. 13–15. *Cytheropteron* cf. *C. sinense* Zhao (Yi-Chun), Wang and Zhang, 1985. 16. *Lobosocytheropteron bartolomense* Ishizaki and Gunther, 1974, cf. *Cytheropteron donghaiensis* Zhao (Zhao et al., 2000). 17. *Phlyctocythere reticulosa* Hao (Yi-Chun), 1988. 18. *Bythoceratina?* sp. 19. *Aurila* sp. 20. *Munseyella* sp. cf. *M. ristveti* in Brouwers (1990) and Alvarez Zarikian (in press). 21. *Falsobuntonia taiwanica* Malz, 1982. 22–23. *Pacambocythere buntoniae* Ishizaki, 1981. 24. *Cornucoquimba* sp. 25, 27. *Bradleya japonica* Benson, 1972. 26, 28. *Bradleya albatrossia* Benson, 1972. 29. *Trachyleberidid*. 30. *Legitimocythere acanthoderma*. 31–32. *Acanthocythereis dunelmensis* (Norman, 1865).

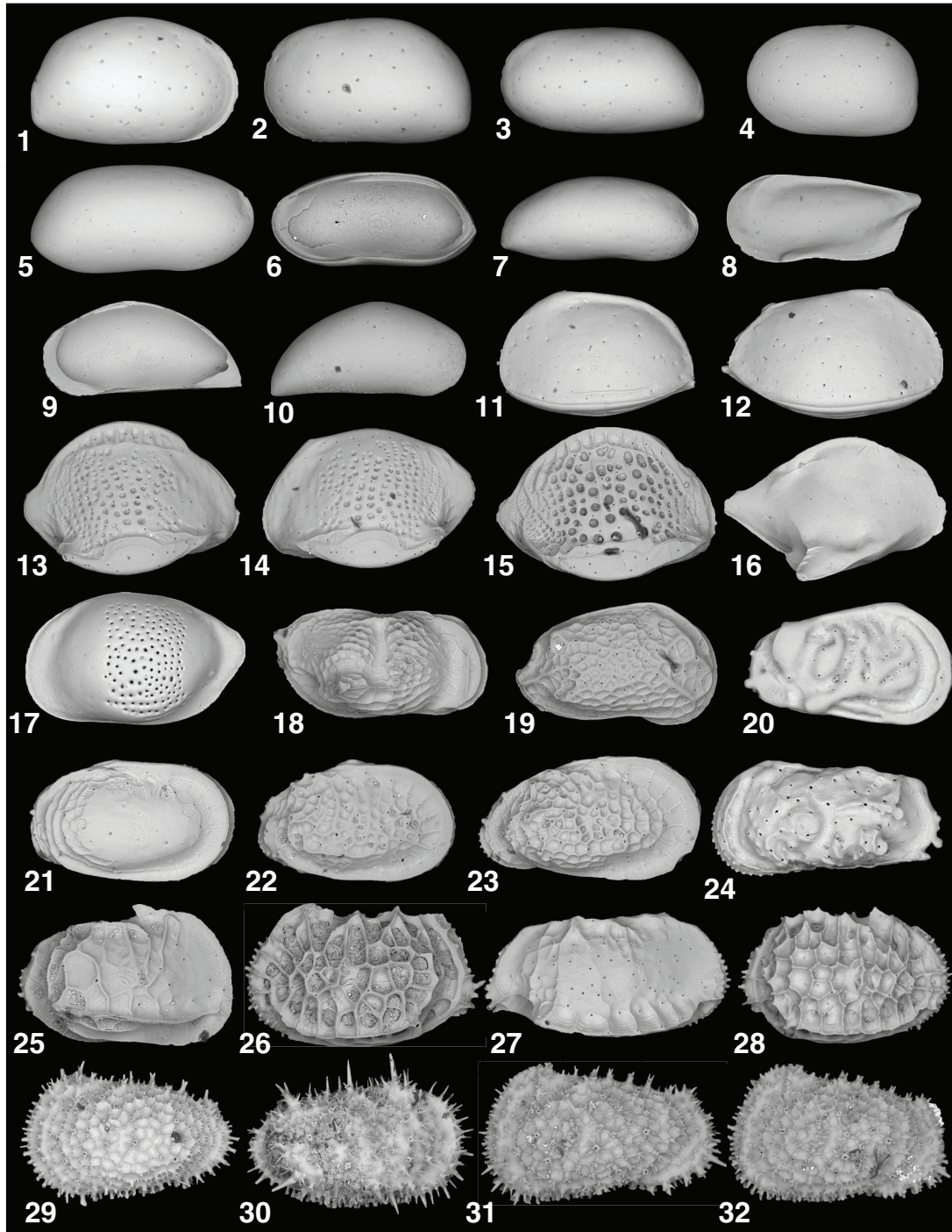


Figure F29. Calcareous and organically cemented, agglutinated foraminifera from Hole U1428A mudline sample. Scale bars = 50 μm . 1. *Bolivina pacifica*. 2. *Bolivina subspinescens*. 3. *Spiroloculina asperula*. 4–6. *Reophax scoriurus*. 7. *Reophax spiculifer*. 8, 9. *Chilostomella oolina*. 10, 11. *Globulimina pacifica*. 12. *Globocassidulina subglobosa*. 13–15. *Fursenkoina bradyi*. 16. *Hyalinea balthica*. 17. *Planulina wuellerstorfi*. 18. *Pullenia bulloides*. 19. *Lenticulina* sp. 20, 21. *Bulimina aculeate*. 22. *Uvigerina peregrina*.

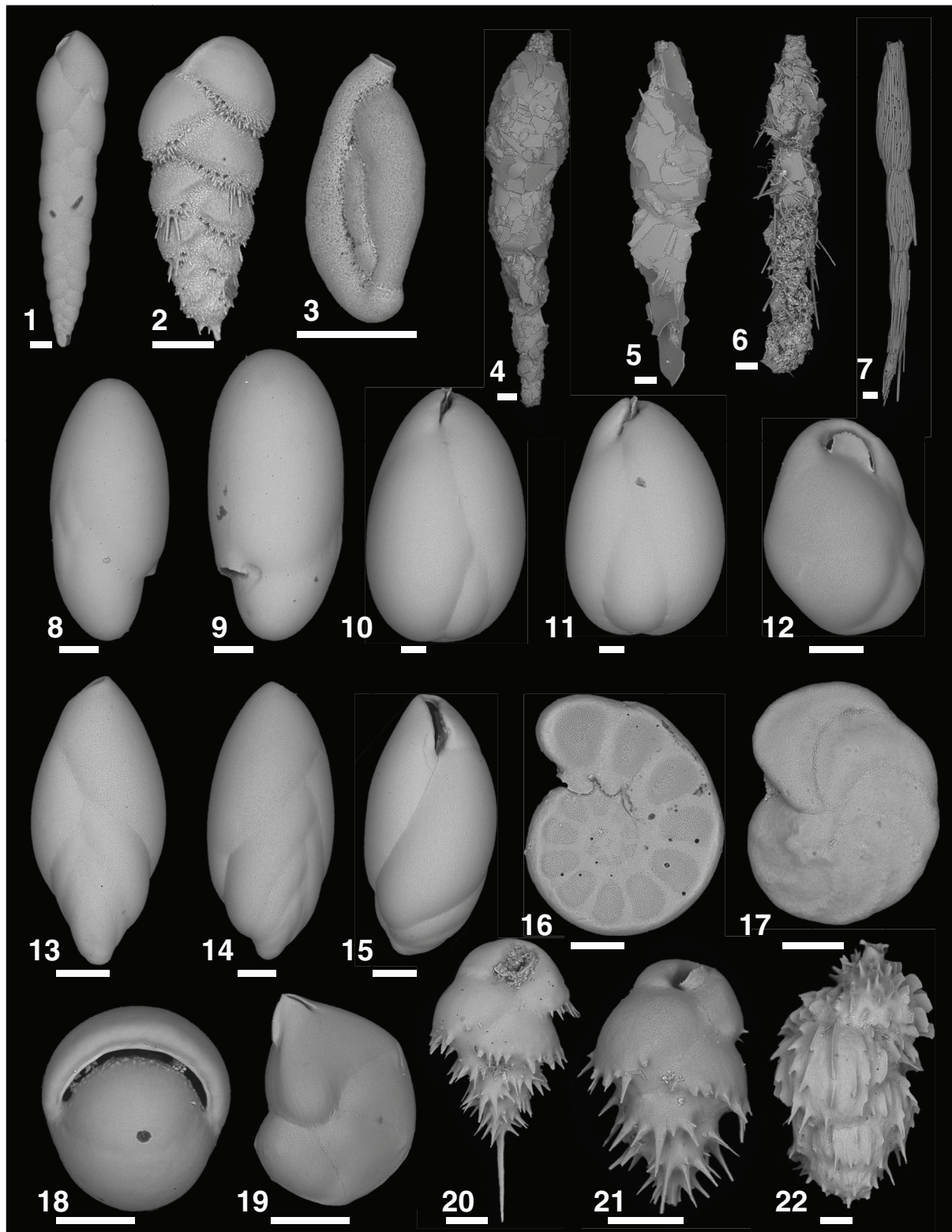


Figure F30. Overview of mudline benthic foraminiferal assemblage in slide, Sites U1428 and U1429. The assemblage is dominated by high productivity and dysoxia indicators including *Chilostomella oolina*, *Fursenkoina bradyi*, and *Globobulimina pacifica*. Live specimens are stained red with rose bengal.

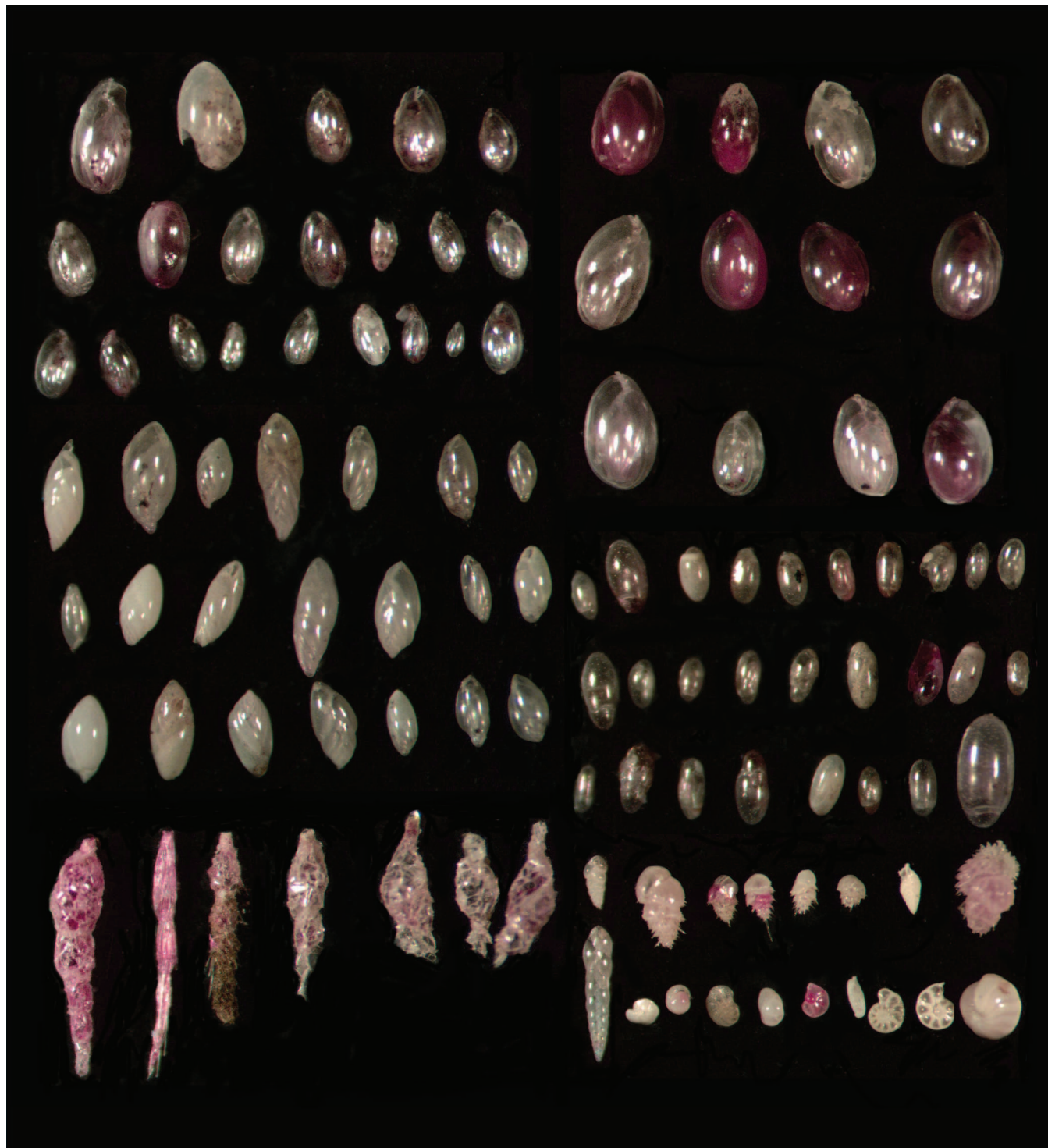


Figure F31. Calcareous nannofossils from Hole U1428A mudline sample. Scale bars = 2 μm . 1, 2. *Calcidiscus leptoporus*; (1) distal view; (2) proximal view. 3. *Florisphaera profunda*. 4, 5. *Umbilicosphaera sibogae*; (4) proximal view; (5) distal view. 6, 12. *Helicosphaera carteri*; (6) distal view; (12) proximal view. 7, 8. *Helicosphaera wallichii*. 9. *Rhabdosphaera clavigera*. 10, 11. *Syracosphaera* cf. *pulchra*. 13. *Calciosolenia murrayi*. 14–16. *Gephyrocapsa oceanica*. 17, 18. *Emiliana huxleyi*; (17) coccosphere; (18) coccolith. Photos taken using SEM.

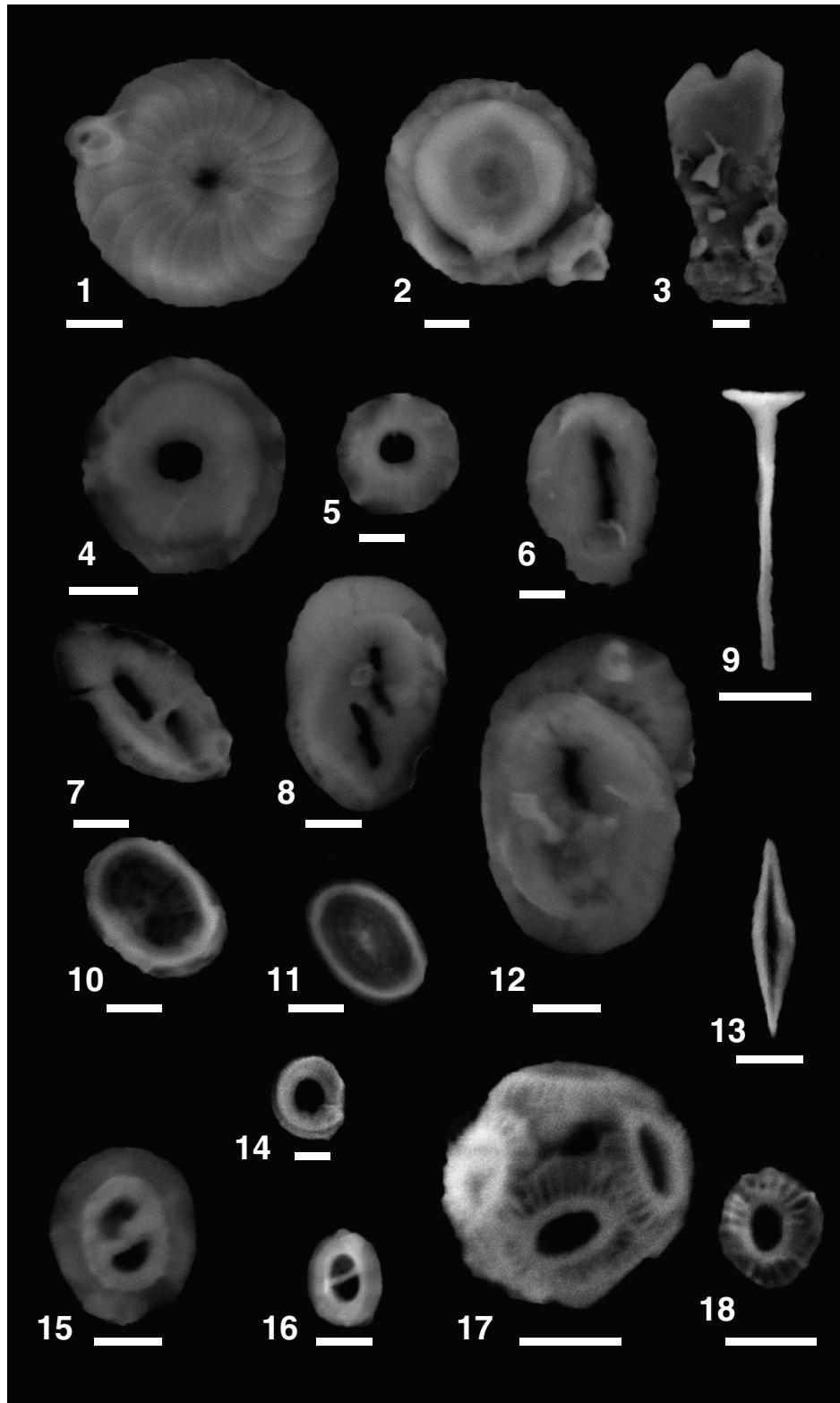


Figure F32. Solid-phase geochemistry of discrete sediment samples, Site U1428. TC = total carbon, TOC = total organic carbon, TN = total nitrogen.

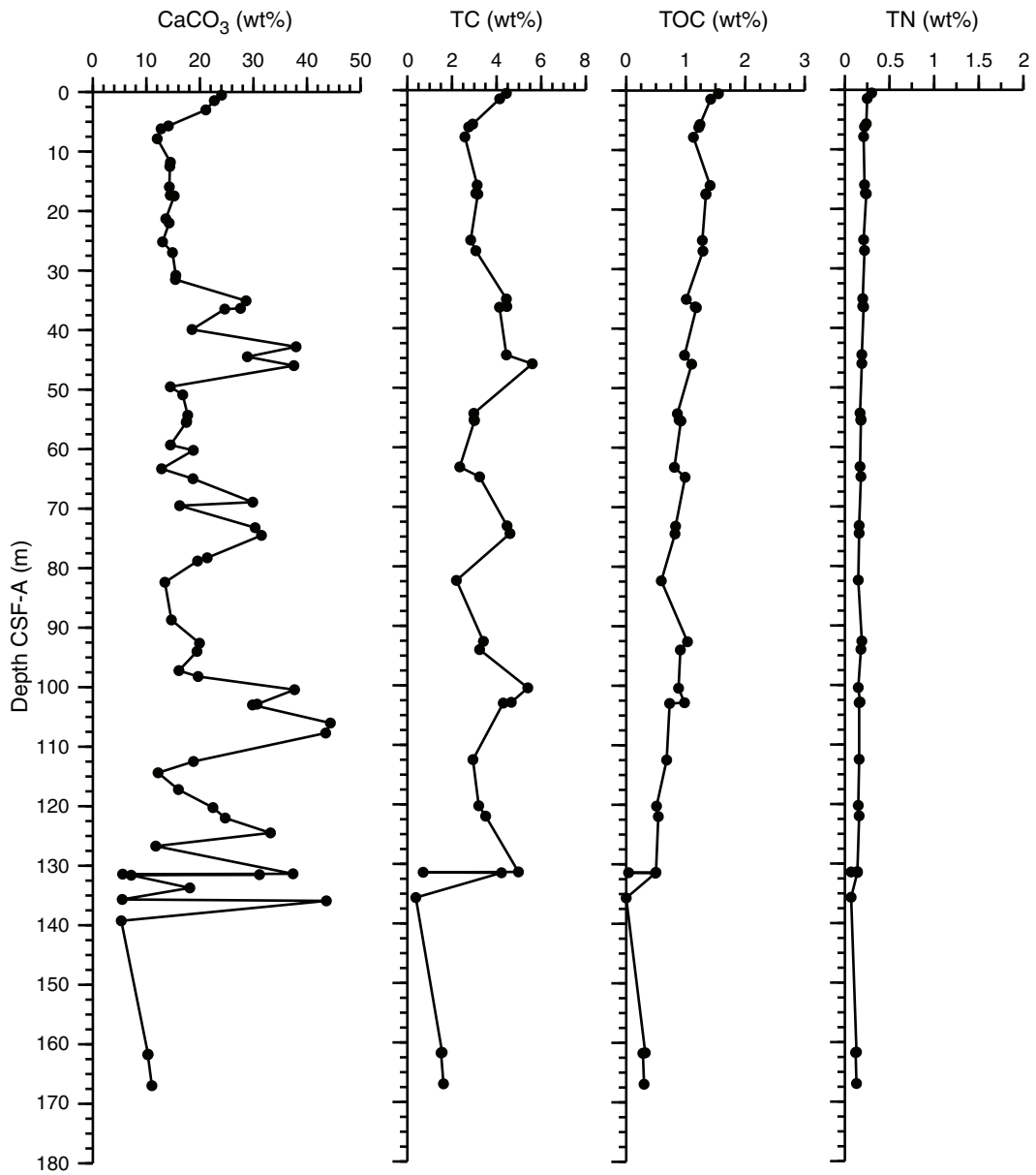


Figure F33. Solid-phase geochemistry of discrete sediment samples, Site U1429. TC = total carbon, TOC = total organic carbon, TN = total nitrogen.

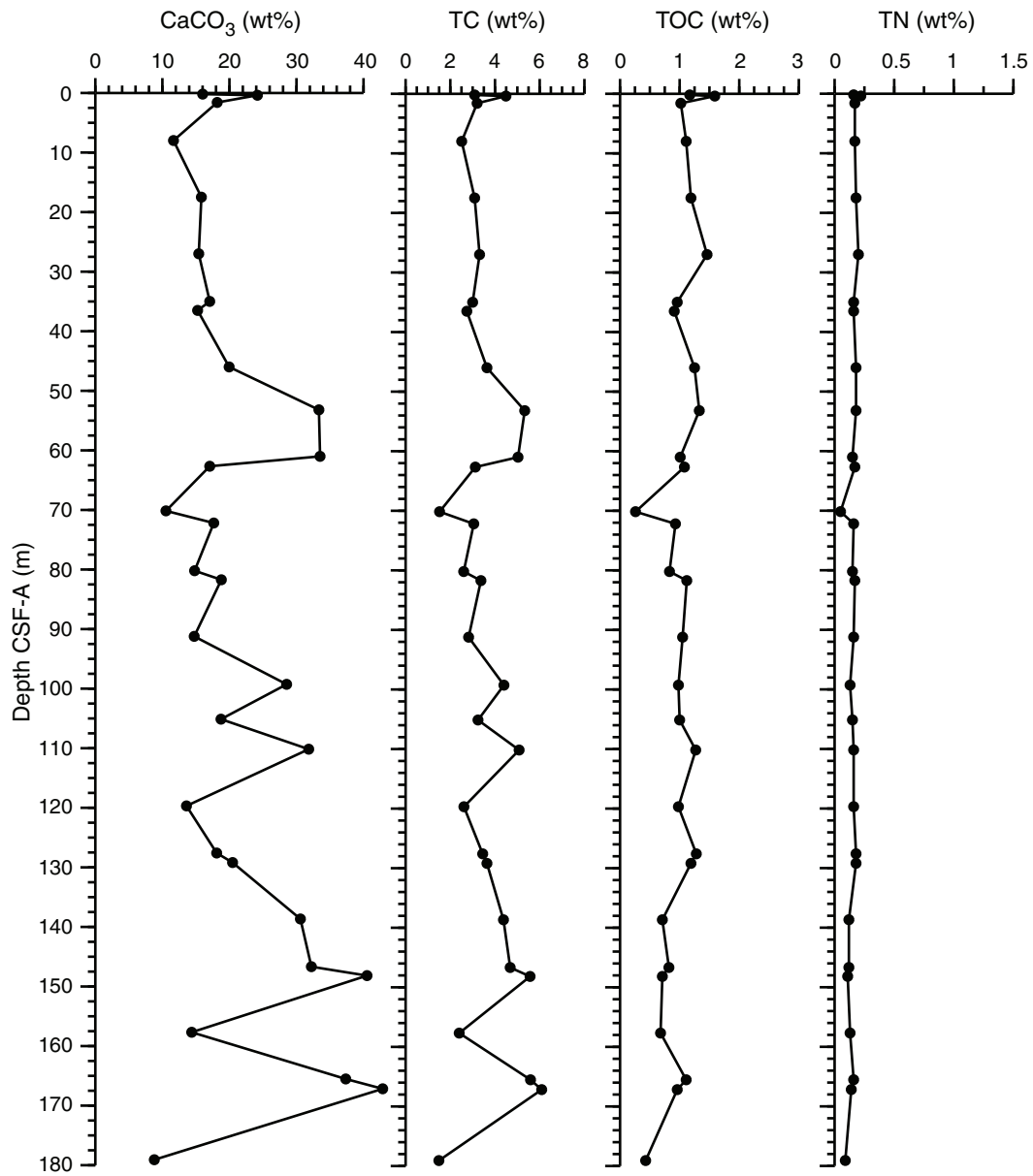


Figure F34. Alkalinity and sulfate from squeezed (IW-sq) and Rhizon samples. A. Site U1428. B. Site U1429.

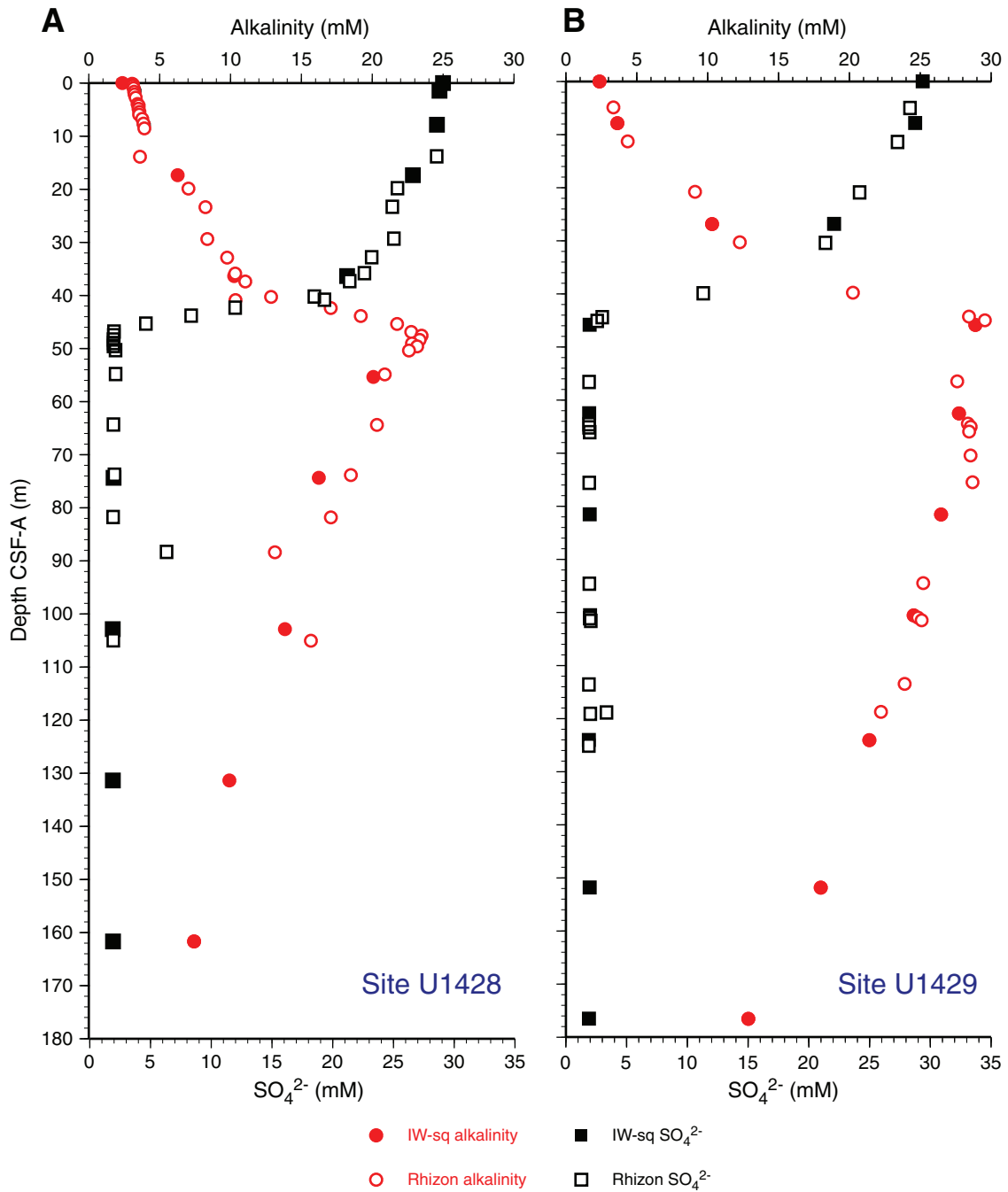


Figure F35. Headspace CH_4 concentrations, Sites U1428 and U1429. **A.** Complete profile with CH_4 concentrations on a log scale and other sites plotted for comparison. **B.** The upper 250 m CSF-A of Holes U1428A and U1429A to highlight the SMT. Note that concentration values are not meaningful at depths where CH_4 surpasses saturation at 1 atm pressure ($\sim 10,000$ ppm at ~ 20 m CSF-A). Also note that measured concentrations and ratios decrease with depth because of differential gas solubility with temperature.

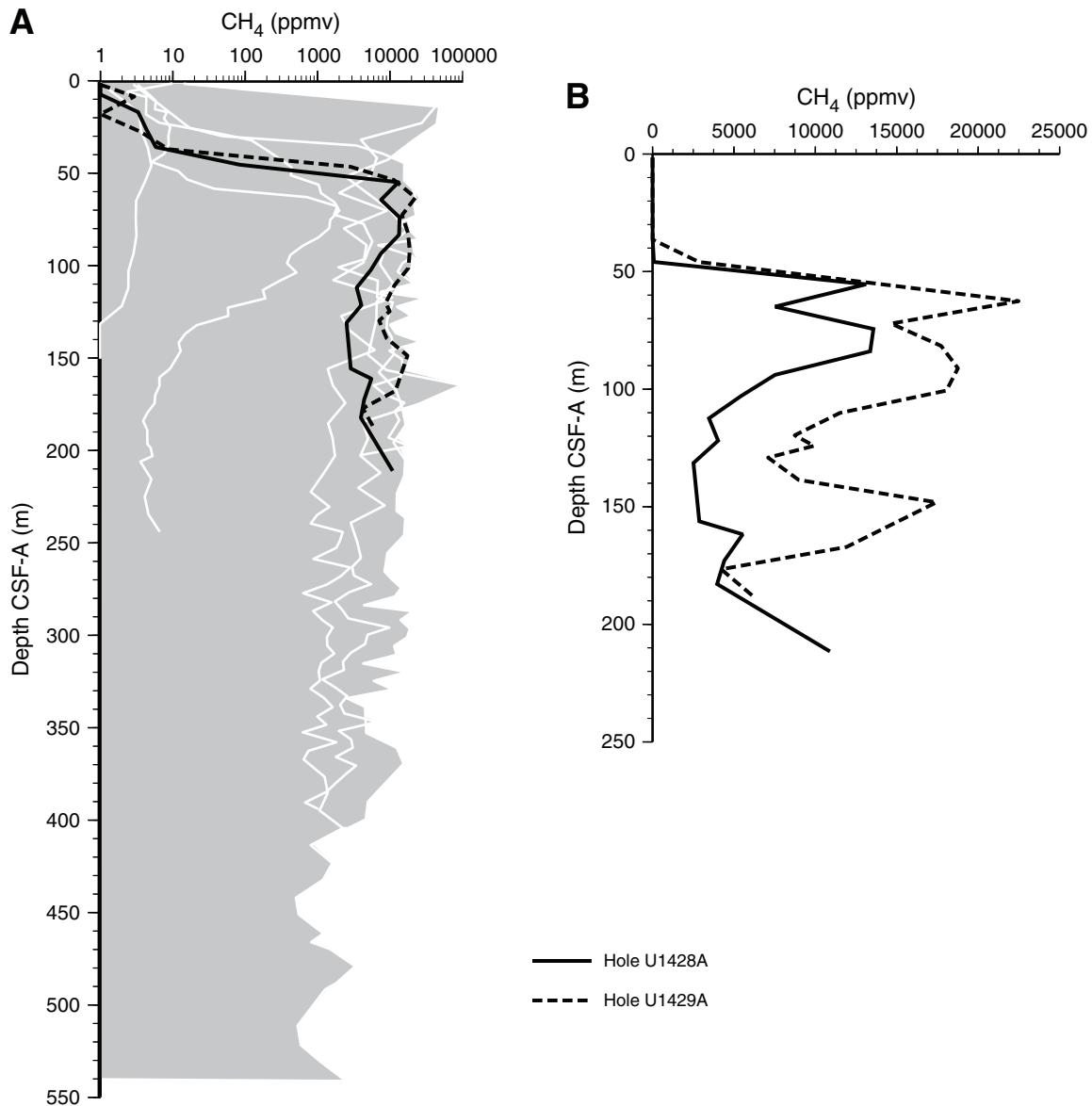


Figure F36. Dissolved barium profiles from squeezed and Rhizon samples with depth, Site U1428 and U1429.

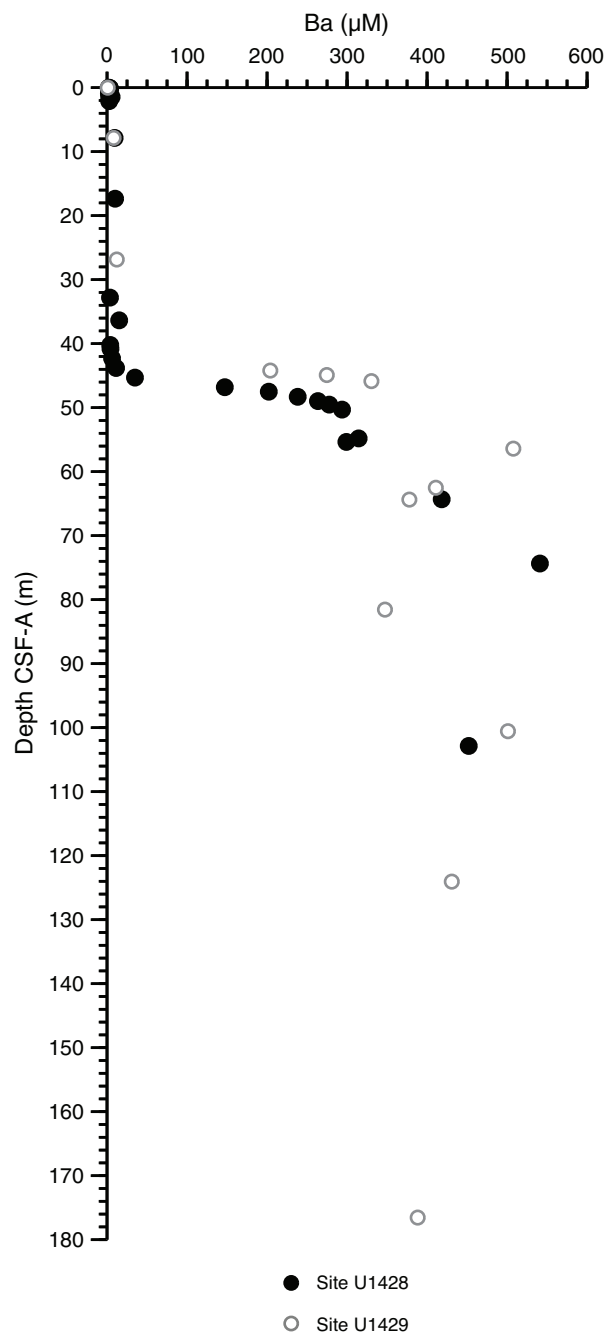


Figure F37. Dissolved calcium, magnesium, and strontium profiles in squeezed interstitial water (IW-sq) and Rhizon samples, Sites U1428 and U1429.

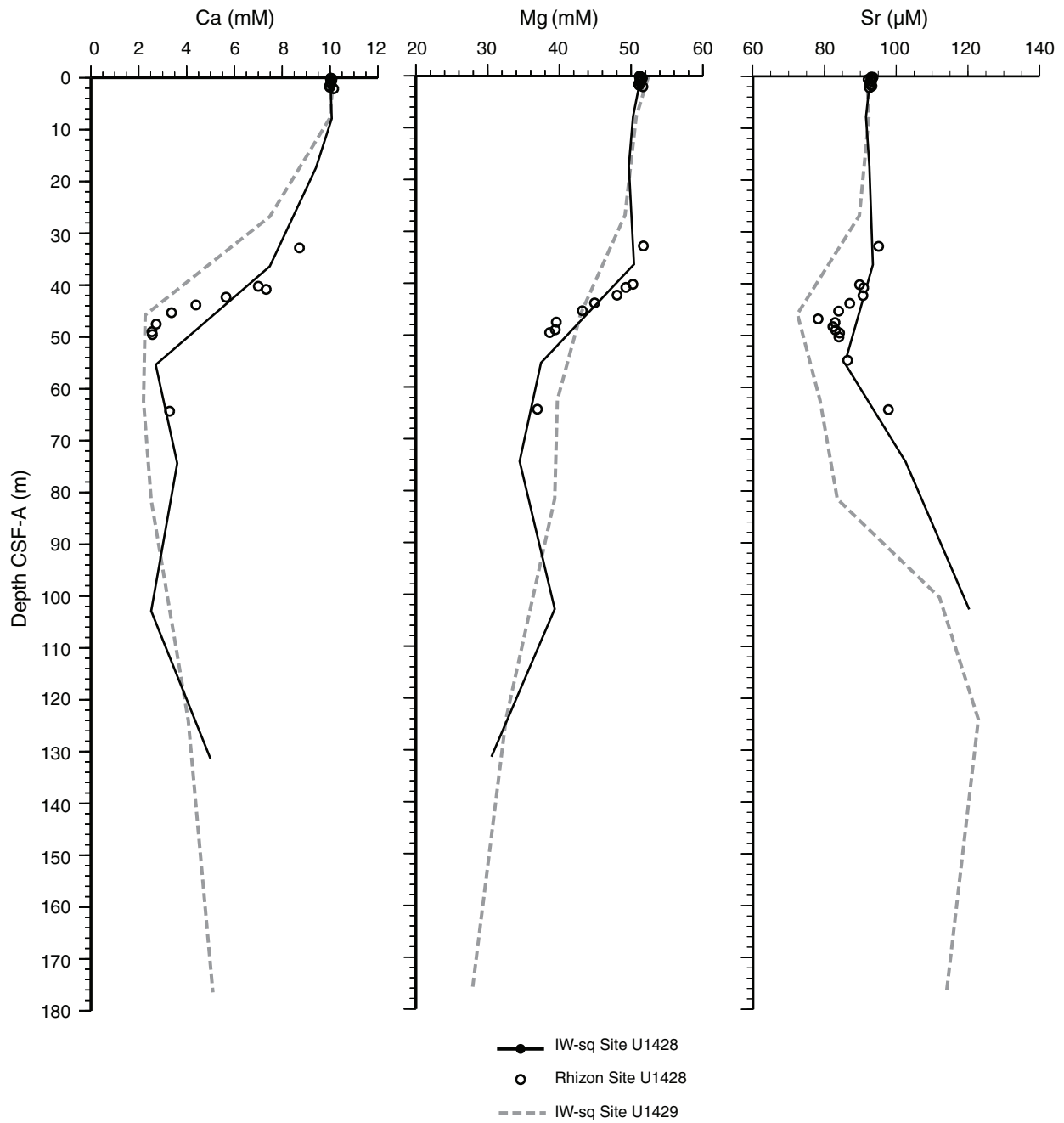


Figure F38. Dissolved bromide concentrations over the entire depth. A. Site U1428. B. Site U1429. IW-sq = squeezed interstitial water.

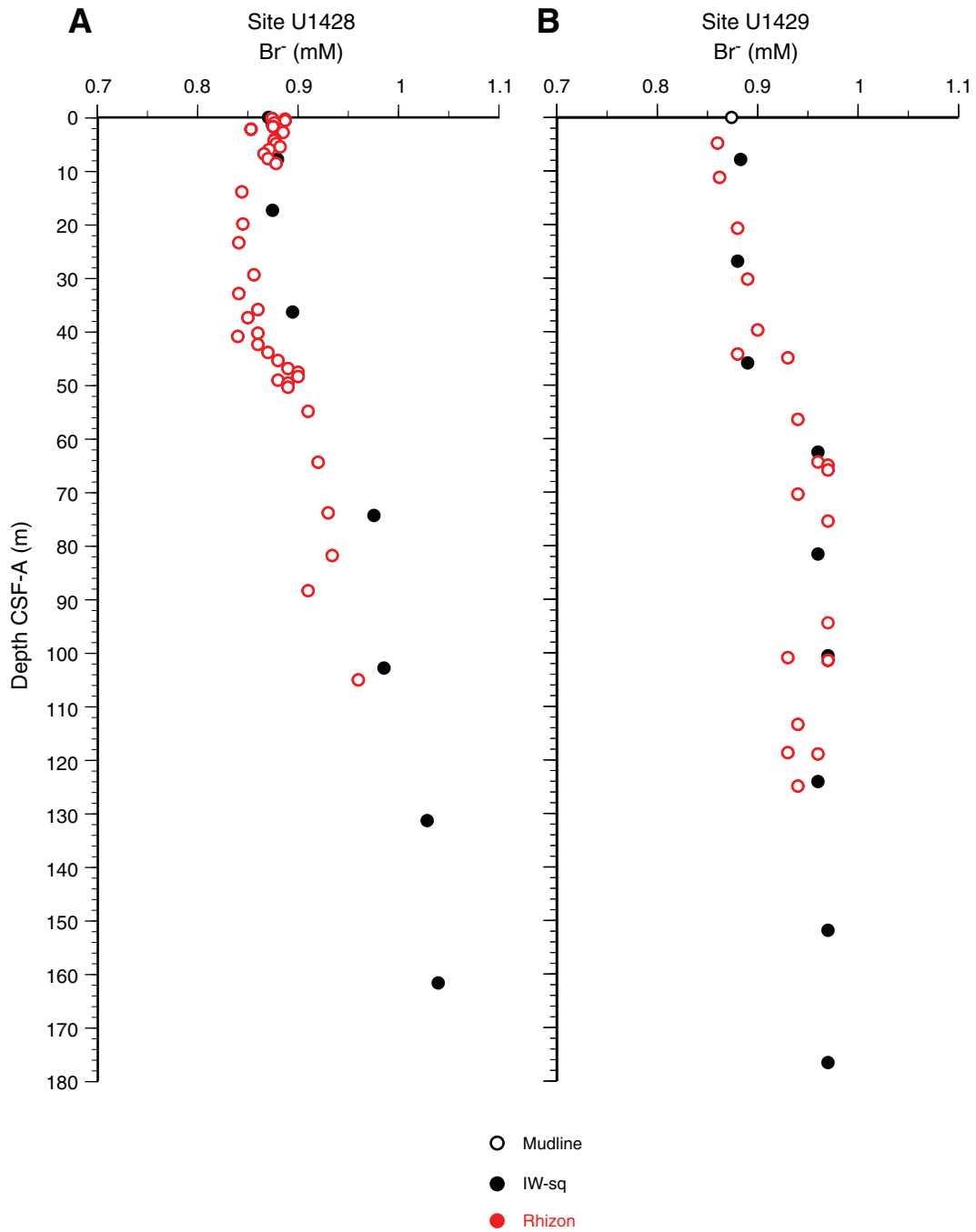


Figure F39. Concentrations of ammonium and phosphate in interstitial water, Sites U1428 and U1429. Note for completeness of the geochemical stratigraphy, the phosphate profile combines interstitial water from squeeze cakes and Rhizons.

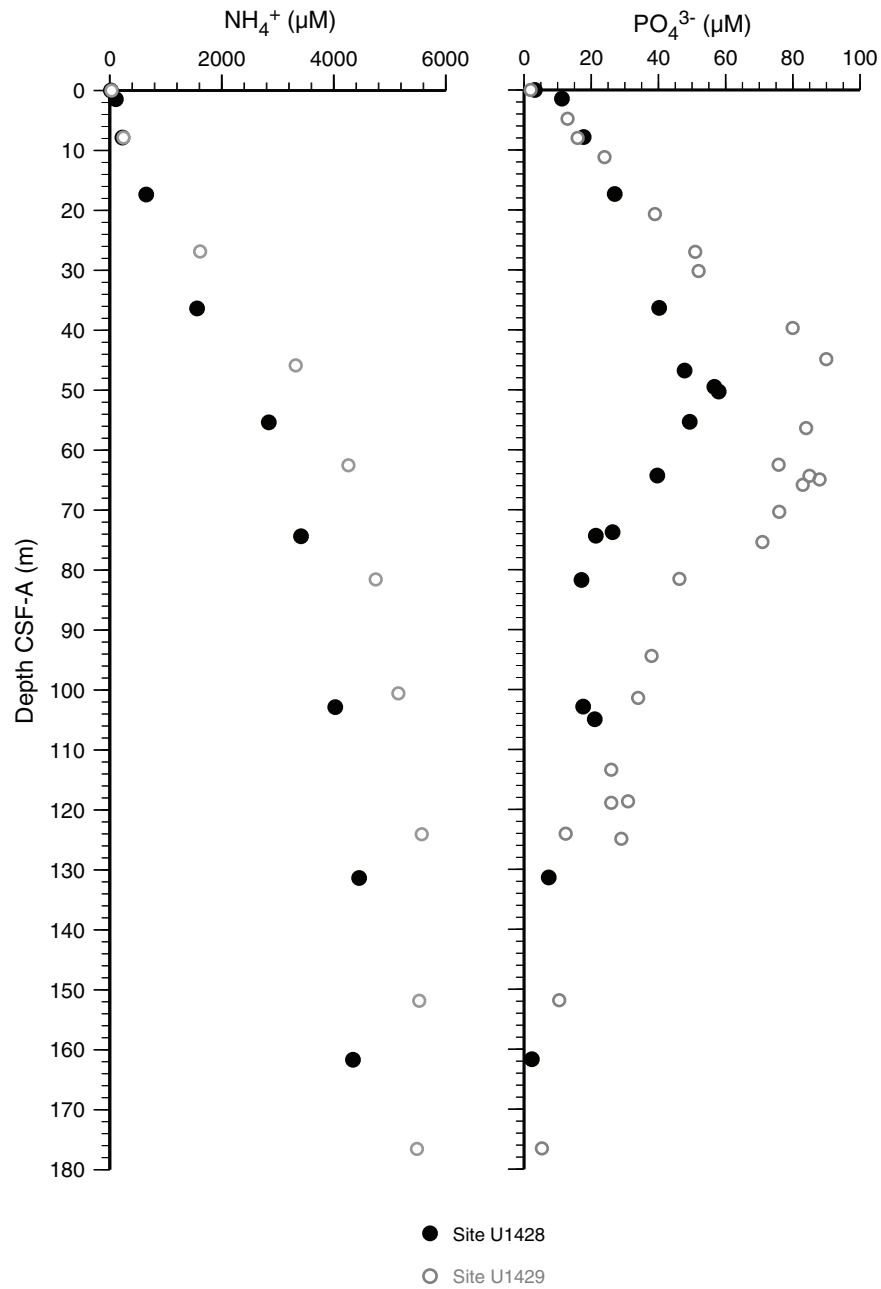


Figure F40. Concentrations of ammonium from mudline, squeezed (IW-sq), and Rhizon samples in the upper 10 m CSF-A, Site U1428.

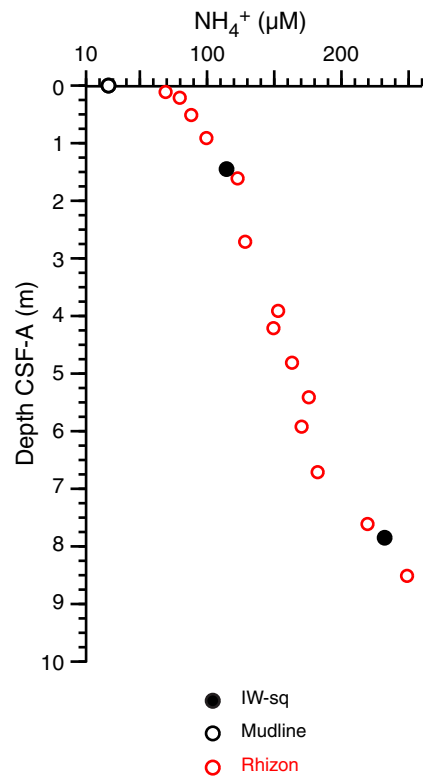


Figure F41. Dissolved iron and manganese profiles, Sites U1428 and U1429. **A.** Full depth of sites. **B.** Uppermost 3 m below the seafloor at Site U1428. IW-sq = squeezed interstitial water. Rhizon = Rhizon water sampler.

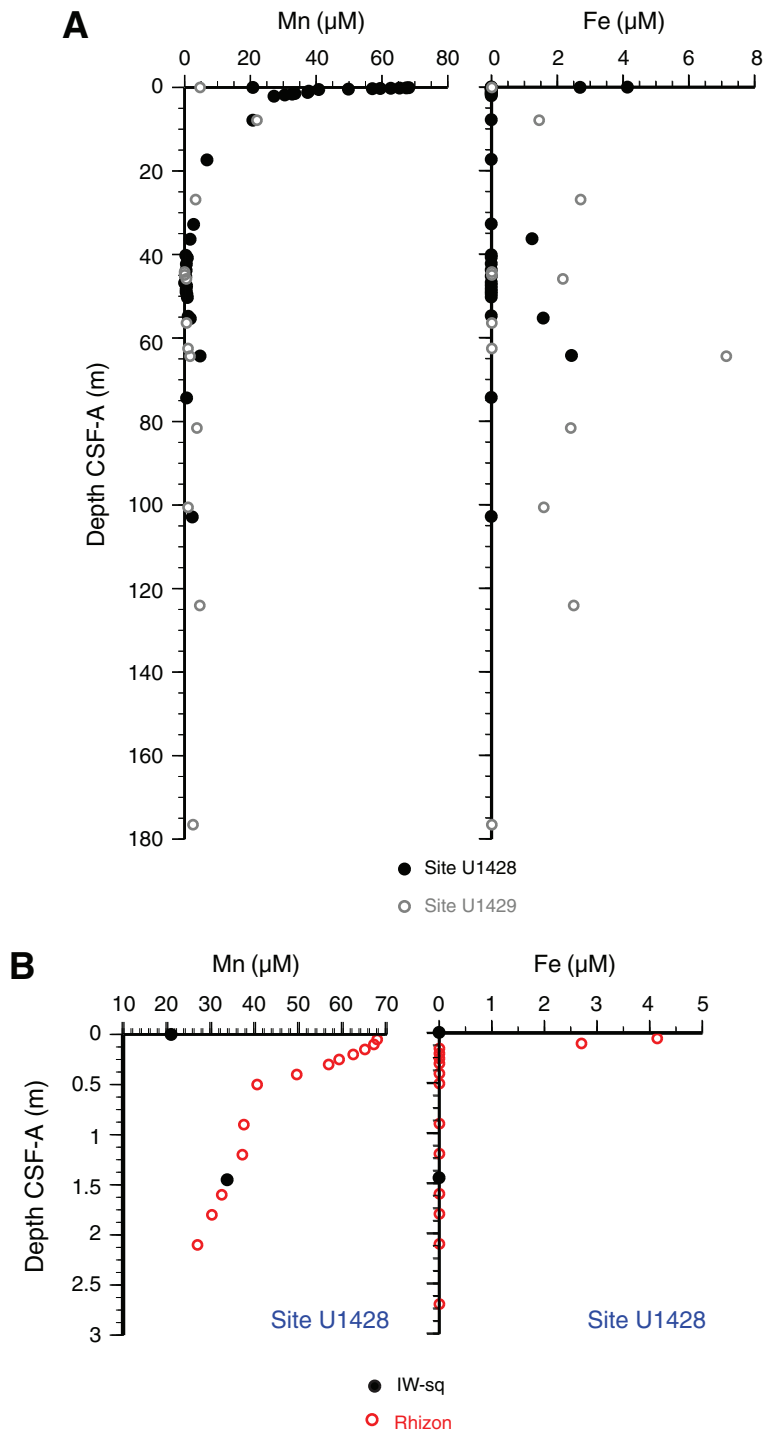


Figure F42. Concentrations of chloride from mudline, squeezed (IW-sq), and Rhizon samples. **A.** Site U1428. **B.** Site U1429.

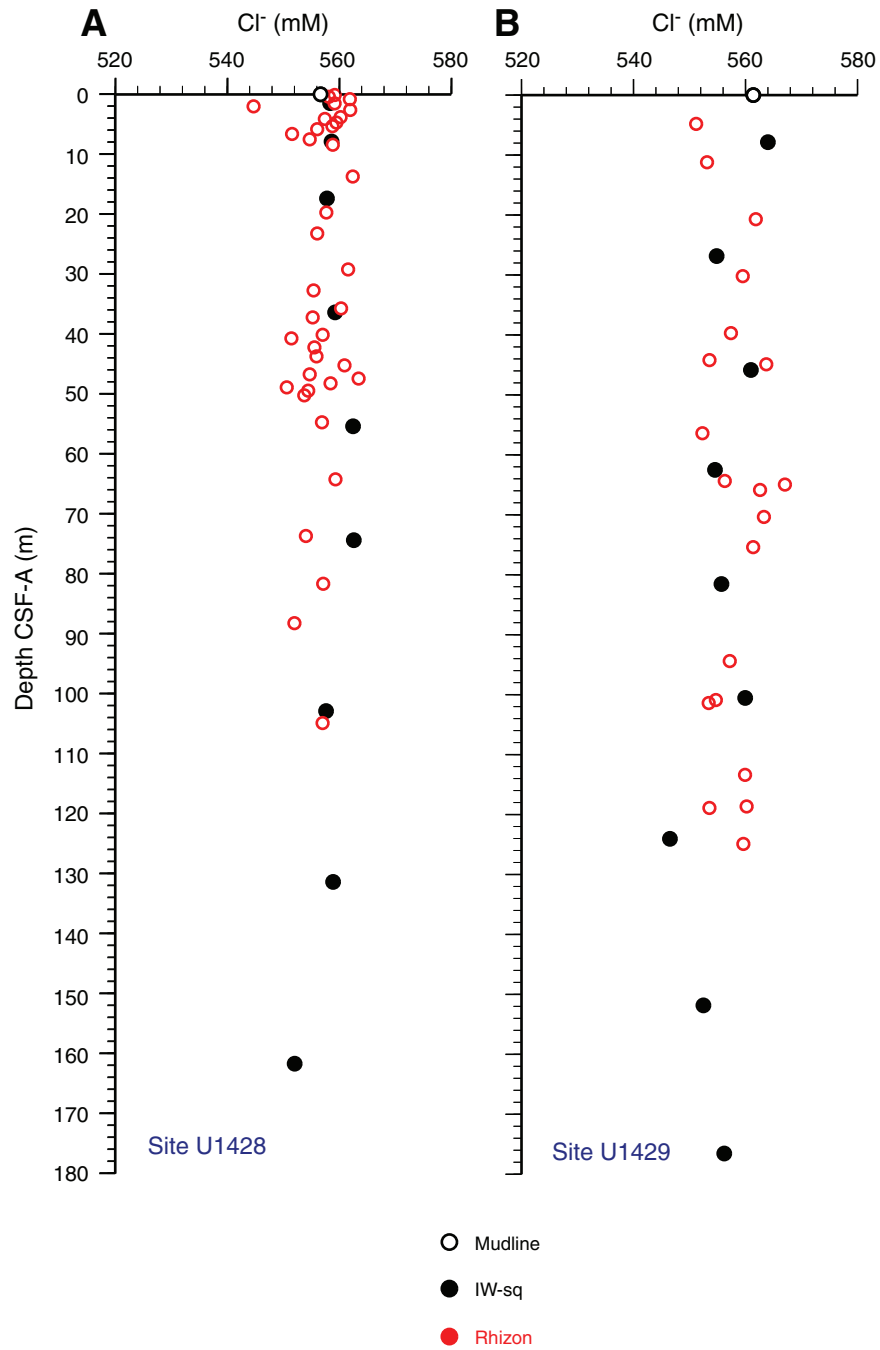


Figure F43. Na concentrations from squeezed (IW-sq) and Rhizon samples, Sites U1428 and U1429.

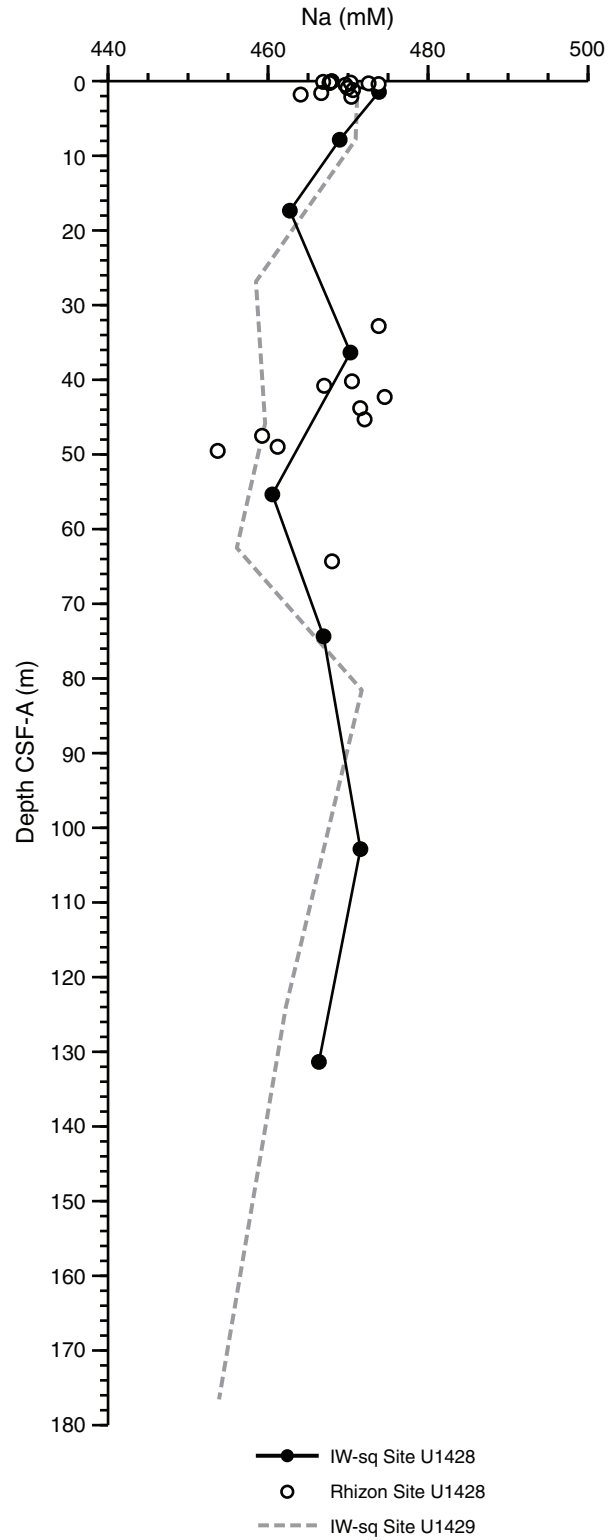


Figure F44. Dissolved K concentrations from squeezed (IW-sq) and Rhizon samples, Sites U1428 and U1429.

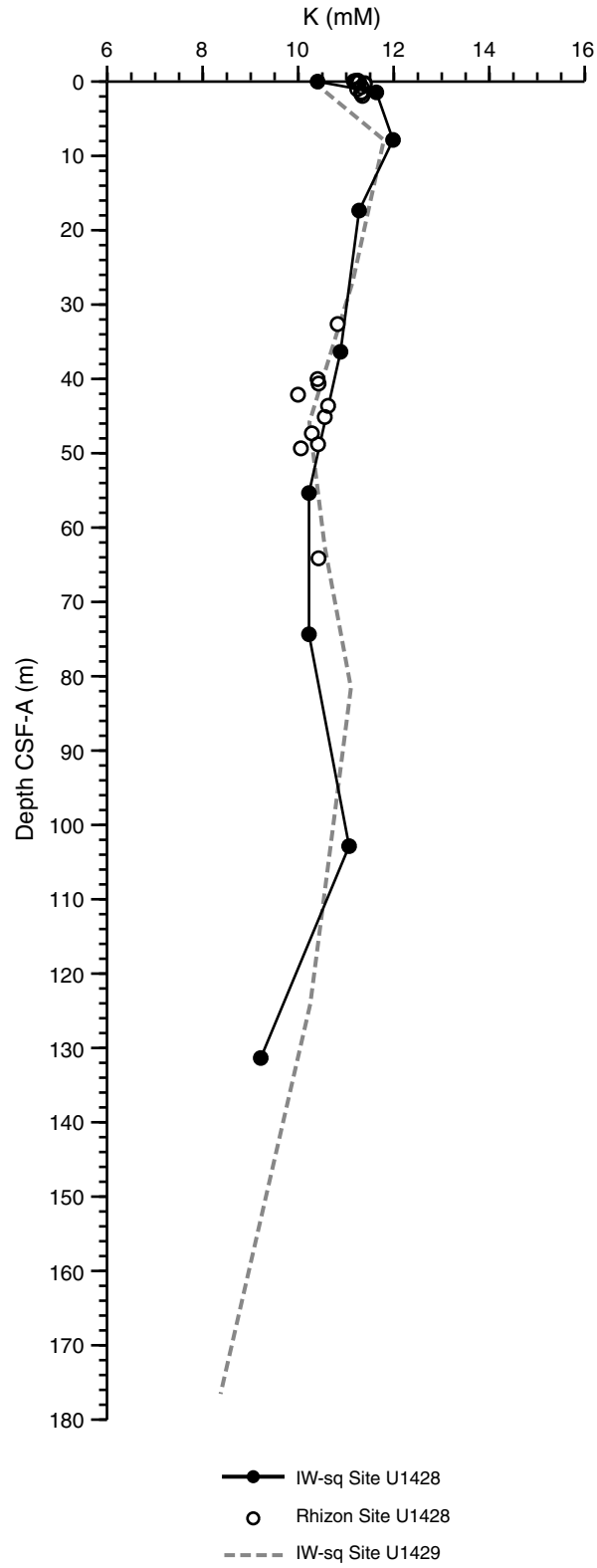


Figure F45. Dissolved boron and lithium profiles at Sites U1428 and U1429 from squeezed samples.

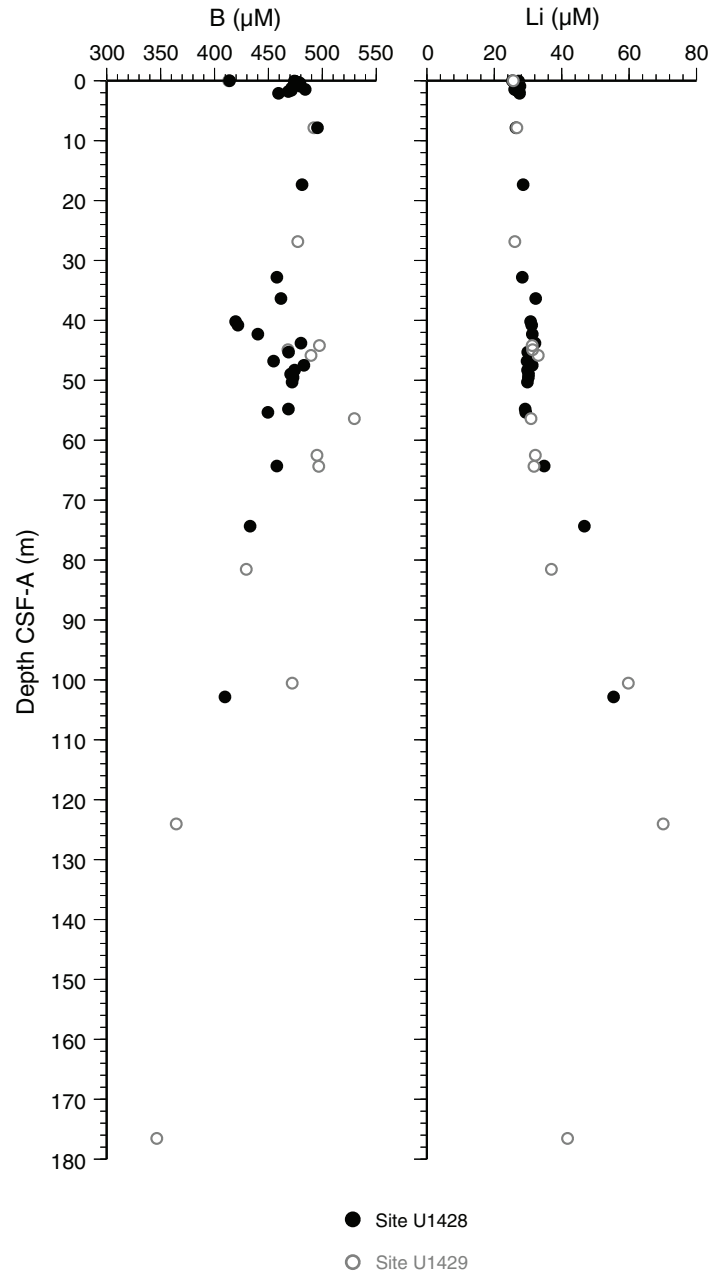


Figure F46. Dissolved Si at Sites U1428 and U1429 from Rhizons and squeeze cake (IW-sq) samples, comparing spectrophotometric (Spect.) and inductively coupled plasma–atomic emission spectroscopy (ICP) methods.

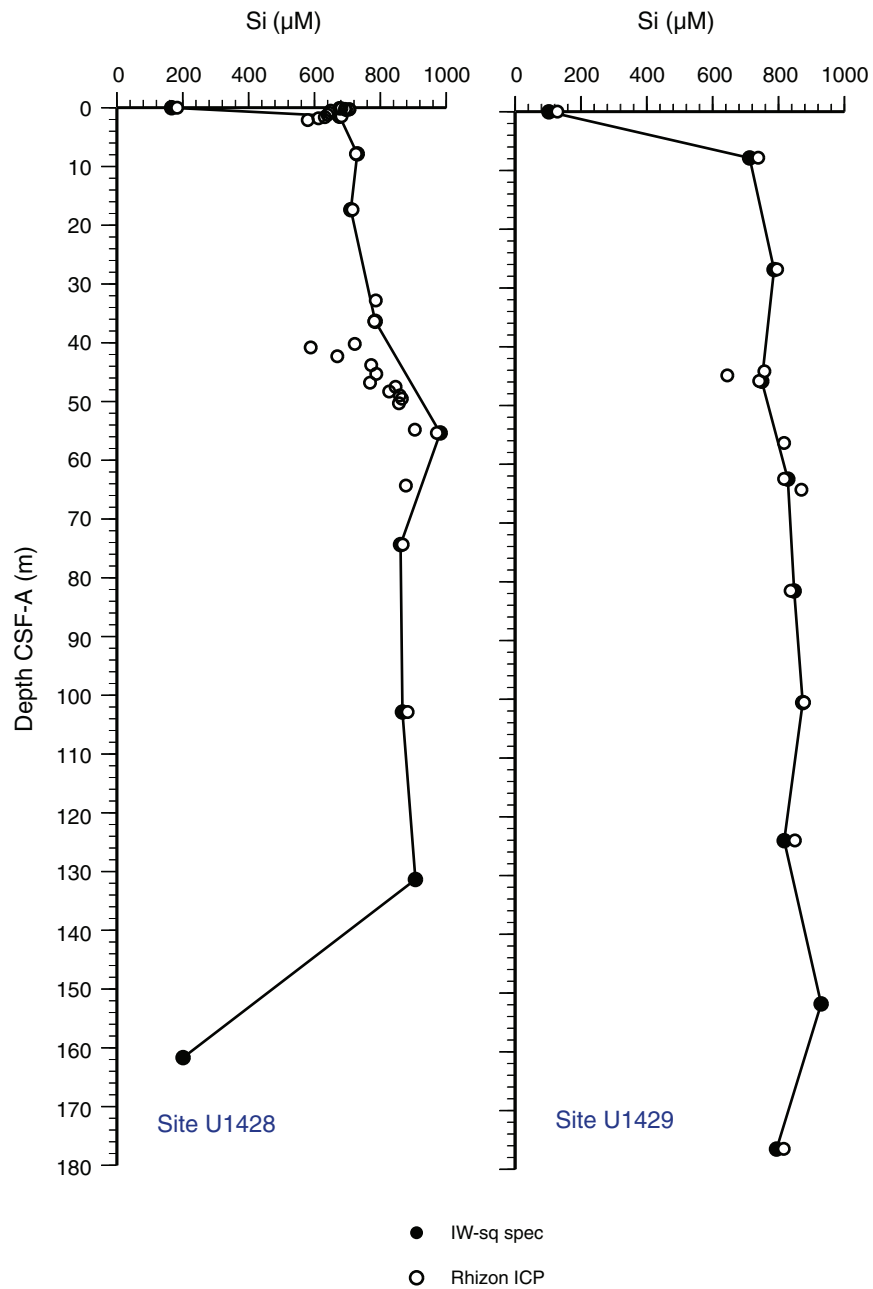




Figure F47. Paleomagnetism after 20 mT AF demagnetization, Site U1428/U1429. Chron column: black = normal polarity, white = reversed polarity, gray = zones or polarity boundaries without clear magnetostratigraphic interpretation. Inclination column: thin black dashed lines = expected geocentric axial dipole inclinations at the site latitude during reversed (left) and normal (right) polarities, triangles along the left side mark depths where discrete paleomagnetic cube samples were collected (orange = discrete samples measured during the expedition). Declination column: gray dots = measured declination values, green dots = declination values corrected using core orientation data collected by the FlexIT tool. Susceptibility column: SHMSL and WRMSL measured values are shown in magenta and gray dots, respectively. **A.** Hole U1428A. (Continued on next four pages.)

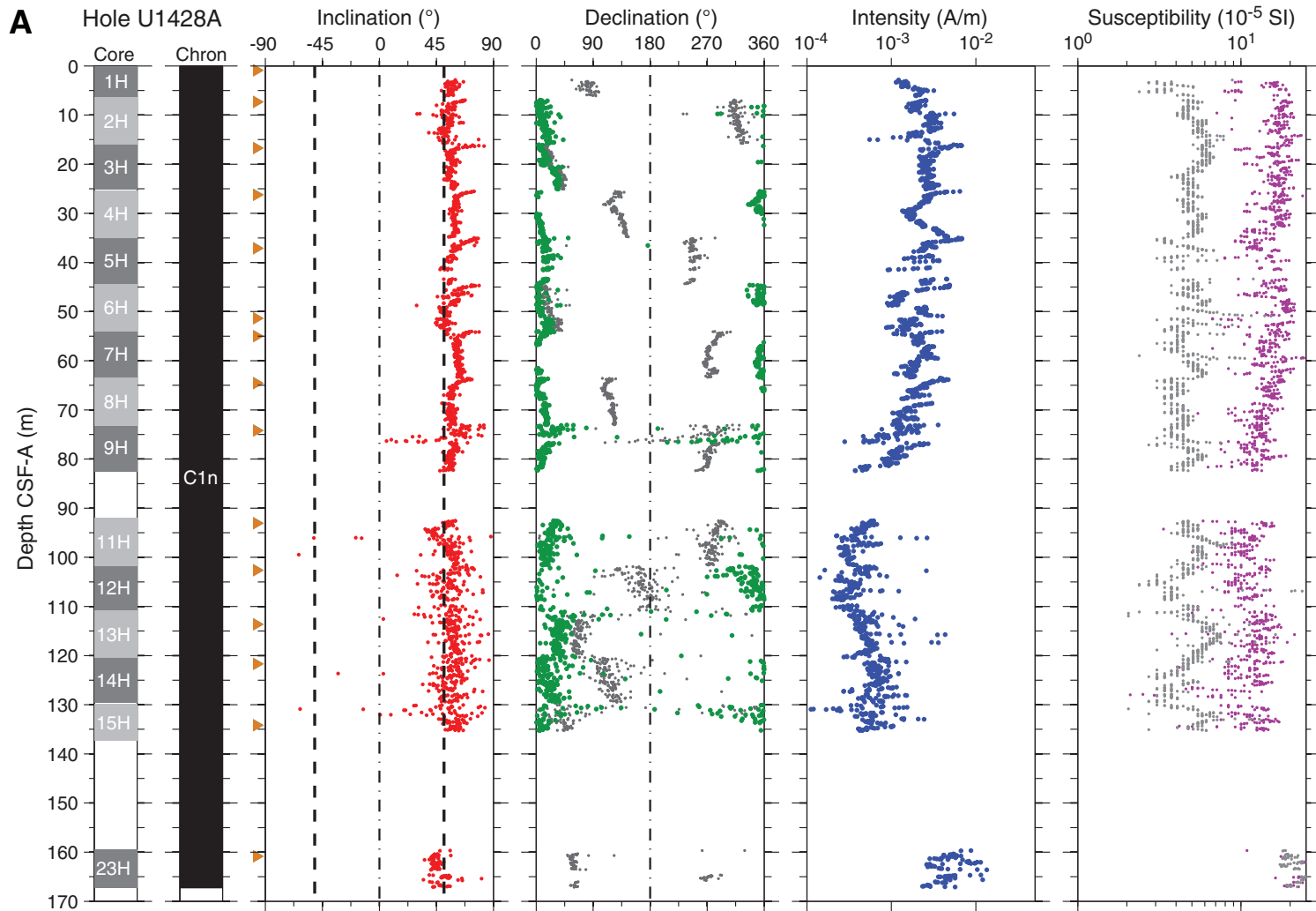




Figure F47 (continued). B. Hole U1428B. (Continued on next page.)

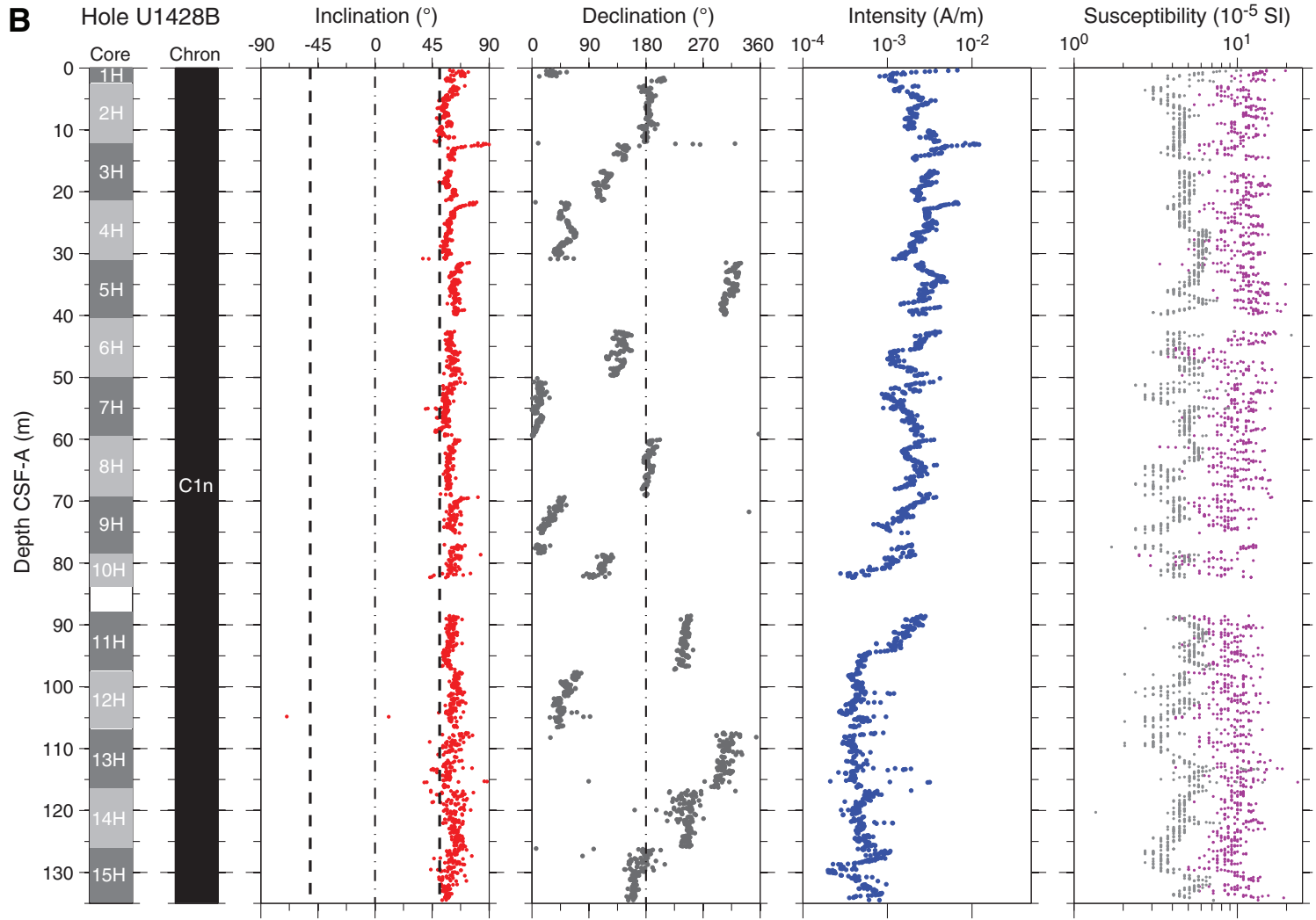




Figure F47 (continued). C. Hole U1429A. (Continued on next page.)

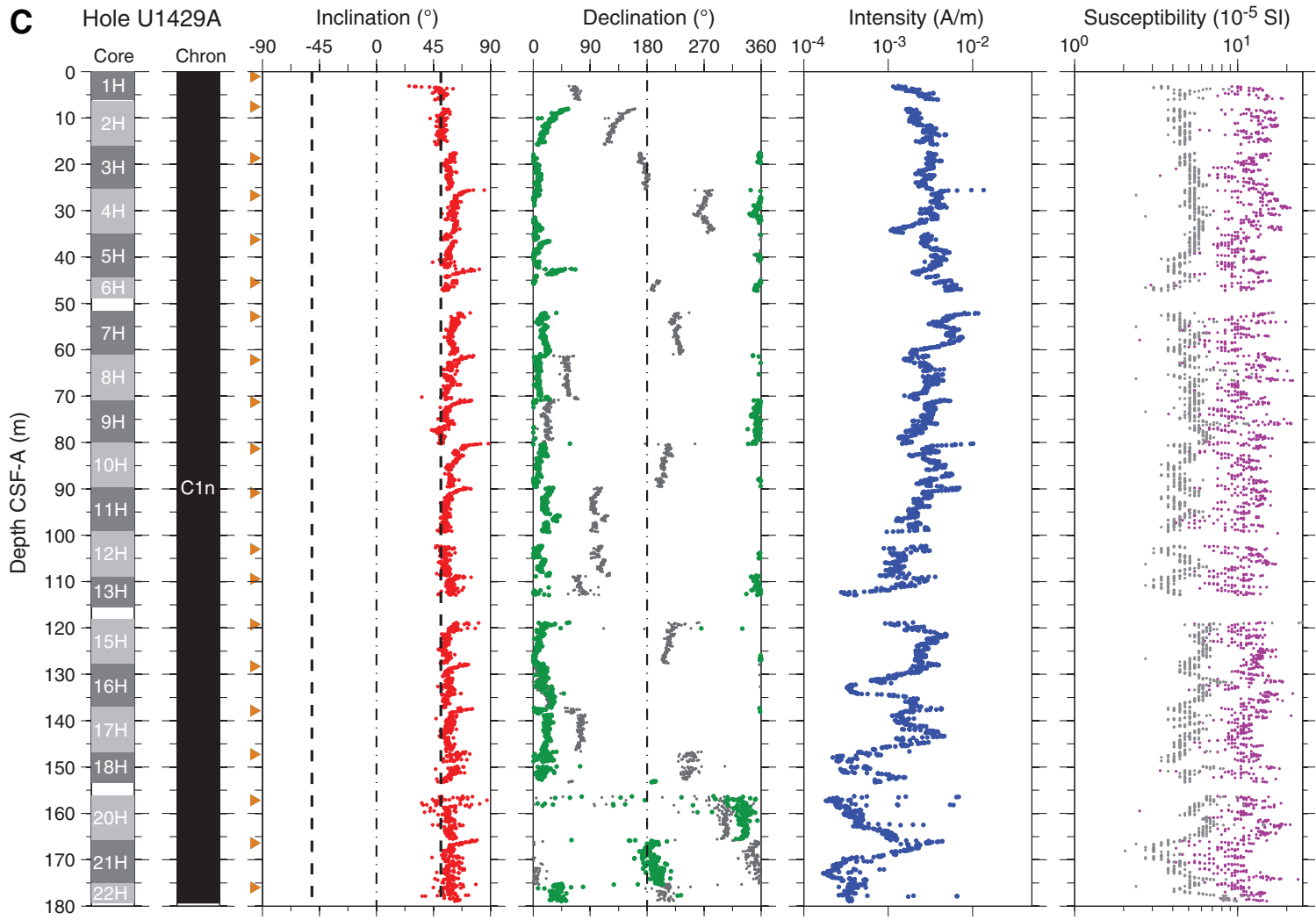




Figure F47 (continued). D. Hole U1429B. (Continued on next page.)

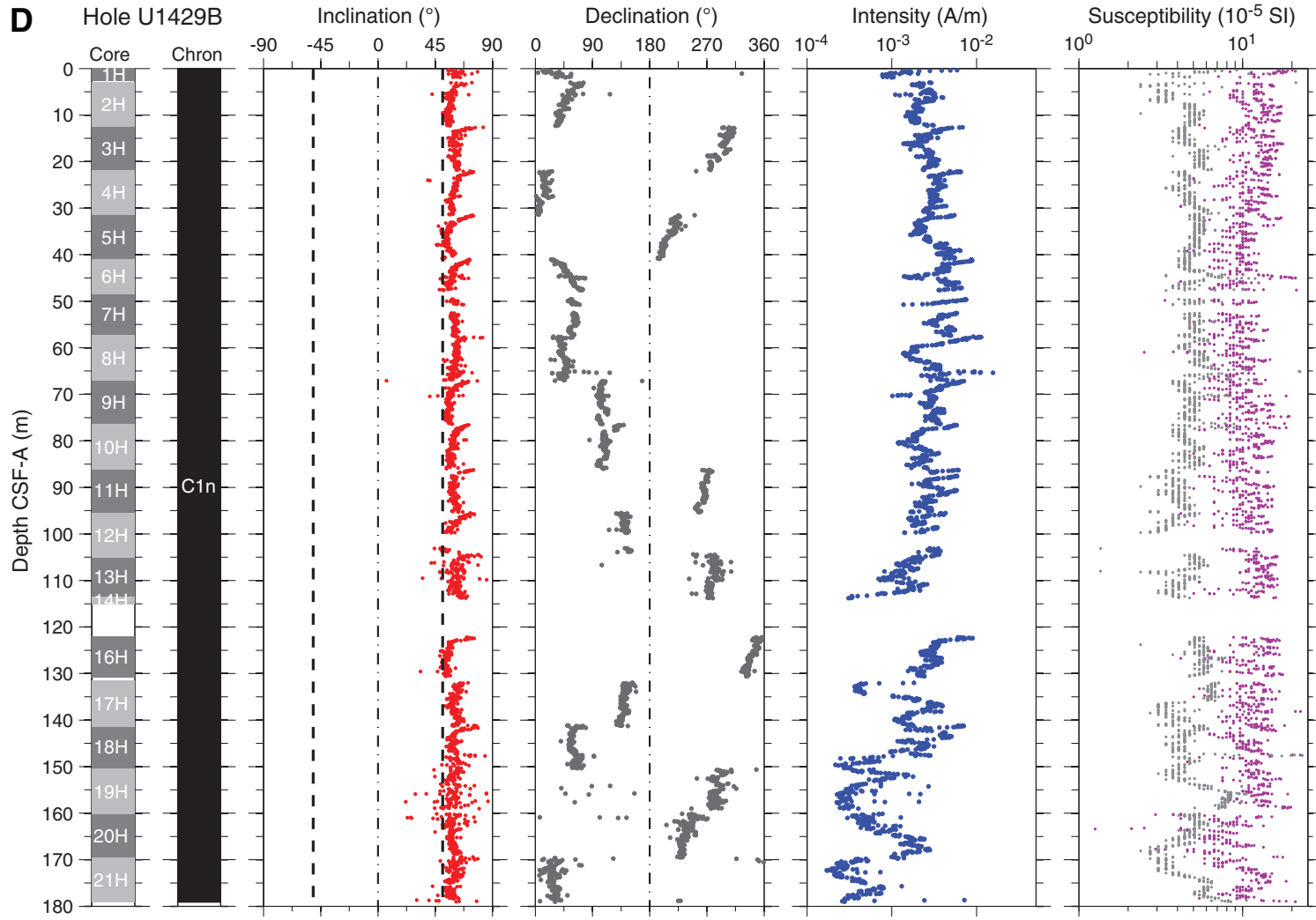


Figure F47 (continued). E. Hole U1429C.

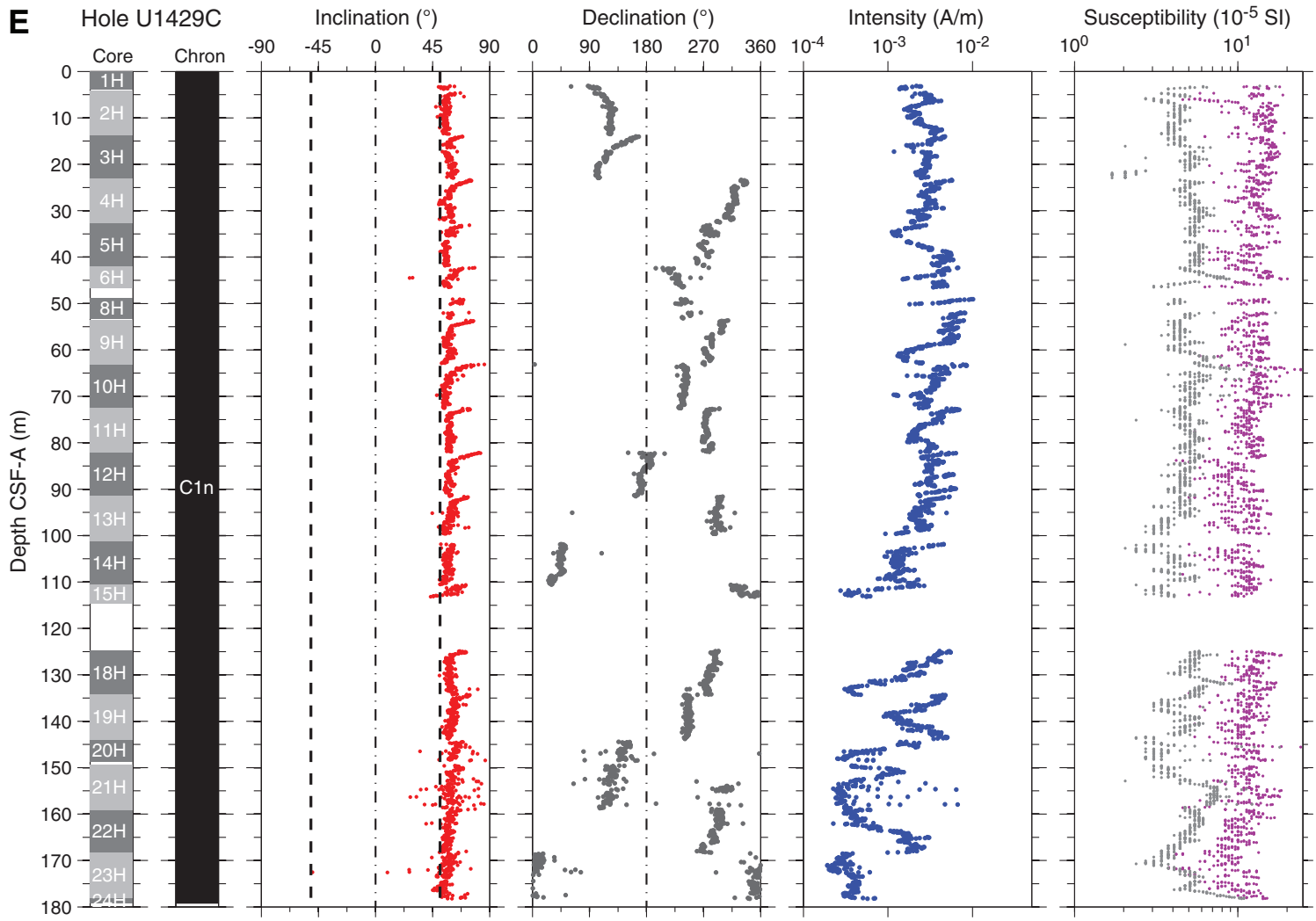




Figure F48. AF demagnetization results for discrete samples, Hole U1428A. For each sample, the left plot shows the intensity variation with progressive demagnetization. The middle and right plots show the NRM vector measured after each demagnetization treatment on an orthogonal projection (Zijderveld) and on an equal area projection respectively. In the orthogonal projection plot, squares = horizontal projections, circles = vertical projections. In the equal area projection plot, closed circles = projection data with positive inclinations, open circles = projection data with negative inclinations. Note that on the orthogonal projection (Zijderveld) plot, NRM data before demagnetization have been removed to better display the demagnetized data. **A–H.** Discrete cube samples from 64.57 m CSF-A and shallower. (Continued on next page.)

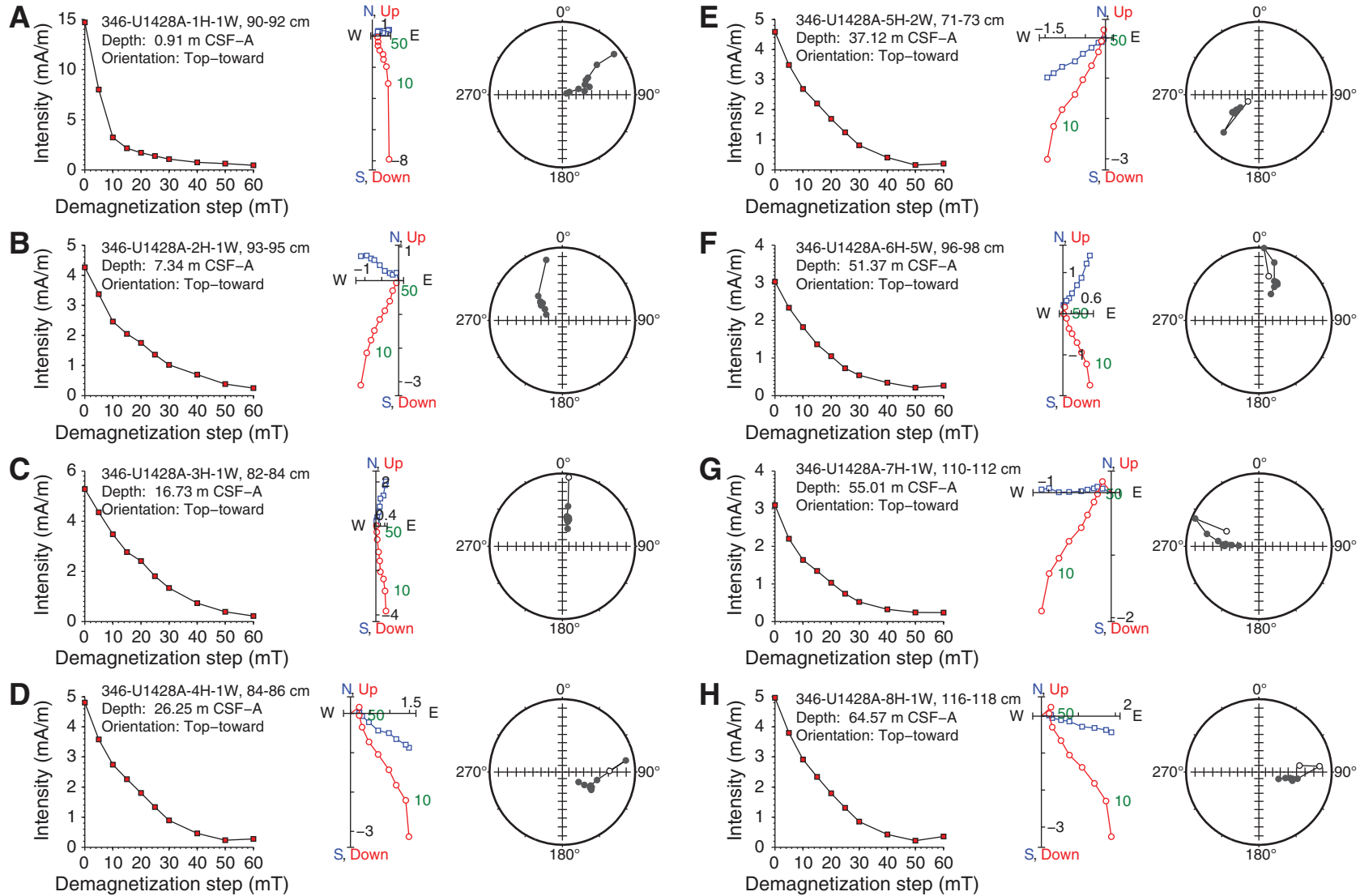




Figure F48 (continued). I–O. Discrete cube samples from 74.19 m CSF-A and deeper.

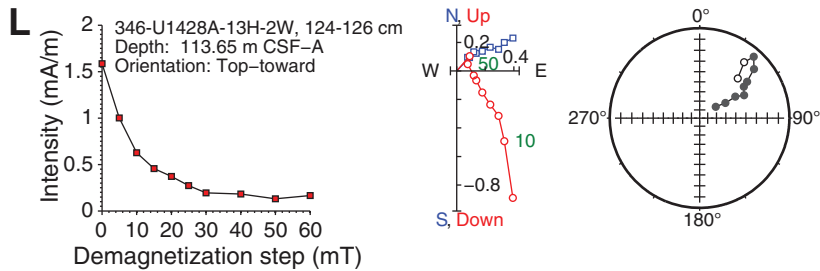
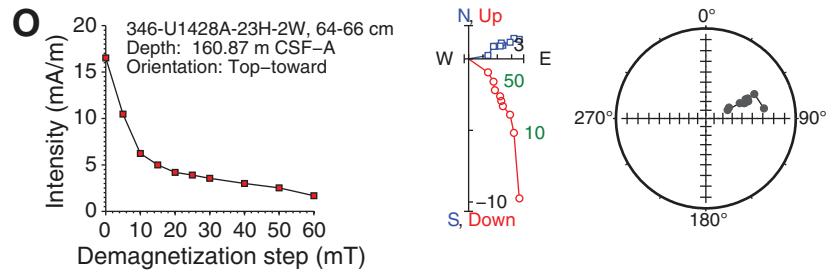
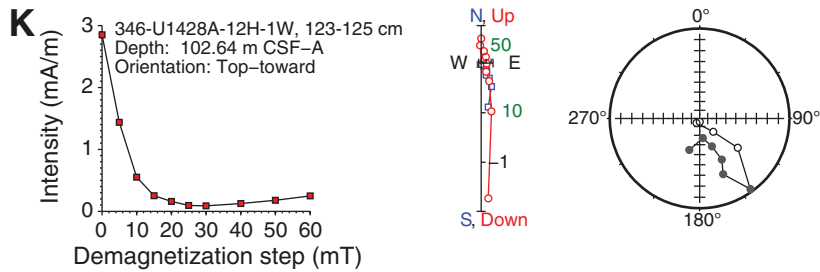
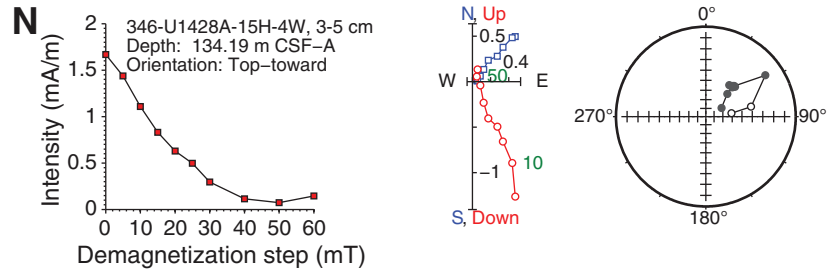
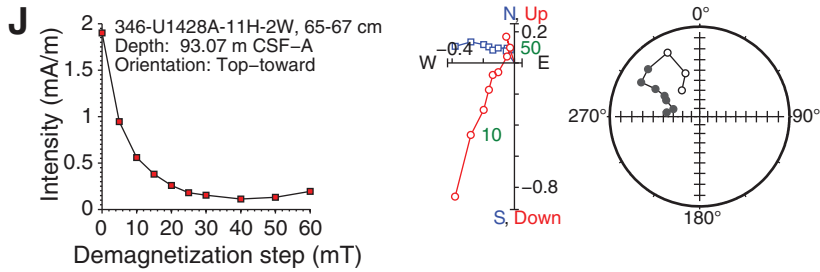
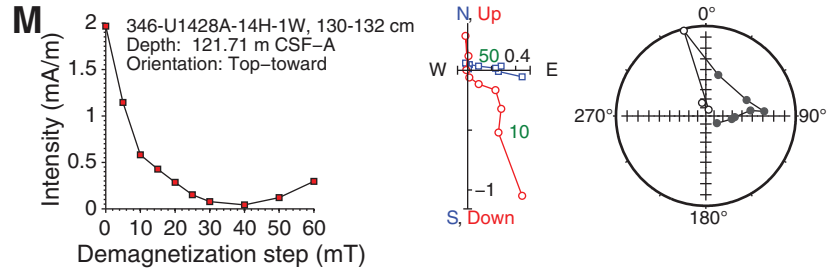
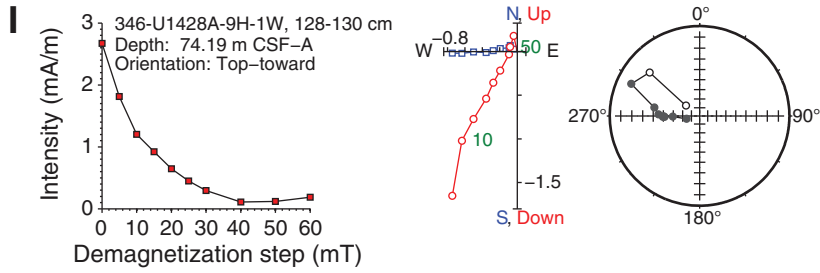




Figure F49. AF demagnetization results for discrete samples, Hole U1429A. For each sample, the left plot shows the intensity variation with progressive demagnetization. The middle and right plots show the NRM vector measured after each demagnetization treatment on an orthogonal projection (Zijderveld) and on an equal area projection respectively. In the orthogonal projection plot, squares = horizontal projections, circles = vertical projections. In the equal area projection plot, closed circles = projection data with positive inclinations, and open circles = projection data with negative inclinations. Note that on the orthogonal projection (Zijderveld) plot, NRM data before demagnetization have been removed to better display the demagnetized data. **A–H.** Discrete cube samples from 62.21 m CSF-A and shallower. (Continued on next two pages.)

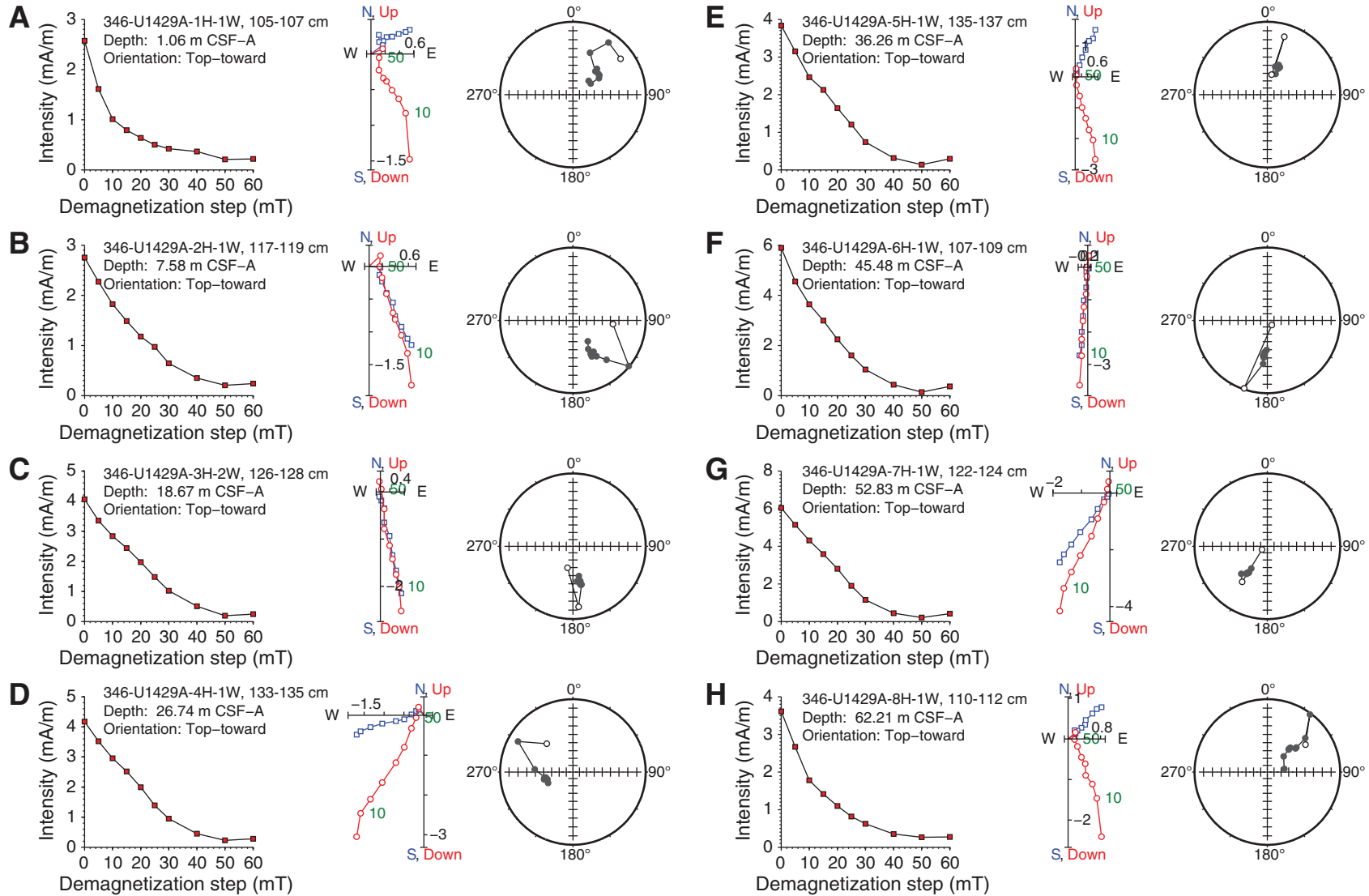




Figure F49 (continued). I–P. Discrete cube samples from 71.3 to 137.86 m CSF-A. (Continued on next page.)

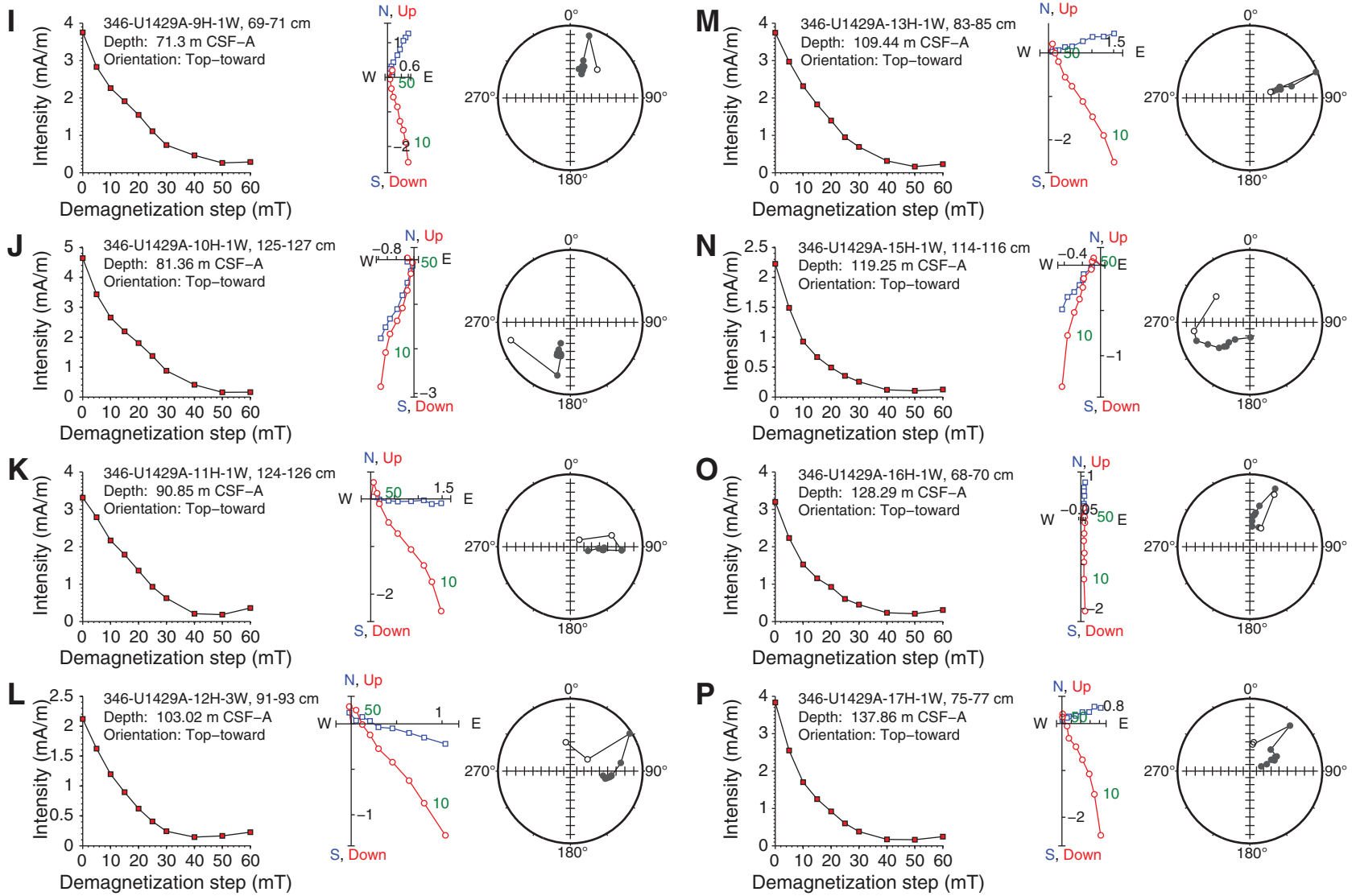


Figure F49 (continued). Q–T. Discrete cube samples from 147.25 m CSF-A and deeper.

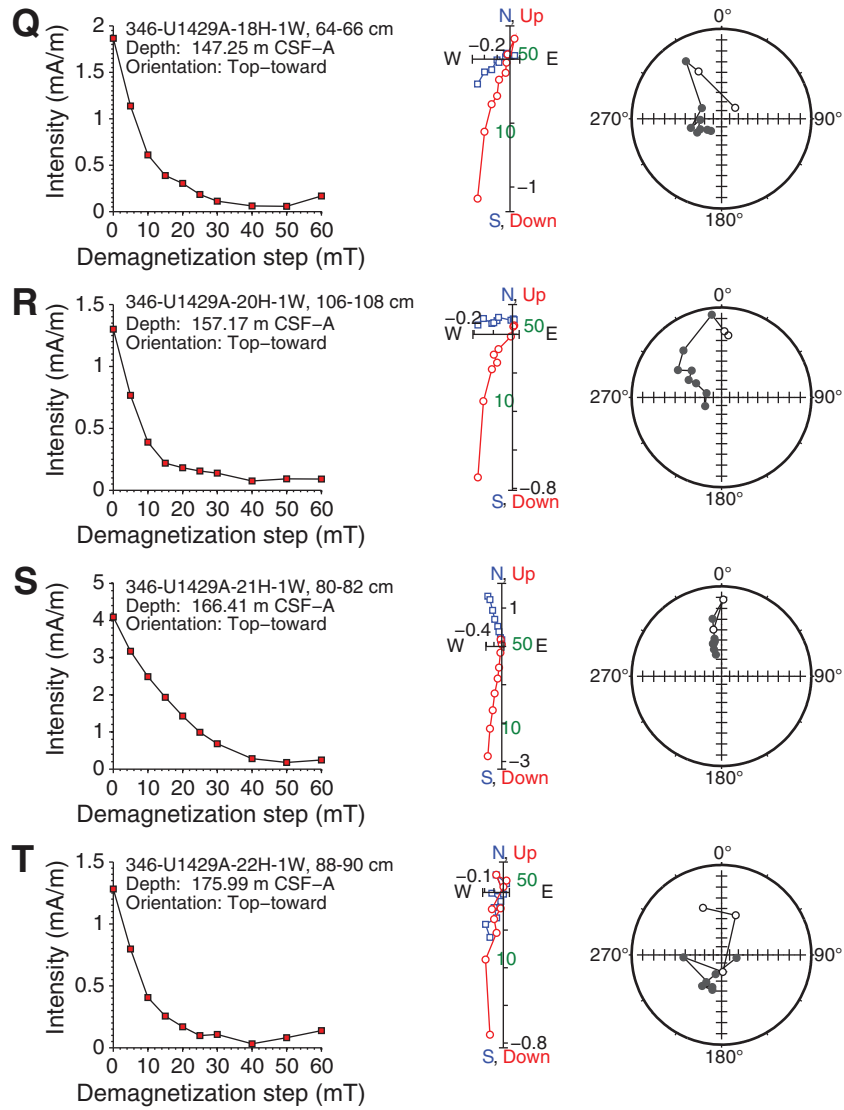


Figure F50. Suite of physical properties measured in Holes U1428A and U1428B. The first magnetic susceptibility panel shows WRMSL data of Hole U1428A, whereas the second panel shows point SHMSL susceptibility data of Hole U1428A. Gamma ray attenuation (GRA) bulk density is from Hole U1428A. Natural gamma radiation (NGR) is from Hole U1428A. *P*-wave velocity panel shows combined data from WRMSL of Holes U1428A and U1428B. Solid horizontal line = lithologic Unit A/B boundary.

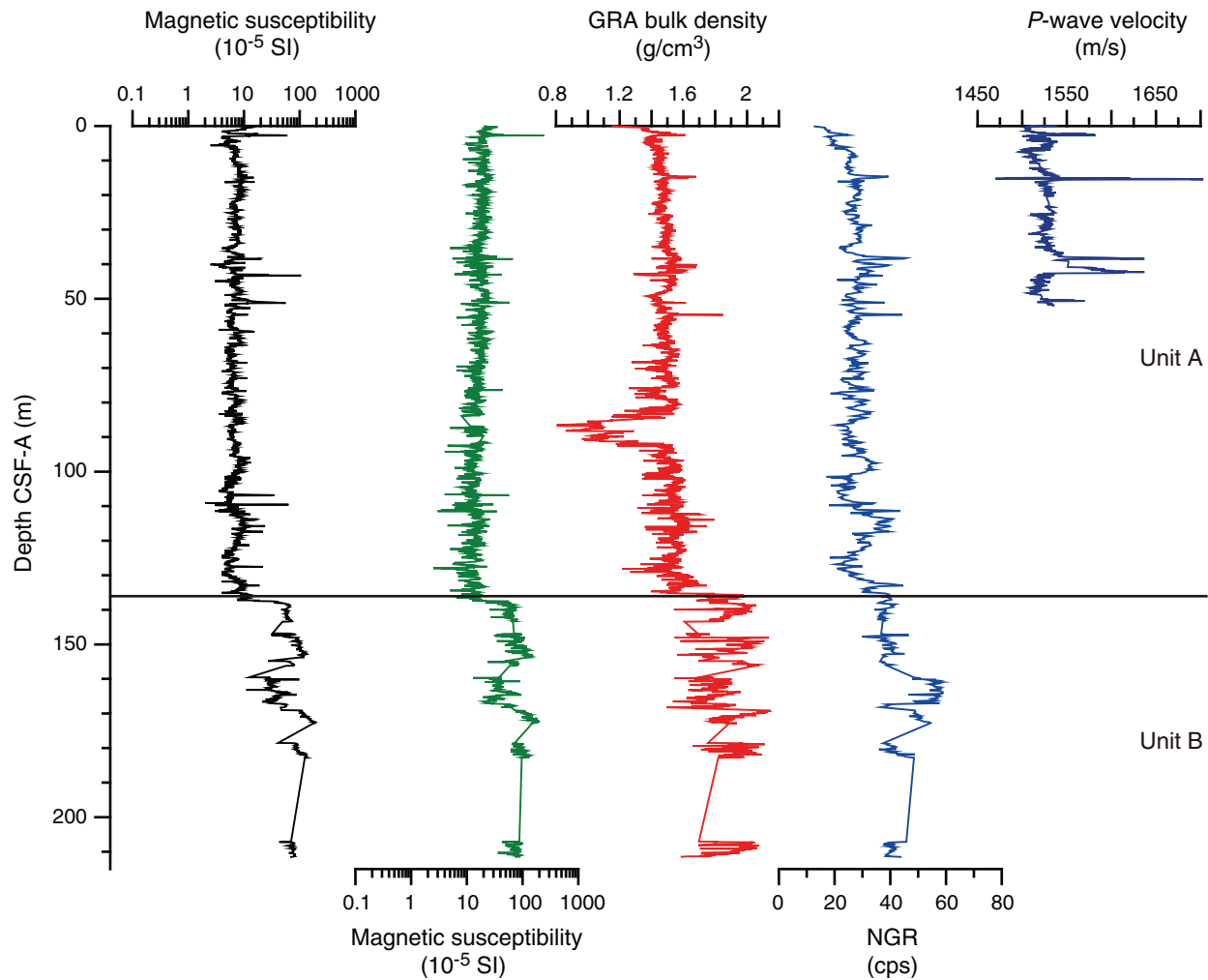


Figure F51. Suite of physical properties measured in Holes U1429A, U1429B, and U1429C. The first magnetic susceptibility panel shows WRMAL data of Hole U1429A, whereas the second panel shows point SHMSL susceptibility data of Hole U1429A. Gamma ray attenuation (GRA) bulk density is from Hole U1429A. Natural gamma radiation (NGR) is from Hole U1429A. *P*-wave velocity panel shows combined data from WRMSL of Holes U1429A, U1429B, and U1429C. Solid horizontal line = lithologic Unit A/B boundary.

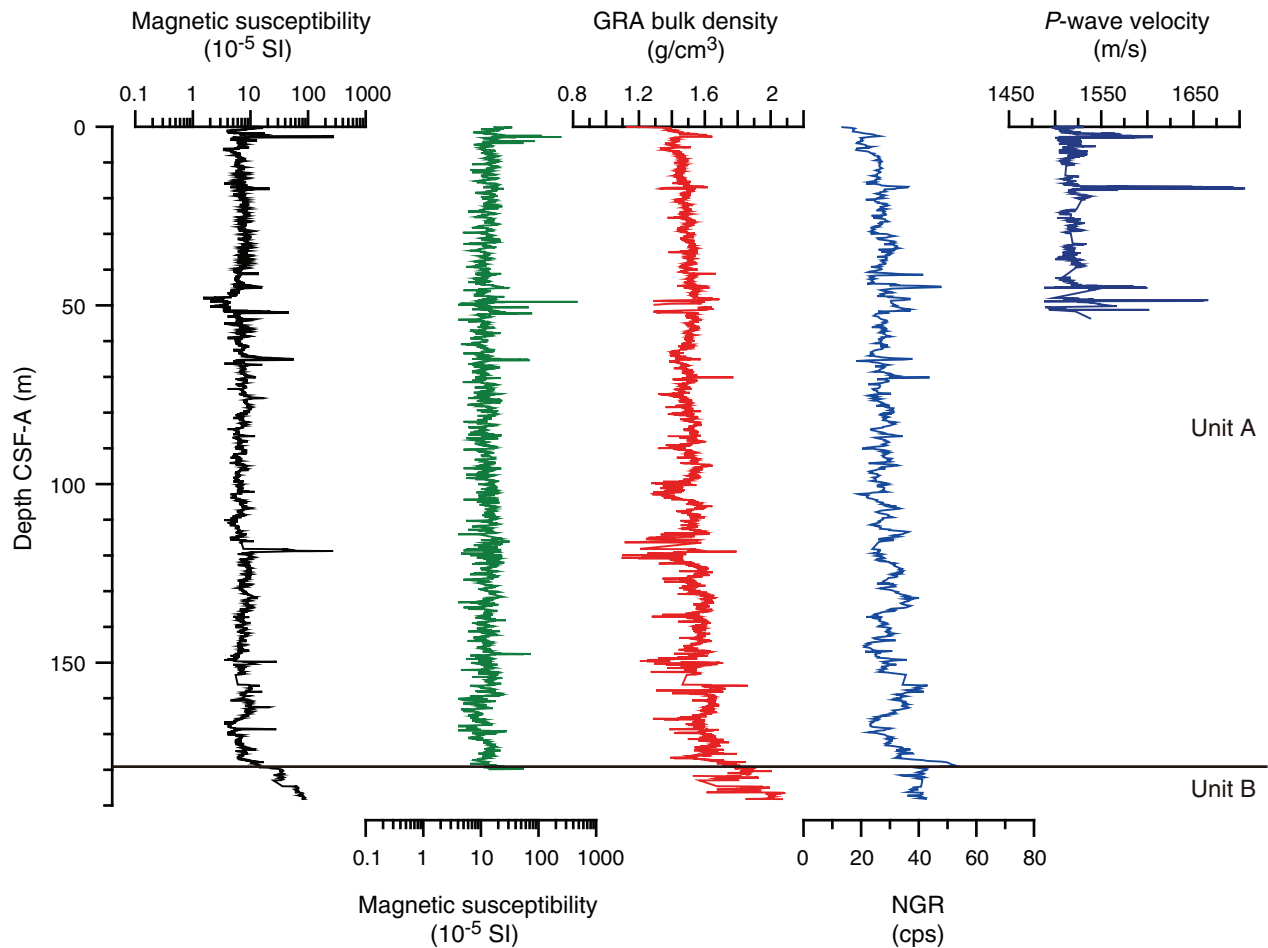


Figure F52. Discrete bulk density, grain density, porosity, water content, and shear strength, Hole U1428A. Solid horizontal line = lithologic Unit A/B boundary.

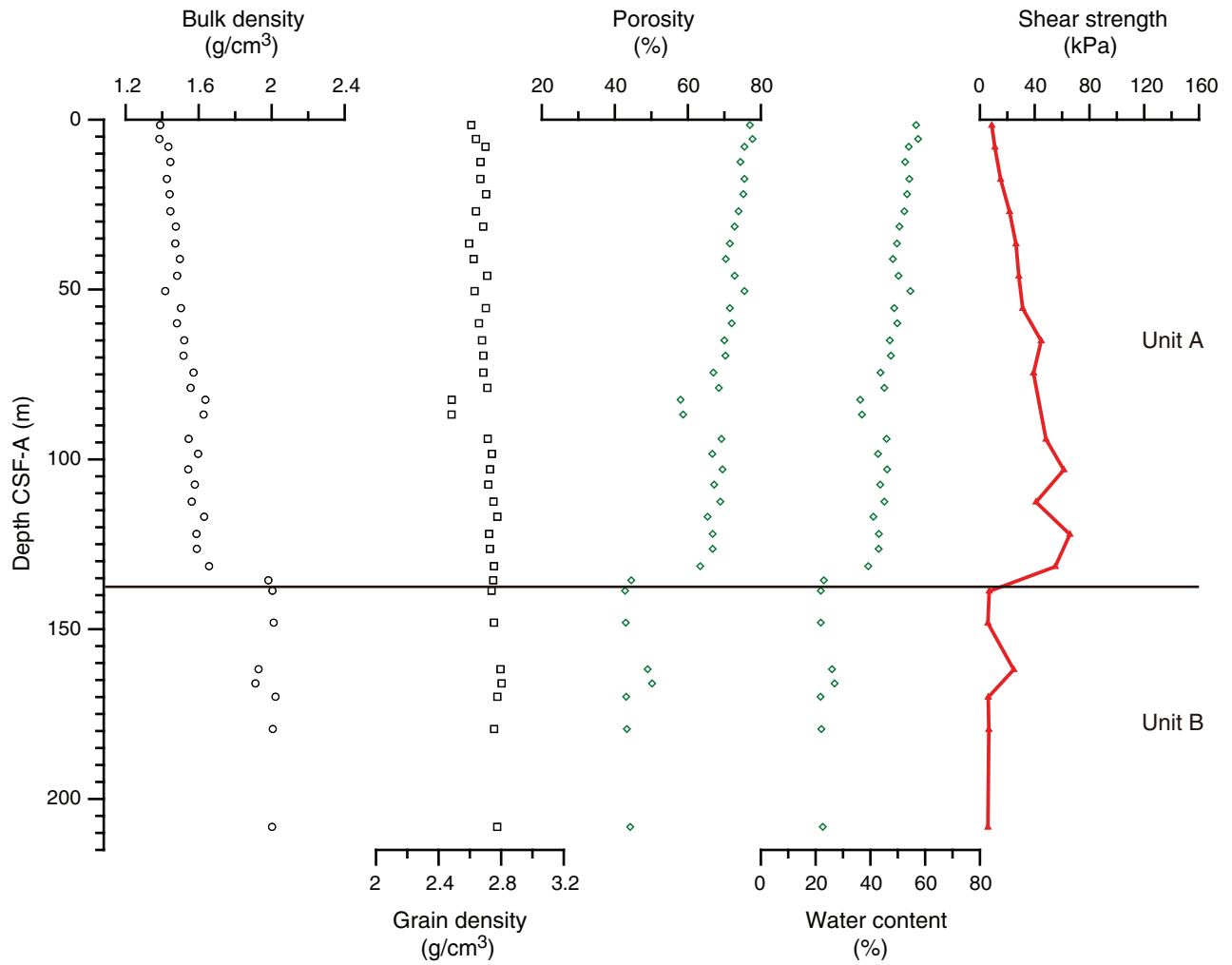


Figure F53. Discrete bulk density, grain density, porosity, water content, and shear strength, Hole U1429A. Solid horizontal line = lithologic Unit A/B boundary.

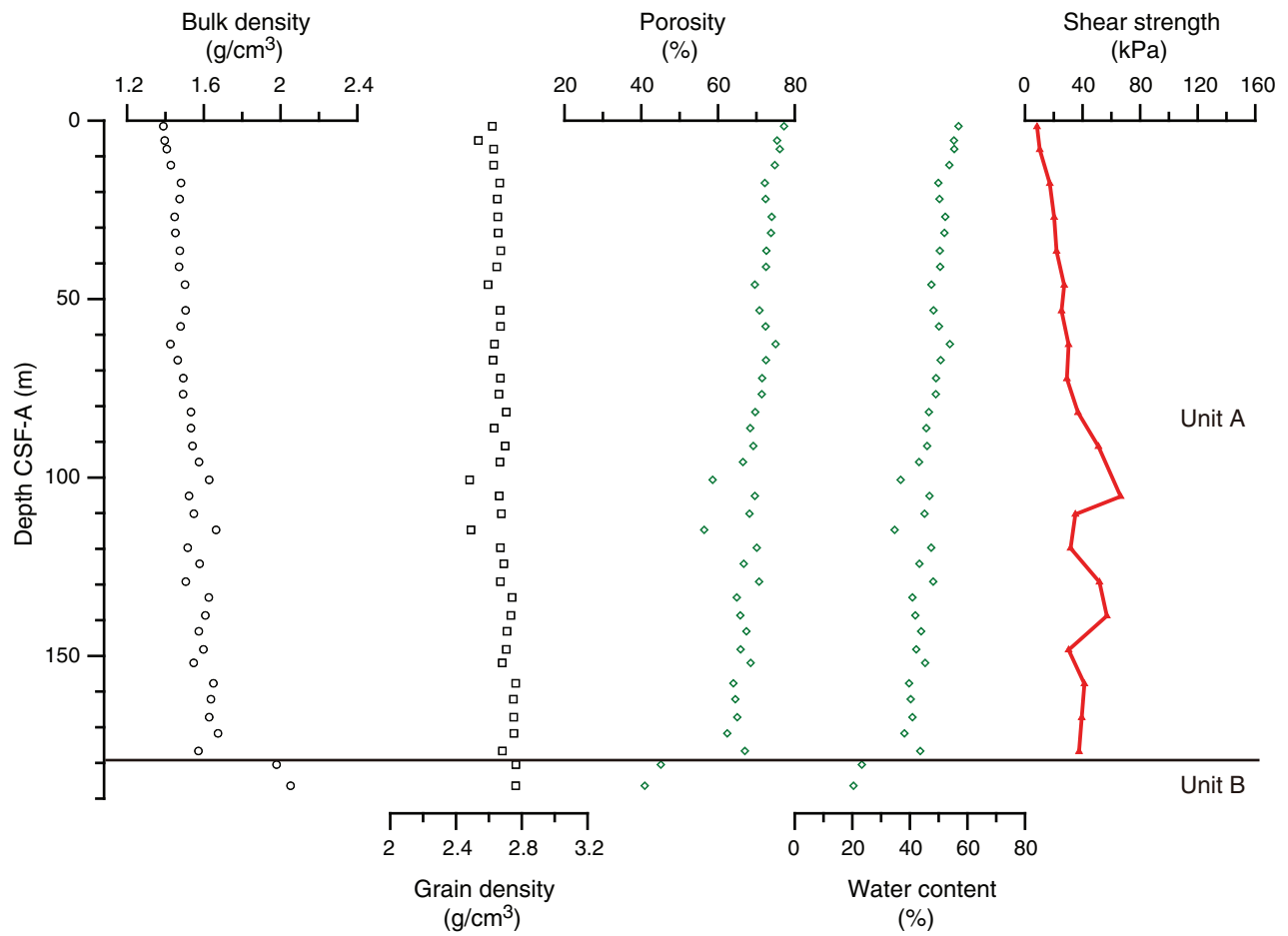


Figure F54. Color reflectance (L^* , a^* , and b^*), Hole U1428A. Solid horizontal line = lithologic Unit A/B boundary.

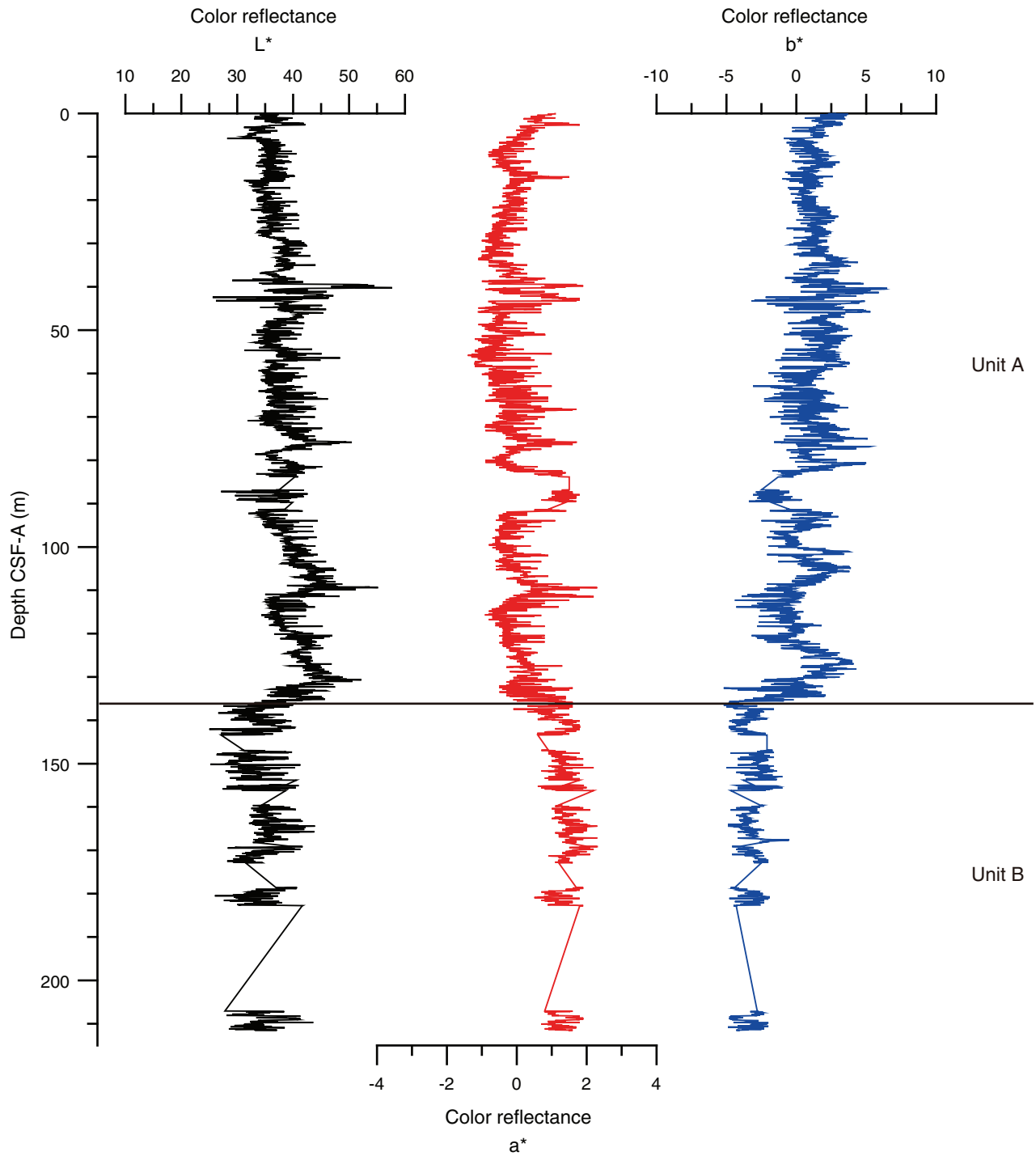


Figure F55. Color reflectance (L^* , a^* , and b^*), Hole U1429A. Solid horizontal line = lithologic Unit A/B boundary.

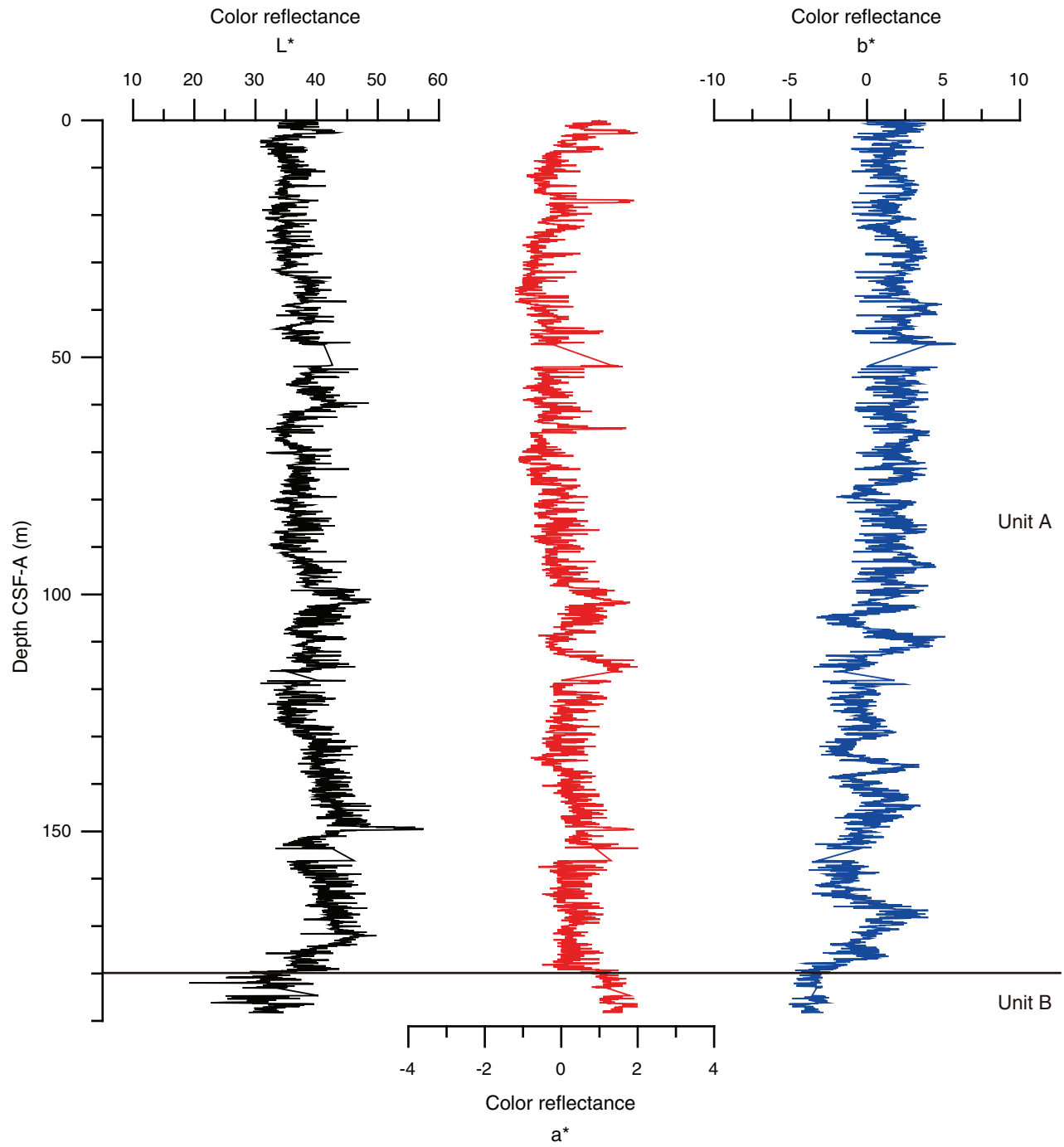


Figure F56. Diffuse reflectance data comparison between Sites U1425, U1427, U1428, and U1429 in L*-a* color spaces. Average L* for each site is depicted by lines.

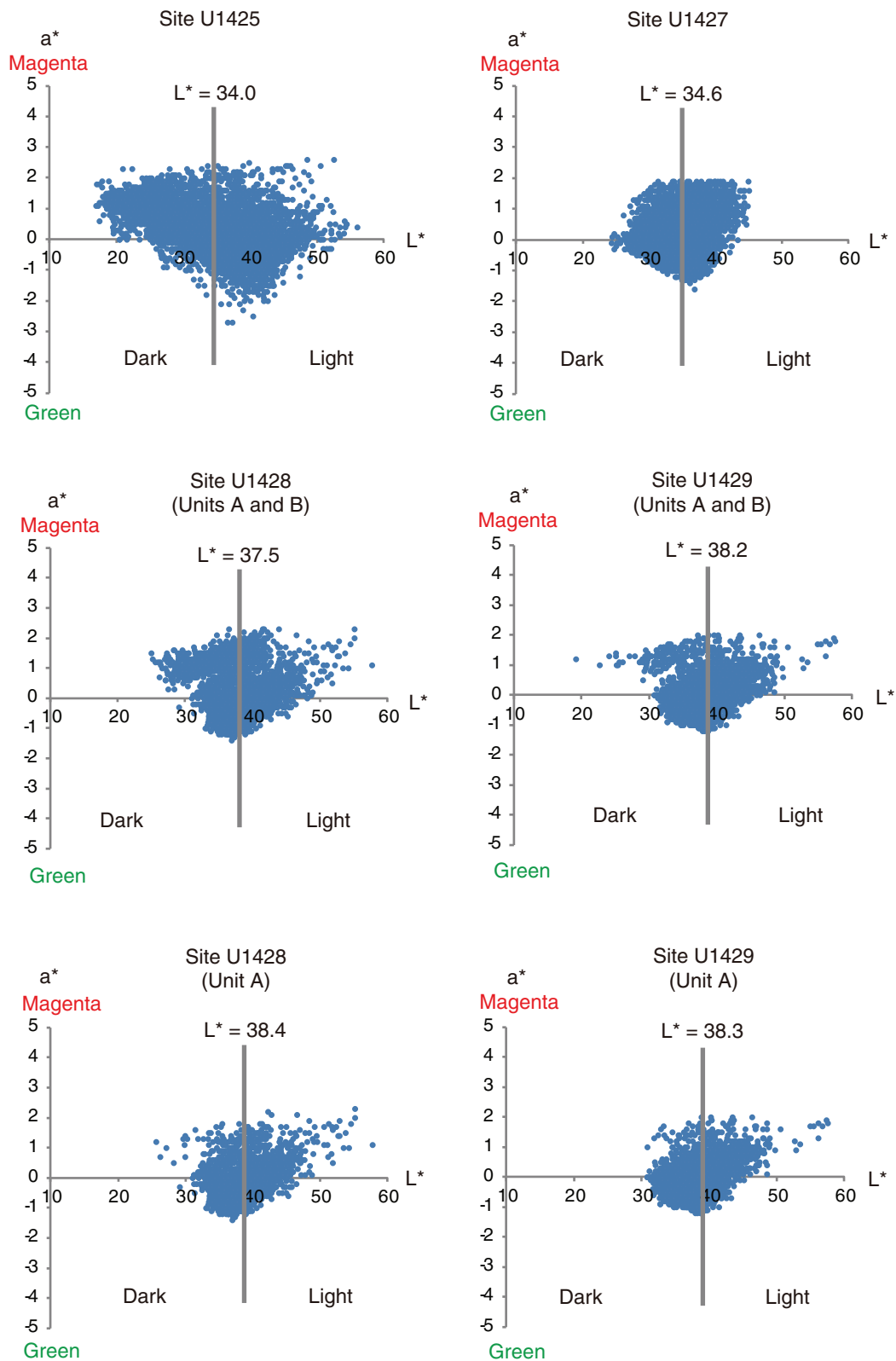


Figure F57. Plots of heat flow calculations, Hole U1428A. **A.** In situ sediment temperatures from advanced piston corer temperature tool (APCT-3) measurements with average values for Cores 346-U1428A-4H, 7H, 10H, and 13H (circles) and linear fit (excluding the mudline). **B.** In situ thermal conductivity data (squares) with calculated thermal resistance (solid line). **C.** Bullard plot of heat flow calculated from a linear fit of temperature vs. thermal resistance data.

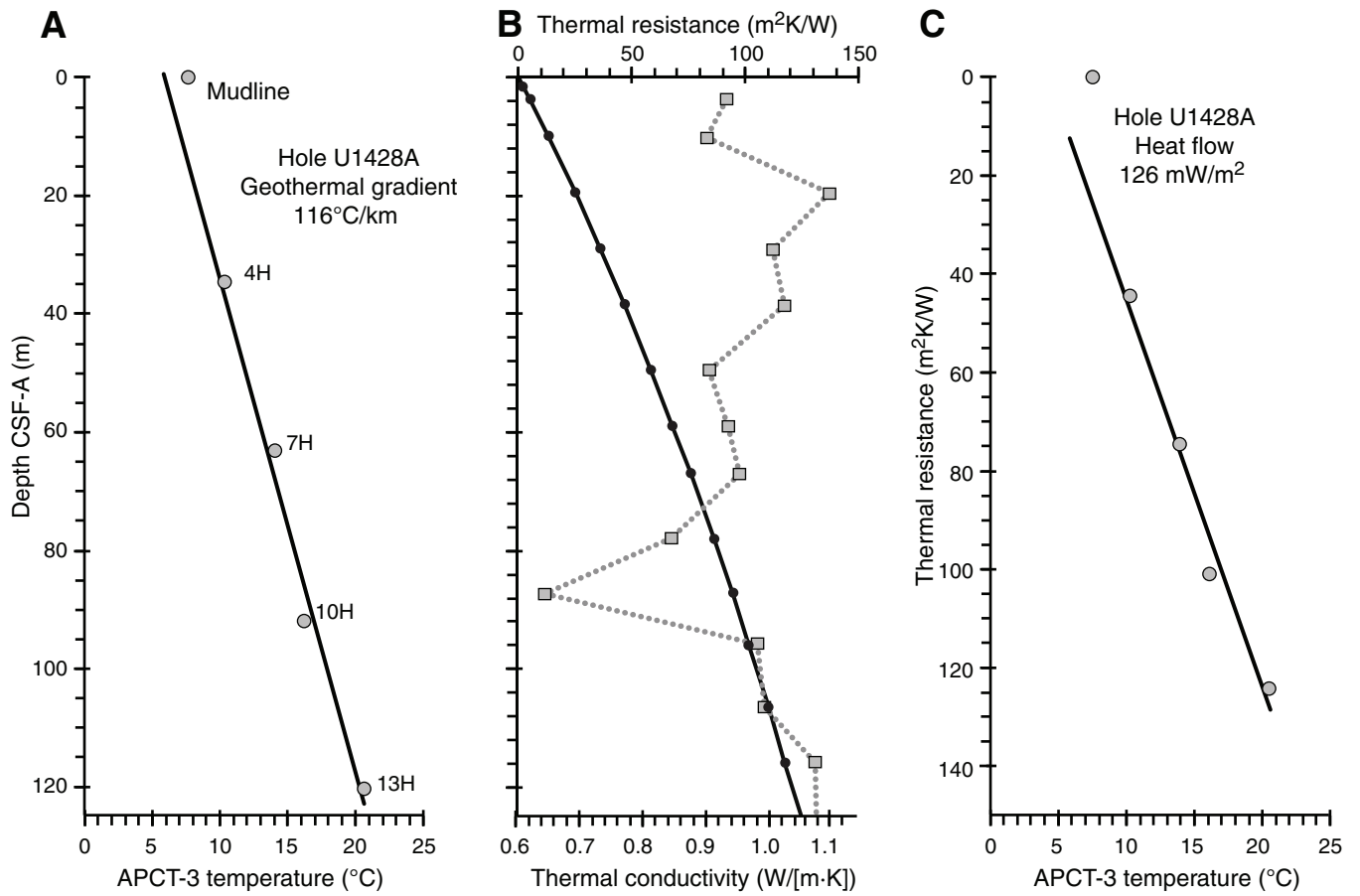


Figure F58. Plots of heat flow calculations, Hole U1429A. **A.** In situ sediment temperatures from advanced piston corer temperature tool (APCT-3) measurements with average values for Cores 346-U1429A-4H, 7H, 10H, and 13H (circles) and linear fit (excluding measurements for the mudline and Core 13H). **B.** In situ thermal conductivity data (squares) with calculated thermal resistance (solid line). **C.** Bullard plot of heat flow calculated from a linear fit of temperature vs. thermal resistance data.

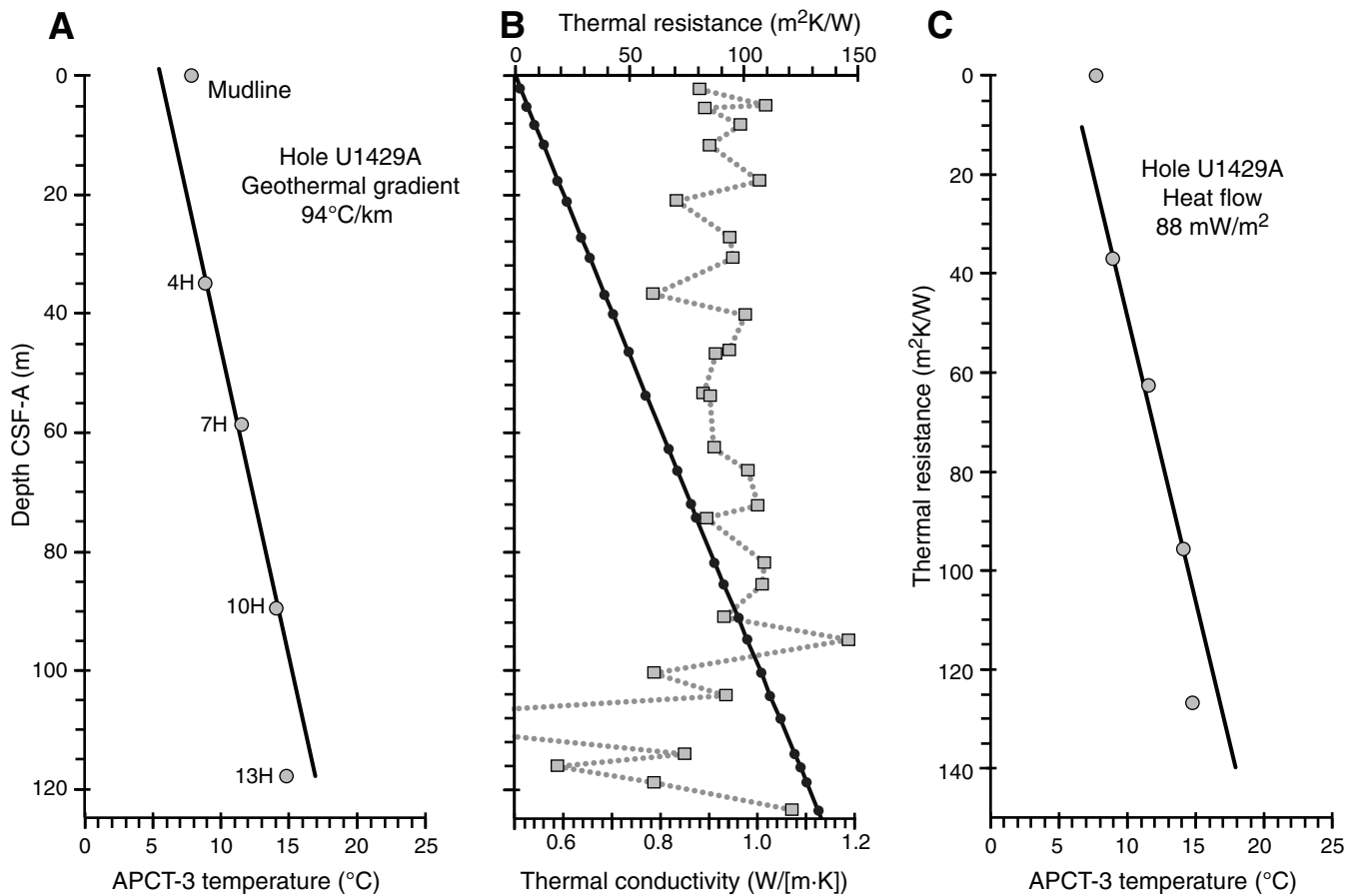




Figure F59. Compositing cores and splice, Site U1428. Each core is adjusted (in depth) by a constant amount to align it with adjacent cores at a chosen tie point (typically a distinctive feature in one of the data sets). Other features may or may not align among adjacent cores because of differential squeezing and stretching during the coring process or because of variable expansion characteristics. The splice is constructed from the composited cores by selecting intervals from different holes such that coring gaps are avoided and drilling disturbances are minimized. Data included in the splice are plotted on the CCSF-D scale, whereas data not included in the splice are plotted on the CCSF-A scale. Short light blue lines indicate tie points where the splice changes from one hole to another. Only the splice is plotted on the correct y -axis scale; data from Holes U1428A and U1428B are offset by 40 and 80 units, respectively, for illustrative purposes. One and two point spikes are artifacts generated when the track sensor measures beyond the end of the ~150 cm sections. A. 0–50 m CCSF-A. (Continued on next page.)

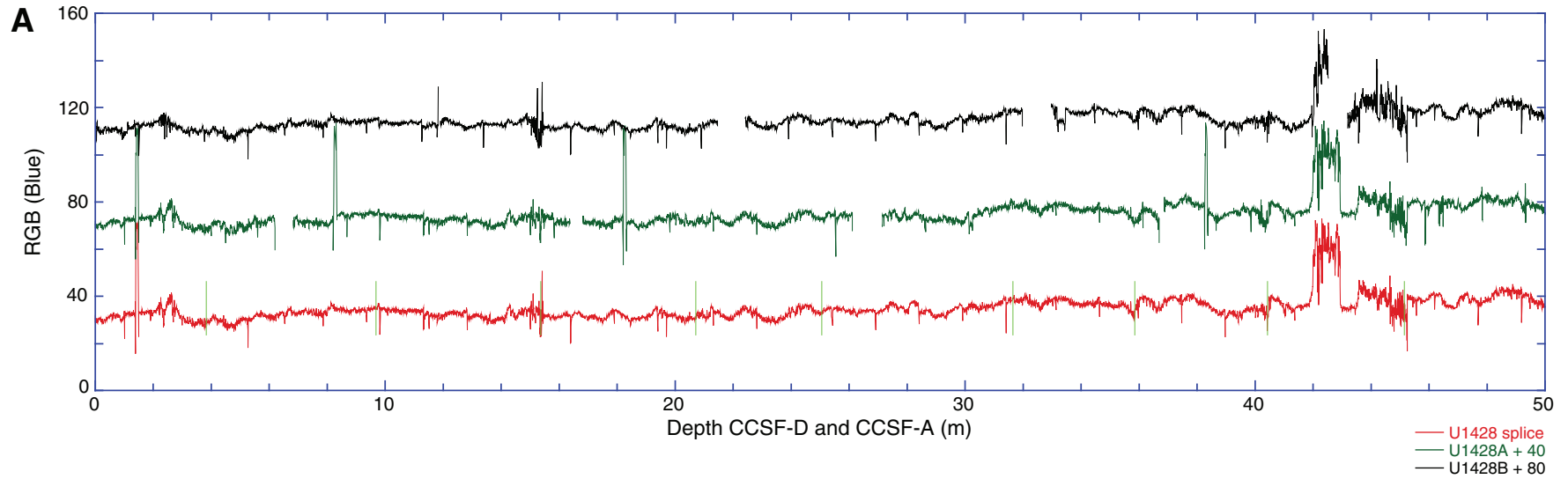




Figure F59 (continued). B. 50–150 m CCSF-A.

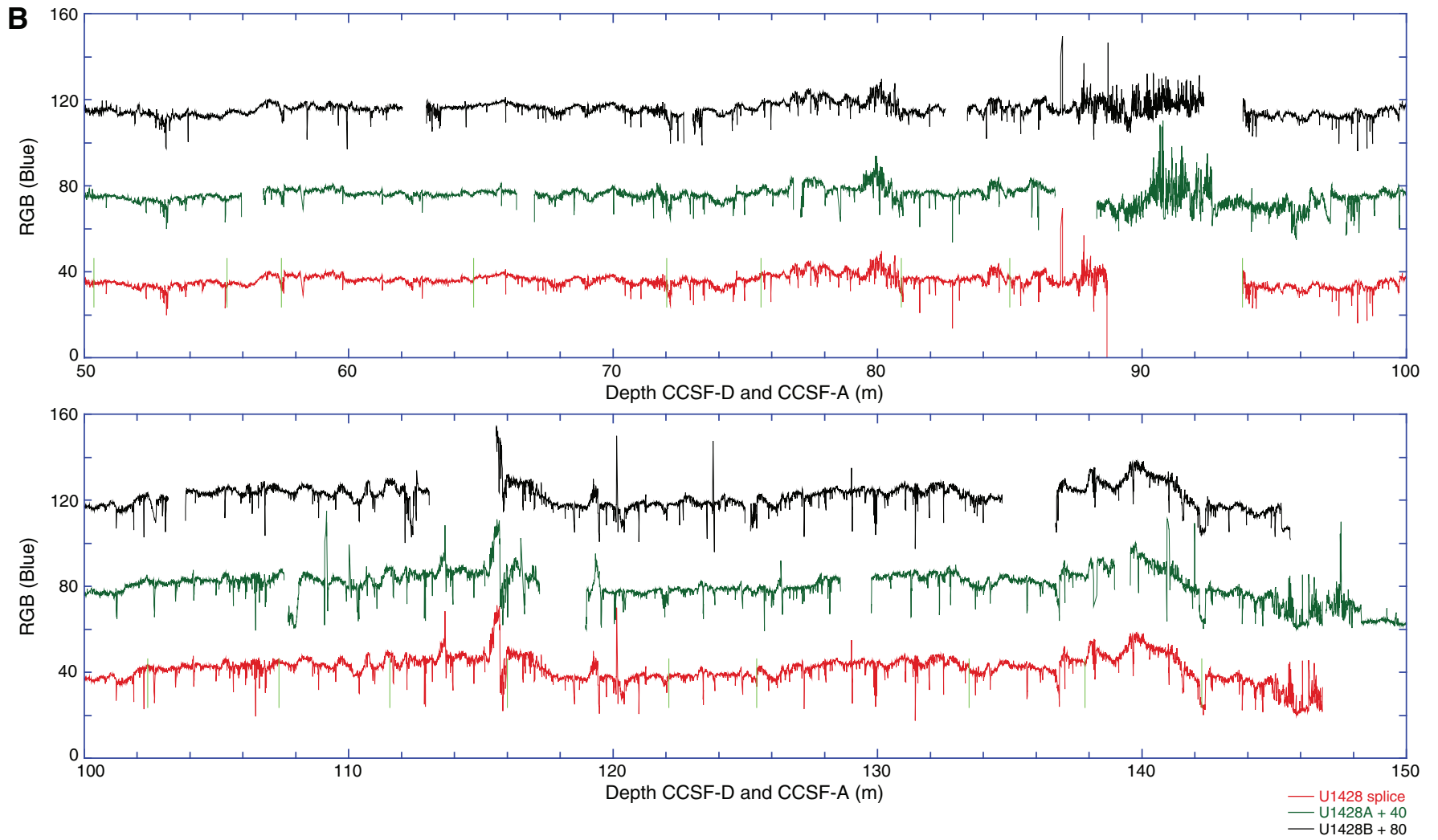




Figure F60. Spliced magnetic susceptibility (MS) records comparing Sites U1428 and U1429. Arrows indicate correlative features. Ovals indicate anomalous changes in the magnetic susceptibility structure that occur within cores (not at splice ties) in both holes, possibly indicating hiatuses.

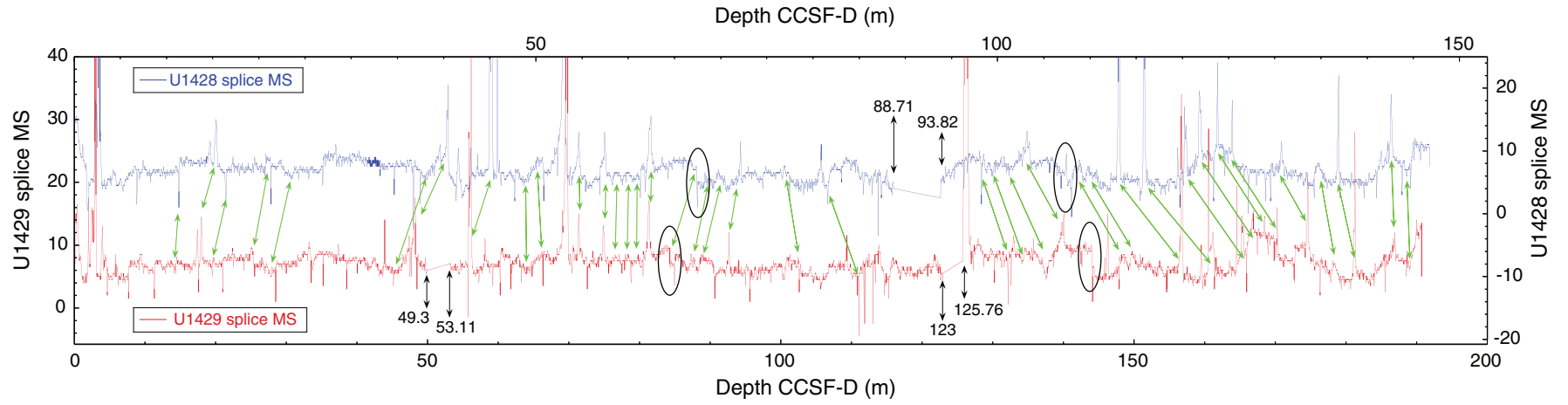




Figure F61. Composited cores and splice, Site U1429. Each core is adjusted (in depth) by a constant amount to align it with adjacent cores at a chosen tie point (typically a distinctive feature in all of the data sets). Other features may or may not align among adjacent cores because of differential squeezing and stretching during the coring process or because of variable expansion characteristics. The splice is constructed from the composited cores by selecting intervals from different holes such that coring gaps are avoided and drilling disturbances are minimized. Data included in the splice are plotted on the CCSF-D scale, whereas data not included in the splice are plotted on the CCSF-A scale. Short light blue lines indicate tie points where the splice changes from one hole to another. Only the splice is plotted on the correct γ -axis scale; data from Holes U1429A, U1429B, and U1429C are offset by 40, 80, or 120 units, respectively, for illustrative purposes. One and two point spikes are artifacts generated when the track sensor measures beyond the end of the ~150 cm sections. A. 0–100 m CCSF-A. (Continued on next page.)

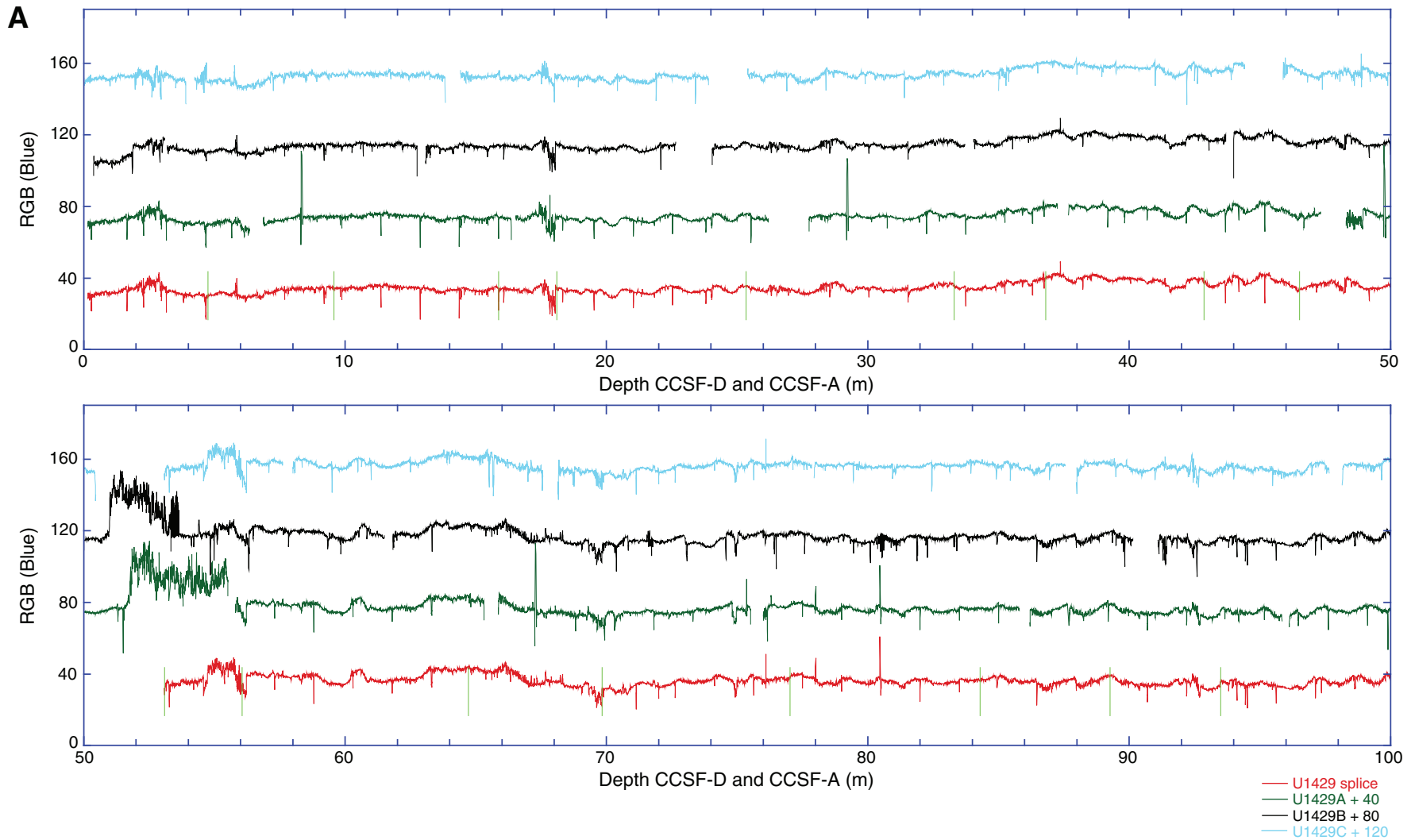




Figure F61 (continued). B. 100–200 m CCSF-A.

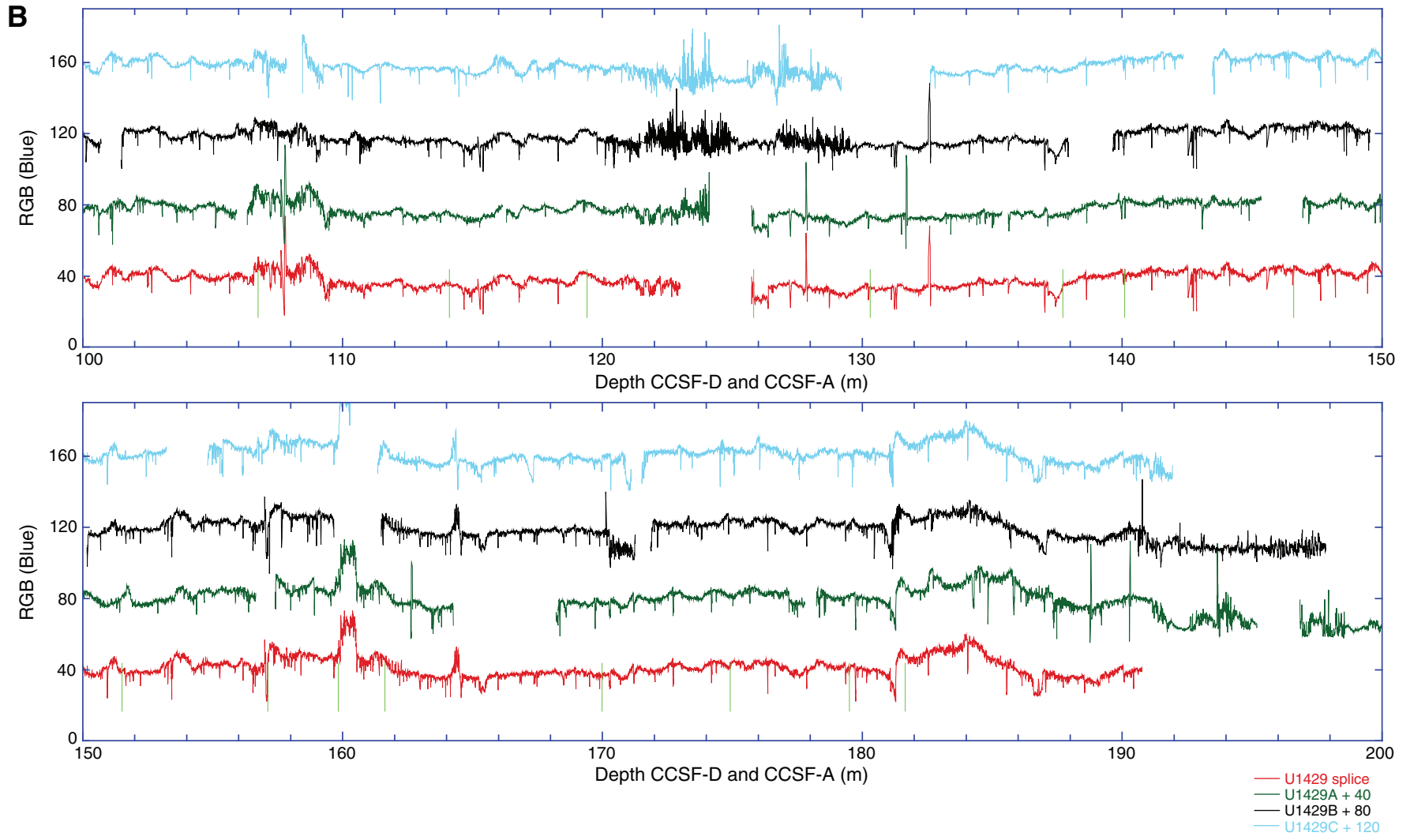




Figure F62. Age model and sedimentation rates. A. Site U1428. B. Site U1429.

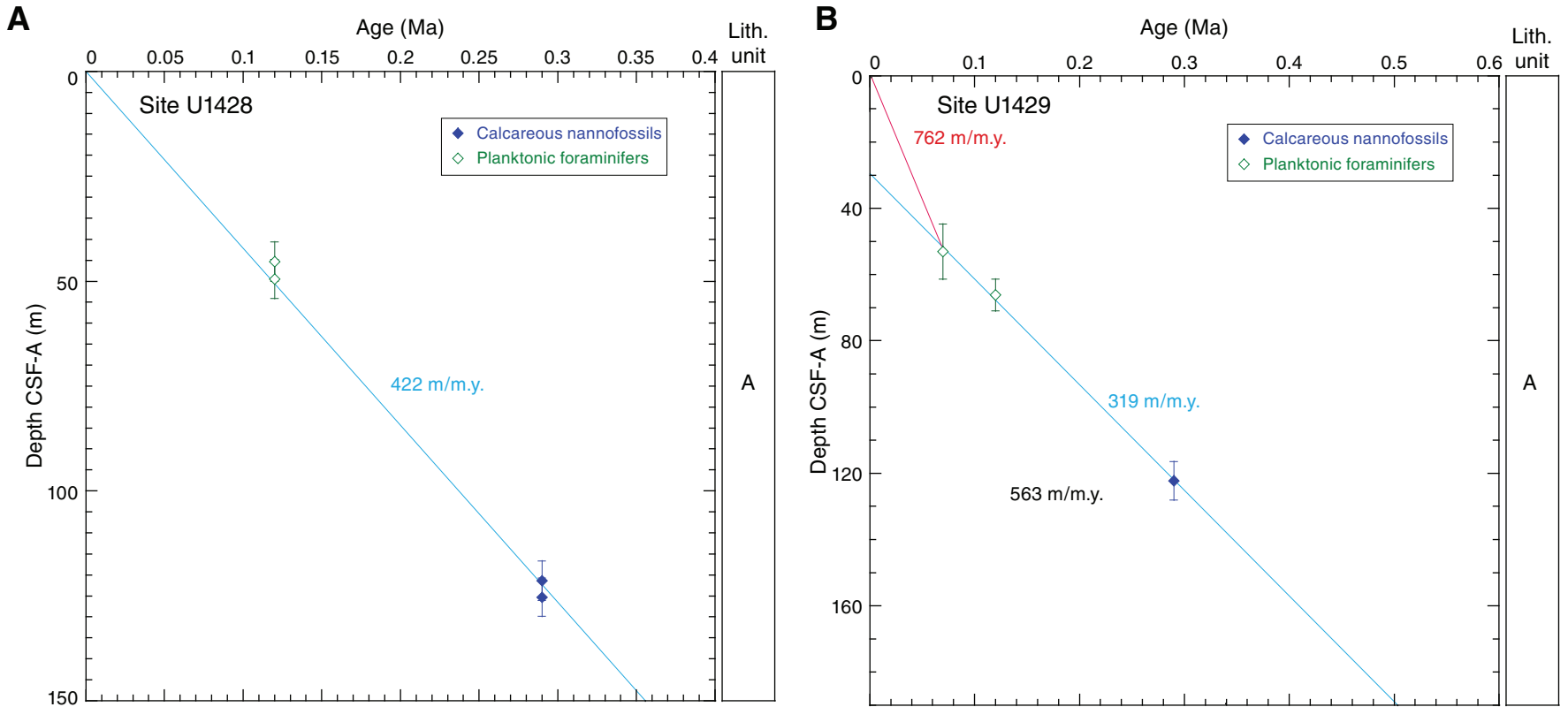


Table T1. Coring summary, Site U1428. (Continued on next page.)

Hole U1428A

Latitude: 31°40.6391'N
 Longitude: 129°02.0003'E
 Water depth (m): 723.86
 Date started (UTC): 2000 h 11 September 2013
 Date finished (UTC): 0124 h 13 September 2013
 Time on hole (days): 1.23
 Seafloor depth DRF (m): 735.4
 Rig floor to sea level (m): 11.54
 Penetration DSF (m): 211.5
 Cored interval (m): 173.9
 Recovered length (m): 178.86
 Recovery (%): 103
 Drilled interval (m): 37.6
 Drilled interval: 6
 Total cores: 26
 APC cores: 26
 XCB cores: 0
 RCB cores: 0
 Other cores: 0

Hole U1428B

Latitude: 31°40.6483'N
 Longitude: 129°02.0004'E
 Water depth (m): 724.1
 Date started (UTC): 0430 h 15 September 2013
 Date finished (UTC): 1918 h 15 September 2013
 Time on hole (days): 0.62
 Seafloor depth DRF (m): 735.8
 Rig floor to sea level (m): 11.70
 Penetration DSF (m): 143.3
 Cored interval (m): 143.3
 Recovered length (m): 145.85
 Recovery (%): 102
 Drilled interval (m): NA
 Drilled interval: 0
 Total cores: 16
 APC cores: 16
 XCB cores: 0
 RCB cores: 0
 Other cores: 0

Site U1428 totals

Number of cores: 42
 Penetration (m): 354.8
 Cored (m): 317.2
 Recovered (m): 324.71 (102.5%)

Core	Date (Sep 2013)	Time (h)	Top depth of cored interval DSF (m)	Bottom depth of cored interval DSF (m)	Interval advanced (m)	Top depth of recovered core CSF (m)	Bottom depth of recovered core CSF (m)	Length of core recovered (m)	Curated length (m)	Recovery (%)
346-U1428A-										
1H	12	0340	0.0	6.4	6.4	0.0	6.37	6.37	6.37	100
2H	12	0500	6.4	15.9	9.5	6.4	16.25	9.85	9.85	104
3H	12	0520	15.9	25.4	9.5	15.9	25.43	9.53	9.53	100
4H	12	0555	25.4	34.9	9.5	25.4	35.40	10.00	10.00	105
5H	12	0615	34.9	44.4	9.5	34.9	44.88	9.98	9.98	105
6H	12	0645	44.4	53.9	9.5	44.4	54.22	9.82	9.82	103
7H	12	0715	53.9	63.4	9.5	53.9	63.89	9.99	9.99	105
8H	12	0740	63.4	72.9	9.5	63.4	73.46	10.06	10.06	106
9H	12	0805	72.9	82.4	9.5	72.9	82.77	9.87	9.87	104
10H	12	0845	82.4	91.9	9.5	82.4	91.89	9.49	9.49	100
11H	12	0935	91.9	101.4	9.5	91.9	102.20	10.30	10.30	108
12H	12	0955	101.4	110.9	9.5	101.4	111.55	10.15	10.15	107
13H	12	1035	110.9	120.4	9.5	110.9	120.88	9.98	9.98	105
14H	12	1105	120.4	129.9	9.5	120.4	129.91	9.51	9.51	100
15H	12	1130	129.9	137.3	7.4	129.9	137.35	7.45	7.45	101
16H	12	1230	137.3	143.5	6.2	137.3	143.50	6.20	6.20	100
17I	12	1240			*****Drilled from 143.5 to 146.8 mbsf*****					
18H	12	1310	146.8	150.1	3.3	146.8	153.88	7.08	7.08	215
19H	12	1440	150.1	150.1	0	150.1	150.13		0.03	

Table T1 (continued).

Core	Date (Sep 2013)	Time (h)	Top depth of cored interval DSF (m)	Bottom depth of cored interval DSF (m)	Interval advanced (m)	Top depth of recovered core CSF (m)	Bottom depth of recovered core CSF (m)	Length of core recovered (m)	Curated length (m)	Recovery (%)	
202	12	1510			*****Drilled from 150.1 to 154.8 mbsf*****						
21H	12	1525	154.8	156.3	1.5	154.8	156.26	1.46	1.46	97	
22H	12	1530	156.3	159.5	3.2	156.3	157.76		1.46		
23H	12	1600	159.5	169.0	9.5	159.5	168.37	8.87	8.87	93	
24H	12	1640	169.0	173.0	4.0	169.0	172.94	3.94	3.94	99	
254	12	1700			*****Drilled from 173.0 to 178.5 mbsf*****						
26H	12	1710	178.5	182.9	4.4	178.5	182.90	4.40	4.40	100	
275	12	1730			*****Drilled from 182.9 to 188.0 mbsf*****						
28H	12	1745	188.0	188.0	0.0	188.0	189.46		1.46		
296	12	1800			*****Drilled from 188.0 to 197.5 mbsf*****						
30H	12	1830	197.5	197.5	0.0	197.5	198.96		1.46		
317	12	1840			*****Drilled from 197.5 to 207.0 mbsf*****						
32H	12	2030	207.0	211.5	4.5	207.0	211.56	4.56	4.56	101	
Total advanced (m):					211.5	Total recovered (m):					178.86
346-U1428B-											
1H	15	0745	0.0	2.5	2.5	0.0	2.49	2.49	2.49	100	
2H	15	0805	2.5	12.0	9.5	2.5	12.30	9.80	9.80	103	
3H	15	0835	12.0	21.5	9.5	12.0	21.73	9.73	9.73	102	
4H	15	0900	21.5	31.0	9.5	21.5	31.28	9.78	9.78	103	
5H	15	0925	31.0	40.5	9.5	31.0	40.68	9.68	9.68	102	
6H	15	0955	40.5	50.0	9.5	40.5	50.14	9.64	9.64	101	
7H	15	1040	50.0	59.5	9.5	50.0	59.87	9.87	9.87	104	
8H	15	1120	59.5	69.0	9.5	59.5	69.54	10.04	10.04	106	
9H	15	1150	69.0	78.5	9.5	69.0	78.86	9.86	9.86	104	
10H	15	1215	78.5	88.0	9.5	78.5	87.78	9.28	9.28	98	
11H	15	1245	88.0	97.5	9.5	88.0	97.72	9.72	9.72	102	
12H	15	1310	97.5	107.0	9.5	97.5	107.21	9.71	9.71	102	
13H	15	1335	107.0	116.5	9.5	107.0	116.74	9.74	9.74	103	
14H	15	1400	116.5	126.0	9.5	116.5	126.19	9.69	9.69	102	
15H	15	1425	126.0	135.5	9.5	126.0	135.02	9.02	9.02	95	
16H	15	1450	135.5	143.3	7.8	135.5	143.30	7.80	7.80	100	
Total advanced (m):					143.3	Total recovered (m):					145.85

DRF = drilling depth below rig floor, DSF = drilling depth below seafloor, CSF = core depth below seafloor. APC = advanced piston corer, XCB = extended core barrel, RCB = rotary core barrel. H = APC system, numeric core type = drilled interval. NA = not applicable.

Table T2. Coring summary, Site U1429. (Continued on next two pages.)**Hole U1429A**

Latitude: 31°37.0388'N
 Longitude: 128°59.8509'E
 Water depth (m): 732.14
 Date started (UTC): 0300 h 13 September 2013
 Date finished (UTC): 0000 h 14 September 2013
 Time on hole (days): 0.88
 Seafloor depth DRF (m): 743.7
 Rig floor to sea level (m): 11.56
 Penetration DSF (m): 188.3
 Cored interval (m): 184.2
 Recovered length (m): 190.29
 Recovery (%): 103
 Drilled interval (m): 4.1
 Drilled interval: 2
 Total cores: 21
 APC cores: 21
 XCB cores: 0
 RCB cores: 0
 Other cores: 0

Hole U1429B

Latitude: 31°37.0469'N
 Longitude: 128°59.8512'E
 Water depth (m): 731.64
 Date started (UTC): 0000 h 14 September 2013
 Date finished (UTC): 1310 h 14 September 2013
 Time on hole (days): 0.55
 Seafloor depth DRF (m): 743.2
 Rig floor to sea level (m): 11.56
 Penetration DSF (m): 186.2
 Cored interval (m): 186.2
 Recovered length (m): 200.92
 Recovery (%): 108
 Drilled interval (m): NA
 Drilled interval: 0
 Total cores: 22
 APC cores: 22
 XCB cores: 0
 RCB cores: 0
 Other cores: 0

Hole U1429C

Latitude: 31°37.0315'N
 Longitude: 128°59.8503'E
 Water depth (m): 732.44
 Date started (UTC): 1310 h 14 September 2013
 Date finished (UTC): 0342 h 15 September 2013
 Time on hole (days): 0.61
 Seafloor depth DRF (m): 744
 Rig floor to sea level (m): 11.56
 Penetration DSF (m): 179.2
 Cored interval (m): 174.3
 Recovered length (m): 180.7
 Recovery (%): 104
 Drilled interval (m): 4.9
 Drilled interval: 2
 Total cores: 22
 APC cores: 22
 XCB cores: 0
 RCB cores: 0
 Other cores: 0

Site U1429 totals

Number of cores: 65
 Penetration (m): 553.7
 Cored (m): 544.7
 Recovered (m): 571.91 (105%)

Table T2 (continued). (Continued on next page.)

Core	Date (Sep 2013)	Time (h)	Top depth of cored interval DSF (m)	Bottom depth of cored interval DSF (m)	Interval advanced (m)	Top depth of recovered core CSF (m)	Bottom depth of recovered core CSF (m)	Length of core recovered (m)	Curated length (m)	Recovery (%)
346-U1429A-										
1H	13	1200	0.0	6.4	6.4	0.0	6.40	6.40	6.40	100
2H	13	1220	6.4	15.9	9.5	6.4	16.16	9.76	9.76	103
3H	13	1250	15.9	25.4	9.5	15.9	25.88	9.98	9.98	105
4H	13	0125	25.4	34.9	9.5	25.4	35.32	9.92	9.92	104
5H	13	0150	34.9	44.4	9.5	34.9	44.83	9.93	9.93	105
6H	13	0215	44.4	51.6	7.2	44.4	51.63	7.23	7.23	100
7H	13	0305	51.6	61.1	9.5	51.6	61.43	9.83	9.83	103
8H	13	0330	61.1	70.6	9.5	61.1	71.02	9.92	9.92	104
9H	13	0355	70.6	80.1	9.5	70.6	80.67	10.07	10.07	106
10H	13	0430	80.1	89.6	9.5	80.1	90.20	10.10	10.10	106
11H	13	0455	89.6	99.1	9.5	89.6	99.78	10.18	10.18	107
12H	13	0525	99.1	108.6	9.5	99.1	109.19	10.09	10.09	106
13H	13	0610	108.6	116.4	7.8	108.6	116.47	7.87	7.87	101
14I	13	0615				****Drilled from 116.4 to 118.1 mbsf****				
15H	13	0635	118.1	127.6	9.5	118.1	128.10	10.00	10.00	105
16H	13	0700	127.6	137.1	9.5	127.6	137.65	10.05	10.05	106
17H	13	0730	137.1	146.6	9.5	137.1	147.16	10.06	10.06	106
18H	13	0755	146.6	153.7	7.1	146.6	153.73	7.13	7.13	100
19I	13	0800				****Drilled from 153.7 to 156.1 mbsf****				
20H	13	0830	156.1	165.6	9.5	156.1	165.98	9.88	9.88	104
21H	13	0900	165.6	175.1	9.5	165.6	175.79	10.19	10.19	107
22H	13	0925	175.1	184.6	9.5	175.1	183.12	8.02	8.02	84
23H	13	0955	184.6	188.3	3.7	184.6	188.28	3.68	3.68	99
			Total advanced (m):		188.3	Total recovered (m):		190.29		
346-U1429B-										
1H	14	1240	0.0	2.9	2.9	0.0	2.93	2.93	2.93	101
2H	14	0105	2.9	12.4	9.5	2.9	12.64	9.74	9.74	103
3H	14	0130	12.4	21.9	9.5	12.4	22.33	9.93	9.93	105
4H	14	0155	21.9	31.4	9.5	21.9	31.93	10.03	10.03	106
5H	14	0220	31.4	40.9	9.5	31.4	41.28	9.88	9.88	104
6H	14	0255	40.9	47.9	7.0	40.9	50.66	9.76	9.76	139
7H	14	0340	47.9	57.4	9.5	47.9	57.84	9.94	9.94	105
8H	14	0430	57.4	66.9	9.5	57.4	67.38	9.98	9.98	105
9H	14	0455	66.9	76.4	9.5	66.9	76.77	9.87	9.87	104
10H	14	0525	76.4	85.9	9.5	76.4	86.46	10.06	10.06	106
11H	14	0555	85.9	95.4	9.5	85.9	95.78	9.88	9.88	104
12H	14	0625	95.4	104.0	8.6	95.4	105.24	9.84	9.84	114
13H	14	0705	104.0	113.5	9.5	104.0	114.20	10.20	9.88	107
14H	14	0735	113.5	115.0	1.5	113.5	118.56	5.06	5.06	337
15H	14	0810	115.0	122.0	7.0	115.0	122.46	7.46	7.46	107
16H	14	0855	122.0	131.5	9.5	122.0	131.66	9.66	9.66	102
17H	14	0920	131.5	141.0	9.5	131.5	141.49	9.99	9.99	105
18H	14	0945	141.0	150.5	9.5	141.0	150.75	9.75	9.75	103
19H	14	1025	150.5	160.0	9.5	150.5	160.29	9.79	9.79	103
20H	14	1050	160.0	169.5	9.5	160.0	169.95	9.95	9.95	105
21H	14	1115	169.5	179.0	9.5	169.5	179.50	10.00	10.00	105
22H	14	1150	179.0	186.2	7.2	179.0	186.22	7.22	7.22	100
			Total advanced (m):		186.2	Total recovered (m):		200.92		
346-U1429C-										
1H	14	0145	0.0	4.1	4.1	0.0	4.16	4.16	4.16	101
2H	14	0210	4.1	13.6	9.5	4.1	14.05	9.95	9.95	105
3H	14	0235	13.6	23.1	9.5	13.6	23.41	9.81	9.81	103
4H	14	0300	23.1	32.6	9.5	23.1	32.85	9.75	9.75	103
5H	14	0325	32.6	42.1	9.5	32.6	42.22	9.62	9.62	101
6H	14	0350	42.1	46.8	4.7	42.1	46.98	4.88	4.88	104
7I	14	0420				****Drilled from 46.8 to 48.8 mbsf****				
8H	14	0430	48.8	53.5	4.7	48.8	53.54	4.74	4.74	101
9H	14	0505	53.5	63.0	9.5	53.5	63.27	9.77	9.77	103
10H	14	0530	63.0	72.5	9.5	63.0	73.02	10.02	10.02	105
11H	14	0555	72.5	82.0	9.5	72.5	82.36	9.86	9.86	104
12H	14	0620	82.0	91.5	9.5	82.0	91.88	9.88	9.88	104
13H	14	0655	91.5	101.0	9.5	91.5	101.49	9.99	9.99	105
14H	14	0735	101.0	110.5	9.5	101.0	110.93	9.93	9.93	105
15H	14	0800	110.5	115.2	4.7	110.5	115.44	4.94	4.94	105
16H	14	0835	115.2	121.8	6.6	115.2	121.98	6.78	6.78	103

Table T2 (continued).

Core	Date (Sep 2013)	Time (h)	Top depth of cored interval DSF (m)	Bottom depth of cored interval DSF (m)	Interval advanced (m)	Top depth of recovered core CSF (m)	Bottom depth of recovered core CSF (m)	Length of core recovered (m)	Curated length (m)	Recovery (%)	
172	14	0900									
18H	14	0925	124.7	134.2	9.5	124.7	134.71	10.01	10.01	105	
19H	14	0955	134.2	143.7	9.5	134.2	144.28	10.08	10.08	106	
20H	14	1020	143.7	149.3	5.6	143.7	149.28	5.58	5.58	100	
21H	14	1110	149.3	158.8	9.5	149.3	159.18	9.88	9.88	104	
22H	14	1135	158.8	168.3	9.5	158.8	168.47	9.67	9.67	102	
23H	14	1200	168.3	177.8	9.5	168.3	178.29	9.99	9.99	105	
24H	15	1225	177.8	179.2	1.4	177.8	179.21	1.41	1.41	101	
Total advanced (m):					179.2	Total recovered (m):			180.70		

DRF = drilling depth below rig floor, DSF = drilling depth below seafloor, CSF = core depth below seafloor. APC = advanced piston corer, XCB = extended core barrel, RCB = rotary core barrel. H = APC system, numeric core type = drilled interval. NA = not applicable.

Table T3. XRD analysis of bulk samples, Site U1428.

Core section, interval (cm)	Top depth CSF-A (m)	Smectite (counts)	Illite (counts)	Kaolinite + chlorite (counts)	Quartz (counts)	K-feldspar (counts)	Plagioclase (counts)	Calcite (counts)	Dolomite (counts)	Halite (counts)	Pyrite (counts)
346-U1428A-											
1H-1, 89.0–90.0	0.89	344	661	559	2326	92	326	3092	0	400	111
2H-1, 91.0–92.0	7.31	364	784	471	3821	150	626	1171	0	326	86
3H-1, 84.0–85.0	16.74	227	392	266	3092	100	368	1759	0	270	73
4H-1, 86.0–87.0	26.26	207	451	266	2976	180	388	1619	0	240	80
5H-2, 70.0–71.0	37.1	230	385	252	2560	98	403	2349	0	224	92
6H-6, 94.0–95.0	52.84	249	560	387	3738	115	427	1433	0	283	45
7H-1, 109.0–110.0	54.99	418	903	518	3332	152	533	1790	100	286	68
8H-1, 119.0–120.0	64.59	337	714	447	3359	154	503	2102	111	249	62
9H-1, 125.0–126.0	74.15	312	483	309	2550	74	289	4047	111	214	120
11H-2, 63.0–64.0	93.04	284	722	436	3148	115	388	2024	240	267	78
12H-1, 120.0–121.0	102.6	293	621	339	2661	70	328	3959	0	216	117
13H-2, 122.0–123.0	113.62	387	812	508	4459	176	581	1254	0	206	40
14H-1, 127.0–128.0	121.67	401	813	451	3207	113	419	3207	0	192	66
15H-4, 9.0–10.0	134.24	547	1532	815	4245	300	776	2428	166	300	80

Table T4. XRD analysis of bulk samples, Site U1429.

Core section, interval (cm)	Top depth CSF-A (m)	Smectite (counts)	Illite (counts)	Kaolinite + chlorite (counts)	Quartz (counts)	K-feldspar (counts)	Plagioclase (counts)	Calcite (counts)	Dolomite (counts)	Halite (counts)	Pyrite (counts)
346-U1429A-											
1H-1, 110.0–111.0	1.1	185	340	316	2382	85	286	3126	0	310	114
1H-2, 123.0–124.0	2.73	247	541	369	3583	100	439	1825	0	292	80
2H-1, 122.0–123.0	7.62	197	474	294	3551	180	400	1362	0	275	95
4H-1, 130.0–131.0	26.7	232	462	304	3311	114	405	1901	0	252	72
5H-1, 130.0–131.0	36.2	266	493	335	3266	110	469	1929	0	235	75
6H-1, 102.0–103.0	45.42	317	524	323	2924	82	330	2754	0	229	68
7H-1, 119.0–120.0	52.79	247	428	296	2163	50	255	4039	0	227	142
8H-1, 105.0–106.0	62.15	320	584	361	3147	82	434	2193	0	306	100
9H-1, 65.0–66.0	71.25	260	663	441	3599	100	469	1743	81	260	69
10H-1, 110.0–111.0	81.2	370	746	404	3785	100	509	2322	70	236	60
11H-1, 120.0–121.0	90.8	349	938	593	4108	140	528	1497	90	261	57
12H-3, 93.0–94.0	103.03	234	402	300	2544	67	310	3429	237	249	99
13H-1, 85.0–86.0	109.45	238	442	295	2677	56	308	3654	248	223	85
15H-1, 113.0–114.0	119.23	250	590	377	3489	155	403	1543	300	221	85
16H-1, 70.0–71.0	128.3	338	834	488	3526	130	529	1952	169	261	50
17H-1, 77.0–78.0	137.87	330	526	365	2462	70	228	4322	70	201	154
18H-1, 63.0–64.0	147.23	284	477	334	2297	48	229	5248	0	197	149
20H-1, 105.0–106.0	157.15	281	709	436	3903	160	477	1371	124	243	50
21H-1, 82.0–83.0	166.42	370	658	380	2283	57	256	5391	50	184	164
22H-1, 87.0–88.0	175.97	413	847	506	4366	150	1145	2734	150	200	73

Table T5. XRD analysis of sand from Unit B, Site U1428.

Core, section, interval (cm)	Top depth CSF-A (m)	Smectite (counts)	Muscovite (counts)	Hornblende (counts)	Chlorite (counts)	Pyroxene (counts)	Quartz (counts)	K-feldspar (counts)	Plagioclase (counts)	Calcite (counts)	Dolomite (counts)
346-U1428A-											
15H-2, 7.0–8.0	131.47	580	2,183	390	1,055	638	16,053	786	6525	590	794
23H-2, 63.0–64.0	160.85	562	1,548	100	1,015	57	7,009	219	694	819	551
32H-2, 5.0–6.0	208.19	1,200	2,591	490	1,355	589	13,705	4,222	4,873	2,038	444



Table T6. Microfossil bioevents, Sites U1428 and U1429.

Core, section, interval (cm)		Event type	Bioevents and epoch boundaries	Age (Ma)	Depth CSF-A (m)				Depth CCSF-A (m)				Comments
Top	Bottom				Top	Bottom	Midpoint	±	Top	Bottom	Midpoint	±	
346-U1428A-5H-CC	346-U1428A-6H-CC	F	LO <i>Globigerinoides ruber</i> (pink)	0.12	44.83	54.17	49.50	4.67	46.80	56.11	51.46	4.65	
13H-CC	14H-CC	CN	FO <i>Emiliana huxleyi</i>	0.29	120.78	129.88	125.33	4.55	128.85	139.25	134.05	5.20	
346-U1428B-5H-CC	346-U1428B-6H-CC	F	LO <i>Globigerinoides ruber</i> (pink)	0.12	40.62	50.09	45.36	4.74	42.59	52.80	52.43	0.37	
13H-CC	14H-CC	CN	Interval occurrence of <i>Emiliana huxleyi</i>	<0.29	116.69	126.14	121.42	4.73	125.27	134.84	130.06	4.78	
14H-CC	NA	F	Co-occurrence <i>Globorotalia flexuosa</i> and <i>Globigerinoides ruber</i> (pink)	<0.40	126.14	NA			134.84				
346-U1429A-5H-CC	346-U1429A-7H-CC	F	LO <i>Globorotalia flexuosa</i>	0.07	44.78	61.38	53.08	8.30	47.57	65.59	56.58	9.01	No core catcher for 6H. Questionable, as very rare occurrence
7H-CC	8H-CC	F	LO <i>Globigerinoides ruber</i> (pink)	0.12	61.38	70.97	66.18	4.80	65.59	75.73	70.66	5.07	
13H-CC	15H-CC	CN	FO <i>Emiliana huxleyi</i>	0.29	116.42	128.05	122.24	5.82	124.13	135.76	129.91	5.78	No core catcher for 14H
21H-CC	NA	F	Co-occurrence <i>Globorotalia flexuosa</i> and <i>Globigerinoides ruber</i> (pink)	<0.40	175.75	NA			188.39				

NA = not available. CN = calcareous nannofossil, F = foraminifer. LO = last occurrence, FO = first occurrence.



Table T7 (continued).

Core, section, interval (cm)	Top depth CSF-A (m)	Bottom depth CSF-A (m)	Preservation	Abundance	<i>Braudosphaera bigelowii</i>	<i>Calcidiscus leptopus</i>	<i>Calcosolenia murrayi</i>	<i>Ceratolithus cristatus</i>	<i>Coccolithus pelagicus</i>	<i>Discoaster barbadensis</i>	<i>Emiliania huxleyi</i>	<i>Florisphaera profunda</i>	<i>Gephyrocapsa caribbeanica</i>	<i>Gephyrocapsa muelleriae</i>	<i>Gephyrocapsa oceanica</i> s.s.	<i>Gephyrocapsa</i> spp. (>4 µm)	<i>Gephyrocapsa</i> spp. large (>5.5 µm)	<i>Gephyrocapsa</i> spp. small (<4 µm)	<i>Helicosphaera carteri</i>	<i>Helicosphaera inversa</i>	<i>Helicosphaera pavimentum</i>	<i>Helicosphaera</i> spp.	<i>Helicosphaera wallichii</i>	<i>Oolithotus fragilis</i>	<i>Pontosphaera japonica</i>	<i>Pontosphaera multipora</i>	<i>Pontosphaera</i> spp.	<i>Pseudoemiliania lacunosa</i>	<i>Reticulofenestra minuta</i>	<i>Rhabdosphaera clavigera</i>	<i>Sphenolithus</i> spp.	<i>Syracosphaera</i> spp.	<i>Umbellosphaera irregularis</i>	<i>Umbellosphaera tenuis</i>	<i>Umbilicosphaera foliosa</i>	<i>Umbilicosphaera sibogae</i>	Comments								
14H-CC	126.14	126.19	G	D	R	R					A	A			C	A	F					R	R																						
15H-CC	134.99	135.02	G	C		R						R	C			A	R			R																									
346-U1429A-																																													
1H-CC	6.35	6.40	G	D		F		F		A		C			A	C	C	A	C	R		F				R			R				F												
2H-CC	16.11	16.16	G	D	R	F	R	F		A		C			A		A	C	R	R		F												F											
3H-CC	25.77	25.82	G	D	F	R	R	R		D		C			A	C	F	A	C	R		R			R										R										
4H-CC	35.27	35.32	G	D	R	C		C		D		C			A	F	D	F				F													R										
5H-CC	44.78	44.83	G	A		F	C	R	F	A	C		C		A	A	R	C	R			R			R																				
7H-CC	61.38	61.43	G	A		F		R		D	C				A	C	C	C	C			F	R																						
8H-CC	70.97	71.02	G	A		R				C	C				C	C	F	C	F			R																							
9H-CC	80.62	80.67	G	A		R		F		C	C	R	F		C	C		A	F			R	R	R																					
10H-CC	90.15	90.20	G	A		R				C	C				C	C		F	F																										
11H-CC	99.67	99.72	G	C		R				F	C				F	C		R	C																										
12H-CC	109.14	109.19	G	A		R		F		R	F	F			C		A	F		F		F				R	*																		
13H-4	114.57	114.58	G	C	R	R				R	F	F	R		C					R			R																						
13H-CC	116.42	116.47	G	F											F																														
15H-CC	128.05	128.10	G	A	R	C					F	F			C		F	R		R					R																				
16H-CC	137.60	137.65	G	D		R					A	F			A		D	F								F																			
17H-CC	147.12	147.16	G	D		F		F				A			C		D	F																											
18H-6	153.45	153.46	G	C		R		R	C		F	C	R		C		A								R																				
18H-CC	153.69	153.73	G	R					R						R					R																									
20H-CC	165.93	165.98	G	D		C	R				A	D			A		A	C			R	R																							
21H-CC	175.75	175.79	G	A		R					C	A	F		R		C	R																											
22H-2	178.04	178.09	G	F		R					F	C			F		F																												
23H-CC	188.23	188.28	M	F											F		F																												

* = reworked specimens. Preservation: G = good, M = moderate, P = poor. Abundance: D = dominant, A = abundant, C = common, F = few, R = rare, B = barren. Shaded intervals = barren. SEM = scanning electron microscope.



Table T9. Preservation and estimated abundance of diatoms, Holes U1428A and U1429. (Continued on next page.)

Core, section, interval (cm)	Top depth CSF-A (m)	Bottom depth CSF-A (m)	Preservation	Abundance	Actinocyclus curvatulus	Actinopychus senarius	Freshwater spp.	Azpeitia nodulifera	Chaetoceros spp. and similar spores	Cocconeis scutellum	Coccinodiscus marginatus	Coccinodiscus oculus-iridis	Coccinodiscus radiatus	Cyclotella striata	Diploneis bombus	Fragilariopsis doliolus	Hemidiscus cuneiformis	Paralia sulcata	Proboscía curvirostris	Rhizosolenia bergonii	Rhizosolenia styliformis	Shionodiscus oestrupii	Stephanopyxis turris	Thalassionema nitzschioides	Thalassiosira eccentrica	Thalassiosira leptopus	Thalassiosira lineata	Thalassiosira nidulus	Thalassiosira pacifica	Comments								
346-U1428A-																																						
1H-CC	6.32	6.37	G	A	F	R	A	R					C							D			R	A	A													
2H-CC	16.20	16.25	G	C		R	A	A					C							R	A		R	A	A	C							Silicoflagellates					
3H-CC	25.38	25.43	G	A		F	A	A					A	A	R					A			R	A	A	F	R						Silicoflagellates					
4H-CC	35.35	35.40	G	A	R		C	A				F	A	A	R					R			R	A	A	C	A						Silicoflagellates, reworked					
5H-CC	44.83	44.88	G	C	C	C	C	C					F							R	F			A										Silicoflagellates				
6H-CC	54.17	54.22	G	C	F	A	C	C				R	C	R						R	A		F	A														
7H-CC	63.84	63.89	G	A	C	C	C	C		R	F	C	A								A		R	F	A	A			R						Silicoflagellates, reworked			
8H-CC	73.41	73.46	M	C				F					R	R					R	F			A	A										Silicoflagellates, reworked				
9H-CC	82.72	82.77	M	C			C	R				F	R	R		R	R	C	R			R	A	A	A													
10H-CC	91.82	91.89																																	Sand			
11H-CC	102.15	102.20	M	F			R															F	A															
12H-CC	111.50	111.55	M	F				F					R							F				R	F	F										Silicoflagellates, reworked		
13H-CC	120.78	120.83	G	C			A	C					A	A						A			R	C	A											Silicoflagellates		
14H-CC	129.88	129.91		B																																		
15H-CC	137.30	137.35																																				
16H-CC	143.45	143.50																																				
18H-CC	153.83	153.88																																				
19H-CC	150.10	150.13																																				
346-U1429A-																																						
1H-CC	6.35	6.40	G	C		F	F	A					R	F	F					A				A	A													
2H-CC	16.11	16.16	G	A	C	R	A	A					F	R	F	R				A			R	A	A													
3H-CC	25.77	25.82	G	D	F	F		A					A	A	F					A			R	A	A													
4H-CC	35.27	35.32	G	C		F		F					R	A						F				C	F													
5H-CC	44.78	44.83	G	A	R		C	A					C	C	F	R				A				A	A													
7H-CC	61.38	61.43	G	C			F	R					R	R	F	R							R	A	F	R												
8H-CC	70.97	71.02	G	C			A						R										R	R	A	F												
9H-CC	80.62	80.67	G	C	R		C						F	A		R	R			A			R	A	A													
10H-CC	90.15	90.20	G	A	A			A					A	A									F	A														
11H-CC	99.67	99.72	G	C				F					C		R					A				R	R													
12H-CC	109.14	109.19	G	C			C	R					R	A	R	C				A			F	C														
13H-4, 149-150	114.57	114.58											F																									
13H-CC	116.42	116.47																																				
15H-CC	128.05	128.10	G	A	R								A	F						A				A	F													
16H-CC	137.60	137.65	G	C	R			A															F	A	R													
17H-CC	147.12	147.16	G	F				F					R		R									C	R		R											
18H-6, 0-2	153.45	153.46	G	A			R	F					A	F	R					A				R	F													
18H-CC	153.69	153.73																																				
20H-CC	165.93	165.98	G	F			C																	A	R													
21H-CC	175.75	175.79	G	C				R					R	F	R									A														



Table T9 (continued).

Core, section, interval (cm)	Top depth CSF-A (m)	Bottom depth CSF-A (m)	Preservation	Abundance	<i>Actinocyclus curvatulus</i> <i>Actinopychus senarius</i> Freshwater spp. <i>Azpeitia nodulifera</i> Chaetoceros spp. and similar spores <i>Cocconeis scutellum</i> <i>Coscinodiscus marginatus</i> <i>Coscinodiscus oculus-iridis</i> <i>Coscinodiscus radiatus</i> <i>Cyclotella striata</i> <i>Diploneis bombus</i> <i>Fragilariopsis doliolus</i> <i>Hemidiscus cuneiformis</i> <i>Paralia sulcata</i> <i>Proboscia curvirostris</i> <i>Rhizosolenia bergonii</i> <i>Rhizosolenia styliformis</i> <i>Shionodiscus oestrupii</i> <i>Stephanopyxis turris</i> <i>Thalassionema nitzschioides</i> <i>Thalassiosira eccentrica</i> <i>Thalassiosira leptopus</i> <i>Thalassiosira lineata</i> <i>Thalassiosira nidulus</i> <i>Thalassiosira pacifica</i>	Comments			
22H-2, 145–150	178.04	178.09		R					
23H-CC	188.23	188.28					R		Sand

Preservation: G = good, M = moderate. Abundance: D = dominant, A = abundant, C = common, F = few, R = rare, B = barren. Shaded intervals = barren.

Table T12. Ostracod abundance, Hole U1428A.

Core, section, interval (cm)	Top depth CSF-A (m)	Bottom depth CSF-A (m)	Preservation	Abundance	Ambocythere ?	Argilloecia	Aurila	Bradleya	Callistocythere	Cytheropteron	Henryhowella	Krithe	Legitimocythere	Loxococheidea	Munseyella	Pelecocythere	Propontocypris	Puriana ?	Falsoburtonia sp.	Bythoceratina sp.	Burtonia reticulosa	Undetermined 1	Undetermined 2	Undetermined 3	Subtotal ostracods
346-U1428A-1H-CC	6.32	6.37			2	1						5	8												16
2H-CC	16.20	16.25			1	1	1					14	3					1	2						23
3H-CC	25.38	25.43							2			14	3						1						20
4H-CC	35.35	35.40					2				1	22	1			1									27
5H-CC	44.83	44.88			1		9					9	6	1					3						29
6H-CC	54.17	54.22								1		2	6			3	3				1				15
7H-CC	63.84	63.89			3		2					6	6	1	1						1				20
8H-CC	73.41	73.46					4		1		1	11	2									2			20
9H-CC	82.72	82.77			2		1					5													8
10H-CC	91.82	91.89			2	2		1				2													7
11H-CC	102.15	102.20							1			15										1	1		19
12H-CC	111.50	111.55					2					9	5										1	4	21
13H-CC	120.78	120.83			3				1	1		5	3												13
14H-CC	129.88	129.91					1					1			1										3
15H-CC	137.30	137.35		B																					0
18H-CC	153.83	153.88		B																					0
19H-CC	150.10	150.13		B																					0
21H-CC	156.21	156.26		B																					0
23H-CC	168.32	168.37		B																					0
24H-CC	172.91	172.94		B																					0
26H-CC	182.90	182.90		B																					0
32H-CC	211.53	211.56		B																					0

Abundance: B = barren. Shaded intervals = barren.

Table T13. Calcium carbonate, total carbon (TC), total organic carbon (TOC), and total nitrogen (TN) contents on interstitial water squeeze cake sediment samples and additional discrete sediment samples (CARB and SRA), Site U1428. (Continued on next page.)

Core, section, interval (cm)	Top depth CSF-A (m)	Calcium carbonate (wt%)	TC (wt%)	TOC (wt%)	TN (wt%)
346-U1428A-1H-1, 53-54	0.53	24.0	4.44	1.55	0.30
1H-1, 145-150	1.45	22.7	4.14	1.42	0.25
1H-5, 9-11	5.70	14.1	2.93	1.24	0.24
1H-5, 57-58	6.18	12.7	2.75	1.22	0.22
2H-1, 145-150	7.85	12.0	2.58	1.13	0.21
2H-5, 6-8	12.46	14.7	2.99	1.24	0.23
3H-1, 5-6	15.95	14.3	3.13	1.41	0.22
3H-1, 145-150	17.35	14.5	3.07	1.34	0.23
3H-2, 6-8	17.46	15.2	3.16	1.34	0.24
3H-7, 56-57	25.18	13.0	2.84	1.28	0.21
4H-2, 8-10	26.98	14.9	3.07	1.29	0.22
5H-1, 18-19	35.08	28.6	4.44	1.01	0.20
5H-1, 145-150	36.35	27.6	4.46	1.16	0.20
5H-2, 7-9	36.47	24.6	4.13	1.18	0.21
5H-7, 58-59	44.48	28.9	4.44	0.98	0.19
6H-2, 7-9	45.97	37.6	5.60	1.10	0.19
7H-1, 40-41	54.30	17.7	2.98	0.86	0.17
7H-1, 145-150	55.35	17.5	2.99	0.89	0.18
7H-2, 11-13	55.51	17.4	3.01	0.92	0.18
7H-7, 40-41	63.30	12.8	2.35	0.81	0.17
8H-2, 7-9	64.97	18.7	3.24	0.99	0.18
9H-1, 30-31	73.20	30.3	4.47	0.83	0.16
9H-1, 145-150	74.35	30.1	4.48	0.86	0.17
9H-2, 9-11	74.49	31.5	4.60	0.82	0.16
9H-7, 50-51	82.37	13.5	2.20	0.59	0.15



Table T13 (continued).

Core, section, interval (cm)	Top depth CSF-A (m)	Calcium carbonate (wt%)	TC (wt%)	TOC (wt%)	TN (wt%)
11H-2, 20–21	92.61	19.9	3.41	1.03	0.19
11H-3, 8–10	93.99	19.4	3.24	0.91	0.18
11H-7, 59–60	100.42	37.7	5.40	0.88	0.15
12H-1, 145–150	102.85	30.7	4.66	0.98	0.17
12H-2, 8–10	102.98	29.8	4.30	0.73	0.16
13H-2, 8–10	112.48	18.8	2.94	0.68	0.16
13H-7, 39–40	120.23	22.4	3.20	0.51	0.15
14H-2, 8–10	121.98	24.7	3.51	0.54	0.16
15H-1, 145–150	131.35	37.4	4.98	0.50	0.14
15H-2, 1–3	131.41	5.6	0.71	0.04	0.07
15H-2, 9–11	131.49	31.1	4.22	0.49	0.14
15H-5, 24–25	135.66	5.5	0.38	0.00	0.07
23H-2, 145–150	161.67	10.3	1.56	0.32	0.13
23H-3, 3–5	161.75	10.3	1.51	0.28	0.12
23H-6, 105–106	166.95	11.0	1.62	0.30	0.13
346-U1428B-					
2H-1, 50–52	3.00	21.1			
2H-7, 30–32	11.80	14.5			
3H-1, 50–52	12.50	14.4			
3H-7, 30–32	21.30	13.6			
4H-1, 50–52	22.00	14.3			
4H-7, 30–32	30.80	15.5			
5H-1, 50–52	31.50	15.4			
5H-6, 140–142	39.90	18.5			
6H-2, 80–82	42.80	38.0			
6H-7, 30–32	49.52	14.5			
7H-1, 88–90	50.88	16.8			
7H-7, 30–32	59.30	14.5			
8H-1, 70–72	60.20	18.8			
8H-7, 40–42	68.91	29.9			
9H-1, 50–52	69.50	16.2			
9H-7, 30–32	78.26	21.4			
10H-1, 30–32	78.80	19.6			
11H-1, 70–72	88.70	14.7			
11H-7, 30–32	97.21	16.1			
12H-1, 70–72	98.20	19.7			
12H-7, 20–22	106.02	44.4			
13H-1, 70–72	107.70	43.5			
13H-6, 20–22	114.38	12.2			
14H-1, 70–72	117.20	16.0			
14H-6, 62–64	124.48	33.2			
15H-1, 70–72	126.70	11.8			
15H-4, 130–132	131.59	7.2			
15H-6, 50–52	133.72	18.1			
16H-1, 40–42	135.90	43.6			
16H-4, 40–42	139.25	5.3			

Table T15. Headspace (HS) gas concentrations, Site U1428.

Core, section, interval (cm)	Top depth CSF-A (m)	Sample type	Sediment volume (cm ³)	CH ₄ (ppmv) measured	Ethane (ppmv) measured	CH ₄ (ppmv) normalized	Ethane (ppmv) normalized	C ₁ /C ₂
346-U1428A-								
1H-2, 0-5	1.5	HS	4	0	0	0.00	0.00	
2H-2, 0-5	7.9	HS	4	0	0	0.00	0.00	
3H-2, 0-5	17.4	HS	3.2	2.12	0	3.31	0.00	
4H-2, 0-5	26.9	HS	3	2.59	0	4.32	0.00	
5H-2, 0-5	36.4	HS	3.4	3.95	0	5.81	0.00	
6H-2, 0-5	45.9	HS	3	50	0	83.33	0.00	
7H-2, 0-5	55.4	HS	3	7,869	0	13,115.00	0.00	
8H-2, 0-5	64.9	HS	3.2	4,815.18	0	7,523.72	0.00	
9H-2, 0-5	74.4	HS	3.2	8,683.05	0	13,567.27	0.00	
10H-2, 0-5	83.9	HS	2.8	7,486.25	0	13,368.30	0.00	
11H-3, 0-5	93.91	HS	3.6	5,417.79	0	7,524.71	0.00	
12H-2, 0-5	102.9	HS	3	3,262.51	0	5,437.52	0.00	
13H-2, 0-5	112.4	HS	3.2	2,218.66	0	3,466.66	0.00	
14H-2, 0-5	121.9	HS	3	2,416.89	0	4,028.15	0.00	
15H-2, 0-5	131.4	HS	3.2	1,608.42	0	2,513.16	0.00	
21H-1, 140-141	156.2	HS	4	2,297.54	0	2,871.93	0.00	
23H-3, 0-5	161.72	HS	3	3,323.53	0	5,539.22	0.00	
24H-4, 107-108	172.9	HS	3	2,644.49	0	4,407.48	0.00	
26H-5, 100-101	182.86	HS	4	3,172.5	0	3,965.63	0.00	
32H-4, 115-116	211.52	HS	3	6,537.19	4.13	10,895.32	6.88	1,582.85

Table T16. Calcium carbonate, total carbon (TC), total organic carbon (TOC), and total nitrogen (TN) contents on discrete sediment samples (CARB and SRA), Site U1429.

Core, section, interval (cm)	Top depth CSF-A (m)	Calcium carbonate (wt%)	TC (wt%)	TOC (wt%)	TN (wt%)
346-U1429A-					
1H-1, 19-20	0.19	16.0	3.09	1.17	0.16
1H-1, 38-39	0.38	24.2	4.49	1.59	0.22
1H-2, 9-11	1.59	18.2	3.20	1.02	0.17
2H-2, 8-10	7.98	11.7	2.51	1.11	0.17
3H-2, 9-11	17.49	15.8	3.09	1.19	0.18
4H-2, 9-11	26.99	15.4	3.31	1.46	0.20
5H-1, 9-10	34.99	17.1	3.00	0.96	0.16
5H-2, 10-12	36.50	15.3	2.74	0.91	0.16
6H-2, 9-11	45.99	20.0	3.64	1.25	0.18
7H-2, 9-11	53.19	33.3	5.33	1.33	0.18
7H-7, 40-41	61.00	33.5	5.03	1.01	0.15
8H-2, 10-12	62.66	17.1	3.12	1.08	0.17
8H-7, 9-10	70.15	10.5	1.52	0.26	0.05
9H-2, 9-11	72.19	17.7	3.05	0.93	0.16
9H-7, 60-61	80.20	14.8	2.60	0.83	0.15
10H-2, 12-14	81.72	18.8	3.37	1.12	0.17
11H-2, 12-14	91.22	14.8	2.82	1.05	0.16
11H-7, 66-67	99.27	28.5	4.40	0.98	0.13
12H-5, 2-4	105.12	18.7	3.24	1.00	0.15
13H-2, 6-8	110.16	31.8	5.08	1.27	0.16
15H-2, 8-10	119.68	13.6	2.61	0.98	0.16
15H-7, 50-51	127.59	18.1	3.45	1.28	0.18
16H-2, 8-10	129.19	20.5	3.64	1.19	0.18
17H-2, 8-10	138.66	30.6	4.38	0.71	0.12
17H-7, 64-65	146.67	32.2	4.68	0.82	0.12
18H-2, 7-9	148.17	40.5	5.57	0.71	0.11
20H-2, 8-10	157.68	14.4	2.40	0.68	0.13
20H-7, 46-47	165.52	37.4	5.59	1.11	0.16
21H-2, 7-9	167.17	42.9	6.09	0.96	0.14
21H-2, 7-9	167.17	42.5			
22H-2, 6-8	176.65	16.9	3.12	1.09	0.16
22H-3, 99-100	179.08	8.8	1.49	0.43	0.09

Table T17. Interstitial water chemistry, Site U1429.

Core, section, interval (cm)	Top depth CSF-A (m)	Sample type	Alkalinity (mM) Titration	pH ISE	Salinity (‰) Refract	Cl ⁻ (mM) Titration	Cl ⁻ (mM) IC	SO ₄ ²⁻ (mM) IC	Br ⁻ (mM) IC	Na (mM) ICP	Ca (mM) ICP	Mg (mM) ICP	K (mM) ICP	B (μM) ICP	Ba (μM) ICP	Fe (μM) ICP	Li (μM) ICP	Mn (μM) ICP	Si (μM) ICP	Sr (μM) ICP	NH ₄ ⁺ (μM) Spec	PO ₄ ³⁻ (μM) Spec	H ₄ SiO ₄ (μM) Spec		
346-U1429A-																									
1H-1, 0-5	0	ML	2.37	7.60	35.00	552.28	561.39	29.37	0.87	471.03	10.14	52.46	10.28	413.14	1.28	BD	25.62	4.71	127.52	91.70	25.05	1.70	103.69		
2H-1, 145-150	7.85	IW-Sq	3.63	7.48	35.50	547.67	564.00	28.75	0.88	470.78	9.99	50.73	11.76	492.15	8.68	1.44	26.69	22.00	737.41	92.24	237.79	15.96	713.31		
4H-1, 145-150	26.85	IW-Sq	10.31	7.53	35.00	546.50	554.85	22.08	0.88	458.32	7.48	49.17	11.11	477.22	12.60	2.70	26.09	3.34	794.79	89.60	1607.05	50.66	787.39		
6H-1, 145-150	45.85	IW-Sq	28.89	7.41	34.00	556.73	560.96	1.96	0.89	459.47	2.27	43.00	10.20	489.47	330.90	2.16	33.04	0.54	740.40	72.32	3314.17		750.15		
8H-1, 141-146	62.51	IW-Sq	27.73	7.47	34.00	558.37	554.55	1.92	0.96	455.93	2.20	39.74	10.52	495.00	411.42	BD	32.18	1.04	816.03	78.63	4254.91	75.81	829.21		
10H-1, 145-150	81.55	IW-Sq	26.47	7.54	34.00	551.62	555.71	1.96	0.96	471.55	2.52	39.37	11.07	429.45	347.85	2.40	36.94	3.74	835.81	83.44	4742.52	46.29	848.53		
12H-1, 145-150	100.55	IW-Sq	24.54	7.45	34.00	550.22	559.94	1.99	0.97					472.03	501.56	1.58	59.77	1.05	876.48	111.95	5146.93		874.42		
15H-4, 145-150	124.05	IW-Sq	21.41	7.62	33.00	547.97	546.51	1.89	0.96	462.05	4.07	32.58	10.22	364.53	431.36	2.49	70.11	4.62	848.77	122.77	5564.41	12.44	818.26		
18H-4, 123-128	151.83	IW-Sq	17.98	7.48	33.00	549.37	552.48	1.96	0.97												5519.93	10.51	930.38		
22H-1, 144-149	176.54	IW-Sq	12.87	7.60	33.00	551.47	556.21	1.90	0.97	453.71	5.10	27.87	8.34	346.46	388.74	BD	41.74	2.56	814.84	113.92	5479.01	5.36	794.96		
1H-4, 30-31	4.8	IW-Rh	3.35	7.43			551.19	28.33	0.86														13.43		
2H-4, 30-31	11.2	IW-Rh	4.36	7.56			553.13	27.30	0.86															24.12	
3H-4, 30-31	20.7	IW-Rh	9.11	7.58			561.84	24.18	0.88															38.68	
4H-4, 30-31	30.2	IW-Rh	12.27	7.53			559.51	21.37	0.89															51.80	
5H-4, 30-31	39.7	IW-Rh	20.25	7.52			557.40	11.31	0.90															80.31	
5H-7, 30-31	44.2	IW-Rh	28.44	7.71			553.57	3.00	0.88					497.26	204.51	BD	31.23	BD	756.11	69.54					
6H-1, 50-51	44.9	IW-Rh	29.56	7.54			563.71	2.58	0.93					468.10	275.12	BD	31.36	BD	643.48	71.71				89.52	
7H-4, 30-31	56.4	IW-Rh	27.61	7.52			552.31	1.91	0.94					529.65	508.27	BD	30.89	0.58	815.92	79.21				84.02	
8H-3, 30-31	64.36	IW-Rh	28.36	7.58			556.30	1.92	0.96					496.64	378.34	7.13	31.78	1.65	868.56	79.12				84.64	
8H-3, 90-91	64.96	IW-Rh	28.56	7.49			567.04	1.91	0.97															88.24	
8H-4, 30-31	65.86	IW-Rh	28.45	7.52			562.60	1.96	0.97																82.83
8H-7, 30-31	70.36	IW-Rh	28.55	7.58			563.29		0.94																76.15
9H-4, 30-31	75.4	IW-Rh	28.69	7.73			561.37	1.93	0.97																71.45
11H-4, 30-31	94.4	IW-Rh	25.21	7.53			557.19	1.93	0.97																38.18
12H-2, 30-31	100.9	IW-Rh	24.84	7.56			554.71	1.96	0.93																
12H-2, 80-81	101.4	IW-Rh	25.10	7.45			553.43	2.05	0.97																34.47
13H-4, 30-31	113.38	IW-Rh	23.90	7.70			559.92	1.90	0.94																26.06
15H-1, 55-56	118.65	IW-Rh	22.23	7.36			560.20	3.34	0.93																31.01
15H-1, 80-81	118.9	IW-Rh					553.56	2.01	0.96																25.56
15H-5, 80-81	124.9	IW-Rh					559.62	1.89	0.94																29.28

ML = mudline, IW-Sq = interstitial water from whole-round squeezing, IW-Rh = interstitial water from Rhizons. ISE = ion-selective electrode, Refract = refractometer, IC = ion chromatograph, ICP = inductively coupled plasma-atomic emission spectroscopy, Spec = UV-VIS spectrophotometer. BD = below detection.



Table T18. Headspace (HS) gas concentrations, Site U1429.

Core, section, interval (cm)	Top depth CSF-A (m)	Sample type	Sediment volume (cm ³)	CH ₄ (ppmv) measured	CH ₄ (ppmv) normalized
346-U1429A-					
1H-2, 0-5	1.5	HS	3	0	0.00
2H-2, 0-5	7.9	HS	3	1.76	2.93
3H-2, 0-5	17.4	HS	3.6	0	0.00
4H-2, 0-5	26.9	HS	3.4	2.41	3.54
5H-2, 0-5	36.4	HS	3	5.2	8.67
6H-2, 0-5	45.9	HS	3.4	1,937.78	2,849.68
7H-2, 0-5	53.1	HS	3	6,837.98	11,396.63
8H-2, 0-5	62.56	HS	3	13,488.71	22,481.18
9H-2, 0-5	72.1	HS	3	8,794.02	14,656.70
10H-2, 0-5	81.6	HS	3	10,635.06	17,725.10
11H-2, 0-5	91.1	HS	3	11,254.57	18,757.62
12H-2, 0-5	100.6	HS	3	10,828.38	18,047.30
13H-2, 0-5	110.1	HS	3.1	7,135.92	11,509.55
15H-2, 0-5	119.6	HS	2.9	5,065.31	8,733.29
15H-5, 0-5	124.1	HS	3.1	6,149.63	9,918.76
16H-2, 0-5	129.11	HS	3.1	4,400.85	7,098.15
17H-2, 0-5	138.58	HS	3.2	5,743.78	8,974.66
18H-2, 0-5	148.1	HS	3	10,463.75	17,439.58
21H-2, 0-5	167.1	HS	3	7,150.06	11,916.77
22H-2, 0-5	176.59	HS	3	2,530.25	4,217.08
23H-4, 93-98	188.18	HS	3	3,718.59	6,197.65

Table T19. Core disturbance intervals, Sites U1428 and U1429. (Continued on next five pages.)

Core, section, interval (cm)	Comments on disturbance	Drilling disturbance intensity	Comments
346-U1428A-			
1H-1, 0-140	Soupy	Slight	
1H-2, 0-130	Soupy and mixed with ash		
1H-CC, 0-15		Slight	
2H-1, 0-50	Slightly mixed sediments		
2H-6, 67-108	Soupy and mixed with ash		
3H-CC, 0-21		Slight	
4H-CC, 0-42		Slight	
5H-3, 10-62	Soupy and mixed with ash		
5H-4, 55-152	White soupy ash		
5H-5, 0-7	White soupy ash		
5H-5, 63-149	Soupy and mixed with gray ash		
5H-6, 0-92	Soupy gray ash-pumice		
6H-1, 0-18	Disturbed	Severe	
6H-5, 55-85	Ash patches		
6H-5, 85-97	Microfault		
8H-4, 0-70	Ash and mixed layers		
10H-1, 0-151	Soupy ash	Moderate	Not measured
10H-2, 0-136	Soupy ash		Not measured
10H-3, 0-150	Soupy ash		Not measured
10H-4, 0-150	Soupy ash		Not measured
10H-5, 0-150	Soupy ash		Not measured
10H-6, 0-151	Soupy ash		Not measured
10H-7, 0-54	Soupy ash		Not measured
11H-1, 0-51	Excluded on rig floor		
11H-1, 0-51	Void		
11H-2, 80-89		Slight to moderate	
11H-4, 79-84	Red-brown ash		
11H-7, 20-27	Gas expansion		
11H-7, 85-110	Gas expansion		
12H-1, 0-47	Void		
12H-2, 80-89	Void		
12H-2, 111-117	Soupy ash		
12H-4, 62-73	Gas expansion		
12H-4, 143-147	Void		
12H-5, 25-26	Crack		
12H-6, 0-90	White + gray ash mixed with sediments		

Table T19 (continued). (Continued on next page.)

Core, section, interval (cm)	Comments on disturbance	Drilling disturbance intensity	Comments
12H-6, 138–150	Void		
13H-1, 35–62	Ash		
13H-1, 138–146	Microfault		
13H-1, 147–150	Void		
13H-4, 145–150	Void		
13H-5, 145–150	Void		
13H-7, 29–30	Crack		
14H-2, 108–111	Crack		
14H-5, 56–60	Void		
14H-5, 110–125	Ash + mixed sediments		
14H-6, 108–122	Void		
14H-7, 66–71	Gas expansion	Slight	
15H-2, 93–94	Void		
15H-2, 110–126	Sand		
15H-3, 0–10	Sand		
15H-5, 0–73	Sand		Not measured
15H-6, 0–101	Sand		Not measured
16H-1, 0–132	Sand		Not measured
16H-2, 0–131	Sand		Not measured
16H-3, 0–123	Sand		Not measured
16H-4, 0–139	Sand		Not measured
16H-5, 0–84	Sand		Not measured
18H-1, 0–122	Sand		Not measured
18H-2, 0–104	Sand		Not measured
18H-3, 0–113	Sand		Not measured
18H-4, 0–118	Sand		Not measured
18H-5, 0–131	Sand		Not measured
18H-6, 0–109	Sand		Not measured
19H	Only CC		
21H-1, 0–141	Sand		Not measured
23H-1, 25–60	Gas expansion	High	
23H-4, 50–130	Mass transfer deposit	High	
23H-5, 98–118	Gas expansion		
23H-5, 0–17	Sand	High	
23H-6, 36–75	Gas expansion	High	
23H-6, 125–135	Sand	High	
23H-7, 0–102	Soupy ash	High	
24H-1, 0–84	Sand	High	Not measured
24H-2, 0–111	Sand		Not measured
24H-3, 0–85	Sand		Not measured
24H-4, 0–109	Sand		Not measured
26H-1, 0–85	Suck in	High	Not measured
26H-2, 0–92	Sand		Not measured
26H-3, 0–82	Sand		Not measured
26H-4, 0–76	Sand		Not measured
26H-5, 0–100	Sand		Not measured
32H-1, 0–114	Sand		Not measured
32H-2, 0–100	Sand		Not measured
32H-3, 0–122	Sand		Not measured
32H-4, 0–116	Sand		Not measured
346-U1428B-			
1H-1, 0–39	Soupy	Slight	
1H-2, 78–89	Soupy ash		
2H-1, 0–39	Soft tephra layer	Slight	
3H-1, 0–11	Mousselike	Slight to moderate	
3H-3, 0–150	Soupy ash + suck in		
4H-1, 0–17	Soupy		
4H-CC, 0–21		Slight	
5H-1, 0–23	Soupy	Slight to moderate	
5H-1, 22–49	Crack	Moderate to high	
5H-5, 122–150	Soupy ash		
5H-7, 0–57	Soupy ash		
5H-CC, 0–11		Slight	
6H-1, 0–150	Mousselike ash	Moderate to high	
6H-2, 0–58	Mousselike ash	Moderate	
7H-1, 0–5	Mousselike	Slight	
7H-1, 18–70	Sand mixed		
8H-1, 0–55	Mousselike	Slight to moderate	
8H-2, 77–80	Crack		

Table T19 (continued). (Continued on next page.)

Core, section, interval (cm)	Comments on disturbance	Drilling disturbance intensity	Comments
8H-6, 108–151	Ash		
8H-7, 0–29	Ash + gas expansion		
8H-7, 50–51	Crack		
8H-CC, 0–29		Slight	
9H-1, 0–38	Mousselike	Moderate	
9H-5, 25–151	Ash mixed		
9H-6, 0–57	Ash mixed		
9H-CC, 0–29		Slight	
10H-2, 50–57	Gas expansion		
10H-2, 57–63	Void		
10H-2, 119–125	Crack		
10H-3, 53–60	Void		
10H-4, 0–130	Soupy ash		
10H-5, 0–150	Soupy ash and sand suck in	High	Not measured
10H-6, 0–117	Soupy ash and sand suck in	High	Not measured
10H-7, 0–98	Soupy ash and sand suck in	High	Not measured
10H-CC, 0–33	Soupy ash and sand suck in	High	Not measured
11H-1, 0–54	Mousselike	High	
11H-3, 120–121	Crack		
11H-4, 28–29	Crack	Slight	
11H-4, 40–40	Crack		
11H-4, 49–55	Crack		
11H-6, 65–66	Crack		
11H-6, 104–105	Crack		
11H-7, 24–27	Gas expansion	Moderate	
11H-7, 34–38	Crack		
11H-CC, 0–34		Moderate	
12H-7, 0–41	Disturbed		
13H-1, 0–40	Soupy	High	
13H-1, 100–103	Crack		
13H-1, 126–130	Gas expansion		
13H-2, 26–35	Gas expansion		
13H-2, 145–150	Void		
13H-3, 66–98	Ash		
13H-4, 29–70	Gas expansion		
13H-6, 80–80	Crack		
13H-6, 102–109	Gas expansion		
14H-1, 0–26	Gas expansion	Moderate	
14H-2, 45–56	Gas expansion + void		
14H-3, 95–100	Void		
14H-4, 29–42	Gas expansion		
14H-5, 37–48	Gas expansion		
15H-1, 0–11	Gas expansion		
15H-4, 52–56	Sand mixed		
15H-4, 116–141	Sand		
15H-7, 22–58	Sand		
16H-1, 0–19	Sand mixed		Not measured
16H-1, 57–69	Gas expansion + void		Not measured
16H-1, 70–109	Sand mixed		Not measured
16H-2, 0–94	Sand		Not measured
16H-3, 0–133	Sand		Not measured
16H-4, 0–107	Sand		Not measured
16H-5, 0–140	Sand		Not measured
16H-6, 0–118	Sand		Not measured
16H-7, 0–80	Sand		Not measured
346-U1429A-			
1H-1, 0–150	Soupy		
1H-2, 0–150	Soupy + ash		
2H-1, 0–145	Mixed sediments?		
3H-1, 0–150	Soupy ash		
5H-1, 20–26	Microfault		
6H-1, 0–66	Gray ash		
6H-3, 0–150	Suck in	High	
6H-4, 0–150	Suck in	High	Not measured
6H-5, 0–123	Suck in	High	Not measured
7H-1, 0–44	Ash fall-in	Slight	
8H-3, 60–116	Ash		
9H-1, 0–16	Soupy	High	
9H-2, 50–52	Void		

Table T19 (continued). (Continued on next page.)

Core, section, interval (cm)	Comments on disturbance	Drilling disturbance intensity	Comments
9H-3, 147–150	Void		
10H-5, 15–55	Ash		
11H-3, 78–79	Crack		
11H-4, 45–55	Crack		
12H-1, 0–130	Ash		
12H-1, 130–150	Void		
12H-2, 0–149	Ash		
12H-3, 0–17	Disturbance		
12H-3, 145–150	Void		
12H-CC, 0–26		Slight	
13H-4, 0–149	mixed with ash		
13H-5, 0–103	Soupy ash		
13H-6, 0–80	Soupy ash		Not measured
15H-1, 0–73	Fall-in + sand	Moderate	
15H-1, 144–150	Void		
15H-2, 59–65	Void		
15H-CC, 0–35		Slight	
16H-7, 20–31	Gas expansion		
16H-CC, 0–31		Slight	
17H-1, 23–31	Gas expansion		
17H-7, 30–56	Gas expansion		
17H-CC, 0–34		Slight	
18H-2, 80–114	Ash		
18H-3, 0–55	Ash		
18H-5, 73–82	Gas expansion	Moderate to high	
18H-CC, 0–27	Suck in	Moderate to high	
20H-1, 0–15	Fall-in	Moderate	
20H-2, 0–4		Moderate	
20H-CC, 0–30		Slight	
21H-1, 0–8		Slight	
21H-2, 125–149	Ash		
21H-3, 0–8	Ash		
21H-CC, 0–23		Slight	
22H-3, 85–127	Sand + soupy	Suck in?	
22H-4, 0–102	Sand + soupy	Suck in?	Not measured
22H-5, 0–103	Sand + soupy	Suck in?	Not measured
22H-6, 0–88	Sand + soupy	Suck in?	Not measured
22H-7, 0–67	Sand + soupy	Suck in?	Not measured
22H-CC, 0–16	Sand + soupy	Suck in?	
23H-1, 0–93	Sand + soupy	Suck in?	Not measured
23H-2, 0–77	Sand + soupy		Not measured
23H-3, 0–91	Sand + soupy		Not measured
23H-4, 0–97	Sand + soupy		Not measured
346-U1429B-			
1H-1, 0–30	Soupy		
1H-2, 45–124	Ash + suck in	High	
2H-1, 0–13	Soupy		
2H-1, 110–149	Ash patches		
3H-1, 0–20	Soupy	High	
3H-4, 0–47	Soupy	High	
4H-1, 0–10	Soupy		
4H-2, 70–105	Soupy		
5H-1, 0–12	Soupy		
6H-5, 80–150	Ash + suck in	Severe	
6H-6, 0–150	Soupy ash suck in	Severe	Not measured
6H-7, 0–66	Soupy ash suck in	Severe	Not measured
6H-CC, 0–10	Suck in	Severe	
7H-1, 0–150	Soupy ash suck in	Severe	
7H-3, 0–150	Ash	High	
8H-1, 0–18	Disturbed		
9H-1, 0–19	Soupy		
9H-4, 34–36	Crack		
9H-6, 125–140	Gas expansion		
10H-1, 0–18	Soupy		
10H-7, 31–34	Void		
10H-2, 39–41	Crack		
10H-7, 32–46	Void		
11H-1, 0–33	Gas expansion		
11H-1, 100–140	Ash		

Table T19 (continued). (Continued on next page.)

Core, section, interval (cm)	Comments on disturbance	Drilling disturbance intensity	Comments
11H-3, 40–41	Crack		
12H-3, 54–56	Crack		
12H-4, 0–152	Ash	High	
12H-5, 0–150	Ash	High	
12H-6, 0–13	Ash	High	
12H-7, 0–96	Suck in	High	
13H-1, 0–26	Extruded onto the drill floor	Slight	Not measured
13H-3, 144–150	Void		
13H-5, 20–22	Crack		
13H-5, 30–32	Crack		
14H-1, 0–150	Suck in	Severe	Not measured
14H-2, 0–68	Soupy ash suck in		Not measured
14H-3, 0–78	Soupy ash suck in		Not measured
14H-4, 0–88	Soupy ash suck in		Not measured
14H-5, 0–57	Soupy ash suck in		Not measured
14H-6, 0–36	Soupy ash suck in		Not measured
15H	Suck in	High	Not measured
16H-1, 0–16	Fall-in	Moderate to high	
16H-3, 10–21	Disturbed		
16H-3, 142–150	Void		
16H-7, 10–91	Disturbed		Not measured
17H-1, 0–45	Fall-in	Moderate	
17H-3, 0–22	Gas expansion	Slight to moderate	
17H-4, 143–149	Void		
17H-5, 104–118	Gas expansion		
17H-5, 135–146	Gas expansion		
17H-6, 139–141	Crack		
17H-7, 38–43	Gas expansion		
18H-1, 0–3	Fall-in	Moderate to High	
18H-2, 55–56	Crack		
18H-3, 23–27	Gas expansion	Moderate	
18H-5, 35–43	Gas expansion		
18H-5, 82–92	Soupy tephra	Slight to moderate	
18H-6, 98–108	Gas expansion	Moderate	
18H-6, 117–123	Gas expansion		
18H-6, 134–137	Gas expansion		
19H-1, 0–12	Disturbed		
19H-1, 147–150	Void		
19H-2, 98–100	Crack		
19H-2, 115–149	Soupy ash		
19H-3, 0–12	Ash		
19H-3, 77–113	Ash		
19H-6, 115–120			
19H-7, 9–109	Mousselike, crushed core liner, massive disturbance	High	
20H-1, 0–4	Fall-in	High	
20H-7, 0–34	Ash		
21H-4, 0–10	Sand		
21H-4, 100–150	Sand		
21H-7, 61–64	Void		
22H-1, 0–89	Sand	High	Not measured
22H-2, 0–107	Sand		Not measured
22H-3, 0–132	Sand		Not measured
22H-4, 0–128	Sand		Not measured
22H-5, 0–125	Sand		Not measured
22H-6, 0–136	Sand		Not measured
346-U1429C-			
1H-1, 0–147	Mixed sediments?		
1H-2, 0–151	Ash		
1H-CC, 0–20		Slight	
2H-1, 0–50	Soupy		
2H-CC, 0–36		Slight to moderate	
3H-1, 0–35	Mousselike		
3H-3, 0–63	Soupy ash		
3H-CC, 0–30		Slight to moderate	
4H-1, 0–27	Mousselike	Slight to moderate	
4H-CC, 0–16		Slight	
5H-1, 0–50	Mousselike	Slight to moderate	
5H-3, 0–100	Crack within sediment vertically	Slight to moderate	
6H-1, 0–16	Soupy	Slight to moderate	

Table T19 (continued).

Core, section, interval (cm)	Comments on disturbance	Drilling disturbance intensity	Comments
6H-2, 120–150	Soupy		
8H-1, 0–20	Soupy	Slight to moderate	
8H-2, 0–150	Soupy ash		Not measured
8H-2, 0–17	Sand		
9H-1, 0–10	Soupy	Slight to moderate	
9H-6, 15–20	Disturbed?		
10H-1, 0–13	Disturbed?		
10H-1, 140–150	Ash		
10H-2, 0–27	Ash		
12H-1, 0–10	Disturbed		
12H-3, 130–151	Ash		
12H-4, 0–19	Ash		
13H-6, 70–149	Ash		
13H-7, 0–71	Ash		
14H-1, 0–82	Ash		
14H-2, 25–27	Crack		
15H-3, 15–134	Ash		
15H-4, 0–55	Suck in	High	Not measured
15H-CC, 0–24	Suck in	High	
16H-1, 0–56	Suck in	High	
16H-2, 0–129	Sand		Not measured
16H-3, 0–131	Sand		Not measured
16H-4, 0–128	Sand		Not measured
16H-5, 0–125	Sand		Not measured
16H-6, 0–118	Sand		Not measured
18H-1, 0–18	Sand	Slight	
18H-5, 143–148	Ash		
19H-1, 0–10	Crack		
19H-3, 112–123	Crack		
20H-1, 0–58	Extruded on rig floor, disturbed		
20H-2, 75–78	Crack		
20H-2, 133–139	Ash		
20H-3, 45–48	Ash patches		
20H-5, 0–59	Soupy ash		Not measured
21H-1, 0–20	Fall-in		
21H-2, 135–149	Ash		
21H-3, 0–13	Ash		
21H-3, 80–101	Sand		
21H-7, 48–79	Disturbed		
22H-1, 0–10	Fall-in		
22H-3, 52–57	Crack		
22H-6, 54–62	Crack		
22H-7, 53–69	Ash		
23H-1, 0–15	Fall-in		
23H-4, 95–150	Sand-mixed		
24H-1, 50–141	Sand		

Table T20. FlexIT tool core orientation data, Hole U1428A.

Core	Orientation angle (°)	Orientation standard (°)
346-U1428A-		
2H	53.795	0.427
3H	351.183	0.357
4H	228.572	0.232
5H	128.230	0.366
6H	345.852	0.274
7H	81.580	0.131
8H	252.958	0.195
9H	98.417	0.178
10H	78.355	0.158
11H	99.553	0.215
12H	178.189	0.109
13H	329.190	0.233
14H	263.116	0.141
15H	321.293	0.107
16H	246.720	0.448
18H	314.455	0.116

Table T21. NRM inclination, declination, and intensity data after 20 mT peak field AF demagnetization, Sites U1428 and U1429. (Continued on next page.)

Core, section, interval (cm)	Depth CSF-A (m)	Inclination (°)	Declination (°)	FlexIT-corrected declination (°)	Intensity (A/m)
346-U1428A-					
1H-1	0				
1H-1, 5	0.05				
1H-1, 10	0.1				
1H-1, 15	0.15				
1H-1, 20	0.2				
1H-1, 25	0.25				
1H-1, 30	0.3				
1H-1, 35	0.35				
1H-1, 40	0.4				
1H-1, 45	0.45				
1H-1, 50	0.5				
1H-1, 55	0.55				
1H-1, 60	0.6				
1H-1, 65	0.65				
1H-1, 70	0.7				
1H-1, 75	0.75				
1H-1, 80	0.8				
1H-1, 85	0.85				
1H-1, 90	0.9				
1H-1, 95	0.95				
1H-1, 100	1				
1H-1, 105	1.05				
1H-1, 110	1.1				
1H-1, 115	1.15				
1H-1, 120	1.2				
1H-1, 125	1.25				
1H-1, 130	1.3				
1H-1, 135	1.35				
1H-1, 140	1.4				
1H-1, 145	1.45				
1H-1, 150	1.5				
1H-2	1.5				
1H-2, 5	1.55				
1H-2, 10	1.6				
1H-2, 15	1.65				
1H-2, 20	1.7				
1H-2, 25	1.75				
1H-2, 30	1.8				
1H-2, 35	1.85				

Table T21 (continued).

Core, section, interval (cm)	Depth CSF-A (m)	Inclination (°)	Declination (°)	FlexIT-corrected declination (°)	Intensity (A/m)
1H-2, 40	1.9				
1H-2, 45	1.95				
1H-2, 50	2				
1H-2, 55	2.05				
1H-2, 60	2.1				
1H-2, 65	2.15				
1H-2, 70	2.2				
1H-2, 75	2.25				
1H-2, 80	2.3				
1H-2, 85	2.35				
1H-2, 90	2.4				
1H-2, 95	2.45				
1H-2, 100	2.5				
1H-2, 105	2.55				
1H-2, 110	2.6				
1H-2, 115	2.65				
1H-2, 120	2.7				
1H-2, 125	2.75				
1H-2, 130	2.8				
1H-2, 135	2.85	59.9	56.2		0.001215

Blank cells indicate depth levels where data were either not available (i.e., FlexIT-corrected declination data for nonoriented cores) or removed because of disturbance, voids, or measurement edge effects. Only a portion of this table appears here. The complete table is available in [ASCII](#).

Table T22. Results from APCT-3 temperature profiles, Sites U1428 and U1429.

Core	Minimum temperature at mudline (°C)	Average temperature at mudline (°C)	Depth CSF-A (m)	In situ temperature (°C)	Thermal resistance (m ² K/W)
346-U1428A-					
4H	7.24	7.38	34.9	10.30	44.31
7H	7.64	7.84	63.4	13.98	74.57
10H	6.98	7.53	91.9	16.24	100.96
13H	7.37	7.68	120.4	20.56	124.37
Average:	7.31	7.61			
346-U1429A-					
4H	7.12	7.04	34.9	8.93	37.04
7H	8.11	8.29	61.1	11.48	62.60
10H	7.64	7.83	89.6	14.08	95.80
13H	7.89	7.91	118.1	14.78	126.78
Average:	7.69	7.77			

In situ temperatures were determined using TP-Fit software by Martin Heesemann. Thermal resistance was calculated from thermal conductivity data (see “[Physical properties](#)”) corrected for in situ conditions (see “[Downhole measurements](#)” in the “[Methods](#)” chapter [Tada et al., 2015b]).

Table T23. Vertical offsets required to correlate specific features among cores from adjacent holes, Site U1428.

Core	Vertical offset (m)	Y/N
346-U1428A-		
1H	0	N
2H	0.434	Y
3H	0.924	Y
4H	1.746	Y
5H	1.974	Y
6H	1.943	Y
7H	2.889	Y
8H	3.631	Y
9H	4.204	Y
10H	5.893	Y
11H	5.817	Y
12H	6.314	Y
13H	8.068	Y
14H	9.365	Y
15H	9.667	Y
16H	9.667	N
17X	9.667	N
18H	9.667	N
19X	9.667	N
20X	9.667	N
21H	9.667	N
22X	9.667	N
23H	9.667	N
24H	9.667	N
25X	9.667	N
26H	9.667	N
27X	9.667	N
28X	9.667	N
29X	9.667	N
30X	9.667	N
31X	9.667	N
32H	9.667	N
346-U1428B-		
1H	0.023	Y
2H	-0.224	Y
3H	-0.092	Y
4H	0.922	Y
5H	1.974	Y
6H	2.705	Y
7H	2.439	Y
8H	3.448	Y
9H	4.020	Y
10H	4.909	Y
11H	5.821	Y
12H	6.337	Y
13H	8.584	Y
14H	8.702	Y
15H	10.740	Y
16H	10.740	N

Table T24. Splice intervals, Site U1428.

	Depth in Hole, core, section section (cm)	Depth CSF-A (m)	Depth CCSF-D (m)	Hole, core, section	Depth in section (cm)	Depth CSF-A (m)	Depth CCSF-D (m)	Data used to tie
346-				346-				
U1428A-1H-2	0.00	0.00	0.00	U1428A-1H-3	83.69	3.84	3.84	Blue
U1428B-2H-2	6.06	4.06	3.84	U1428B-2H-5	141.43	9.91	9.69	Blue
U1428A-2H-2	135.70	9.26	9.69	U1428A-2H-6	103.09	14.93	15.36	MS
U1428B-3H-3	45.71	15.46	15.36	U1428B-3H-6	130.34	20.80	20.71	Blue
U1428A-3H-3	88.70	19.79	20.71	U1428A-3H-6	73.97	24.14	25.06	Blue
U1428B-4H-2	114.20	24.14	25.06	U1428B-4H-7	23.81	30.74	31.66	Blue
U1428A-4H-4	1.38	29.91	31.66	U1428A-4H-6	121.32	34.11	35.86	Blue
U1428B-5H-2	138.49	33.88	35.86	U1428B-5H-5	145.97	38.46	40.43	MS
U1428A-5H-3	55.97	38.46	40.43	U1428A-5H-6	78.78	43.19	45.16	MS
U1428B-6H-2	45.74	42.46	45.16	U1428B-6H-5	116.19	47.66	50.37	Blue
U1428A-6H-3	102.39	48.42	50.37	U1428A-6H-7	6.29	53.46	55.41	MS
U1428B-7H-2	146.67	52.97	55.41	U1428B-7H-4	52.36	55.02	57.46	MS
U1428A-7H-1	67.31	54.57	57.46	U1428A-7H-6	44.27	61.84	64.73	Blue
U1428B-8H-2	28.37	61.28	64.73	U1428B-8H-7	8.13	68.59	72.04	MS
U1428A-8H-4	50.87	68.41	72.04	U1428A-8H-6	104.67	71.97	75.60	Blue
U1428B-9H-2	107.75	71.58	75.60	U1428B-9H-6	42.51	76.89	80.91	MS
U1428A-9H-3	80.14	76.70	80.91	U1428A-9H-6	39.72	80.80	85.00	Blue
U1428B-10H-2	9.19	80.09	85.00	U1428B-10H-4	130.00	83.80	88.71	
U1428B-11H-1	0.00	88.00	93.82	U1428B-11H-6	117.49	96.58	102.41	Blue
U1428A-11H-4	117.83	96.59	102.41	U1428A-11H-8	50.96	101.55	107.37	MS
U1428B-12H-3	52.98	101.03	107.37	U1428B-12H-6	56.20	105.22	111.56	Blue
U1428A-12H-3	84.48	105.24	111.56	U1428A-12H-6	84.68	109.69	116.00	MS
U1428B-13H-1	41.71	107.42	116.00	U1428B-13H-5	86.26	113.53	122.12	Blue
U1428A-13H-3	14.81	114.05	122.12	U1428A-13H-5	53.50	117.37	125.44	MS
U1428B-14H-1	24.18	116.74	125.44	U1428B-14H-6	90.15	124.76	133.46	Blue
U1428A-14H-3	69.84	124.10	133.46	U1428A-14H-6	76.29	128.48	137.85	Blue
U1428B-15H-1	110.76	127.11	137.85	U1428B-15H-4	124.07	131.53	142.27	Blue
U1428A-15H-2	120.36	132.60	142.27	U1428A-15H-6	101.00	137.18	146.85	

MS = magnetic susceptibility, Blue = RGB blue datum.

Table T25. Vertical offsets required to correlate specific features among cores from adjacent holes, Site U1429.

Core	Vertical offset (m)	Y/N	Core	Vertical offset (m)	Y/N
346-U1429A-			13H	6.663	Y
1H	0.173	Y	14H	6.624	Y
2H	0.478	Y	15H	7.186	Y
3H	0.640	Y	16H	6.301	Y
4H	2.352	Y	17H	8.152	Y
5H	2.793	Y	18H	9.172	Y
6H	3.911	Y	19H	10.989	Y
7H	4.211	Y	20H	11.865	Y
8H	4.762	Y	21H	11.629	Y
9H	5.406	Y	22H	11.629	N
10H	6.105	Y	346-U1429C-		
11H	6.528	Y	1H	0	N
12H	7.235	Y	2H	0.157	Y
13H	7.709	Y	3H	0.825	Y
14X	7.709	N	4H	2.309	Y
15H	7.646	Y	5H	2.410	Y
16H	8.031	Y	6H	3.796	Y
17H	9.858	Y	7X	3.796	N
18H	10.822	Y	8H	4.296	Y
19X	10.822	N	9H	4.506	Y
20H	12.128	Y	10H	5.140	Y
21H	12.643	Y	11H	5.457	Y
22H	12.248	Y	12H	5.996	Y
23H	12.248	N	13H	6.661	Y
346-U1429B-			14H	7.458	Y
1H	0.380	Y	15H	7.458	N
2H	0.300	Y	16H	7.227	Y
3H	0.686	Y	17X	7.227	N
4H	2.150	Y	18H	7.926	Y
5H	2.663	Y	19H	9.273	Y
6H	3.100	Y	20H	11.115	Y
7H	3.943	Y	21H	12.052	Y
8H	4.436	Y	22H	12.726	Y
9H	4.649	Y	23H	12.745	Y
10H	3.985	Y	24H	12.745	N
11H	5.208	Y			
12H	6.086	Y			

Table T26. Splice intervals, Site U1429.

Hole, core, section	Depth in section (cm)	Depth CSF-A (m)	Depth CCSF-D (m)	Hole, core, section	Depth in section (cm)	Depth CSF-A (m)	Depth CCSF-D (m)	Data used to tie
346-				346-				
U1429A-1H-1	0.00	0.00	0.00	U1429A-1H-4	9.09	4.59	4.76	MS
U1429B-2H-2	6.36	4.46	4.76	U1429B-2H-5	37.68	9.28	9.58	Blue
U1429A-2H-2	119.87	9.10	9.58	U1429A-2H-7	0.64	15.41	15.88	Blue
U1429B-3H-2	129.82	15.20	15.88	U1429B-3H-4	51.25	17.41	18.10	MS
U1429A-3H-2	5.87	17.46	18.10	U1429A-3H-6	131.14	24.71	25.35	Blue
U1429B-4H-1	130.13	23.20	25.35	U1429B-4H-7	26.83	31.17	33.32	MS
U1429A-4H-4	106.70	30.97	33.32	U1429A-4H-7	6.15	34.46	36.81	Blue
U1429B-5H-2	125.05	34.15	36.81	U1429B-5H-6	130	40.20	42.86	Blue
U1429A-5H-4	66.97	40.07	42.86	U1429A-5H-6	132.91	43.73	46.52	Blue
U1429B-6H-2	102.15	43.42	46.52	U1429B-6H-4	149	46.89	49.99	
U1429C-8H-1	0.00	48.80	53.10	U1429C-8H-2	146.94	51.77	56.07	Blue
U1429A-7H-1	25.46	51.85	56.07	U1429A-7H-6	141.39	60.51	64.73	Blue
U1429B-8H-2	138.93	60.29	64.73	U1429B-8H-6	50.46	65.40	69.84	Blue
U1429C-10H-2	20.05	64.70	69.84	U1429C-10H-6	139.28	71.89	77.03	Blue
U1429A-9H-1	102.74	71.63	77.03	U1429A-9H-6	79.12	78.89	84.30	Blue
U1429B-10H-3	88.19	80.31	84.30	U1429B-10H-6	127.99	85.29	89.27	Blue
U1429A-10H-3	6.97	83.17	89.27	U1429A-10H-5	130.6	87.41	93.51	Blue
U1429B-11H-2	90.32	88.30	93.51	U1429B-11H-6	139.51	94.83	100.03	Blue
U1429C-13H-2	37.20	93.37	100.03	U1429C-13H-6	110.27	100.10	106.76	Blue
U1429A-12H-1	42.87	99.53	106.76	U1429A-12H-6	33.04	106.88	114.12	Blue
U1429B-13H-4	32.24	107.45	114.12	U1429B-13H-7	110.37	112.74	119.41	Blue
U1429A-13H-3	7.71	111.70	119.41	U1429A-13H-5	71	115.29	123.00	
U1429A-15H-1	0.00	118.10	125.75	U1429A-15H-4	6.72	122.67	130.31	Blue
U1429B-16H-2	50.26	124.01	130.31	U1429B-16H-7	68.47	131.42	137.73	MS
U1429C-18H-4	59.95	129.80	137.73	U1429C-18H-5	148.41	132.18	140.11	MS
U1429B-17H-1	45.76	131.96	140.11	U1429B-17H-5	94.66	138.45	146.60	MS
U1429C-19H-3	17.59	137.33	146.60	U1429C-19H-6	56.9	142.25	151.52	Blue
U1429B-18H-1	135.03	142.35	151.52	U1429B-18H-5	95.47	147.95	157.13	MS
U1429C-20H-3	22.12	146.01	157.13	U1429C-20H-5	4	148.72	159.84	Blue
U1429A-18H-2	91.3	149.01	159.84	U1429A-18H-4	20.97	150.81	161.63	Blue
U1429B-19H-1	14.27	150.64	161.63	U1429B-19H-6	100.54	159.01	169.99	MS
U1429A-20H-2	26.64	157.87	169.99	U1429A-20H-5	71.49	162.79	174.92	MS
U1429B-20H-3	5.83	163.06	174.92	U1429B-20H-6	14.07	167.64	179.51	Blue
U1429A-21H-1	126.26	166.86	179.51	U1429A-21H-3	41.1	169.01	181.65	Blue
U1429C-23H-1	60.89	168.91	181.65	U1429C-23H-CC		78.03	190.78	

MS = magnetic susceptibility, Blue = RGB blue datum.